Universitat Autònoma de Barcelona

Automatized Nanoparticle Models Generation and Application to the Oxygen Evolution Reaction Catalyzed by IrO_2. Slab vs Nanoparticle Models.

Danilo GONZÁLEZ FORERO

UNIVERSITAT AUTÒNOMA DE BARCELONA

DOCTORAL THESIS

Automatized Nanoparticle Models Generation and Application to the Oxygen Evolution Reaction Catalyzed by IrO_2. Slab *vs* Nanoparticle Models.

Author:
Danilo GONZÁLEZ FORERO

Supervisors:
Dr. Luis RODRÍGUEZ SANTIAGO
Dr. Mariona SODUPE ROURE
Dr. Xavier SOLANS MONTFORT

A thesis submitted in fulfillment of the requirements for the degree of Doctor of Philosophy in the

Department of Chemistry

November 19, 2020

Abstract

Nanoparticles have a large impact in multiple scientific fields mainly due to i) their large specific surface area and ii) the possibility of tuning the electronic structure of the material by modifying its size and shape. This has been particularly relevant in the field of catalysis with precious transition metals. To characterize the nanoparticle catalytic properties several experimental and computational techniques have been developed. Most of the computational efforts devoted to understand the catalytic activity of nanoparticles, however, employ extended surfaces to represent the material. Indeed, to the best of our knowledge, few examples of reactions catalyzed by metal oxide nanoparticles have been studied by using nanoparticles models. This limits the exploration of particular sites only present in the nanoparticle surfaces and thus, the use of more realistic models is desirable. One of the bottlenecks in the use of realistic nanoparticle models is the fact that model construction is not straightforward, particularly for multicomponent materials such as transition metal oxides.

This thesis has two main parts. Firstly, we develop a computational tool able to construct nanoparticle models for multicomponent compounds with controlled stoichiometry and surface termination in an automatized manner, which removes human subjectivity and bias. Secondly, we use slab and nanoparticle models to evaluate the key factors that determine the water adsorption and the catalytic performance of IrO_2 for the oxygen evolution reaction (OER) by using DFT simulations. The OER performance of IrO_2

has been explored through the water nucleophilic attack (WNA) and oxo-coupling (I2M) mechanisms for both surfaces and nanoparticle models.

We have found that the water dissociation is controlled by the intrinsic material properties like the Ir acidity, the O_{br} basicity, the nature of the vacant site and the cooperative effects between adsorbed water molecules. Concerning the OER mechanism, our results suggest that both the WNA and the I2M mechanisms require radical intermediates to be feasible. Moreover, the WNA mechanism seems to be the most favorable for almost all studied sites on surfaces and nanoparticles. Indeed, the I2M mechanism only seems to be the preferred one on the (011) surface, were the oxyl character of O atoms on the surface is larger and the interatomic distance between the oxyl groups is rather short. Furthermore, and quite remarkably, the tip site of the nanoparticle exhibits an OER potential that is only slightly larger than the ideal one, thereby suggesting that tetracoordinated sites should be explored to improve the catalytic performance of IrO_2 for the OER.

Contents

1 Introduction

Nanoparticles commonly have characteristics that are significantly different from those of the same material in larger scale. This opens the door to obtain materials with new properties for several applications which includes biomedicine, catalysis, imaging, energy storage or art conservation among others. Their working mechanisms are, however, not well understood in most cases, which hinders their rational improvement. In this context, the use of computational chemistry based tools can help to rationalize these processes. For that, it is important to develop realistic nanoparticle models. This thesis is devoted to the development of a computational tool able to automatically build nanoparticle models of binary materials and the study of the oxygen evolution reaction catalyzed by IrO_2. This chapter includes an overview of the relevance of nanoparticles in modern science, their synthesis and characterization, stressing out their applications in catalysis. We also review the state of the art of nanoparticle modelling and the use of nanoparticles for the oxygen evolution reaction.

1.1 Nanomaterials

Nanoparticles can be defined as a group of atoms or formula units in the nanoscale. This includes sizes between 1 and 100 nm that have different physical and chemical properties than the bulk material. Many different factors are related with the properties variation at the nanoscale, one of them being the size which modifies the specific surface, and consequently, the catalytic, electronic and morphological properties.

One type of properties that are closely related with the nanoparticle size are the optical ones. For instance, gold nanoparticles solutions are in the range of red and purple, depending on their size, instead of the macroscopic yellow gold color. These color changes are related with the electron confinement that modifies their interaction with light. Similarly, other physical and chemical size dependent properties can be tuned by increasing or decreasing the nanoparticle size.

Another advantage of nanometric materials is that they have a large surface area compared with macroscopic ones, making them ideal for catalytic applications since the number of active sites per material quantity significantly increases. Catalysis with nanoscale materials is widely employed in diverse fields like petrochemistry, water treatment or clean fuels among others.[1] Several studies showed that the catalytic properties of nanoparticles are connected with their size and shape.[2–4] However, the connection between size, shape and nanoparticle activity is not always straightforward, in fact, it is very difficult to control the different variables during the synthesis.

Computational chemistry can help to clarify the relation between morphology and catalysis. The main limitations to employ computational chemistry techniques are the computational resources and the difficulty to build nanoparticle models. To study the electronic structure of nanoparticles, computational chemistry tools based on quantum chemistry are the most appropriated ones.

However, computational cost increases exponentially with the number of atoms. For instance, if we double the number of atoms, the computational cost is increased eight times. Regardless the elevated computational cost, some approaches to model nanoparticles have been employed. In an early stage the most common approach was to use small clusters. The main problem of a cluster approach is that a

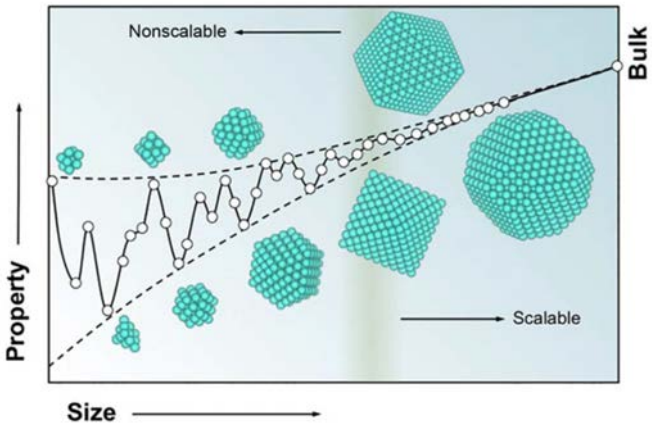

Figure 1.1: Property oscillation on nanoparticles by size change. The figure has been taken from[5]

small change on the atoms number or distribution strongly modifies

the properties, making difficult to scale them for larger nanoparticles. This can be observed in Fig. 1.1 where for small nanoparticles, an hypothetical property oscillates largely by small changes in the number of atoms. These small structures belong to the non-scalable regime. By increasing the cluster size, the property value oscillation decreases until it achieves convergence to bulk values. It is worth mentioning that each property could converges at different sizes.[2–4]

From a catalytic point of view, adsorption and desorption of chemical species on the nanoparticle surface are important properties. The influence of the nanoparticle size on catalysis has been particularly addressed on metallic systems. In these works the main conclusion is that for small nanoparticles, adsorption differs from this on extended surface which is related to three main facts: the flexibility of the nanoparticle surface, the electronic states separation and the lower coordination environments around the adsorption site.[4,6–10] As an example, experimental results shows that small gold nanoparticles are active to oxidize carbon monoxide whereas larger ones are inactive.[11] This could be related to CO and O adsorption. A theoretical study showed that small nanoparticles have higher adsorption energies and that for CO and O converges for nanoparticles larger than 561 atoms, the final adsorption energies being very similar to those on gold surfaces. The changes on the adsorption energy are related with the electronic perturbation due to the intrinsic nature of the adsorption site, mainly, the coordination of the nearest atoms. The O adsorption induces a large perturbation on smaller clusters that becomes local as the size of the cluster increases.[4] In Fig. 1.2 the charge density differences are represented.

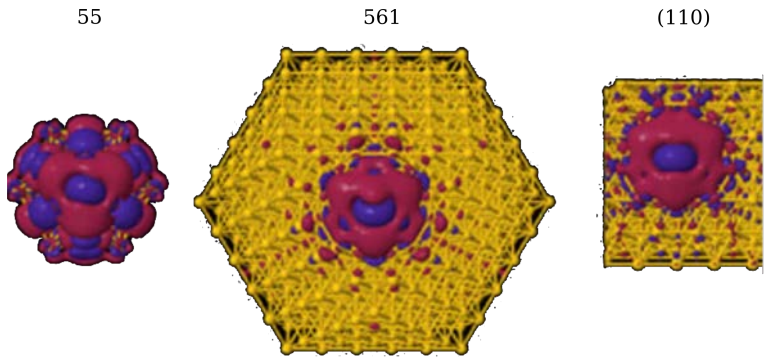

Figure 1.2: Charge density differences for adsorbed O on Au_{55}, Au_{561} nanoparticles and Au (110) periodic surface. The figure has been adapted from[4]

Not only the interaction between reactants and the material is different in nanoparticles and extended surfaces, but also, it is expected that their behavior diverges as function of the nanoparticle size. For example, the water dissociation process on Pt nanoparticles has been studied for clusters ranging from 13 to 140 atoms. Authors found that the computed adsorption energy varies slightly between sizes. However, the reaction and activation energies show different behavior and they fluctuate along the size range. In Fig. 1.3 the changes in activation energy due to the nanoparticle size are shown. These oscillations are related with the electronic and morphological properties of each model, hindering the extrapolation to other nanoparticles.[12]

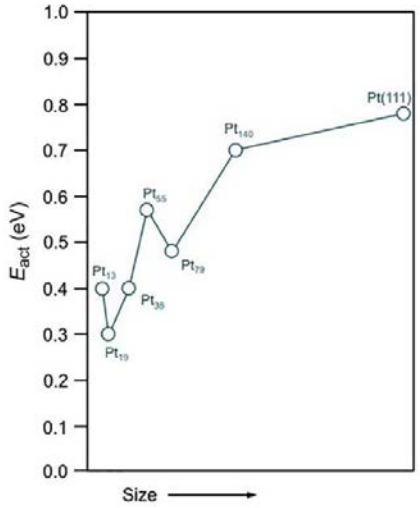

Figure 1.3: Oscillation of the activation energy by size changes on Pt nanoparticles. Larger nanoparticles are expected to be correctly reproduced using slab models. The figure has been adapted from[5]

.

1.2 Nanoparticle Synthesis and Shape Control

A very important requirement in the nanoparticle synthesis is the control of the structure, size and shape, or at least to exhibit a narrow size distribution of these properties. The most widely used techinques in nanoparticle syntesis consist in growing nanoparticles from a supersaturated precursor solution in aqueous or organic media in presence of capping agents. Such methods, like hydro-solvothermal or two phase techiques among others, allows to get the desired nanoparticles shape and sizes by tunning the reaction parameters, such as the time, temperature, preasure and reactants concentrations.[13–16]

In solutions, nanoparticle growth has been described by LaMer's model, which involves three main phases, the nucleation, the seed formation and the nanoparticle growing.[17] To ensure the uniformity of sythetized nanoparticles only one and sharp nucleation phase is desired.[13,15,16,18] Once the nucleation phase ends, particles grow fast forming seeds. Recently, it has been recognized that seeds facilitate shape control. Assuming epitaxial growth, the nanoparticle shape is determined by the seed morphology and thus by adding capping agents, the final shape can be easily altered by changing the surface stability. The capping molecules can selectively adsorb in an specific crystal facet controlling the particle shape at the atomic level. The selection of capping molecules is case dependent since strong adsorbed molecules limit nanoparticle growth, whereas weakly bound ones yield large particles or aggregates.

For metal oxide nanoparticles the usual capping agents are composed of a coordinating head group and a long alkyl chain. This provides a dynamic organic capping layer which renders the oxide nanoparticles highly stable in solution and also mediates their growth. For instance, TiO_2 nanoparticles have been modified by adding lauric acid surfactant. Carboxilyc acids bind strongly to anatase {001} facets, so lauric acid presence during the nanoparticle synthesis avoids epitaxial growing along these facets. As shown in Fig. 1.4, depending on the lauric acid concentration in solution one can obtain several nanoparticle shapes from the same seed, from (a) a octahedral bipyramidal seeds with eight {101} and two {001} faces, (b) bullet, (c) diamond and (d) rod-like.[19]

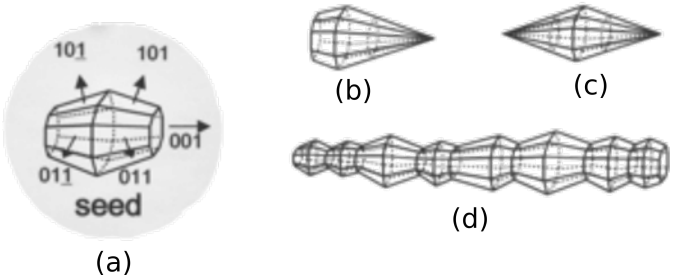

Figure 1.4: TiO_2 nanoparticle shape control by capping ligands. From (a) seed, (b) bullet, (c) diamond and (d) rod are obtained. Modified from[19]

The same kind of shape control mechanism also works for nanoparticles with exposed polar surfaces. For instance, ZnO-wurtzite nanoparticles have an hexagonal rod-shape with exposed (001) and (00$\bar{1}$) polar surfaces and a large population of nonpolar {010} facets. Experimental evidence suggest that the (00$\bar{1}$) facet is oxygen-rich and the (001) surface is Zn rich, being the latter responsible for their photocatalytic activity. The percentage of polar surfaces on ZnO nanoparticles can be increased by using capping agents that stabilize the polar surfaces. Citrate anions bind strongly to the Zn-(001) surface, therefore, the ZnO nanoparticle only grows in <010> directions producing hexagonal-nanoplates with a large presence of polar surfaces.[20]

As previously mentioned, capping agents can stabilize particular crystallographic orientations by decreasing the surface energy, thus changing the nanoparticle shape by thermodynamic control. However, the final nanoparticle shape is also under kinetic control, which means that perturbations in the temperature or in the available precursors can also determine the nanoparticle shape. Under equilib-

rium conditions, the nanoparticle shape is determined by the Wulff-Gibbs theorem, that relates the surface energy and the surface area. Thus crystallographic orientation with large surface energies have an small exposed area. Hence, the nanoparticle shape tend to be dominated by the most stable surfaces.

From a kinetic point of view, a pseudo Wullf theorem has been proposed suggesting that the unstable surfaces grow faster to reduce the surface area or disappear completely and stable surfaces grow slowly and dominate the final shape.[21] The reaction kinetics can be modified by changing the concentration or the temperature. For instance, $SmVO_4$ nanoparticles synthesized at low concentrations have a dot shape, whereas at high concentrations the nanoparticles become elongated from dot to rods (See Fig. 1.5). At low monomer

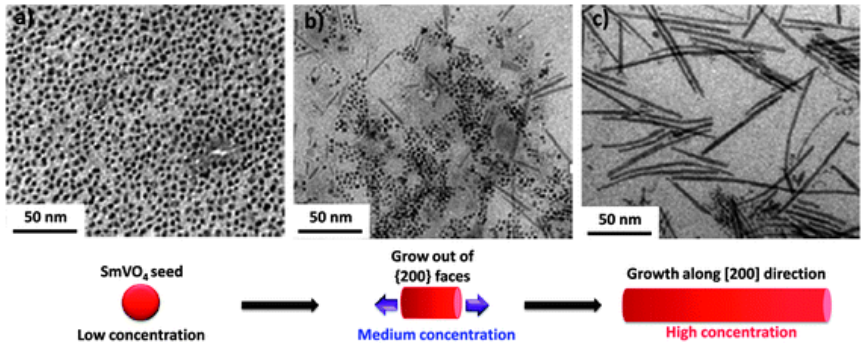

Figure 1.5: Effect of the precursor monomer concentration in the bulk solution on the shape evolution from nanocores to nanowires of $SmVO_4$. Adapted from[22]

concentrations, the reaction system reaches an equilibrium by dissolution of monomers from the less stable facet and the growing of

more stable ones, thus, spherical nanoparticles are obtained. In contrast, a higher monomer concentrations, the growing of less stable surfaces is faster than the dissolution process, therefore, rod nanoparticles being formed.[22]

Furthermore, assuming that the monomers adsorbed on the less stable surfaces moves through diffusion to more stable surfaces, temperature rising can play a role due to an increment of the diffusion rates. This is the case of Mn_3O_4 nanoparticles, that form cubic nanoparticles at low temperature, that are converted to spherical ones by increasing the temperature.[23]

Nanoparticle surface Due to the diverse synthesis methods, nanoparticle surface can have multiple kinds of terminations. Although it is clear that by adjusting the synthesis conditions, the final nanoparticle shape can be tunned, controlling the surface structure is quite difficult because multiple kind of processes are involved in the nanoparticle growing. Usually, once the nanoparticles are synthesized, they are washed and cleaned to remove synthesis precursors. However, in some cases, the capping agents are firmly attached to the nanoparticle surface and can include additional capabilities. For instance, Ru dyes with bidentate dicarboxylate groups like malonate or succinate have been used as a capping agent for the synthesis of IrO_2 nanoparticle. Those dyes can control the nanoparticle size and as photosensitizers stimulating the photochemical oxygen evolution reaction.[24]

Assuming that capping agent as well the synthesis precursors are removed, the exposed surface could have a crystalline surface with

or without point defects. For instance, TEM revealed defects like interstitial Ce atoms on {100} surfaces or even the presence of CeO_2 clusters on {110} and {100} facets of crystalline ceria nanoparticles in the early synthesis stages (See Fig. 1.6).[25]

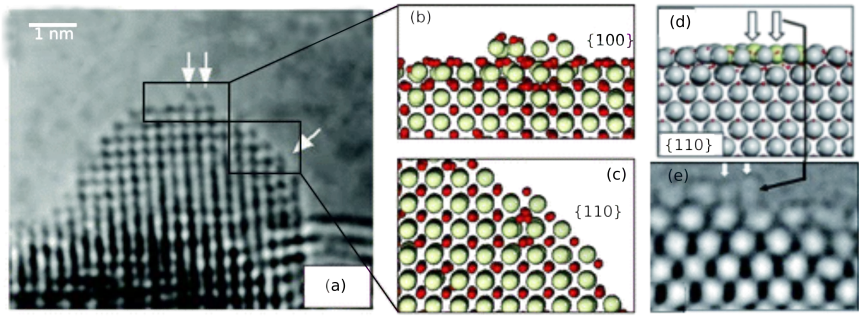

Figure 1.6: TEM images and model atomistic structures of ceria nanoparticles. (a,b,c) CeO_2 nanoparticle in early synthesis stages with amorphous terraces on {100} and {110} facets. (d) Interstitial Ce atoms on {100} surface.

In the case of nanoparticles with exposed polar surfaces, another kind of termination to stabilize these polar surfaces are possible, for instance, the Zn-(001) surface of ZnO-wurtzite nanoparticles can be hydroxylated in aqueous environments or fully oxidized on oxygen rich ones.[20,26]

1.3 Nanoparticles Characterization

The characterization of the plethora of generated nanoparticles requires the development of robust analytical techniques and the associated protocols to structurally characterize these materials. Among

the major problems of these protocols are the low amount of samples, the variety of sizes and shapes (even for the same batch production) and the diversity of synthetic procedures. Moreover, the available physicochemical techniques track down specific parts of the structure so is highly recommended to use a combination of those techniques to have an adequate characterization.[27,28] In this sense, in the last years, great progress has been done in the characterization of nanostructured materials by means of experimental techniques, even at the atomistic level. Here we only focus in the most commonly used techniques to characterize nanoparticles.

Transmission Electron Microscopy (TEM) Transmission electron microscopy allows to study the size, shape and structure of nanoparticles. When electrons interact with the nanoparticle, some of them are scattered and others are transmitted. The final image is built from the transmited electrons. TEM uses a high energy electron beam (usually in a range of 60 to 150 keV) on a small fixed sample to produce images with 0.05-0.1 nm resolution. In a TEM image it is possible to identify the size and shape and the internal structure of the nanoparticle. Although it provides the morphological information of the nanoparticle, not all types of materials can be used, since the image is obtained from the electrons that pass through the sample. Therefore, the samples should be as fine as possible to allow the electrons to penetrate. Moreover, by using high energy electrons, the measurement can damage the sample, particularly if it is an organic material. Finally, high energy electron sources are expensive to maintain.[29]

Scanning Electron Microscopy (SEM) Scanning electron microscopy uses lower energy electrons compared to TEM (<30 keV), therefore, it has a lower penetration on the material characterizing the sample surface. Electrons interacting with the prove surface can be scattered through two main ways: elastic or inelastic scattering. For the former, the electrons are scattered lossing around 50%. The number of scattered electrons is a function of the atomic number, the higher the atomic number, the higher the number of scattered electrons. Thus, processing the scattered electrons gives information about the surface atomic composition. For the latter, the interaction of the beam electrons with the material ones ejects an electron, commonly called secondary electron (SE). If the SE came from the inner electronic shell, an outer shell electron decays producing X-rays. SEs have an energy lower than 50 eV, hence, only the SE produced on the outermost atoms can escape from the surface. Thus, by counting the SEs, the surface topology can be reconstructed. Moreover, the X-rays can be processed to identify the surface elements. Commonly on SEM, only the SE are processed by an ETD or TLD detectors to get details of the material surface. However, additional detectors like BSED, to capture the scattered electrons, or EDS to detect the produced x-rays can be employed to get the chemical composition of the sample. To use SEM is mandatory to have a conductor surface. Thus to analyze non conducting materials, the sample has to be covered with a thin metallic film, which changes the material surface. This modification has to be taken into account to process the signals.[30]

Atomic Force Microscopy (AFM) In SEM and TEM, the measurements are related to the direct or indirect interaction with electrons. In atomic force microscopy, a sharp tip coupled to the end of a cantilever is used to interact with the material surface. The attraction or repulsion between the surface and the tip deflects the cantilever, a laser beam measures it, and the interaction force is constructed by processing the deflection. As a result, AFM gives a topological map of the surface of the material. One advantage of this technique is that it does not require surface modification. Moreover, the sample is not damaged. AFM is capable of giving the height of the nanoparticles as well as the size and shape. The resolution of AFM is closely related to the diameter of the probe, which ranges between 0.1 nm in vertical interactions and 30 nm for lateral ones. Besides size and shape, this method can be used to study the chemical and magnetic force, as well as the surface potential.[31]

In Fig. 1.7 an example of AFM, TEM and SEM characterization of spherical SiO_2 nanoparticles is shown. The illustration of AFM data has a grayscale on the right side that allows to include height details in the plot. The height information is commonly used to determine the diameter of the nanoparticles. By comparison with TEM and SEM, the predicted sizes obtained by AFM are larger.

X-Ray Methods Unlike the previously described techniques, X-ray methods can provide detailed information about the composition, crystal structure, surface state, bonding environment, and physical properties of the nanoparticle. When X-rays irradiate a nanoparticle, the light-matter interaction could lead to scattering, absorption,

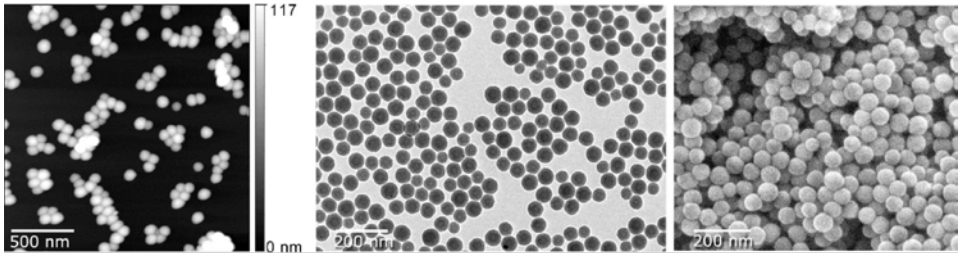

Figure 1.7: SiO_2 nanoparticles characterized by (a) AFM, (b) TEM and (c) SEM.Figure taken from[32]

emission refraction and reflection, or interference. Based on each effect or a combination of them, the nanoparticle properties can be determined. For instance, in X-ray diffraction (XRD) the diffraction angles are used to identify the diffracting (hkl) lattice planes. The width of diffraction peaks depends on the number of diffracting lattice planes, so it is possible to calculate the number of material layers in a corresponding direction. Thus, the entire diffraction pattern for a specific shape is morphology specific. Nevertheless, not all diffraction signals are obtained by the material's symmetry. Also, peaks for less abundant surfaces could disappear in the signal noise.[33]

X-rays could also induce the photoemission of an electron from the surface atoms inner shell electrons, the analysis of this ejected electrons leas to the fo called X-ray photoelectron spectroscopy (XPS). XPS is used to determine the chemical composition of the nanoparticle surface. This is done by measuring the kinetic energy of the ejected electrons. Therefore, the XPS spectra give straightforward information of the chemical composition of each element and oxidation state of each element existing in the nanoparticles.[34]

X-ray absorption techniques (XAS) are closely related to XPS. The main difference is that XAS gives a detailed track of the electronic transitions and ionizations. This is achieved by tuning the photon energy to a range where core electrons can be excited (0.1-100 eV). When the energy matches with an electronic ionization, a sharp edge in the absorbance is registered. For example, the highest energy edge corresponds to the ionization potential of the innermost 1s electron. Each element has a unique set of absorption edges corresponding to the binding energies of its electrons.[33]

Moreover, in addition to electron ionization, XAS can detect the 1s electronic transition to unoccupied orbitals and diverse scattering processes. The XAS spectrum can be divided into two main regions. One around 30-40 eV around the edge, and other beyond 40 eV. The first one is called x-ray absorption near-edge structure spectroscopy (XANES) and the second one is called extended x-ray absorption fine-structure spectroscopy (EXAFS).

XANES is highly sensitive to the formal oxidation state and the geometrical structure of the absorbing atom. Regarding the oxidation state, the ionization of less oxidated adsorbing ions requieres less energy than this for the more oxidated ones. For instance, the K-edge of Mn+4 is higher in energy than this for Mn^{+2}. Thus, XANES could be used to identify the oxidation state. However, other factors like coordination environment and the nature of the coordinated species has to be taken into account to analyze the XANES.

For energies higher than the K-edge, the photoelectron propagates from the absorbing atom as a spherical wave. This wave may then be backscattered by neighboring atoms producing oscillations in the

spectra. The interference between the outgoing and backscattered waves gives rise to the EXAFS. At higher energies above the edge (50-1000 eV), the photoelectron gains enough energy to just be scattered by one neighboring atom. Therefore, from EXAFS is possible have information about the distance, the number and the identity of the scattering neighboring atoms.[35]

Besides presented TEM, SEM, ATM and X-Ray based techniques, several additional techniques are available including mass spectroscopy, NMR, Electron tomography, among others.

1.4 Computational Approach to Nanocatalysis

Characterization of nanoparticles using the experimental described techniques allows establishing relationships between the structure of the nanomaterials and their chemical properties. As a powerful complementary tool, computational chemistry is usually used for assist in the establishment of these relationships. Indeed, a combination of both computational modelling and experimental data has been demonstrated to be a successful strategy to obtain detailed and accurate information of nanoparticles and their properties.[36–38] As remarked previously in Section 1.1, the main limitations of computational methods are the computational cost and the difficulty to build reliable nanoparticle models. The cluster approach is assumed to be

suited for the smaller size nanoparticles. However, for large nanoparticles, one can assume that the nanoparticle surfaces can be represented as crystalline surfaces as explained in the next subsection.

Crystalline materials, as well as extended surfaces, have translational symmetry, which implies that the whole structure is built by replicating the unit cell. For surfaces, the unit cell can be replicated on the two periodic dimensions or in three dimensions adding a large vacuum space on the surface direction. That is, the surface is represented as an slab after cutting the bulk along with the chosen crystallographic orientation. Slab models are films formed by a few atomic layers parallel to the surface plane of interest. Using the proper number of layers, these models could give an accurate representation of the macroscopic surface.

Building slabs for single component materials, like metals, gives only one possible surface termination, meanwhile for ionic ones, several terminations have to be taken into account. Those surfaces can be classified into three categories, known as Tasker's types:[39]

- Type 1: The slab has neutral layers with the same stoichiometry of the bulk material.
- Type 2: The slab has charged layers arranged symmetrically and the surface does not have a dipole moment perpendicular to the surface.
- Type 3: the slab has charged layers and the repeated unit has a net dipole normal to the surface.(polar surfaces)

Surfaces of types 1 and 2 are stable, but those of type 3, also known as polar surfaces, are unstable. The polar surfaces can be stabilized by intrinsic or extrinsic mechanisms that depolarize the surface. The intrinsic mechanisms correspond to the modification of the surface charges due to the electronic relaxation or the modification of the surface region composition by molecular reconstruction, whereas the extrinsic ones result from the adsorption species present in the medium. These mechanisms are not incompatible and can both occur on a polar surface depending on the conditions. Reviews and books devoted to identify and rationalize the depolarizing mechanisms can be found in references.[40–42] Once the slab model is constructed, one can optimize it to get the surface energy. This optimization changes the position of the surface atoms from their bulk positions to more stable new ones. In most cases, the surface atom positions suffer a minor change. This kind of reorganization is known as relaxation. However, in other cases the atomic positions could suffer a more considerable distortion, also forming new bonds, which is referred as surface reconstruction.

The resulting slab models have been successfully used to study nanoparticle catalytic properties, especially when modelling larged sized particles of the nano regime. For instance, the ammonia synthesis catalyzed by Ru nanoparticles has been studied using Ru slabs instead of larger and computationally more costly nanoparticle models.[43]For this reaction, experimental evidences suggest that the active catalytic sites are steps on the (001) nanoparticle facet[44] which were modeled using a slab of the (001) surface where two close-packed rows were

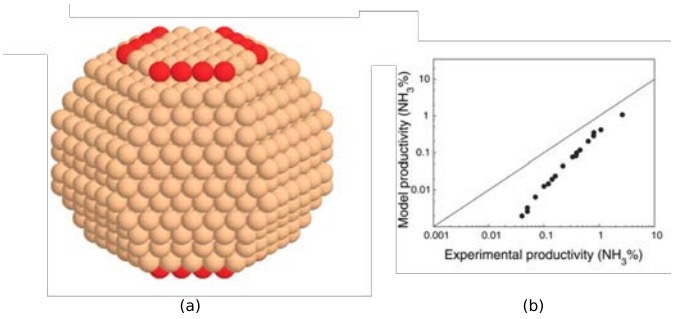

Figure 1.8: (a) Ru Wulff construction, in red active centers, (b) Comparison between theoretical and experimental values. Adapted from[43]

removed to form a step. Once the most active centers were determined, the number of active sites was estimated using a Wulff-like nanoparticle and the productivity of the active nanoparticle sites was calculated by Monte Carlo simulations. The direct comparison of the calculated and measured NH_3 can be observed in Fig. 1.8 and shows excellent agreement, proving the validity of the slab approach. Alternatively, in many cases, the reactivity of the nanoparticle is assumed to be similar to that of the most abundant surfaces. This approach does not take into account the role of tips, corner, edges which have a lower coordination than those in facets, thus they present slightly different properties.

1.4.1 Nanoparticle Model Construction

Slab models are well suited for large nanoparticles; however, it is difficult to take into account the effects of unique sites like tips, edges or

corners. Thus when the ratio of these sites in front of the clean sample is essential, modelization of the whole nanoparticle is mandatory. In addition, for nanoparticles with a few formula units and sizes under 5 Å, clear structures with experimental techniques are difficult to obtain. Unfortunately, computational modelling of NPs is not trivial, mainly because of the large variety of NP sizes and shapes that can be synthesized for any particular material. Thus, the reliability of the obtained computational models can be evaluated by calculating an observable, like vibrational spectra, and comparing it with the experimental one. Two usual strategies for designing realistic structural NP models are (i) the bottom-up[3,45–47] and (ii) the top-down approaches.[48–51]

Bottom-up The bottom-up procedure builds up NPs by joining atomic /molecular / cluster-sized entities, and it is useful when one aims to work in the lowest limits of the nanoworld. As we said previously, a nanoparticle contains several atoms, so a system with N atoms has 3N-6 degrees of freedom. Thus, the potential energy of the system is a 3N-6-dimensional surface energy, also called energy hypersurface or energy landscape. The energy landscape contains all the possible nanoparticle atomic conformations. In this energy landscape, we are interested in stationary points. A stationary point is that one that has all atomic forces equal to 0, so the idea is that modifying the structure in such a way that the atomic forces decrease, we can manage to find it.

One example of a stationary unstable point is a local maximum, where all forces are equal to 0, but at least one vibrational frequency

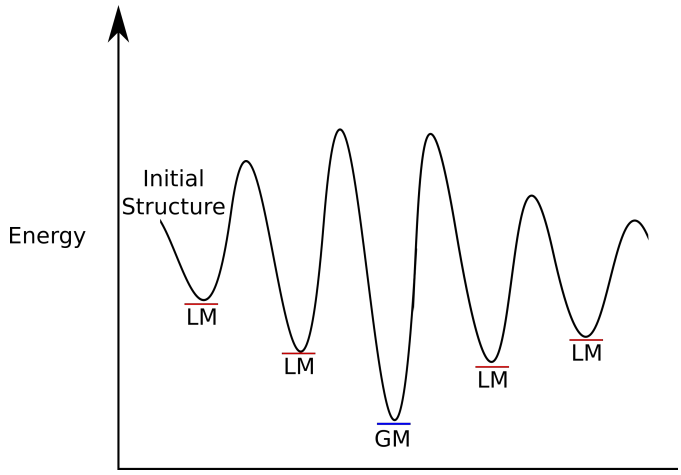

Figure 1.9: Global optimization algorithm allow to visit multiple local minimum (LM) and the global minimum(GM) configurations.

is negatives, thus, a change in the atomic positions produce a change in energy. Alternatively, a local minima are characterized by all positive vibrational frequencies, at they any structural distortion increases they potential energy.

The energy landscape usually has multiple LM and only one global minimum (GM). The main difference is that the LM is not the lowest point in the energy landscape; meanwhile, the global minimum is. Fig. 1.9 shows a unidimensional energy landscape and LM and GM are indicated. Thus, a confident theoretical study must unravel the rich energy landscape, including all the NP isomers.

The most employed algorithms to find GM are genetic algorithms,[52] basin hopping,[53] particle swarm optimization,[54] artificial bee colony (ABC),[55] simulated annealing[56] and minima Hopping[57] among others. The computational cost of those algorithms increases with the

nanoparticle size and the energy calculation theory level. For instance, get the GM using DFT methods for larger systems are completely untreatable. These approaches have been employed for pure metal nanoparticles, metallic alloys, metal oxides and also more complex compounds like forsterite among others.[2,58–62]

A common way to use those algorithms is to first use a cheap energy calculator, like molecular mechanics-based force-field, to get initial candidates, and then, use refined DFT calculations to find the GM. With these approaches it is possible to see the limit between non-bulk and bulk structures, also phase changes between different polymorphs. As an example, ZnO GM switches from non-crystalline bubble like structures (single and multilayered cages (SC,MC)), to wurtzite (WZ), sodalite (SOD) and body centered tetragonal (BCT) crystalline polymorphs along a range of 10 and 1026 formula units. In Fig. 1.10 the transition is shown. The crystalline structures starts to appear for 6 formula units, but become the most stable conformations from 324 formula units. This work also predicts that wurtzite nanoparticles are the most stable for sizes larger than 2200 formula units.[63,64] It should be pointed out that the transition between non-crystalline and crystalline structures is totally material dependent and can not be generalized.

Top-down For large nanoparticles the common approach is to assume that their morphology is closely related to that of crystal bulk. The nanoparticle crystalline shape depends on the energy to form surfaces, edges and vertices as well as strain effects. From a certain size, strain effects are negligible and the formation energy of edges

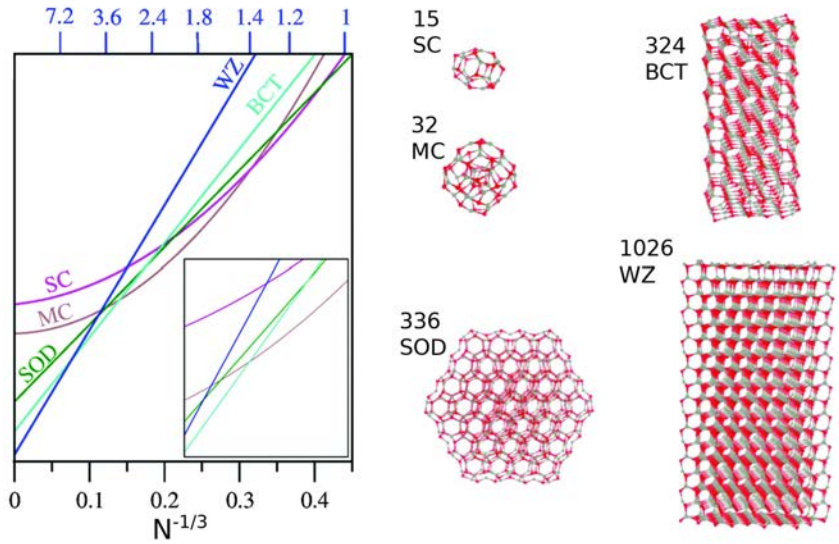

Figure 1.10: Fit lines of calculated relative energies of nanoclusters/nanoparticles and bulk phases with respect to $N^{-1/3}$ (lower x-axes) and approximate diameter (upper x-axes) for single-layered cages (SC), multi-layered cages (MC), sodalite (SOD), body centered tetragonal (BCT), and wurtzite (WZ) ZnO polymorphs and some example structures. Adapted from.[64]

and vertices is less decisive. Thus, the crystal morphology is obtained by the Wulff construction, which is based in the Gibbs-Wulff theorem, that postulates that under thermodynamic equilibrium a crystal has the structure that minimizes the surface energy. The surface contribution can be estimated by a vector perpendicular to the surface (i) from the center of a crystallite, whose length (l_i) is proportional to its surface free energy (γ_i):

$$l_i = c_i \gamma_i, \tag{1.1}$$

where c_i is a proportionality coefficient. The final Wulff construction is a polyhedron whose shape only depends on the ratios of surface energy and the proper material symmetry.[21,51,65–72] For instance, in Fig. 1.11, the Wulff construction and the bulk material of IrO_2-Rutile are shown. To get the Wulff construction nanoparticle, also called Wullf-like nanoparticle, atoms beyond the Wulff polyhedron should be removed.

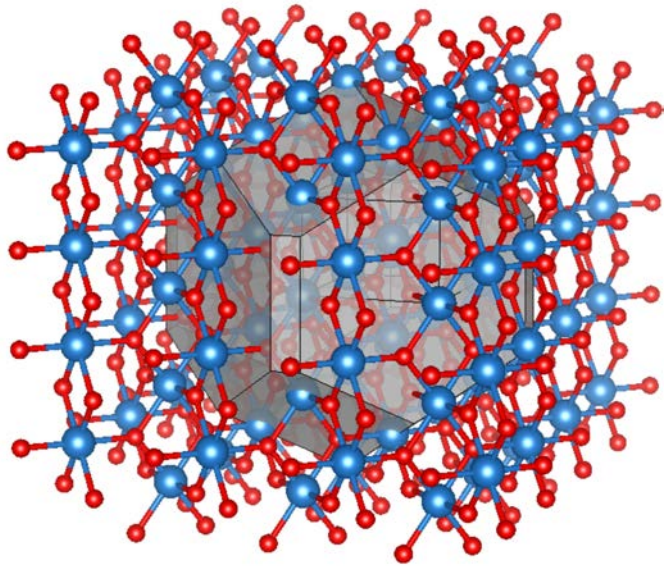

Figure 1.11: Wulff construction based nanoparticle. In gray the Wulff polyhedron that delimitate the nanoparticle.

Even though Wulff construction ensures that the obtained nanoparticle has the smallest free energy, it is well known that exposed shells of the material can suffer relaxation or reconstruction, so this nanoparticle can also be employed as a starting geometry for GM search. As we said previously, the structure of nanoscale entities can not be

assumed per se, but it is usually accepted that nanoparticles larger than 2-3 nm are probably crystalline.[46,64,65,69]

There are several available codes capable of building Wulff constructions from the surface energy ratios and the symmetry group of the material.[73–77] Some of them allow obtaining atomistic models for single-component materials. As an example, the suite of Python tools implemented in the atomic simulation environment (ASE) allows generating Wulff-shaped nanoparticle models of metals.[73] Moreover, multicomponent nanoparticle models for some materials where stoichiometry is obtained without further manipulation can be generated with some other pieces of software.[73–77] However, the procedure is not general for all binary systems, since, in most cases, post-processing is mandatory to obtain stoichiometric and charge electroneutral models. The most usual post-processing operation is the hand cleaning, that is, the removal of the excess atoms or the addition of missing ones to reach the desired structure. As a consequence, the success on obtaining a realistic model strongly depends on the user abilities and subjectivity. Accordingly, the models can suffer from human bias, and mistakes are likely to happen.

Noteworthy stoichiometric nanoparticles are not always the most representative models for some particular systems. In this context, the presence of singly coordinated atoms in the final nanoparticle model may lead to structures with lower stabilities than non-stoichiometric materials, where some of the ions are oxidized or reduced. In addition, sometimes, the exposed surfaces are polar, which

are known to be highly unstable. Therefore, their presence is generally accompanied by an important surface reconstruction or addition of medium ions to reduce the polarity.[41,42,78,79] As a consequence, the design of any automatic protocol for generating nanoparticle models requires including some optionality accounting for these non-stoichiometric surface terminations. Indeed, the development of a computational tool able to generate binary and ternary nanoparticles with controlled termination is one of the main objectives of this present thesis. The catalytic activity for the oxygen evolution reaction of some of the designed models will be also studied in the second part of the thesis with the aim of understanding the difference between periodic surface and discrete systems.

1.5 Oxygen Evolution Reaction

Energy conversion and storage from renewable sources is the most promising solution to significantly reduce the consumption of non-environmental friendly resources, like coal or petrol. Photo-electrocatalytic water splitting is one of the brighter and active research fields. Inspired by photosynthesis, where the main goal is to harvest solar energy and saving it in chemical bonds, water splitting aims to store energy as hydrogen molecules. The splitting of H_2O harvest energy as H_2 by producing it and O_2 from water. Afterwards, the stored energy can be used in a fuel cell by recovering the H_2O from H_2 and O_2.Thus, the spliting of H_2O implies two procesess: The formation of H_2 is ussually refered as hydrogen evolution reaction and in an electrochemical cell occurs in the cathode. The

formation of O_2 is called oxygen evolution reaction and it occurs in the anode. The OER is know to be the electrochemical limiting process as it presents slow kinetics and requieres high potentials to occur. Indeed, the OER is associated with a Gibbs energy (ΔG) of 4.92 eV. Since the global process implies four electrons, the electrochemical potential required to start the reaction is the energy of the global process divided by four. Thus leads to a ideal potential of 1.23 V vs NHE. However, the water splitting requieres potentials higher than the minimum one. The difference between the requiered and the ideal potential is called overpotential (η).

OER is a complex multistep reaction that involves several electron transfers and bond breaking and formation. This complex process requires a catalyst to take place, that can be a bare metal, molecular complexes or a transition metal oxide surfaces or nanoparticles. To convert the promising OER to a feasible economic way to store energy it is necessary to find an effective electrocatalyst that can lower the overpotential. The OER can be done in three pH regimes, alkaline, neutral and acidic, being the latter easy to scale to massive production. In particular, RuO_2 and IrO_2 catalysts are among the most promising ones as they are the most stable in acidic conditions. RuO_2 is the one that has the best catalytic performance, but is quite sensitive to corrosion, reducing the electrodes lifetime. IrO_2 has a good performance and strong resistance to corrosion making electrodes more stable.[80–82] Thus, we focus on OER in an acidic regime.

To the best of our knowledge, the mechanism of OER reaction is not completely understood, given space for some proposals. Two main reactions have been proposed: The water nucleophilic attack (WNA)

and oxo coupling (I2M) that involves one or two neighbor metallic centers, respectively. The WNA involves four reactions:

$$\begin{aligned} M + H_2O &\longrightarrow M{-}OH + H^+ + e^- \quad (1) \\ M{-}OH &\longrightarrow M{-}O + H^+ + e^- \quad (2) \\ M{-}O + H_2O &\longrightarrow M{-}OOH + H^+ + e^- \quad (3) \\ M{-}OOH &\longrightarrow M + O_2 + H^+ + e^- \quad (4) \end{aligned}$$

I2M involves 3 main reactions:

$$\begin{aligned} 2\,M + 2\,H_2O &\longrightarrow 2\,M{-}OH + 2\,H^+ + 2\,e^- \\ 2\,M{-}OH &\longrightarrow 2\,M{-}O + 2\,H^+ + 2\,e^- \\ 2\,M{-}O &\longrightarrow 2\,M + O_2 \end{aligned}$$

Theoretical studies of OER using DFT calculations commonly assumes that the proton and electron transfer are coupled and do not considered additional surrounding water molecules.[83–88] Each of the previously proposed equations has an associated ΔG that is directly related to the electrode potential. An ideal electrocatalyst is the one operating at zero overpotential. That means satisfying

$$\Delta G = 4 \times 1.23 \text{ eV} = 4.92 \text{ eV}. \quad (1.2)$$

That is, all proton coupled electron transfer reactions will take place at a potential just above 1.23 eV. However,real catalysts do not show this behavior. The catalytic performance is estimated by the magnitude of the potential determining step, that is the reaction step with the largest ΔG

$$G^{OER} = max[\Delta G]. \quad (1.3)$$

The thermodynamic overpotential is given by:

$$\eta^{OER} = (G^{OER}/e) - 1.23V. \tag{1.4}$$

To reduce the overpotential, the binding energies of $-$OH, $-$O and $-$OOH has to be optimum, that means that the adsorbate has to be adsorbed strongly enough to promote the reaction and but sufficiently weak to be easily removed at the end of the process. This is particularly important for the $-$OOH and $-$OH species that have been suggested from computational chemistry to be essential in determining the overpotential.[83]

Theoretical modelization can contribute to the understanding of the nature of the active sites and the elementary steps involved in the OER. This knowledge is fundamental to unveil the OER mechanism and for the rational design of new OER catalysts with lower overpotentials.

OER catalyzed by IrO_2 Under acidic conditions, it is widely recognized that amorphous IrO_2 materials show a lower overpotential and higher currents per surface area than their rutile-like crystalline analogues.[89–94] The larger catalytic activity has been associated with the presence of Ir(III) metal cations.[90–93] However, amorphous IrO_2 materials are less stable than the crystalline analogues and the deactivation mechanisms are under discussion.[95,96]

As previously explained, while the OER mechanism has not been well determined, some valuable mechanistic insights have been reported. Experimental evidences suggest that WNA and OC could occur on IrO_2, and that part of the O_2 evolves from the material surface.[95,97] Regarding the oxidation states, it has been proposed that Ir active centers can be Ir(V),[98] Ir(IV)[99,100] even Ir(III) or a mixture of oxidation states.[101] Clearly, the oxidation state of the Ir metallic centers in OER is not well defined. For the adsorbed intermediates, XPS shows that M−OH and M−O coexist in the process.[98] Further spectroscopic evidences also suggest the presence of M−OOH species.[102]

To the aim of getting meaningful information of the OER at the atomic level, several computational works have been done.[83–88] To the best of our knowledge, the seminal works of Rossmeisl and coworkers give the fundamental methodological background for theoretical thermochemistry of OER on solids.[83] The method consists on the computation of the binding energy of oxygen intermediates to a multilayer slab using DFT and include entropic and zero-point corrections for each step. For IrO_2 (110) surface, an overpotential of 0.56 V was predicted. The reported experimental values for this surface are close to 0.4 V.[103]

Furthermore, Gauthier and collaborators have shown that neighboring adsorbed species plays an important role on the stability of adsorbed species.[87]For instance, M−O neighbor can stabilize the M−OH intermediate by hydrogen bond formation or induce the M−OOH decomposition forming M−OO and M−OH. When the explicit solvent is included, the hydrogen bonds are preferably formed with the

water molecules instead of neighboring adsorbed species, M−OOH being the most stabilized intermediate. Despite this, the M−OOH formation still being the potential determining step and the overpotential is slightly increased.

In the previously described works, the DFT calculations have been done using a constant number of electrons, instead of the constant potential conditions of the electrochemical experiments. Ping and collaborators use a constant potential DFT implementation to study the OER reaction on IrO_2 (110) surface.[104] It is shown that at potentials larger than 1.50 eV, the IrO_2 (110) surface is fully oxidated, which means that in all catalytic sites there is an O ion adsorbed. Therefore water molecule attacks M−O forming the M−OOH intermediate by transferring one H to the neighbor O. The surface is further oxidated, and finally, an O_2 molecule is produced recovering the catalytic site.

Moreover, in this work, they also explored the transition states of water dissociation and the production of O_2 from M−OO intermediate. For the water dissociation they tested three possible transition states by changing the proton receptor: (i) proton transfer to M−O (0.58 eV), (ii) proton transfer to O_{br} (0.59 eV) or (iii) transfer to an additional water molecule (0.61 eV). The small difference among the barrier heights suggests that the reaction could occur through any of these mechanisms. Moreover, this work suggest that the formation of M−OOH and −OH species is concerted. Regarding the O_2 desorption, they have shown that the production of O_2 and the filling of the oxygen vacancy by a water molecule has a barrier of 0.56 eV,

slightly lower than the water dissociation step. Therefore, they propose that the rate determining step is the water dissociation to get the M−OOH and −OH species.

It is worth mentioning that the OER mechanism on the (110)-IrO_2 surface is the only one that has been studied in detail, whereas other relevant surfaces like (011), (001) and (100) have been barely studied, despite the experimental evidence suggest that these facets for rutile materials are also more active.[105–108]

In this thesis, we have developed a computational user friendly tool entitled bulk-cut nanoparticle model (BCN-M) that can generate atomistic Wulff-like nanoparticles with controlled stoichiometry in a systematic and reproducible way for ionic binary compounds. The models obtained with BCN-M can serve as starting points to study diverse processes. For example, to study OER on IrO_2 nanoparticles.

1.6 Aims

As mentioned, the nanoparticle structure determines its catalytic behavior beyond that of its more abundant surface. In addition, to study computationally its catalytic properties it is mandatory to obtain models without going through expensive protocols, like GM. To the best of our knowledge, computational catalytic studies has been only done for metal nanoparticles, mainly because the demanding process to obtain nanoparticle models. This thesis can be summarized in three main topics, construction of nanoparticle models for

crystalline binary and ternary compounds, material-water interactions and catalytic performance of IrO_2 surfaces and nanoparticles on the oxygen evolution reaction.

The main objectives of this work are:

- Develop a friendly user tool capable to construct nanoparticle models based on Wulff construction with controlled stoichiometry and termination for binary compounds and extend it to ternary compounds.
- Analyze water interaction in IrO_2 nanoparticles and extended surfaces.
- Characterize the catalytic performance of IrO_2 extended surfaces and nanoparticles for OER reaction.

2 Computational Methods

2.1 Electronic Structure Methods

The starting point of the majority of electronic stucture methods is the time-independent Schrödinger equation,[109]

$$\hat{H}\Psi = E\Psi \tag{2.1}$$

where Ψ corresponds to the wavefunction, a mathematical object that specifies completely the state of a quantum system. $\hat{H}$ is the Hamiltonian operator that acting on Ψ extracts the eigenvalues of the observable energy E from the wavefunction.

The Hamiltonian operator for a multiple electronic system can be expressed as

$$\hat{H} = \hat{T} + \hat{V}, \tag{2.2}$$

where $\hat{T}$ and $\hat{V}$ are the kinetic and potential energy operators respectively. To have a unified syntaxis during the present document all equations are written in Hartree atomic units ($h = m_e = 4\pi/\epsilon_0 = 1$).

For a system with M nuclei and N electrons, the kinetic energy operator can be represented as

$$\hat{T} = \hat{T}_n + \hat{T}_{el} = -\frac{1}{2}\sum_{\alpha}^{M}\frac{\nabla_\alpha}{M\alpha} - \frac{1}{2}\sum_{i}^{N}\nabla_i, \tag{2.3}$$

where the first term, ($\hat{T}_n$), is the kinetic energy of nuclei and the second one, ($\hat{T}_{el}$), is the kinetic energy of electrons. The Laplacian operator ∇ in cartesian coordinates is

$$\nabla = \frac{\partial^2}{\partial x^2} + \frac{\partial^2}{\partial y^2} + \frac{\partial^2}{\partial z^2}. \tag{2.4}$$

The potential energy operator evaluates the nuclei-nuclei($\hat{V}_{n-n}$), electron-electron ($\hat{V}_{el-el}$) and nuclei-electron ($\hat{V}_{n-el}$) interactions and can be expressed as

$$\hat{V} = \hat{V}_{n-n} + \hat{V}_{el-el} + \hat{V}_{n-el} = \sum_{\alpha}\sum_{\beta>\alpha}\frac{Z_\alpha Z_\beta}{r_{\alpha\beta}} + \sum_{i}\sum_{j>i}\frac{1}{r_{ij}} - \sum_{i}\sum_{\alpha}\frac{Z_\alpha}{r_{i\alpha}}, \tag{2.5}$$

where Z_α are the nuclei charges, $r_{\alpha\beta}$, r_{ij}, and $r_{i\alpha}$ are the internuclear, interelectronic and nucleous electronic distances respectively.

This Hamiltonian does not include external electronic or magnetic fields, neither relativistic effects nor spin dependent terms.

Solving the Schrödinger equation (Eq. (2.1)) involves to find a proper

wavefunction of the Hamiltonian operator. This equation has an exact solution for simple systems like a particle in multidimensional boxes, rings, sphere, the harmonic oscillator, and hydrogen-like atoms, meaning hydrogen atoms and ions with only one electron, like Li^{2+}. However, it can not be solved for systems with more than one electron. Therefore, approximations are required for obtaining approximate solutions.

2.1.1 Born-Oppenheimer Approximation

For systems with more than one electron like many electron atoms, molecules or solids, it is not possible to have an exact solution, therefore, we have to include approximations like the Born-Oppenheimer approximation (BOA). The BOA states that the electrons adapts to heavy nuclei movement instantaneously allowing to split the total wavefunction as a product of electronic wavefunction $\Phi_{el}(\mathbf{r};\mathbf{R})$ and nuclear wavefunction $\chi_{nuc}(\mathbf{R})$,

$$\Psi = \Phi_{el}(\mathbf{r};\mathbf{R}) \cdot \chi_{nuc}(\mathbf{R}), \tag{2.6}$$

where $\Phi_{el}(\mathbf{r};\mathbf{R})$ depends of the electron coordinates ($\mathbf{r}$) and parametricaly of nuclei positions (($\mathbf{R}$)), and $\chi_{nuc}(\mathbf{R})$ only depends on $\mathbf{R}$.

This approximation allows to decompose the Schrödinger equation (Eq. (2.1)) in two equations, one for the electronic part,

$$[\hat{H}_{el} + \hat{V}_{n-n}]\Phi_{el}(\mathbf{r};\mathbf{R}) = U(\mathbf{R})\Phi_{el}(\mathbf{r};\mathbf{R}), \tag{2.7}$$

where the electronic Hamiltonian is

$$\hat{H}_{el} = \hat{T}_{el} + \hat{V}_{n-el} + \hat{V}_{el-el}, \tag{2.8}$$

and other for the nuclei movement,

$$[\hat{T}_n + U(\mathbf{R})]\chi_{nuc}(\mathbf{R}) = E\chi_{nuc}(\mathbf{R}). \tag{2.9}$$

As a consequence of this approximation, the electronic Schrödinger equation (Eq. (2.7)) is solved for an specific nuclei positions.

2.1.2 Electronic Wavefunction

The electronic wavefunction $\Phi_{el}(\mathbf{r};\mathbf{R})$ must be an exact or approximated solution of the electronic Schrödinger equation (Eq. (2.7)), and has to be normalized and antisymmetric with respect to the permutation of two electrons.[110–112] The simplest function that satisfies the latter property is the Slater determinant,[113] which is the antisymmetrized product of one electron wavefunctions (ϕ), composed by the product of spatial (ψ) and spin (η) components.

For a N-electron system the determinant is

$$\Phi(1,..,N) = (N!)^{-\frac{1}{2}}|\phi_a(1)\phi_b(2)...\phi_n(N)|, \tag{2.10}$$

where $(N!)^{-\frac{1}{2}}$ is a normalization factor. Spin functions can be α ($\uparrow$) or β ($\downarrow$) and they form an orthogonal set. From now on we will focus on the spatial part of the Slater determinant.

2.1.3 The Hartree-Fock Method

The Hartree-Fock method is a variational method that uses an Slater determinant as a trial function. Thus, the approximated energy (ε) is calculated as the expectation value of the normalizated wavefunction by

$$\varepsilon = \langle \Phi | \hat{H}_{el} | \Phi \rangle \geq E_0. \tag{2.11}$$

Where ε is an upper limit of the true energy of the ground state (E_0).

Operating with $\hat{H}_{el}$ we obtain one and two-electron integrals.

$$\langle \Phi | \hat{H}_{el} | \Phi \rangle = \sum_{i}^{N} \langle i | \hat{h}_i | i \rangle - \frac{1}{2} \sum_{ij}^{N} \left(\langle ii | jj \rangle - \langle ij | ji \rangle \right). \tag{2.12}$$

The one electron integral can be expressed as

$$\langle i | \hat{h} | i \rangle = \int \phi_i^*(1) \hat{h}(1) \phi_i(1) dr_1, \tag{2.13}$$

where $\hat{h}_i$ is the one electron Hamiltonian, that describes their kinetic and potential energy by the nuclear field and only depends on the coordinates of one electron. The two electron integrals are: the Coulomb ,

$$\langle ii | jj \rangle = \int \phi_i^*(1) \phi_i(1) \frac{1}{r_{12}} \psi_j(2)^* \psi_j(2) dr_1 dr_2, \tag{2.14}$$

and the exchange integrals,

$$\langle ij | ji \rangle = \int \phi_i^*(1) \phi_j(1) \frac{1}{r_{12}} \phi_j^*(2) \phi_i(2) dr_1 dr_2. \tag{2.15}$$

The Coulomb integral represent the classical repulsion between the charge distributions represented by $\phi_i^2(1)$ and $\phi_j^2(2)$. The exchange integral has no classical interpretation and it is a consequence of the antisymmetric nature of the Slater determinant. The task now is to find the best set of spin-orbitals that make the energy a minimum through the variational principle. The variation of the trial wavefunction composed by those spin-orbitals, however, shall maintain them orthogonal and normalized, condition that can be handled by using the Lagrange multipliers. The optimum spin-orbitals must satisfy the Hartre-Fock equations

$$\hat{f}_i \phi_i = \epsilon_i \phi_i, \tag{2.16}$$

where $\hat{f}_a$ is Fock opperator defined as

$$\hat{f}_i = \hat{h}_i + \sum_b^N (\hat{J}_i - \hat{K}_i), \tag{2.17}$$

where $\hat{J}_i$ is the Coulomb operator and $\hat{K}_i$ is the exchange operator.

The Hartree-Fock equation is a pseudo-eigenvalue equation, because their solution depends on the solutions of all the spin-orbitals via the Coulomb and exchange operators. Because of this restriction, a procedure based on the variational principle, the Self-Consistent Field (SCF) method is used. This method works iteratively: first, a guessed set of spin-orbitals forms the initial trial wavefunction, after the Fock operator is constructed, and then the Hartree-Fock equations are solved, providing a second set of spin-orbitals, that

are used in the next iteration. This process runs until the the convergence of the energy and the wavefunction. Further details on the HF-SCF method can be found on detail in literature.[114]

The HF method provides approximate solutions to the electronic Schrödinger equation, the real electron-electron interaction being replaced by an average interaction. HF wave function is capable to bring almost 99% of the total energy, but in many cases this is not enough. The difference between the best HF energy and the real lowest energy of a system is called electron correlation (EC). Inclusion of EC is mandatory for the description of many chemical molecules. Therefore many computational methods have been developed to include it.

The EC can be separated into two categories, dynamic and static correlation. The dynamic correlation is related to the instant relative electron movement, such as those occupying the same spatial orbital. The static part is is due to the monodeterminatal nature of the Hartree-Fock method, which can not give a good description of the electronic state in cases where other Slater determinants with similar energy to that of the ground state exist.

Finding methods to include electron correlation is one of the main research lines of computational chemistry. A large variety of *ab-initio* methods based on the HF wavefunction have been developed: Configuration Interaction (CI), Many-Body perturbation Theory (MBPT) and Coupled Cluster being within the most important ones. The main disadvantage of these methods is that they are highly computationally demanding, thus they can be applied to small systems.

Other alternatives have been developed to include electron correlation throught more affordable methods obtaining good approximated results. The most successful theory in this regard is the Density Functional Theory (DFT).

2.2 Density Functional Theory (DFT)

Density functional methods represent an alternative to post-Hartree-Fock methods for recovering electron correlation. Due to their low computational cost, they have been successful in treating a wide variety of systems. One of the main advantages of density functional theory over wavefunction approaches is that the electronic density in a particular point in the space is an experimental observable that does not depends explicitly on the 3N-electronic coordinates (4N if the spin is considered) but on three spatial variables. In density functional theory (DFT), the electronic density for a N electron system at $(\mathbf{r_1})$ can be calculated by

$$n(\mathbf{r_1}) = N \int \Psi(\mathbf{r_1}, \mathbf{r_2}, \cdots, \mathbf{r_N}) \Psi^*(\mathbf{r_1}, \mathbf{r_2}, \cdots, \mathbf{r_N}) ds_1 d\mathbf{r_2} \cdots d\mathbf{r_N}, \tag{2.18}$$

where $\mathbf{r}$ indicates the electron coordinates, and s the spin coordinate. This definition reduces the computational time without losing the meaningful information about the system.

DFT is based on two fundamental mathematical theorems proved by Hohenberg and Kohn,[115] and the Kohn and Sham approximation.[116]

The first Hohenberg-Kohn theorem states that in a finite system with interacting electrons, there is a one-to-one correspondence between the external potential V_{ext} (electrostatic Coulomb interaction between nuclei and electrons) and the ground state density. In other words, the external potential is a unique functional of the ground state density. All the properties of a N-electron system, including the energy, are in principle, determined by the ground state density.

The second theorem of Hohenberg-Kohn provides the variational principle, which is analogous to the one used in wavefunction based approaches. For a given electron density n, that intergrates to the total number of electrons, in an external potential V_{ext} there is a functional of n, represented as $E^{HK}_{V_{ext}}$, that satisfies the variational principle

$$E^{HK}_{V_{ext}}[n] \geq E_0. \tag{2.19}$$

where n is the ground state density that corresponds to the ground state energy E_0.

E_0 can be found by minimizing $\langle\Phi|\hat{H}_{el}|\Phi\rangle$. This means that we search over all antisymmetric N electron wavefunctions until E_0 is found. This search can be carried out in two steps. First we search over all Φ's that produce a given density $n(\mathbf{r})$ and minimize over those wavefunctions:

$$\min_{\Phi\to n}\langle\Phi|\hat{H}|\Phi\rangle = \min_{\Phi\to n}\left\langle\Phi\left|\hat{T}+\hat{V}_{\mathrm{e-e}}\right|\Phi\right\rangle + \int V_{ext}(\mathbf{r})n(\mathbf{r})\mathrm{d}^3r, \tag{2.20}$$

where we have all wavefunctions that yield the same density $n(\mathbf{r})$. Then we define the universal density functional $F[n]$:

$$F[n] = \min_{\Phi \to n} \left\langle \Phi \left| \hat{T} + \hat{V}_{\mathrm{e-e}} \right| \Phi \right\rangle = \left\langle \Phi_n^{\min} \left| \hat{T} + \hat{V}_{\mathrm{e-e}} \right| \Phi_n^{\min} \right\rangle, \quad (2.21)$$

where $\Phi_n^{\min}$ is that wavefunction which delivers the minimum $F[n]$ for a given n. Finally we minimize over all densities $n(\mathbf{r})$ that describes N electrons under the influence of V_{ext}:

$$E_{V_{ext}}^{HK}[n] = \min_n \left\{ F[n] + \int \hat{V}_{ext}(\mathbf{r}) n(\mathbf{r}) \right\} \mathrm{d}^3 r. \quad (2.22)$$

This equation only has approximate solutions because the universal functional is unknown.

The Hohenberg-Kohn theorems relate the electronic density and the ground state energy but they do not give any form to get $n(\mathbf{r})$ or to calculate the E. In this sense, Kohn-Sham (KS) provides a method to find $n(\mathbf{r})$.[116]

KS considers as a reference system with non-interacting electrons that has the same ground state density $n_s(\mathbf{r})$ of the real system $n(\mathbf{r})$. Thus, the energy functional can be re-written as

$$E_{V_{ext}}^{HK}[n] = T_s[n] + V_{ne}[n] + J[n] + E_{xc}[n], \quad (2.23)$$

where $T_s[n]$ is the kinetic energy of the non-interacting electron system, $V_{ne}[n]$ is the nuclear-electron potential, $J[n]$ is the electron-electron coulomb interaction and $E_{xc}[n]$ is the exchange-correlation functional which contains all the non-classical corrections to electron-electron

interaction and the kinetic correlation, that arises from the interacting nature of electrons:

$$E_{xc}[n] = [T[n] - T_s[n]] + [E_{e-e}[n] - J[n]] \tag{2.24}$$

where $T[n]$ and $E_{e-e}[n]$ are the exact kinetic energy and electron-electron interactions, respectively. The above definition is such that it ensures that the Kohn-Sham formulation is exact. However, the actual form of E_{xc} is not known. As a consecuence, E_{xc} is evaluated approximately.

With Kohn-Sham approach, the electronic density can be obtained as the sum of the square of the non-interacting single electron KS-orbitals φ,

$$n_s(\mathbf{r}) = \sum_{i}^{N} |\varphi_i|^2, \tag{2.25}$$

and the KS-orbitals can be obtained by solving the one-electron KS equations

$$\hat{h_{ks}}\varphi_i(\mathbf{r}) = \epsilon_i \varphi_i(\mathbf{r}). \tag{2.26}$$

where $\hat{h_{ks}}$ is the KS hamiltonian, that can be expressed as

$$\hat{h_{ks}} = -\frac{1}{2}\nabla^2 - \sum_{\alpha}^{M} \frac{Z_\alpha}{r_{1\alpha}} + \int \frac{n(\mathbf{r}_j)}{r_{ij}} d^3 r_j + V_{xc}. \tag{2.27}$$

The third term in Eq. (2.27) is the Hartree potential ($\hat{V}_H$) that evaluates the interaction between one electron and the total electronic density. The last term is the exchange-correlation potential (V_{xc}) and is represented by

$$V_{xc}(\mathbf{r}) = \frac{\partial E_{xc}[n]}{\partial n(\mathbf{r})}. \tag{2.28}$$

As in the Hartree-Fock method, the Kohn-Sham equations (Eq. (2.26)) can be solved iteratively until self-consistency is achieved. The algorithm can be summarized as:

- Define an initial electron density $n(\mathbf{r})$ determined by initial φ.
- Solve the Kohn-Sham equations (Eq. (2.26)) for this density to find the KS orbitals.
- Calculate the electron density from the KS orbitals (Eq. (2.25)).
- Compare the new density and the initial density. If the difference is lower than an established limit, replace the initial density by the new density and repeat until the difference is negligible.
- If the difference is negligible, calculate the energy (Eq. (2.23)).

2.2.1 Spin-polarized DFT

Up to this point, Hartree-Fock and Kohn-Sham methods allows to compute the energy and the electronic properties of close-shell systems, i.e. systems where the number of electrons of each spin state

are equal. However, for open-shell systems like radical species or transition metal complexes, the difference of the number of electrons per spin state arises a measurable magnetic moment. Therefore, for this kind of systems spin effects should be considered. One option is to describe the total electronic density as the sum of densities for each spin state ($n = n_\uparrow + n\downarrow$). Thus, Kohn-Sham equations for each spin state can be expressed as

$$\Big[-\frac{1}{2}\nabla^2 + V_{ext}(\mathbf{r}) + V_H(\mathbf{r}) + V_{xc,\sigma}[n_\uparrow, n\downarrow](\mathbf{r}) \Big] \varphi_{i,\sigma}(\mathbf{r}) = \epsilon_{i,\sigma}\varphi_{i,\sigma}(\mathbf{r}), \tag{2.29}$$

where the subindex σ indicates the spin component ($\uparrow$ or $\downarrow$). Only the exchange-correlation potential is spin dependent and can be expressed as

$$V_{xc,\sigma}[n_\uparrow, n\downarrow](\mathbf{r}) = \frac{\partial E_{xc}[n_\uparrow, n\downarrow]}{\partial n_\sigma(\mathbf{r}).} \tag{2.30}$$

where

$$n_\sigma(\mathbf{r}) = \sum_i^{N_\sigma} |\phi_{i,\sigma}(\mathbf{r})|^2, \tag{2.31}$$

and N_σ is the number of occupied spin orbitals for a specific spin state.

From this approach, the magnetization density $m(\mathbf{r})$ an additional descriptor of the electronic state arises. It is calculated as the difference between the densities of each spin component,

$$m(\mathbf{r}) = n_\uparrow(\mathbf{r}) - n_\downarrow(\mathbf{r}). \tag{2.32}$$

For non spin-polarized systems, this approach reduces to a standard Konh-Sham equation (Eq. (2.26)). In cases where spin densities are different, we have a spin-polarized system. This leads to compute two sets of KS equations increasing more than twice the computational time.[117–120]

2.2.2 Exchange-correlation Functionals

The exact exchange-correlation functional is unknown, although their existence is assured. To overcome this issue, several approximations has been developed. For instance, the most relevant ones are the Local Density Approximation (LDA) and Generalized Gradient Approximation (GGA).

In LDA, the electronic density in a uniform electron gas is isotropic, so the exchange-correlation potential is represented by

$$V_{xc}^{LDA}(\mathbf{r}) = V_{xc}^{\text{electron gas}}[n(\mathbf{r})]. \tag{2.33}$$

Considering a uniform density is a strong approximation. Nonetheless, LDA yields remarkable results in systems where the electronic density slightly changes. For instance, in metallic systems where the electron density is homogeneously distributed. The well-known problems for this functional include an overestimation of lattice parameters and adsorption energies, reduced band gaps, inaccurate description of magnetic states and poorly description for materials enclosing weak hydrogen bonds or other non-covalent interactions.[121,122]

Electron density is not homogeneous in most of the systems. To include information of its local variations, we can use the gradient of the density. This approach is known as generalized gradient approximation (GGA), and it improves the description of electronic properties of materials and molecules. In GGA, the V_{xc} functional can be written as

$$V_{xc}^{GGA} = V_{xc}[n(\mathbf{r}), \nabla n(\mathbf{r})]. \tag{2.34}$$

Perdew-Wang 91[123](PW91) and Perdew-Burke-Ernzenhof[124] (PBE) functionals are examples of GGA functionals.

In addition to GGA functionals, meta-GGA functionals includes information of the second derivative of the electron density ($\nabla^2 n(\mathbf{r})$) and the Kohn-Sham orbital kinetic-energy. Hybrid functionals includes the GGA or meta-GGA approximation and a percentage of exact exchange.[125]

2.2.3 Dispersion Interactions

The London forces are poorly described with standard functionals because they yield to an inaccurate description of long-range electron correlations. To encompass these interactions it is possible to add an energetic empirical correction by atom pairs as Grimme and colaborators proposed,[126]

$$E_{DFT-D2} = E_{DFT} - s_6 \sum_{i \neq j}^{N_{atoms}} \frac{C_6^{ij}}{R_{ij}^6} f_{dmp}\left(R_{ij}\right), \tag{2.35}$$

the first term is the energy obtained by standard DFT calculations and the second is the empirical correction. Here, R_{ij} is the interatomic distance, C_6^{ij} is an dispersion coefficient tabulated for individual atoms, $f_{dmp}(R_{ij})$ is a damping function that avoids unphysical behavior at short distances and s_6 is an empirical scaling factor defined for each functional.[126] More sophisticated methods that incorporates groups of three atoms or atomic charges computed semiempirically have been developed.[127,128]

To complete our methodological and conceptual background of KS-DFT and to obtain accurate physical-chemical properties, we have to consider two key components of the method: Basis sets and pseudopotentials.

2.3 Basis Sets

Solving the electronic structure problem requires several approximations. One approximation is to represent the one-electron orbitals as a linear combination in a set of known functions. This set of functions is called a basis set. The basis set should reflect the nature of the problem and facilitate the computation of the one and two-electron integrals. Several types of basis set are available and they can be grouped in local and non-local basis sets. Local basis set are the most popular choice for atoms and molecules whose orbitals are highly

localized around each atomic center. KS orbitals are represented as combinations of basis functions of a particular basis set. The most common basis sets are Slater type orbitals (STOs) and Gaussian type orbitals (GTOs).

Non-local basis sets are more suitable for systems where electrons are largely delocalized, like metals and other extended systems. In both cases, the orbitals coalesce into bands, since the energy spacing between distinct levels vanishes. Those bands are commonly described in a basis set of plane waves (PW) whose general form in the real space is $e^{i\mathbf{k}\mathbf{r}}$ where $\boldsymbol{k}$ is any vector in the reciprocal space.[129] The selection of PW satisfy some properties that make them ideal for solid state systems (see Section 2.4).

Pseudopotentials Electrons can be classified as core and valence electrons. Core electrons includes highly localized electrons in the inner shells of an atom. The valence electrons occupy the external shell of the atom and they play a key rol in the chemical activity of the system e.g. bond formation.

To reduce the computational cost, we define the ionic core i.e, electrons of the core plus nucleus as one entity. Nevertheless, the ionic core does not have the same behavior as the nuclei due to the presence of core electrons, that interact with the valence ones, so the Coulombic interaction is replaced by a pseudopotential that includes those interactions. Several methodologies have been developed to construct pseudopotentials. For solids, the most relevant ones are the plane augmented wave (PAW) method[130] and the ultrasoft pseudopotentials (USPP).[131]

2.4 Solving the Kohn-Sham DFT Equations for Periodic Systems

For extended systems, like crystalline solids, powerful theoretical and computational tools solve the DFT equations for a small representation of the system (unit cell). Replication of the unit cell by translational symmetry accounts for the full material. Hence, the properties determined in this representation are the same for the whole system.

The first step to exploit this scheme is to assume that the material can be reconstructed by repeating a unit cell in a Bravais lattice. The Bravais lattice includes the geometry of underlying periodic structure, regardless of what the actual units may be. A Bravais lattice consist of all points with position vectors $\mathbf{T}$ of the form

$$\mathbf{T} = n_1\mathbf{a} + n_2\mathbf{b} + n_3\mathbf{c}, \tag{2.36}$$

where $\mathbf{a}, \mathbf{b}$ and $\mathbf{c}$ are the primitive vectors not all in the same plane and n_1, n_2, n_3 range through all integer values.

To reconstruct the crystal, primitive or conventional unit cells can be employed. Primitive cells are the smallest entities that allows to reconstruct the crystal replicating it through all the vectors in the Bravais lattice filling all the space without either overlapping itself or leaving voids.

The obvious primitive cell to associate with a particular set of primitive vectors is the parallelipiped defined by **a**, **b** and **c**. There is always one lattice point per primitive cell, which is made up from the lattice points at each of the corners. Unfortunately, this choice often does not reflect the full symmetry of the Bravais lattice.

Alternative primitive cells that satisfy the symmetry requirement can be defined being the most common the Wigner-Seitz cell. The Wigner-Seitz cell around a lattice point is the region of space that is closer to that point than to any other lattice point. For a particular lattice point, the Wigner-Seitz cell be constructed by drawing lines connecting it with all others points in the lattice, bisecting each line with a plane, and taking the smallest polyhedron containing the point bounded by these planes.

Larger cells can also fill all the space. The conventional unit cell contains more than one lattice point. Thus, fills all the space without any overlapping when is translated through some subset of the vectors of a Bravais lattice.

An example of unit cells for bulk, slabs and molecules is shown in (Fig. 2.1). It is worth mentioning that for slabs and molecules, the unit cell must be large enough to avoid undesirable interactions between replicas.

Up to this point, we have all mandatory information to reconstruct the large material by replicating the unit cell. We need some theoretical framework allowing to connect the electronic properties of the infinite system -that can not be computed- with the electronic properties of the unit cell.

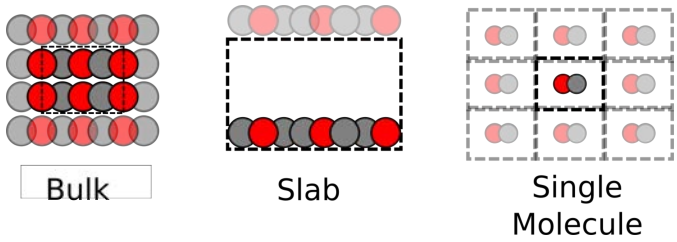

Figure 2.1: Unit cell for a bulk material, slabs and molecules or atoms. Dotted lines delimitates the cell.

Because of the translational symmetry of the unit cell the external potential V_{ext}, the wavefunctions and the electronic density are periodic functions that have the same unit cell periodicity. For the potential, this is formally represented by

$$V_{ext}(\mathbf{r}+\mathbf{T}) = V_{ext}(\mathbf{r}) \tag{2.37}$$

for any general lattice vector $\mathbf{T}$.

The Bloch theorem states that for a system with a periodic potential, the wavefunction can be written as a product of a function $u_{\mathbf{k}}(\mathbf{r})$ -with the same periodicity as the potential- and a phase factor $e^{i\mathbf{kr}}$,

$$\psi_{\mathbf{k}}(\mathbf{r}) = e^{i\mathbf{kr}} u_{\mathbf{k}}(\mathbf{r}). \tag{2.38}$$

In this equation, $\mathbf{k}$ is the wave vector that characterizes the electron quantum state in the crystal. As an example, the wavefunction at ($\mathbf{r}$+$\mathbf{T}$) has the form

$$\psi_{\mathbf{k}}(\mathbf{r}+\mathbf{T}) = e^{i\mathbf{kT}} \psi_{\mathbf{k}}(\mathbf{r}). \tag{2.39}$$

Due to the nature of the phase factor, the density at $\mathbf{r}+\mathbf{T}$, $|\psi_{\mathbf{k}(\mathbf{r})}|^2$, is the same as inside the unit cell. This condition is fulfilled for a particular set of wave vectors $\mathbf{k}$ such that, the phase factors are equal to one. Thus, the wavefunction is in phase with the cell replicas. This set of wave vectors can be defined by the reciprocal lattice vectors $\mathbf{a}*$, that are biorthogonal with the cell vectors,

$$\mathbf{a}_i \cdot \mathbf{a}*_j = 2\pi\delta_{ij}. \tag{2.40}$$

Starting from this relationship, a reciprocal space lattice primitive vectors can be obtained by

$$\mathbf{a}^* = 2\pi\frac{\mathbf{b}\times\mathbf{c}}{\nu}; \mathbf{b}^* = 2\pi\frac{\mathbf{c}\times\mathbf{a}}{\nu}; \mathbf{c}^* = 2\pi\frac{\mathbf{a}\times\mathbf{b}}{\nu}; \tag{2.41}$$

where ν is the cell volume. The volume defined by such reciprocal vectors receives the name of first Brillouin zone (FBZ), i.e, the Wigner-Seitz cell in the reciprocal space (Fig. 2.2).[132]

The convenience of choosing the FBZ is that any $\mathbf{k}'$ vector outside of it, can be represented as the sum of a vector inside the FBZ and the reciprocal lattice vector $\mathbf{G}$.

$$\mathbf{k}' = \mathbf{k} + \mathbf{G}. \tag{2.42}$$

$\mathbf{G}$ is a reciprocal lattice vector represented as

$$\mathbf{G} = n_1\mathbf{a}^* + n_2\mathbf{b}^* + n_3\mathbf{c}^*. \tag{2.43}$$

The Bloch's theorem shows that the electronic properties of an extended material can be obtained by finding the wavefunction on the unit cell. Nevertheless, this reduction is not enough, because we have to find solutions for an infinite set of **k** vectors. Infinite systems are intractable, but a finite set of vectors gives us approximately all the information about the whole system. It is possible to define a finite subset of **k**-points inside the FBZ. The FBZ can be reconstructed by symmetry from the irreducible Brioullin Zone (IBZ). All the required quantities can be computed on IBZ for a finite set of **k**-points and then reconstruct them to all the FBZ.

The sampling of **k**-point inside the IBZ is a critical step for this approach because an inappropriate sampling can result in nonphysical properties for the material or increase the computational cost without accuracy improvement. The selected sampling must be a balance between computational efficiency and a well-represented system. The most general method of IBZ sampling is the Monkhorst-Pack.[133] It generates a grid of **k**-points evenly spaced all over the FBZ. Only the points that belong to IBZ are used.

Sometimes, one point is enough to ensure a proper description of properties. This is the case of large unit cells, that have a small FBZ. This is an special point called gamma point (**Γ**) and it is located at the center of the FBZ. **Γ** is vital to study non-periodic systems like molecules, clusters or nanoparticles. Fig. 2.2 shows a summary of the aproximations for periodic systems.

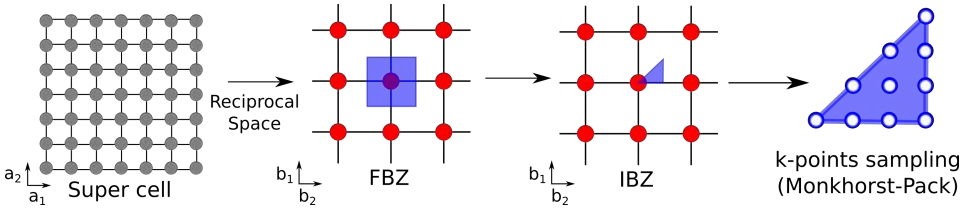

Figure 2.2: Approximations employed on periodic DFT calculations

2.4.1 Konh-Sham DFT Equations for Periodic Systems with PW Basis Set

To determine the properties of a solid using a DFT method, we need a proper representation of one-electron orbitals. The combination of those orbitals has to satisfy the Bloch's theorem,

$$\varphi_j^{(\mathbf{k})}(\mathbf{r}) = e^{i\mathbf{k}\mathbf{r}} \sum_{\alpha=1}^{M} c_{j\alpha}^{(\mathbf{k})} \phi_\alpha^{(\mathbf{k})}(\mathbf{r}), \tag{2.44}$$

where the j labels the monoelectronic orbital. The sum runs over all the basis functions $\phi_\alpha^{(\mathbf{k})}(\mathbf{r})$ up to the dimension M of the basis set. $c_{j\alpha}$ are the expansion coefficients and $\mathbf{k}$ is the wave vector in the FBZ. The basis functions also includes a periodic phase factor,

$$\phi_\alpha^{(\mathbf{k})}(\mathbf{r}) = e^{i\mathbf{k}\mathbf{r}} \phi_\alpha(\mathbf{r}). \tag{2.45}$$

Functions that are periodic in real space, will have a Fourier transform that is non-zero only at discrete points in the reciprocal space,

thus for the wave function we have

$$\varphi_j^{(\mathbf{k})}(\mathbf{r}) = e^{i\mathbf{kr}} \sum_{\mathbf{G}=0}^{\infty} C_{j\mathbf{k}}(\mathbf{G}) \phi_{\mathbf{G}}(\mathbf{r}). \tag{2.46}$$

In this equation $C_{j\mathbf{k}}$ are the Fourier coefficients and $\phi_{\mathbf{G}}(\mathbf{r})$ are the cell normalized plane wave functions

$$\phi_{\mathbf{G}}(\mathbf{r}) = \frac{1}{\sqrt{\Omega}} e^{i\mathbf{Gr}}, \tag{2.47}$$

where Ω is the reciprocal cell volume. The phase factor can be inserted into the basis function definition as

$$\phi_{\mathbf{G}}^{(\mathbf{k})}(\mathbf{r}) = \frac{1}{\sqrt{\Omega}} e^{i(\mathbf{k}+\mathbf{G})\mathbf{r}}, \tag{2.48}$$

leading into a PW expansion

$$\varphi_j^{(\mathbf{k})}(\mathbf{r}) = \sum_{\mathbf{G}=0}^{\infty} C_{j\mathbf{k}}(\mathbf{G}) \phi_{\mathbf{G}}^{(\mathbf{k})}(\mathbf{r}), \tag{2.49}$$

meaning that all one-electron solutions restricted to the FBZ, are also **k** dependent.

As the wavefunction, the interaction potentials, that are also periodic can be represented as a Fourier expansion in the reciprocal space

$$V(\mathbf{r}) = \sum_{G} e^{i\mathbf{Gr}} V(\mathbf{G}), \tag{2.50}$$

where $V(\mathbf{r})$ is the sum of $V_{ext}(\mathbf{r})$, $V_H(\mathbf{r})$, and $V_{xc}(\mathbf{r})$.

Using the PW expansion(Eq. (2.49)) to solve DFT equations (Eq. (2.26)) leads us to an eigenvalue equation,

$$\sum_{\mathbf{G}} \Big(-\frac{1}{2}|\mathbf{k}+\mathbf{G}|\delta_{\mathbf{G},\mathbf{G}'} + V(G-G') \Big) C_{j\mathbf{k}}(\mathbf{G}) = \epsilon_{j\mathbf{k}} C_{j\mathbf{k}}(\mathbf{G}), \quad (2.51)$$

for each j-one-electron KS orbital, its elements are defined by

$$T^{\mathbf{k}}_{\mathbf{G},\mathbf{G}'} = -\frac{1}{2}\langle \phi^{\mathbf{k}}_{\mathbf{G}} | \nabla | \phi^{\mathbf{k}}_{\mathbf{G}'} \rangle = -\frac{1}{2}|\mathbf{k}+\mathbf{G}|\delta_{\mathbf{G},\mathbf{G}'} \quad (2.52)$$

and

$$V^{\mathbf{k}}_{\mathbf{G},\mathbf{G}'} = \langle \phi^{\mathbf{k}}_{\mathbf{G}} | \hat{V} | \phi^{\mathbf{k}}_{\mathbf{G}'} \rangle = \frac{1}{\nu} \int V(\mathbf{r}) e^{i(\mathbf{G}-\mathbf{G}')r} d\mathbf{r} = \tilde{V}(G-G'), \quad (2.53)$$

where $\tilde{V}(G-G')$ is the Fourier transformation of the interaction potential. The matrix form for a set of PW is

$$\boldsymbol{Hc} = \boldsymbol{\epsilon c}, \quad (2.54)$$

where $\mathbf{H}$ is the Hamiltonian matrix, $\mathbf{c}$ is the coefficient's vector of PW wavefunctions and $\boldsymbol{\epsilon}$ is the diagonal matrix of eigenvalues. This equation can be solved iteratively as the DFT equations described in (Eq. (2.26)).

2.4.2 Kinetic Energy Cutoff

The kinetic energy of a PW is

$$E_{kin} = \frac{1}{2}|\mathbf{k} + \mathbf{G}|^2, \tag{2.55}$$

so is possible to reduce the amount of PWs in the calculations. To do this, we consider only PWs with kinetic energy lower than a cutoff value. The constrained periodic wavefunctions are

$$\psi_{\mathbf{k}(\mathbf{r})} = e^{i\mathbf{kr}} \sum_{|\mathbf{k}+\mathbf{G}|\mathbf{cut}} C_{\mathbf{k}+\mathbf{G}} e^{i\mathbf{Gr}}. \tag{2.56}$$

The cutoff value is obtained by maximizing the kinetic energy when changing the number of plane waves until convergence. This procedure allows to find a good balance between the number of PWs and the calculation time. Once we find a cutoff value, we solve the DFT eigenvalues equation (Eq. (2.51)), ensuring the right amount of PWs.

2.4.3 Band Structure and Density of States

From the solution of the equation (Eq. (2.54)), we obtain a set of eigenvalues ϵ_{nk} that can be plotted as a function of $\mathbf{k}$ in the FBZ to analyze the energy distribution of electronic states, thus obtaining the band structure. The band structure gives the energy distribution of different electronic states which depend on the k-points at the FBZ. For instance, Fig. 2.3 (a) shows the band structure for the semi-conductor TiO_2.It can be observed that the energies form two well defined bands separated by a gap. One band is above the Fermi energy (conduction band), and the other band is below it (valence band).

The Fermi energy is the energy of the highest occupied KS orbital. A gap between the valence and conduction bands may exist or not depending on the nature of the material. For instance, conductor materials do not present a band gap, while insulators have a band gap larger than those of semi-conductors.

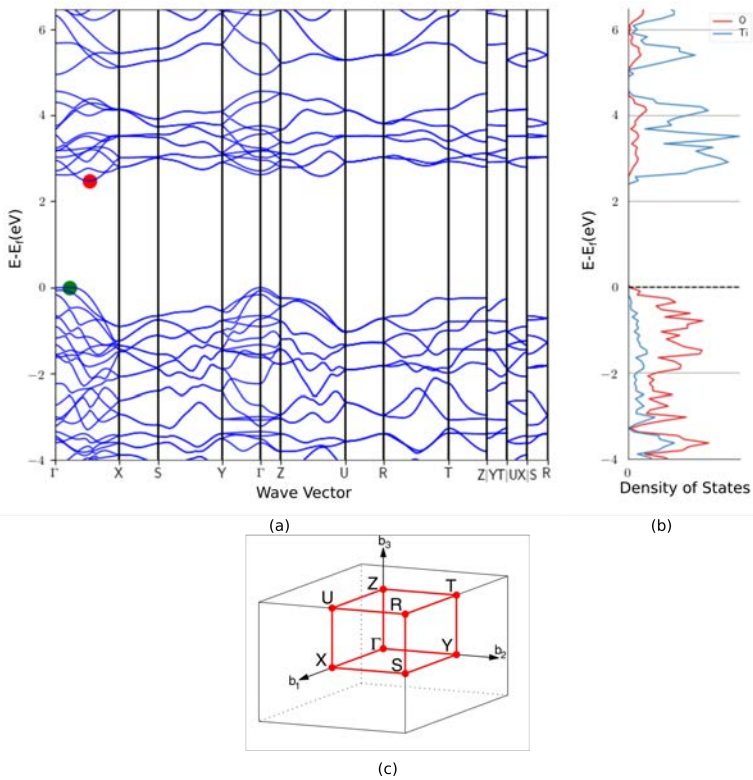

Figure 2.3: Electronic structure insights for TiO_2 bulk material, (a) band structure , (b) PDOS per element and (c) FBZ. In (a), the red and green dots shows the lowest energy unoccupied point and the highest energy occupied point respectively.

Additional information about the electronic properties of the material can be extracted from the density of states (DOS). The DOS refers

to the number or electronic states in a particular energy range. The shape of the bands reflects the amount of KS orbitals that belong to an specific energy window. It is possible to decompose it to get more detailed information. Fig. 2.3 shows for a bulk TiO_2 a bidimensional representation of the band structure (a), the projected DOS per element (b) and the FBZ (c) for TiO_2. Further details on DFT treatment of periodic systems can be found in literature.[134–136]

2.4.4 Solvent Effects for Periodic Systems

Solute-solvent interactions can be computed mainly in two ways. One way is the inclusion of explicit solvent molecules. Another way is to treat the solvent as a continuum that interacts with the solute. Both methods provide information about the solvent effect on the electronic and geometric properties of the solute. The explicit approach requires the addition of large number of solvent molecules making the calculation more challenging by increasing both the system size and its complexity. An alternative approach is to treat the solvent as a continuum, which means that the solute is immersed in a bath of solvent whose electronic properties are characterized by their permittivity ϵ.

The solute-solvent interface region can be conveniently defined using the solute electronic density, $n(\mathbf{r})$. The solvent occupies the volume of the unit cell where $n(\mathbf{r})$ is zero.

In the interface region, where $n(\mathbf{r})$ changes from zero towards bulk values inside the solute, the permittivity also changes from solvent

bulk values to 1 in the solute region. Thus, the relative permittivity is defined by

$$\epsilon\left(n(\mathbf{r})\right) = 1 + (\epsilon - 1)\, S\left(n(\mathbf{r})\right). \tag{2.57}$$

Here $S\left(n(\mathbf{r})\right)$ is the cavity shape function, given by

$$S\left(n(\mathbf{r})\right) = \frac{1}{2}\,\mathrm{erfc}\left\{\frac{\log\left(n(\mathbf{r})/n_c\right)}{\sigma\sqrt{2}}\right\}, \tag{2.58}$$

where erfc is the complementary error function that gives values in a range of 0 and 2. The parameter n_c determines at what density value the cavity is formed and σ is a diffusion factor. This definition ensures that the electric permittivity varies smoothly along the solute-solvent interface from 1 on the solute region to ϵ in the solvent region.

Therefore, the solute-solvent free energy can be defined as follows

$$\begin{aligned} E[n(\mathbf{r}), \phi(\mathbf{r})] = {} & E_{\mathrm{TXC}}[n(\mathbf{r})] \\ & + \int \phi(\mathbf{r}) n_s(\mathbf{r}) d^3r - \int \epsilon(\mathbf{r}) \frac{|\nabla\phi|^2}{8\pi} d^3r \\ & + E_{\mathrm{cav}}. \end{aligned} \tag{2.59}$$

where E_{TXC} is kinetic and exchange-correlation contribution from DFT, $\phi(\mathbf{r})$ is the solute electrostatic potential in a polarizable medium and $n_s(\mathbf{r})$ the solute total density (defined as the sum of nuclear and

electronic densities). In this equation, the second and third terms accounts for solute-solvent electrostatic interactions.

Solute-solvent interactions not captured for the electrostatic terms are included by the cavitation energy, E_{cav} , given by

$$E_{\text{cav}} = \tau \int |\nabla S(n(\mathbf{r}))| d^3 r, \tag{2.60}$$

where τ is the effective surface tension parameter.[137]

Solving Eq. (2.59) requires finding $\phi(\mathbf{r})$ for each self-consistent iteration by using the Poisson equation

$$\nabla \cdot [\varepsilon (n(\mathbf{r})) \nabla \phi] = -4\pi n_s(\mathbf{r}). \tag{2.61}$$

More details of this methodologic frame to include solvent effects can be found in literature.[138–147]

2.5 Thermodynamic Corrections

Up to this point we can include solvent effects to electronic structure calculations but to relate these calculations with macroscopic experimental observables like Gibbs free energy, we have to include thermal effects. All the previously described calculations was under the Born-Oppenheimer approximation i.e, the electronic structure solution for a specific nuclear configuration. At the macroscopic level, the nuclei are moving and molecular vibrations must be considered. This energy contribution at 0 K is called the Zero Point Energy (ZPE).

The vibrational degrees of freedom for a N-atoms molecule are 3N-6 vibrations for the nonlinear and 3N-5 for the linear ones. The ZPE at 0 K in the harmonic approximation is given by

$$ZPE = \sum_{i}^{modes} \frac{1}{2} h\nu_i, \tag{2.62}$$

where ν_i is the harmonic vibrational frequency of the i-th normal mode.

Statistical thermodynamics is the theoretical framework that connects the microscopic and the macroscopic properties of a system. The main quantity in statistical thermodynamics is the partition function, Q. In the canonical ensamble (constant N, V and T) we define Q as follows

$$Q = \sum_{i} e^{-E_i/k_B T}, \tag{2.63}$$

where E_i is the energy of the i-th state, k_B is the Boltzmann constant and T is the temperature. The partition function contains all the thermodynamic information about the system and their value reflects the number of thermally accessible states at the specific temperature.

From the partition function in the canonical ensemble it is possible to get macroscopic values of U,H, S and G of a molecular system by

$$\begin{aligned} U &= k_B T^2 \left(\frac{\partial \ln Q}{\partial T}\right)_{N,V} \\ H &= U + PV \\ S &= k_B \ln Q + k_B T \left(\frac{\partial \ln Q}{\partial T}\right)_{N,V} \\ G &= H - TS \end{aligned} \tag{2.64}$$

However, to calculate the partition function requires knowing all possible quantum states of the system over every possible state. It is only affordable for diatomic and triatomic molecules. For larger systems, some simplifications have to be included.

By assuming the ensemble is an ideal gas of not interacting molecules, the partition function can be rewritten as

$$Q(N,V,T) = \frac{[q(V,T)]^N}{N!} \tag{2.65}$$

where the factor $1/N!$ derives from the quantum mechanical indistinguishably of the molecules and $[q(V,T)]$ is the molecular partition function

$$q(V,T) = \sum_j e_j^{-\varepsilon_j / k_B T} \tag{2.66}$$

where ε_j is the molecular energy of the j state.

Assuming that the molecular energy of a state can be expressed as the sum of electronic, translational, rotational and vibrational parts, is possible to describe the molecular partition function as the product of electronic, translational, rotational and vibrational partition

functions. In this work the electronic energy is obtained by regular electronic structure calculations and the vibrational energy through vibrational frequency calculation using the harmonic oscillator approximation. As mentioned, the translational, rotational and electronic thermal corrections are not take into account mainly due to the solid nature of the studied systems.

2.6 Born-Oppenheimer Ab Initio Molecular Dynamics

The approach to determine the electronic wavefunction at fixed nuclei positions is useful to explain the physical and chemical properties of certain systems. However, in systems where multiple conformations are close in energy, like surface absorbed molecules a fixed nuclei approach is insufficient.

To circumvent this problem, we can use Molecular dynamics simulations (MD). MD describes how a chemical system evolves over time. From the MD trajectory is possible to get the average value of a property A of the system

$$\langle A \rangle = \frac{1}{M} \sum_{i}^{M} A\left(t_i\right), \tag{2.67}$$

where M is the number of times the property is sampled and $A(t_i)$

is the value of the property at time t_i. This is possible via the ergodic hypothesis, which makes the assumption that the average obtained by following the evolution of a small number of particles over a long time is equivalent to averaging over a large number of particles. Thus, it is possible to get meaningful values of macroscopic properties from MD simulations.

In MD the potential energy surface is explored by solving Newton's laws of motion of the system. For a set of nuclei treated as classical masses M with an interaction energy $E[\{\mathbf{R}\}]$ dependent upon the position of the particles $\{\mathbf{R}_I\}$, the equations of motion for each nucleus are

$$M_I \ddot{\mathbf{R}}_I = -\frac{\partial E}{\partial \mathbf{R}_I} = \mathbf{F}_I \left[\{\mathbf{R}_J\}\right]. \tag{2.68}$$

In this equation the force acting on particle I is dependent on the position of the other ones, and is the negative of the energy gradient.

Eq. (2.68) can be solved analytically only for simple systems. In general, the solution is obtained by numerical methods using discrete time steps. The size of the time step is directly ligated to the system. The rule of thumb to select it is to ensure that at each time, the positions and the forces are correctly updated. There are several algorithms for numerical integration of Eq. (2.68) which include the position Verlet[148] , velocity Verlet[149] , predictor-corrector[150] among others.

The result of a MD simulation is a trajectory that shows how the system evolves along the time. If the starting point is a low energy

conformation, its trajectory seems likely to sample relevant conformations on the phase space (all the possible conformations).

In classical MD, the forces are calculated using parameterized potential functions, called force fields. The major weakness of those force fields is that are only valid for the potential energy surface region that has been parameterized and are also not capable to study electronic structure related properties, like chemical bond breaking or formation, or magnetic properties.

An alternative and most robust method is the Ab Initio Molecular Dynamics (AIMD),[151] where the forces are computed for each conformation by electronic structure methods increasing the computational cost. The forces calculation is done using the Hellmann-Feynman theorem, that states that the force on an atom is the expectation value of the derivative of the Hamiltonian with respect to the change in the atomic positions.

During a MD simulation, the atomic changes on the system generate a new state each step, that means, the diverse values of the interesting thermodynamic property. After equilibration, the system becomes an ensemble, that is a collection of all possible configurations that have an identical macroscopic state.

For MD various possible ensembles are available. That includes micro-canonical, canonical, isobaric-isotherm and grand canonical. In each ensemble, some thermodynamic variables are fixed characterizing the state. In the present work we employed the canonical ensemble where we have a fixed number of particles, fixed volume, and fixed temperature. This ensemble is usually referred as NVT.

To ensure the constant temperature the system is surrounded by a heat bath that re-scales the particles velocities. For this proposal, the most popular thermostats are Berendsen and Nosé-Hoover.[152,153]

2.7 Computational Details

In this thesis, DFT calculations on IrO_2 material were carried out with the Vienna ab initio simulation package (VASP) code.[154,155] All calculations were performed with the GGA PBE functional including D2 Grimme's correction for dispersion[126] and using the projector augmented wave pseudopotentials[130,156] to describe ionic cores and valence electrons through a plane wave basis with a kinetic energy cutoff equal to 500 eV. Bulk and slab calculations were performed using a Monkhorst-Pack (9,9,9) and (4,4,1) k-point mesh, respectively. For zero periodicity structures, like Wulff-like nanoparticles and single water models, only the Γ point was employed. The energy convergence criteria were fixed to 10^{-5} and 10^{-4} eV for electronic and geometry relaxations, respectively. To minimize replica interactions, for water and nanoparticle models, cubic cells of 15 and 30 Å were employed respectively.

The surface slab models were obtained by cutting it from the optimized bulk structure, giving a (2x2) cell. Also, a thickness calibration was performed until surface energy converges. The *c* parameter was as long as necessary to have at least 15Å between replicas perpendicular to (hkl) surface to minimize replica interactions.

Surface energy can be defined as

$$\Delta E^{n}_{surf} = \frac{E^{n} - nE_{bulk}}{2A}, \tag{2.69}$$

where E^n is the energy of ionic relaxed n-layer slab, E_{bulk} is the energy of the bulk material, and A is the surface area. The $1/2$ factor accounts for the two exposed surfaces, one at the bottom of the cell and other at the top.

The stoichiometric Wulff-like nanoparticles were generated by BCN-M code using the aforementioned optimized bulk parameters (cell and ionic positions) and the minimized surface energies.[157]

Water adsorption was studied on previously optimized slab models and on a $(IrO_2)_{33}$ nanoparticle at two coverages: One water adsorbed in a coordinatively unsaturated site, and monolayer coverage scheme where all the coordination vacancies are fulfilled by water molecules. In this thesis, the adsorption energies are calculated by

$$E_{ads} = \frac{E_{\mathrm{mat+H_2O}} - E_{\mathrm{mat}} - n_{\mathrm{H_2O}} \cdot E_{\mathrm{H_2O}}}{n_{\mathrm{H_2O}}},$$

where $E_{\mathrm{mat+H_2O}}$ is the total energy of the material with the adsorbed water, E_{mat} is the total energy of the bare material, $E_{\mathrm{H_2O}}$ is the total energy of the water molecule, and $n_{\mathrm{H_2O}}$ is the number of adsorbed waters.

Ab Initio Molecular Dynamics (AIMD) were carried out for the most stable water monolayer structures for (110) and (011) surfaces. The

energy convergence criteria were fixed to 10^{-4} eV. AIMDs were carried out considering an equilibration period of 1 ps (1000 steps of 1 fs) and a production period of 7 ps (7000 steps of 1 fs) in the NVT ensemble at 300 K. During both the equilibration and the production periods, only the water monolayer and the first layer of the surface were allowed to move according to the motion's equations, while atoms of the remaining surface later were maintained at fixed positions. This option was chosen in order to avoid unrealistic deformations of the structure and to simulate the actual rigidity of the material.

3 Bulk-cut Nanoparticle Model (BCN-M)

A thorough knowledge of the atomic structure of nanomaterials is of high importance to understand their properties. This requires developing nanoparticle models, which is not always straightforward, particularly in the case of compounds formed by two or more elements. This chapter focuses on the development of Bulk-cut nanoparticle model (BCN-M), a the computational tool to generate Wulff-like models for binary materials with controlled stoichiometry automatically with none or little need for further manipulation from the user. BCN-M has been tested for 15 materials that cover the most relevant binary ionic structures and symmetries (cubic, tetragonal, hexagonal, and monoclinic). Further, as a proof of concept BCN-M has been extended to get forsterite (Mg_2SiO_4) nanoparticles.

3.1 Introduction

As pointed out in the introduction, obtaining realistic models for nanoparticles is a challenging process. As mentioned in Section 1.4.1,

the commonly used approaches to get realistic models are bottom-up and top-down methods. In the bottom-up approach, the nanoparticle model is constructed assemble enough building blocks to reach the desired nanoparticle size. Therefore, the model is optimized to get a stable structure. However, mainly due to the massive computational effort, bottom-up approach is suitable for small size nanoparticles with less than 200 atoms.

In contrast, the top-down approach starts from the bulk structure and reduces it to the nanoscale. The size reduction results in nanoparticle morphologies that are linked to the thermodynamic equilibrium crystal shape of the bulk system, which depends on the energy cost of forming the different surfaces. The Wulff-Gibbs theorem postulates that under thermodynamic equilibrium the nanoparticle shape is the one that has the minimum surface energy. Such theorem can be written as

$$l_{(hkl)} = c_{(hkl)}\gamma_{(hkl)}, \tag{3.1}$$

where $l_{(hkl)}$ is the length of normal vectors to a crystallographic plane from a point **P** (Wulff center or Wulff point), $c_{(hkl)}$ is a proportionality coefficient and $\gamma_{(hkl)}$ is the surface energy. Hence, surfaces with the shortest vectors dominate the crystallite shape. The inscribed polyhedron obtained by connecting the vector tips has the equilibrium shape.[158] This polyhedron is called Wulff polyhedron or Wulff construction. The Wulff construction shape depends only on the ratios between surface energies and the material symmetry point group.[71,72] Therefore, the higher the number of crystallographic facets used to construct the Wulff polyhedron, the higher the difficulty in building it. The range of validity of the nanoparticles based on

the Wulff construction method has been largely discussed, and it is usually accepted for sizes larger than 2-3 nm, depending on the material.[46,64]

The Wulff construction has the equilibrium shape, that is enough for single element nanoparticles. However, there are other aspects to take into consideration for multicomponent nanoparticle models. Some of them are: (i) singly coordinated atoms in the final nanoparticle model may not be the most stable termination and (ii) the presence of exposed polar surfaces requieres additional stabilization by a reconstruction or by reacting with the media. Indeed, singly coordinated atoms are sometimes mandatory to reach stoichiometric and electroneutral models. However, they are usually highly unstable, and thus, at least for some particular cases, nanoparticle models derived from metal reduction or oxidation, by removal of singly coordinated species, are probably more realistic. This redox process maintains electroneutrality, but the resulting model is not stoichiometric. On the other hand, polar surfaces are also highly unstable, and their stabilization is generally accompanied by an important surface reconstruction to reduce the polarity. Three main kinds of reconstruction are possible, the occurrence of which depends on the material and the synthetic conditions: (i) generation of some metal and/or nonmetal vacancies in a few of the outermost layers, which maintains the stoichiometry of the material, (ii) redistribution of the electron density at the outermost layers due to redox processes, which leads to neutral nonstoichiometric surfaces (anion- or metal-rich), and (iii) incorporation of external groups present in the media such as hydrides or hydroxyls. While the former is too

specific of the material under study (hence requiring further manipulation by the user), the other two can be partially included in the automatic nanoparticle generation process.

In this chapter, we present in detail the delevopment of a tool for the generation and refinement of Wulff constructions to get controlled stoichiometric nanoparticle models for binary and a ternary compounds automatically with little need of further manipulations.[157]

3.2 Algorithmic Details

Bulk-Cut Nanoparticle Models (BCN-M) is a computational tool written in Python and uses standard and scientific Python libraries (NumPy,[159] SciPy,[160] ASE,[73] pymatgen,[161] and PyYAML[162]). Its algorithm can be divided in four sections: (i) initial nanoparticle generation, (ii) nanoparticle symmetry and chemical evaluation, (iii) nanoparticle refinement, and (iv) quality indices. The nanoparticle refinement includes the generation of the different types of nanoparticles depending on the material under study and user specifications: (i) stoichiometric nanoparticles, (ii) nanoparticle models without singly coordinated atoms but an excess of the less abundant ion, and (iii) models involving polar surfaces that can either be metal- or nonmetal-rich or saturated with H or OH groups. The automation is intended to save time for the user and remove the bias introduced by the manual modification. However, we are aware that this cannot substitute the scientific rigor of the user who should carefully

validate the models and have a thorough knowledge of the material under consideration. The flow chart of BCN-M is shown in Fig. 3.1

3.2.1 Initial Nanoparticle Generation

The input data required for the generation of the final nanoparticle models (NPF) is (i) the irreducible atoms, types, and positions in fractional coordinates; (ii) the conventional cell parameters; (iii) the space group number of the crystal (1-230); (iv) the Miller indices of the planes constituting the NP and the related surface energies; (v) the size of the desired NP in Å; and (vi) the type of surface termination that the final model should have. According to our experience, using a specific size could not produce suitable models. Therefore, we suggest to explore sizes in a range around the desired size with an step size of 1.0 Å. This will result in at least one NP model. With this initial model, the user will be able to estimate the size of the subsequent realistic models and identify the most relevant Wulff point for the material. This would reduce the computational time specially when trying to construct large nanoparticle models. In relation to the Wulff point, the user can optionally set it. However, by default, the tool explores three different types of nanoparticle centers: (i) the positions of the irreducible atoms, (ii) the origin of coordinates, and (iii) several special positions that present the lower symmetry multiplicity in the unit cell (See Table A.1 for the considered centers for each space group). Within all tested examples, these centers guarantee obtaining at least one set of nanoparticle models.

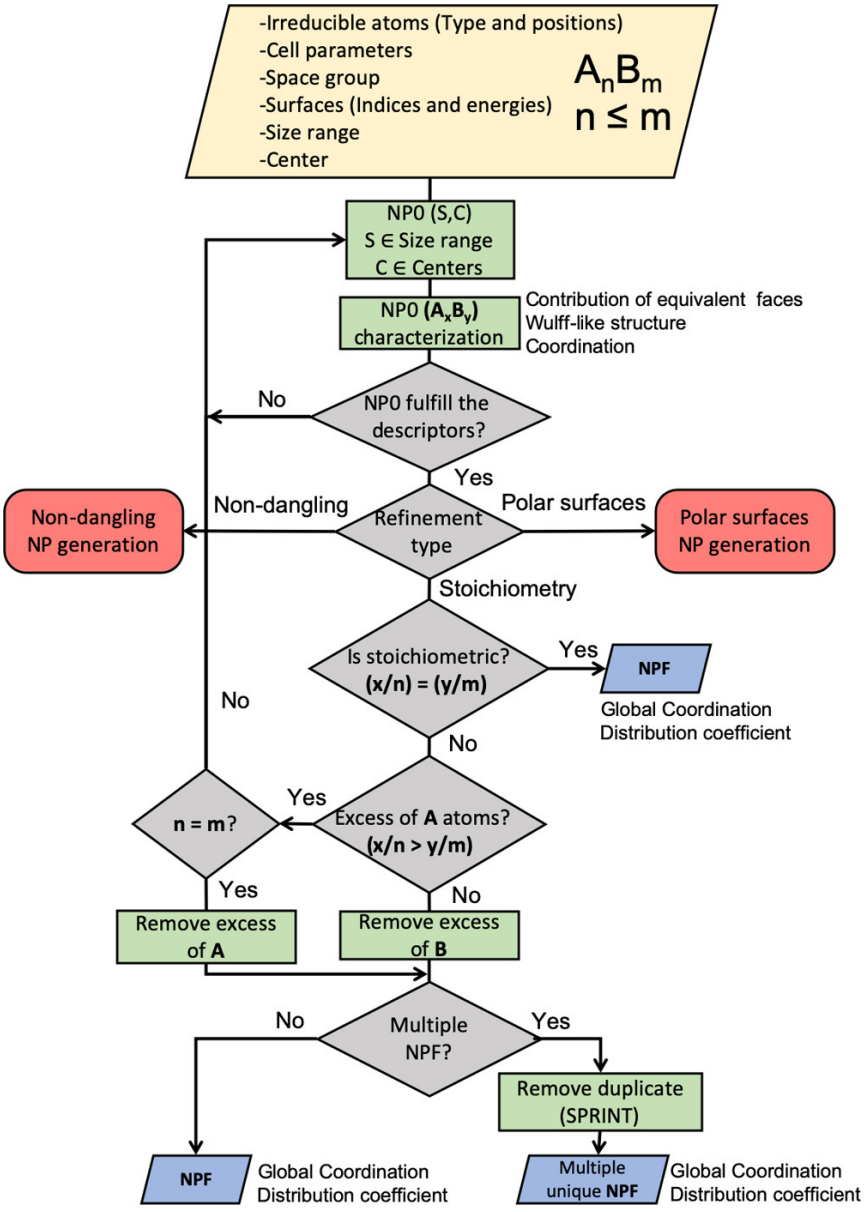

Figure 3.1: BCN-M flow chart. A_nB_m, material formula. NP0, initial nanoparticle. NPF, final nanoparticle model.

With this input data, BCN-M analyzes if any of the surfaces included in the input data is polar and then it constructs n initial NP models, which are called NP0. The polarity of the surface is evaluated by the pymatgen library.[161] If one polar surface is found, but this has not been specified, BCN-M warns the user. The NPs0 are built by cutting the unit bulk material using as a guideline the Wulff construction.

As a first step to get the Wulff construction starts by drawing normal vectors to the user provided planes (hkl) including the symmetry equivalent ones with origin at the Wulff center. The vectors norms, $\|[uvw]\|$, are calculated as the product of the normalized surface energies and the user desired size in Å. Finally, the Wulff construction is obtained by adding perpendicular planes that connect the vectors tips.

Once we have the Wulff construction we need to have sufficient large bulk material to cut a Wulff-like nanoparticle. One way to achieve this is to find the nearest integer that is greater than or equal than the number of material layers for each (hkl) surface as

$$n_{layers(hkl)} = \left\lceil \frac{\|[uvw]\|}{d_{(hkl)}} \right\rceil, \tag{3.2}$$

where $d_{(hkl)}$ is the interplanar distance for the (hkl) surface. Therefore, the number of unit cells to build the bulk material in each direction can be calculated by

$$\mathbf{n}_{(hkl)} = \mathbf{G} \cdot ([uvw] \cdot d_{(hkl)} \cdot n_{layers(hkl)}), \tag{3.3}$$

where **G** is the Crystallographer's reciprocal cell.[163] $\mathbf{n}_{(hkl)}$ is a 3 element vector, each one indicates the number of cells for each lattice direction. By repeating this procedure for the surfaces and their equivalents we have a set of $\mathbf{n}_{(hkl)}$. The final number of cells that has to be replicated are the maximum values per lattice direction. Finally, to get the Wulff-like nanoparticle, atoms beyond the Wulff construction are removed.

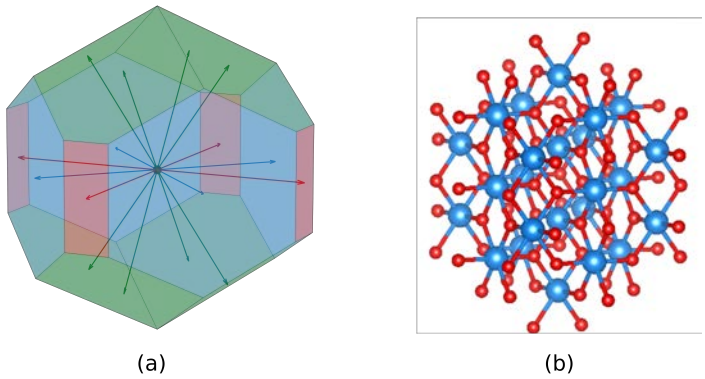

Figure 3.2: (a) Wulff construction and (b) initial Wulff-like nanoparticle for IrO_2 (NP0).

In Fig. 3.2, the Wulff construction (a) and a Wulff-like nanparticle of IrO_2 (b) are shown. The Wulff construction was built by using the lower index surfaces $(110), (011), (100), (001)$, and their DFT computed energies.[164] Remarkably, only the $\{110\}$ (blue), $\{011\}$ (green) and $\{100\}$ (red) family surfaces contribute to the final shape. The initial Wulff-like nanoparticle (b) was obtained by cutting the Wulff construction from the bulk material. This way to proceed can be employed to get Wulff-like nanoparticles for any kind of material

regardless of their structure. Is worth mentioning that the obtained NP0 is oxygen rich and thus further treatment is required.

3.2.2 Symmetry and Chemical Evaluation

The suitability of an NP0 is evaluated by their symmetric and chemical properties. The symmetry criteria are: (i) the contribution of equivalent faces , (ii) its resemblance to the ideal Wulff shape. From the chemical point of view the criterion is (iii) the absence of undercoordinated less abundant ions. If the NP0 does not fulfill one of these criteria, the model is discarded and other centers and sizes are explored. The criteria are explained below.

Equivalent Facets By symmetry, surfaces that belong to the same family have the same surface energy. Therefore, they should have the same contribution to the surface area of NP0. Keeping in mind that the distance from the Wulff center to the exposed surface is proportional to the surface energy, it is possible to use it as a criteria to see if surfaces belonging to the same family have the same contribution on NP0.

The distance for each $[uvw]$ direction is computed as the maximum distance from the Wulff center to the external surface atoms. From those distances it is possible to get the ratio of each facet in the total surface area. If two equivalent facets differ in more than 5%, the model is discarded. However, using the outermost atoms to determine the contribution per facet for materials where exposed surfaces have like-step structures could lead into errors. Nevertheless,

a more robust surface definition like the Gibbs equimolar surface can be used. The Gibbs surface is defined as in each direction as the nearest down integer of the ratio between Wulff center-surface distance and the interlayer distance plus a half of the interlayer distance ($s = \lfloor D/(d_{(hkl)}) \rfloor + 0.5(d_{(hkl)})$, where D is the Wulff center-surface distance and $d_{(hkl)}$ is the interplanar distance.[69] In BCN-M both options are available.

Wulff-like Structure Being the NP0 a Wulff construction it is expected that the ratio between the area contribution and the total area per family planes should be close to the predicted for the Wulff polyhedron. From the distance from the Wulff center to the Gibbs equimolar surface BCN-M computes the percentage surface contribution per facet to the total area and compares it with the values of the Wulff polyhedron. If the contribution order is not the same in NP0 and the Wulff polyhedron, the model is discarded.

Absence of Undercoordinated Less Abundant Ions The presence of undercoordinated centers is usually associated with less stable structures, and thus, they should be avoided in the construction of the NP models. As a consequence, the less abundant ions (e.g., Ti in TiO_2 and O in Cu_2O) are classified as "reasonably coordinated" and "undercoordinated" centers, respectively. The default threshold criterion chosen to identify the so-called undercoordinated atoms is two vacancies of the maximum coordination (max. coord - 2). This means, for example, that in a system where the maximum coordination for the less abundant atom is six (e.g., the case of TiO_2), each

center whose coordination is three or lower will be considered undercoordinated. The presence of a single undercoordinated center is sufficient for the tool to discard the model. It is worth mentioning that, for some materials, the default threshold is too strict and thus, no nanoparticle models are obtained. This is, for example, the case of MgO, where corners are tricoordinated, and Cu_2O, where the maximum coordination of oxygen is 2. For these and similar cases, the user can modify the undercoordinated atom threshold to half of the maximum coordination.

3.2.3 Structure Refinement

Up to this point, the approved NP0 models have the expected shape and absence of undercoordinated less abundant centers, but the surface structure has not been characterized yet. The structure refinement is used to change the NP0 surface termination to get more realistic structures. From the NP0 it is possible to get stoichiometric nanoparticles, nanoparticles without singly coordinated ions, nanoparticles which have exposed polar surfaces that can be metal or non-metal rich, and models with extrinsic compensated polar surfaces that have adsorbed species to reduce the dipole moment. The termination selection is up to the user because the termination depends on the material as well as the synthetic method used to obtain the NP. The methods to get these terminations are described below.

Stoichiometric Nanoparticles

The key issue in this procedure is to ensure that the material stoichiometry is respected in the final model. Therefore, for each generated NP0, the stoichiometry of the model is verified. Models presenting an excess of the less abundant ion in the general formula are discarded. For instance, all TiO_2 models where the O/Ti ratio is smaller than 2 are discarded, while for Cu_2O, the discarded models present less Cu^+ cations than twice the number of O^{2-} atoms. If the model is nonstoichiometric because of an excess of the most abundant element, the extra atoms are removed.

In this cleaning process, two scenarios can happen: either the number of ions to delete matches the number of dangling ions of the NP0 or only a fraction of the dangling ions must be removed to achieve stoichiometry. The first case will only lead to one final NP, whereas the second one leads to many different models because several combinations exist for the removal of atoms. With the aim of obtaining models with larger global coordination numbers, the cleaning process starts eliminating those dangling atoms linked to the most coordinated sites. This is done iteratively until stoichiometry is achieved. If in any of these steps the number of sites exceeds the number of dangling atoms to be removed, the program assumes a random procedure that is repeated 1000 times as default value, thus generating 1000 NP models. While this should be enough to obtain a set of models containing the most representative structures, the user can modify this parameter for a more exhaustive sampling.

Excess ion removal The removal of excess ions of the most abundant element in non-stoichiometric NPs can be done iteratively. Table 3.1 shows an example of 20-atom nanoparticle with 4 extra atoms to be removed. In order to sample all the possible nanoparticles, the following procedure is employed:

- The dangling ions are identified (reported in blue in step 2).
- The centers to which the dangling ions are bound (parent atoms) are selected, and their coordination computed (step 3). The highest coordinated centers (five-coordinated) are in bold red indices, while those least coordinated (four-coordinated) are in plain red.
- A list of dangling and parent atoms along with their connectivity, is created (step 4).
- A list with the indices of the atoms that will be eliminated is created (step 5). There are two different possibilities. If the number of extra atoms is larger than the number of the highest coordinated centers (as in the present example), one dangling per high coordinated parent atom is added to the remove atom list. In the opposite case, this step and steps 6 and 7 are skipped.
- The selected dangling and parent atoms list is updated by eliminating the dangling atoms added to the remove atom list (step 6).
- The coordination of the parent atoms is updated (step 7).

- When the number of parent atoms is larger than the number of atoms to be removed the indices of parent atoms are shuffled (step 8). Starting from the first index, a number of dangling atoms equal to the remaining extra atoms (two atoms in this example) are added to the remove atom list (step 9). Steps 8 and 9 are repeated several times, being 1000 ones the default value, to obtain different representative samples.

Each sample thus results in a model differing from the others on the position of one or several dangling ions, that are bonded to equally coordinated centers.

Table 3.1: Cleaning process of a 20-atom nanoparticle with 4 extra atoms

	Action	20 atom NP example
1	List of atoms	1 2 3 4 5 6 7 8 9 10 11 12 13 14 15 16 17 18 19 20
2	Select dangling atoms	1 2 3 4 5 6 7 8 9 10 11 12 13 14 15 16 17 18 19 20
3	Select parent atoms	1 2 **3** 4 5 6 7 8 **9** 10 11 12 13 14 15 16 17 18 19 20
4	List selected atoms and connectivity	1 2 6 10 11 14 17 **3** 5 **9** 12 20
5	Create remove atom list	10 2
6	Updated dangling atom list	1 6 11 14 17 **3** 5 **9** 12 20
7	Decrease coordination of parent	3 5 9 12 20
8	Shuffle of parent	3 12 5 20 9
9	Add to remove atom list	10 2 1 14 (sample 1)
10	Obtain different samples (up to 1000)	10 2 1 17 (sample 2) 10 2 6 14 (sample 3) 10 2 1 6 (sample 4) 10 2 14 1 (sample 5) . . .
11	Remove equivalent samples	10 2 1 14 (sample 1) 10 2 1 17 (sample 2) 10 2 6 14 (sample 3) 10 2 1 6 (sample 4) . . .

Remove equivalent models Due to symmetry, some of the unique set of ions to be removed produce symmetry equivalent NPFs, so it is valuable to eliminate duplicate structures. By using traditionally employed coordinate systems used in computational chemistry, like cartesian or internal coordinates it is difficult to identify symmetry equivalent structures automatically. To overcome this, BCN-M uses social permutational invariant coordinates (SPRINT),[165] a coordinate system that is permutational, translational and rotational invariant.

The SPRINT coordinate for the i-th atom of a set of N atoms, is calculated as

$$S_i = \sqrt{N}\lambda^{\max} v_i^{\max,\text{sorted}}, \tag{3.4}$$

where $\lambda^{\max}$ is the largest modulus eigenvalue and and $v_i^{\max,\text{sorted}}$ is the i-th element of the sorted eigenvector of the adjacency matrix $\mathbf{A}$.

In this work the elements of $\mathbf{A}$, that represent the connectivity between atoms, were defined as: $a_{ij} = 1$ if i and j atoms are bound, $a_{ij} = 0$ if i and j atoms are not bound, $a_{ii} = 1 + \frac{Z_i}{10}$ for ions with atomic number lower than 100 and $a_{ii} = 1 + \frac{Z_i}{100}$ for ions with atomic number larger or equal to 100. A similar definition has been employed by other authors for akin proposes.[166] Overall, two models presenting the same SPRINT coordinates are equally connected and are considered equivalent, and therefore, one of them is discarded. As shown in Eq. (3.4), to get the SPRINT coordinates of a NP is mandatory to compute the eigenvalues and eigenvectors of the matrix $\mathbf{A}$. It should be pointed out that this calculation for large matrices requires great computational cost, limiting their practical use for

nanoparticles smaller than 2 nm. In this context, BCN-M only eliminates symmetry equivalent models for NPs below 2 nm. Another less expensive way to discard symmetry equivalent structures is to use the eigenvalues of the inertia tensor. Two structures with the same sorted eigenvalues are rotationally equivalent. Unfortunately, this method is only capable to eliminate rotational equivalent structures. Is worth to mention that as the NP models increase the size, less symmetry equivalent conformations are found.

Nanoparticle models without singly coordinated Ions As already mentioned above, the generation of stoichiometric models frequently leads to singly coordinated atoms on the surface. However, these structures are likely unstable, and thus, at least for some particular cases, metal reduction or oxidation to avoid the presence of singly coordinated species is expected to be more realistic. In this context, BCN-M is able to generate models without dangling atoms, if this is specified by the user. This is done by following the same described procedure for the generation of stoichiometric nanoparticles except the procedure discussed in the Remove ions excess loop section, since, in this case, BCN-M removes all singly coordinated ions, regardless of whether stoichiometry is preserved or not. For instance, ceria (CeO_2) fully reduced nanoparticles are employed to study their oxygen storage capacity, that is their capability to capture or release oxygen depending on the medium abundance.[167]

Nanoparticles involving polar surfaces Some nanoparticles like ZnO or PdO ones have polar surfaces, and, as alredy mentioned, are

unstable so that several stabilizing mechanisms have been proposed.[41,42,78] In BCN-M it is possible to include intrinsic reconstructions, forcing those surfaces to have the desired termination, being cation or anion terminated. BCN-M is also capable to include extrinsic depolarizing mechanisms by adding -H or -OH groups on that polar surfaces.

For intrinsic reconstruction, the first step is to adjust the termination of polar surfaces. BCN-M computes the stoichiometry of the exposed surface and determines whether it is cation or anion rich. If the termination does not match with the desired one, the number of atomic layers in that direction is increased until the required termination is achieved. Once the desired termination is obtained for the polar surface, BCN-M removes all dangling atoms of the non-polar surfaces.

For extrinsic depolarization, the user must specify the desired adsorbed species, namely -H or -OH. Is worth to mention that the adsorbed species are oriented parallel to $[uvw]$.

3.2.4 Quality Indices

To make a deeper morphological characterization and guide the user in selecting the model for a particular application, three quality indexes are provided by BCN-M, the so called Wulff-like index, the distribution coefficient and the global coordination.

Wulff-like index This index compares the NP final shape with the Wulff polyhedron as

$$WLI = \sum_{\{hkl\}} \left| RC(\mathsf{WP}_{\{hkl\}}) - RC(\mathsf{NP0}_{\{hkl\}}) \right|, \tag{3.5}$$

where $RC(\mathsf{WP}_{\{hkl\}})$ is the relative contribution per family of surfaces in the ideal Wulff polyhedron and $RC(\mathsf{NP0}_{\{hkl\}})$ is the relative contribution per family of surfaces in the NP0. Smaller values of Wulff-like index suggest that the NP0 shape is close to the Wulff polyhedron.

Distribution coefficient (DC) The distribution coefficient (DC) index is calculated as the standard deviation of the difference among the center of mass of the metals (CMM) and that of the anions (CMA). If the distribution coefficient is 0, the anions are distributed homogeneously around cations of the NP. The rule of thumb is the larger the DC, the more heterogeneous the ion distribution is and thus, the larger the polarity of the model. It is worth mentioning that two models can have the same DC but can differ in their structure.

Global coordination The global coordination index (GC) is calculated as the sum of cations and ions coordination numbers C_i,

$$GC = \sum_i C_i. \tag{3.6}$$

To compute the coordination, BCN-M uses the neighbor-list algorithm implemented in ASE,[73] which is based on the detection of sphere collision. If two spheres overlap they will be counted as neighbors, which in our case reflect bonds. The key parameter to

the correct clash detection is the sphere radius. In BCN-M sphere radius per ion (R_i) is defined as

$$R_i = \frac{\min d(i)}{2.5}, \tag{3.7}$$

where $d(i)$ is the list of the all inter-atomic distances from atom i. By using this definition two spheres never will clash, so an increment has to be included. By default ASE increases the sphere radius by 0.3 Å.

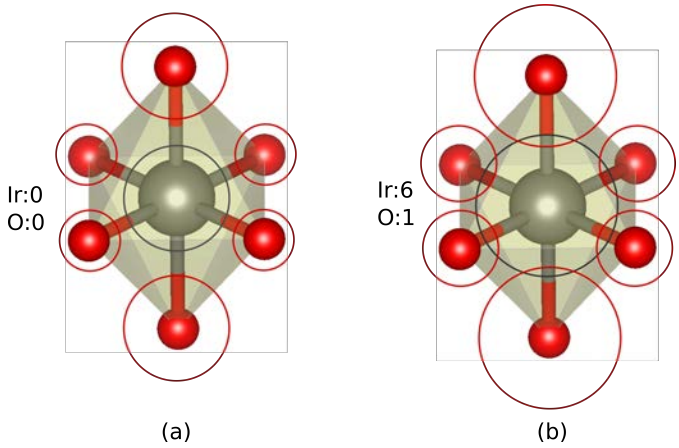

Figure 3.3: Calculation of the coordination of a single crystal of IrO_2-rutile. (a) By using the initial R_i definition the spheres does not overlap. (b) The spheres overlap by increasing 0.3Å. In the left margin of each figure the number of neighboring atoms are shown. The size of the red circles has been adapted to illustrate the concept.

As an example, to calculate the coordination of a single IrO_2-rutile crystal the first step is to identify the shortest distance between ions, the second one is calculate R_i for each specie, then increase R_i by

adding 0.3Å, and finally identify the sphere overlap. In The IrO_2-rutile crystal is an octahedral one with $Ir-O$ distances of 1.946 Å for the axial oxygens and 2.017 Åfor the equatorial ones. Thus, for the O, the shortest distance respect to other ion is the $Ir-O_{ax}$ distance, that is the same for Ir. Therefore, for both ions R_i is 0.778 Å. However, two build spheres of this radius centered on the atomic positions does not overlap, as shown in Fig. 3.3 (a). By using the default increment, R_i increases to 1.078 Å, hence, both spheres overlap identifying it as neighboring atoms (See Fig. 3.3 (b)). The coordination for each ion is calculated by counting the number of neighboring atoms. For this example, the Ir coordination is six and the O coordination is one. This way to proceed works properly for the tested materials. Furthermore, more refined algorithms are available to define the connectivity and the coordination for crystal materials.[168]

3.3 Application

In this section, we present the results of using BCN-M to construct nanoparticles for a set of materials that includes cubic, tetragonal, hexagonal and monoclinic crystalline systems. A detailed list is shown in Table 3.2 and covers the most representative binary ionic compounds structures.

The selected materials allow testing all the nanoparticle generation capabilities of BCN-M like stoichiometric, non-stoichiometric models and nanoparticles with polar surfaces. It must be pointed out that these nanoparticle models are Wulff constructions that arise from

Table 3.2: BCN-M tested materials

Material	Crystallographic system	Space group
Nonpolar surfaces		
MgO(rock salt)	Cubic	$Fm\bar{3}m$
CeO_2(fluorite)	Cubic	$Fm\bar{3}m$
Li_2O(antifluorite)	Cubic	$Fm\bar{3}m$
Cu_2O	Cubic	$Pm\bar{3}m$
In_2O_3(bixbyite)	Cubic	$Ia\bar{3}$
Tio_2(anatase)	Tetragonal	$I4_1/amd$
MO_2(M= Ti, Ru, and Ir)(rutile)	Tetragonal	$P4_2/mnm$
CuO	Monoclinic	$C2/c$
Polar surfaces		
ReO_3	Cubic	$Pm\bar{3}m$
PdO	Tetragonal	$P4_2/mmc$
ZnA(A = O, S, and Se)	Hexagonal	$P6_3mc$

cutting the bulk material without any further manipulation. Thus, their atomic structure is the same as that of the bulk material, so surface relaxation or reconstruction is not explicitly included mainly because is material and surface dependent. The generated models could be used to track down the available vacant sites per size that can help to find the suited size for a particular catalytic process. Also, these models are thought to be used for further simulations, for example to study catalytic process.

3.3.1 Generated Models

Fifteen different test examples have been considered to ensure the performance of the here described algorithm. Appendix A reports the parameters (fractional coordinates, cell parameters, space group

index, Miller indices, and surface energies) to be introduced in BCN-M as input data. Tables 3.3 and 3.4 summarizes the main features of the obtained models. Table 3.3 is focused on materials whose polar surfaces do not contribute to the Wulff structure. Table 3.4 is devoted to models with at least one polar surface. In each case, the nanoparticle center, stoichiometry, size, and number of isomers are reported. For each center, we only report two models. Larger models can be found in Tables A.3 and A.4. Fig. 3.4 shows two models without polar surfaces (stoichiometric nanoparticle and nanoparticle without dangling atoms), and Fig. 3.5 reports two models for the materials including polar surfaces (metal- or nonmetal-rich and with additional H or OH groups). It should be noted that the size difference between two contiguous models with the same center corresponds approximately to twice of the interlayer distance in the direction defining the size of the model.

Nanoparticle Center As we said previously, the NP0 is a cut of the bulk material that has the shape of the Wulff polyhedron, with the origin in the Wulff center. The selection of Wulff center is crucial in the generation of the NP0. BCN-M has an internal database with lower multiplicity points, meaning points that are invariant by the identity operation and at least other symmetry operation of the space group. By default, BCN-M considers three types of centers: (i) the atomic positions of the irreducible atoms, (ii) the origin of coordinates of the irreducible unit cell, and (iii) the lower multiplicity points.

Table 3.3: Selected NP Models without Polar Surfaces Obtained with BCN-M

material	center[a]	formula[b]	isomers	formula[c]	size[d]
MgO	(0.25, 0.25, 0.25)	$(MgO)_{32}$, $(MgO)_{108}$	1, 1	N/A[e]	1.0, 1.7
CeO_2	cation	$(CeO_2)_{19}$, $(CeO_2)_{85}$	1, 1000	$Ce_{19}O_{32}$, $Ce_{85}O_{160}$	1.1, 2.2
	(0.5, 0.0, 0.0)	$(CeO_2)_{44}$, $(CeO_2)_{146}$	2, 1	$Ce_{44}O_{80}$, $Ce_{146}O_{280}$	1.6, 2.7
Li_2O	anion	$(Li_2O)_{19}$, $(Li_2O)_{85}$	1, 999	$Li_{32}O_{19}$, $Li_{160}O_{85}$	1.2, 2.1
	(0.5, 0.0, 0.0)	$(Li_2O)_{44}$, $(Li_2O)_{146}$	2, 999	$Li_{80}O_{44}$, $Li_{280}O_{146}$	1.6,2.5
Cu_2O	cation	$(Cu_2O)_{40}$, $(Cu_2O)_{112}$	12, 1000	$Cu_{55}O_{40}$, $Cu_{175}O_{112}$	1.7, 2.6
In_2O_3	(0.0, 0.0, 0.0)	$(In_2O_3)_{22}$, $(In_2O_3)_{73}$	1, 29	$In_{44}O_{60}$, $In_{146}O_{210}$	1.5, 2.6
	N/A	N/A	N/A	N/A	N/A
RuO_2[f]	(0.5, 0.5, 0.0)	$(RuO_2)_{24}$, $(RuO_2)_{90}$	19, 1000	$Ru_{24}O_{42}$, $Ru_{90}O_{170}$	0.9, 1.5
	cation	$(RuO_2)_{33}$, $(RuO_2)_{115}$	7, 7	$Ru_{33}O_{60}$, $Ru_{115}O_{220}$	1.2, 1.9
IrO_2[f]	(0.5, 0.5, 0.0)	$(IrO_2)_{24}$, $(IrO_2)_{90}$	19, 986	$Ir_{24}O_{42}$, $Ir_{90}O_{170}$	0.9, 1.5
	cation	$(IrO_2)_{33}$, $(IrO_2)_{115}$	7, 644	$Ir_{33}O_{60}$, $Ir_{115}O_{220}$	1.2, 1.8
TiO_2[f]	(0.5, 0.5, 0.0)	$(TiO_2)_{60}$[h]$(TiO_2)_{240}$	19, 1000	$Ti_{60}O_{114}$,[h]$Ti_{240}O_{470}$	2.1, 3.3
	cation	$(TiO_2)_{69}$, $(TiO_2)_{215}$	7, 1000	$Ti_{69}O_{132}$, $Ti_{215}O_{420}$	2.4, 3.0
TiO_2[g]	(0.0, 0.0, 0.5)	$(TiO_2)_{10}$, $(TiO_2)_{84}$	1, 1	N/A	1.0, 2.9
	cation	$(TiO_2)_{35}$, $(TiO_2)_{165}$	1, 1	N/A	2.0, 3.9
CuO	anion	$(CuO)_{40}$, $(CuO)_{110}$	135, 854	$Cu_{40}O_{36}$, $Cu_{110}O_{105}$	1.6, 2.4

[a] Two possible centers (1 and 2) are reported. For each one, the size of the NP model and total number of isomers after removing equivalent structures are shown.
[b] Stoichiometric nanoparticle. [c] Nanoparticle model without dangling atoms.
[d] In nm, measured as the largest distance between cations. [e] Non applicable. [f] Rutile.
[g] Anatase [h] Two smaller models ($(TiO_2)_{42}$ and $(TiO_2)_{51}$) are also obtained.

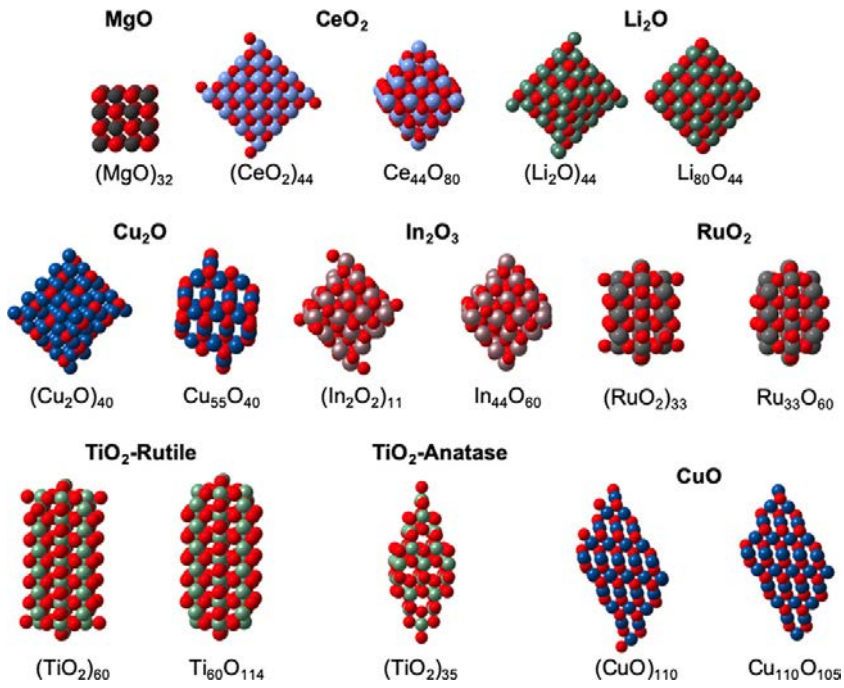

Figure 3.4: Selected NP models of the test cases that do not include polar surfaces

When the Wulff center matches with an atomic position, the generated nanoparticle commonly has an odd number of monomeric units, whereas, the other positions get even numbers. Interestingly, in some cases, only one center can generate stoichiometric nanoparticles.

Fig. 3.6 shows two rutile MO_2 nanoparticle models as an illustrative example of the importance of the Wulff center. When it is set at a cation position, models with an odd number of MO_2 units are obtained. In contrast, when it is located between two cations of the central row of the nanoparticle model (i.e., fractional coordinates of

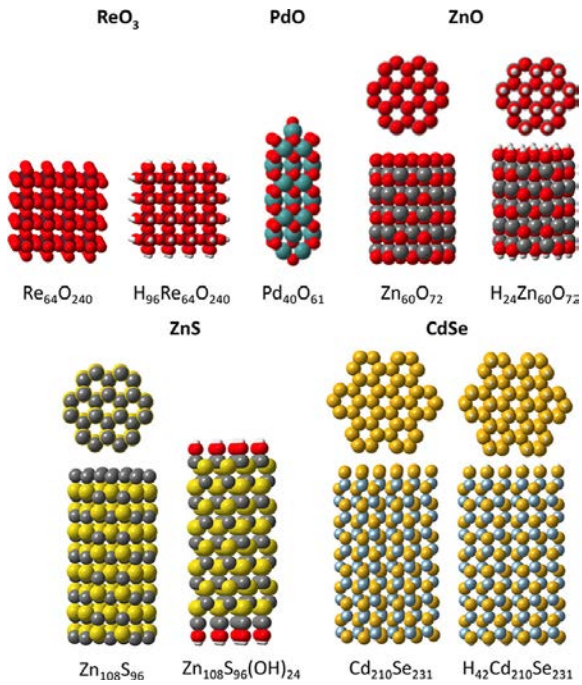

Figure 3.5: Selected NP models of the test cases that include polar surfaces.

0.5, 0.5, and 0.0), another set of Wulff-like NP models, which are characterized by the presence of an even number of MO_2 units, is obtained. The models with an even number of MO_2 units present a larger portion of the {110} family of facets than the models with an odd number of units, and the Wulff-like criterion suggests that models of the former are closer to the Wulff morphology for IrO_2 and RuO_2.

Overall, our experience suggests that exploring these three Wulff

Table 3.4: Selected NP Models with Polar Surfaces Obtained with BCN-M

material	center[a]	formula[b]	formula[c]	size[d]
ReO_3	cation	$Re_{27}O_{108}$, $Re_{125}O_{450}$	$H_{54}Re_{27}O_{108}$, $H_{150}Re_{125}O_{450}$	1.3, 2.6
	(0.5, 0.5, 0.5)	$Re_{64}O_{240}$, $Re_{216}O_{756}$	$H_{96}Re_{64}O_{240}$, $H_{216}Re_{216}O_{756}$	1.9, 3.2
PdO	anion	$Pd_{28}O_{43}$, $Pd_{40}O_{61}$	N/A	1.4, 1.9
ZnO[e]	(0.0, 0.0, 0.0)	$Zn_{60}O_{72}$, $Zn_{216}O_{243}$	$H_{24}Zn_{60}O_{72}$, $H_{54}Zn_{216}O_{243}$	1.4, 2.5
ZnS[e]	(0.0, 0.0, 0.0)	$Zn_{108}S_{96}$, $Zn_{324}S_{297}$	$Zn_{108}S_{96}(OH)_{24}$, $Zn_{324}S_{297}(OH)_{54}$	2.8, 3.9
CdSe[e]	(0.0, 0.0, 0.0)	$Cd_{108}Se_{120}$, $Cd_{210}Se_{231}$	$H_{24}Cd_{108}Se_{120}$, $H_{42}Cd_{210}Se_{231}$	3.1, 3.7

[a] Two possible centers (1 and 2) are reported. For each one, the size of the NP model and total number of isomers after removing equivalent structures are shown. [b] Formula models with either metal or non-metal rich termiation [c] Formula models with additional OH groups [d] In nm, measured as the largest distance between cations [e] Wurtzite

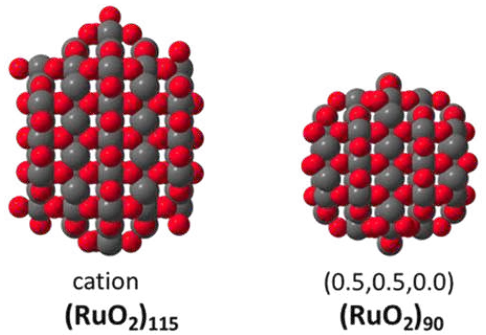

Figure 3.6: Selected examples of RuO_2 nanoparticles obtained with different centers.

centers is sufficient to ensure the generation of realistic and stoichiometric models. However, deciding which one of them is more appropriate in each case is not straightforward.

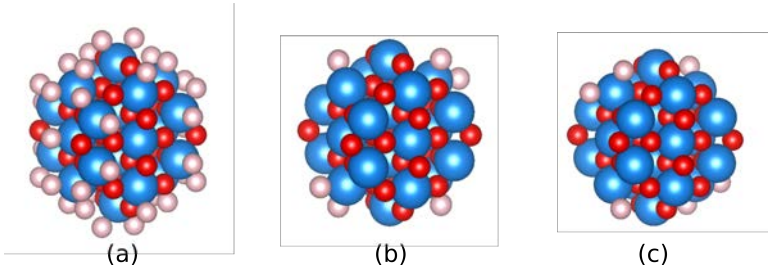

Figure 3.7: Generation of unique stoichiometric models for $Ir_{24}O_{48}$ from $Ir_{24}O_{80}$ Wulff construction. (a) NP0 of $Ir_{24}O_{80}$, singly coordinated O ions are depicted in light pink. (b) and (c) are equivalent obtained structures of stoichiometric $Ir_{24}O_{80}$.

Structure refinement As mentioned, converting the Wulff construction into a realistic nanoparticle it is mandatory to make some structural changes, such as removing or adding ions on the nanoparticle surface. The possible terminations include stoichiometric, nanoparticles without singly coordinated ions, nanoparticles with polar surfaces that can be metal or non-metal terminated and models for which the polarity is reduced by adsorbing extrinsic species like $-H$ or $-OH$. Here each refinement option is explained.

Stoichiometric nanoparticles of binary compounds BCN-M checks the stoichiometry of NP0. There are two possibilities, the NP0 can be stoichiometric or not. For the second option, nanoparticles with an excess of less abundant ion are discarded. IrO_2 nanoparticles can be used as an example to show how models are accepted and processed. IrO_2 nanoparticle models which have a ratio O/Ir lower than 2 are discarded because to achieve stoichiometry the program

one should remove Ir centers that are not singly coordinated, producing surface holes that are not desirable. If the ratio is larger than 2, the extra O ions are removed using the remove ions excess loop. In Fig. 3.7, the NP0 with 24 Ir centers (a) have an excess of 32 O ions, that has to be eliminated from a set of 38 singly coordinated O (depicted in light pink) ions following the aforementioned remove ions excess loop, that reduces gradually the coordination of metallic centers until achieving stoichiometry. In this case, 979 models are obtained and most of them are equivalent. For instance, (b) and (c) structures are rotational equivalent, by using the SPRINT coordinates, one of these models are discarded. By removing redundant structures only 19 unique models are preserved.

Nanoparticles with polar surfaces Polar surfaces are generally highly unstable, and thus, they are less common than nonpolar ones. However, for some particular nanoparticles, their presence is mandatory to achieve the Wulff morphology. The formation of polar surfaces is usually accompanied by an important surface reconstruction that reduces the polarity.[41,42,169] As mentioned, three main reconstructions can occur: (i) generation of metal and/or nonmetal vacancies in the outermost layers, (ii) electron density redistribution to achieve neutral nonstoichiometric surfaces (anion- or metal-rich), and (iii) incorporation of new surface groups such as hydrides or hydroxyls. The computed surface energies for polar facets are usually associated with either a metal or an anion termination, and consequently, the final model obtained with these surface energies cannot be stoichiometric.

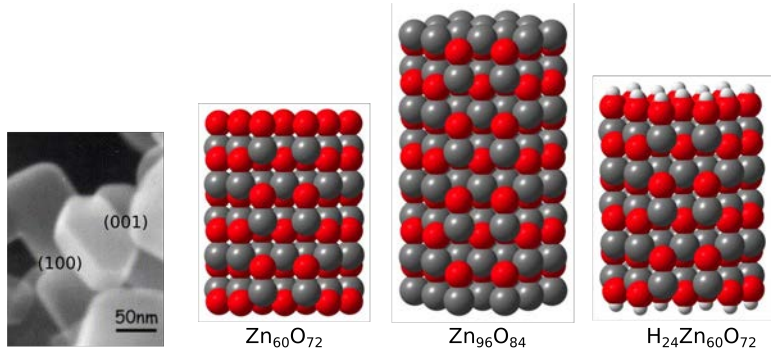

Figure 3.8: ZnO Nanoparticles. (a) SEM image of ZnO powder nanoparticles (Adapted from[170]). A (b) O-terminated, (c) Zn-terminated and (d) -OH terminated models.

Wurtzite-like zinc oxide is a paradigmatic example. Experimental evidences suggest the presence of terraces and/or OH groups when synthetizing films involving the (001) surface.[41,42,169,170] Calculations for ZnO predict that the most stable termination of the polar basal (001) surface implies a shell of zinc atoms at the outermost layer in oxygen-poor environments and an oxygen termination in oxygen-rich conditions.[20,26] As already mentioned, BCN-M is able to distinguish the presence of polar surfaces and treat them differently. Three different terminations are possible: (i) metal-rich, (ii) nonmetal-rich, and (iii) OH terminated. Generating models with BCN-M that include terraces and other large reconstructions described in the literature is, at present, not possible. This kind of reconstructions highly depends on the material and synthetic conditions, and thus, their modeling can hardly be automatized. Experienced users can construct this kind of models by using any of the

three resulting models as starting points.Fig. 3.8 shows the nanoparticle experimental structure (a) and three ZnO nanoparticle models with diverse terminations (b,c,d). The nanoparticle morphology depends on the ratio between the surface energy of the polar (001) surface and that of the stoichiometric (100) one. The surface energy for the (001) facet depends on their termination, but that of the (100) one does not. Consequently, the O-terminated and Zn-terminated nanoparticles present different morphologies. The $-OH$ groups are added perpendicularly to the (001) facet. This leads to M-O-H bond angles of 180°, which are unrealistic. However, the most stable structure is difficult to determine a priori due to the large number of H-bonding possibilities, and thus, the OH-terminated structures should be taken as preliminary models.

Stoichiometric nanoparticles of ternary compounds

In contrast to binary compounds, where general rules can be established, for ternary compounds each case is unique. For instance, in forsterite polymorph of olivine (Mg_2SiO_4), silicate units (SiO_4) have to be preserved and the Mg^{2+} cations on the nanoparticle surface have to be located to minimize the total energy. Thus, keeping in mind these restrictions, we proposed the following procedure to get a stoichiometric nanoparticle from a forsterite NP0.

Once the NP0 is constructed, the next step is to remove or reconstruct lower coordinated silicates, SiO, SiO_2 and SiO_3 moieties. The lower coordinated ones, SiO and SiO_2 are removed and the later is reconstructed. To fill the vacant in SiO_3, the missing O is oriented

at the normal vector of oxygens plane. The vector norm, that is the $Si-O$ bond distance, is set according to the values of the bulk SiO_4.

Once we have all SiO_4 moieties, the next step is to get the maximum number of possible formula units that can have the stoichiometric NP from the NP0. The number of formula units is computed as n-times the unit cell stoichiometry, where n is the smallest number of available ionic species in NP0. From that, it is possible to get also the number of ions in excess. For instance, in a non-stoichiometric nanoparticle $Mg_{108}Si_{50}O_{216}$, the less abundant ion is Si, so if we multiply the number of Si atoms by the cell stoichiometry, that is Mg_2SiO_4, we get that the stoichiometric NP must have fifty times the cell stoichiometry, meaning $Mg_{100}Si_{50}O_{200}$, so the non-stoichiometric NP have an excess of eight Mg^{2+} and sixteen O^{2-}.

The elimination of the remaining O^{2-} anions is straightforward, because they are not bounded to Si ions. For the Mg^{2+} cations in excess, we remove the ones that are weakly attached to the NP structure. Assuming that the the interionic Coulomb potential mainly gives the ion cohesive energy, is possible to identify the ease to remove Mg^{2+} cations. For the i-th magnesium cation, the Coulomb potential is calculated by

$$V_i = \sum \frac{q_j}{\mathbf{r}_{ij}}, \tag{3.8}$$

where q_j is the ionic charge and $\mathbf{r}_{ij}$ is the interionic distance. For this calculation we assume that the ions have their proper ionic charge, namely 2-, 4+, 2+ for O, Si, Mg respectively. Even though those

charges are ideal give insights about the Mg^{2+} experimented potential. To reduce the computational cost of Coulomb potential calculation for each ion we only include neighbour ions closer than 5 Å. In Fig. 3.9, only the magnesium cations of the $Mg_{108}Si_{50}O_{210}$ nanoparticle model are represented. The color scale indicates the normalized Coulomb potential. Mg^{2+} ions in the corners of nanoparticle surface are the ones that experience the weaker Coulomb potential among all magnesium cations (in dark blue) meanwhile the non exposed ones are strongly attached (in dark red). Therefore, the eight Mg^{2+} cations with the smallest Coulombic potential are removed.

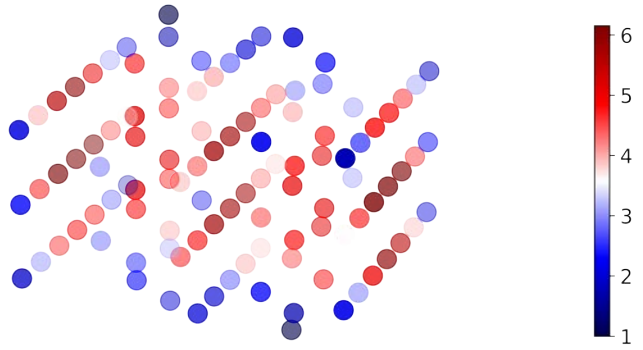

Figure 3.9: Normalized Coulomb potential on Mg^{2+} for $Mg_{108}Si_{50}O_{200}$ forsterite nanoparticle model.

In contrast with the procedure for binary compounds where frequently multiple stoichiometric NPs are obtaiend from one NP0, this algorithm generates only one model. In Fig. 3.10 the initial, intermediate and final structure are shown. From (a) $Mg_{108}Si_{58}O_{232}$ NP0 one gets a (b) $Mg_{108}Si_{50}O_{216}$ by removing SiO and SiO_2 moieties (in light purple). From (b) the excess of O^{2-} and Mg^{2+} (in grey) ions are removed to get the stoichiometric stucture $(Mg_2SiO_4)_{50}$ (c). It should be noted that the obtained nanoparticle maintains the Wulff shape.

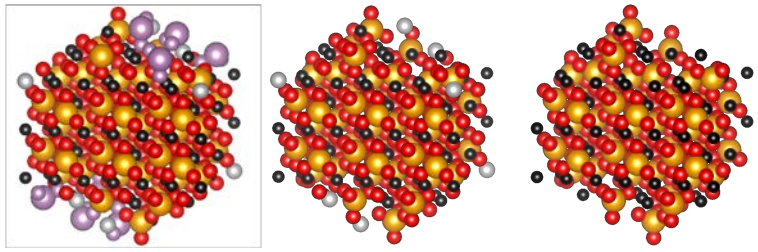

Figure 3.10: Process to get stoichiometric $(Mg_2SiO_4)_{50}$ from a non-stoichiometric Wulff construction. (a) NP0 $Mg_{108}Si_{50}O_{216}$. (b) $Mg_{108}Si_{50}O_{216}$. (c) $(Mg_2SiO_4)_{50}$.

3.3.2 Electronic Properties of Equivalent Models

As a final test, the similarities/differences among the isomers generated by the BCN-M algorithm are analyzed by performing DFT calculations on the seven $(RuO_2)_{33}$ NPF isomers. $(RuO_2)_{33}$ has been taken as a representative example due to the limited number of isomers and its reduced size. The seven $(RuO_2)_{33}$ isomers have the same global coordination and Wulff-like quality criterion value and

only differ on the distribution coefficient. Fig. 3.11 shows the optimized geometries for the seven models and the relative energies of the optimized structures with respect to the most stable isomer (in kJ mol^{-1}). Fig. 3.12 displays (a) the distribution of the Ru−O distance and O−Ru−O angle corresponding to atoms at the surface and (b) the projected density of states (PDOS) associated with the d orbitals of surface Ru atoms and the p orbitals of the surface oxygen atoms of two selected isomers. The PDOS of all other $(RuO_2)_{33}$ species can be found in Fig. A.1 of Appendix A.

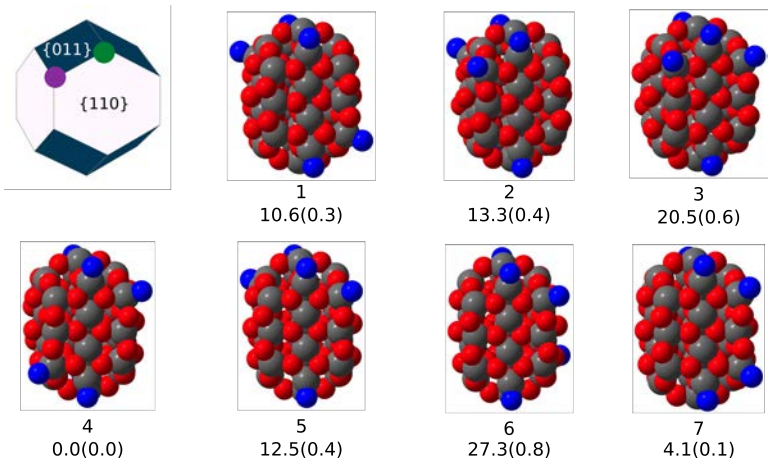

Figure 3.11: Wulff polyhedron and the optimized structures of the seven isomers of $(RuO_2)_{33}$.The green and purple points in the Wulff polyhedron indicates the positions where dangling oxygens are connected. Relative energies with respect the most stable isomer and per formula unit are in parentheses. All energy values in kJ/mol.

The initial structures obtained with the BCN-M algorithm shows six dangling O atoms. Four of these dangling atoms are located at the four tetracoordinated Ru centers of the intersection between two surfaces of the {011} family and one surface of the {110} family

(green dot in Fig. 3.11). The other two are located at the eigth pentacoordinated Ru centers of the intersection of two surfaces of the {110} family and one of the {011} (purple dot in Fig. 3.11). As result, the different isomers arise from the different distributions of the two oxygens in these eight possible sites.

During the DFT optimizations, the seven isomers behave similarly. No surface reconstruction is observed, but a larger reorganization than that observed on periodic surface models takes place.[171] In general, the Ru-O distances are shorter than those of the bulk, which are 1.942 Å (axial) and 1.998 Å (equatorial), and the effect is more pronounced for the Ru-O bond trans to a vacancy (at least 0.06 Å). The ruthenium center exposed on the (110) surface also moves inside the nanoparticle enlarging the $O_{ax}-Ru-O_{eq}$ angle up to around 100° for most cases, as compared to the 90° of the bulk. The major reorganization is observed on ruthenium centers presenting dangling atoms. The $Ru-O_{dangling}$ distance is the shortest $Ru-O$ distance (1.67-1.68 Å in the tetracoordinated centers and 1.70 Å in the pentacoordinated ones), sugggesting the formation of a Ru=oxo species to maintain ruthenium formal oxidation state to +4. The coordination environment of these ruthenium centers becomes a distorted trigonal bipyramid for pentacoordinated ones and a distorted tetrahedron for the tetracoordinated ones. This implies several angles between 150 and 105°. This reorganization occurs for all the isomers considered, regardless of the position of the dangling oxygen atoms in the NP. As a consequence, the largest energy difference between two isomers is rather small (27.3 kJ mol^{-1} or 0.8 kJ mol^{-1} per RuO_2 unit), the relative stabilities between isomers arising mainly from

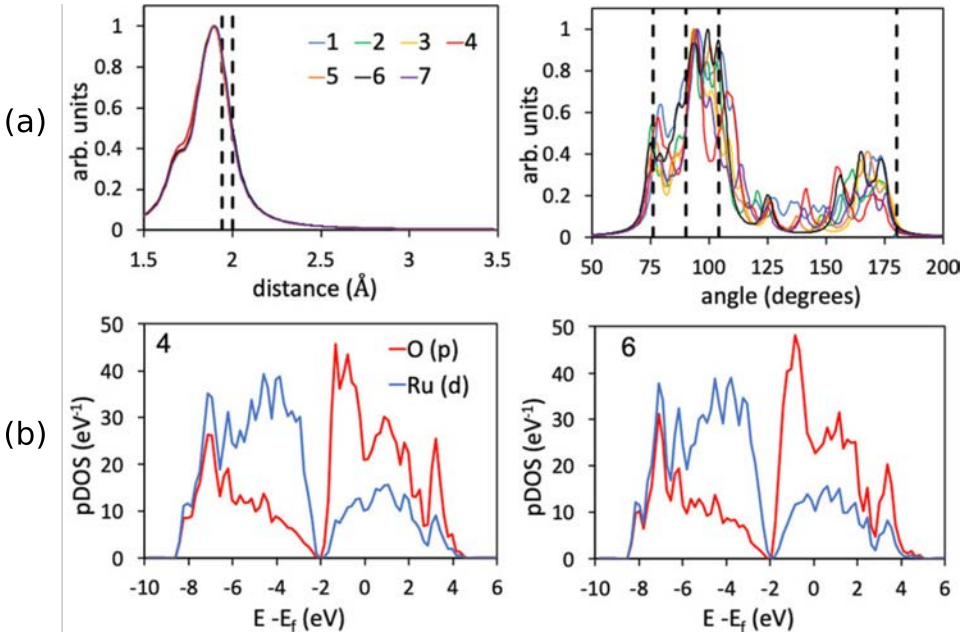

Figure 3.12: Structural and electronic characteristics of $(RuO_2)_{33}$ isomers. (a) Ru−O distance and Ru−O−Ru angle distribution of ions in the nanoparticle surface. The black doted lines shows the bulk values. (b) PDOS of the most stable isomer and the less stable one.

subtle reconstruction differences between the seven nanoparticles.

Furthermore, since the structural difference between nanoparticle isomers comes from the relaxation of surface ions, we can use the projected density of states (PDOS) from those ions to compare between them at electronic level. The common approach to study catalytic properties of metal oxide surfaces is to focus on metal *d*-band and oxygen *p* state energies.[172,173] All isomers have two bands, the first between -9.0/-8.8 eV and -2.1/-1.9 eV, and the second between -2.1/-1.9 eV and +4.9/+5.1 eV relative to the Fermi energy. The lower energy band has a rich metallic character (74-75%) and the higher

one has a larger oxygen contribution (65-67%). PDOS of all structures has almost the same peaks and present the same shape (see Fig. A.1 in Appendix A). Overall, the seven structures generated by BCN-M have similar geometric and electronic structure, pointing out that they all could behave similarly.

3.4 Conclusions

Construction of atomistic nanoparticle models of binary compounds is not always straightforward because it usually involves post-processing to obtain stoichiometric and charge electroneutral systems. This implies manual modification of the NP structures, which is under user subjectivity and bias. The bulk cut nanoparticle model (BCN-M) is a computational tool delivered as a free web platform (http://bcnm.qf.uab.cat) and downloadable utility that is able to generate Wulff-like nanoparticle models with controlled stoichiometry and surface termination. Models are constructed from the crystallographic data of the selected material (cell parameters of the conventional unit cell, space group symmetry, and fractional coordinates of the irreducible atoms), the surface energies of the main crystallographic facets, and information about the desired surface termination. BCN-M explores several different nanoparticle centers to ensure different sets of nanoparticles usually covering even and odd numbers of AXBY units. Moreover, the quality of the resulting models is analyzed with (i) the Wulff-like criterion, which measures the deviation from an ideal Wulff shape, (ii) the global coordination of the atoms of the model, and (iii) the distribution coefficient, which evaluates the polarity of

the model. BCN-M has been tested and applied to 16 cases covering the most representative cubic, tetragonal, hexagonal, and monoclinic crystallographic systems involving only nonpolar surfaces or a combination of both polar and nonpolar ones. Finally, as a proof of concept, we use a ternary compound to the aim to extend developed approach for binary materials to more general ones.

BCN-M models are generated from cutting the bulk structure, and accordingly, they do not take into account the most likely surface reconstruction events. In this context, these models can be used as starting points for further simulations or structure analysis of ideal systems. Because of its user-friendly handling, BCN-M can facilitate the developments of structure–property relationships in nanoscience, that is, atomistic models of nanoparticles can provide information on the number and nature of surface sites, thereby relating their size and shape with its surface properties. In addition, the BCN-M tool can help evaluating how changes in the relative surface energies, which can be modified through capping agents, can influence the nanoparticle shape and surface properties, assisting in the design of new catalysts.

4 IrO_2-Water Interaction

This chapter presents an exhaustive analysis of H_2O-IrO_2 interaction on lower index stable surfaces, namely (011), (100), (001) and (110) as well as a $(IrO_2)_{33}$ Wulff-like nanoparticle model. For each kind of material (surfaces or nanoparticle), the analysis starts by discussing the interaction between IrO_2 and a single water molecule. To determine the role of cooperative effects, in a second step, all iridium coordination vacancies are fulfilled with water molecules forming a monolayer. Moreover, thermal effects were studied by Ab Initio molecular dynamics. Results show that the H_2O-IrO_2 surface interaction strength and degree of dissociation strongly depend on the iridium coordination, nature of the vacant site and basicity of the surface oxygen atoms. In the nanoparticle model, the number of sites increases and they were all considered. Nanoparticle morphology prevents the formation of hydrogen bonding between the adsorbed water and IrO_2 oxygen atoms; therefore, the adsorption energies are usually weaker than in slabs. However, surface Ir and O atoms are, respectively, more acid and basic than in the slab models leading to a larger preference for the dissociative form. Finally, both cooperative and thermal effects tend to favor the adsorption of molecular water being the H_2O degree of dissociation smaller in the case of the monolayer.

4.1 Introduction

IrO_2(rutile) is a widely studied catalyst for energy conversion and storage in chemical bonds by catalytic oxidation of water molecules.[174–176] Thus, the study of the water-material interface is crucial to have a deeper understanding of the catalytic processes. The knowledge of the intrinsic water–IrO_2 interaction as well as how this interaction varies when increasing the water coverage is of high importance. In this context, some works dealing with this interaction have been reported in the literature.[177,178] To the best of our knowledge, only the surface-water on the most stable (110) facet has been addressed through DFT calculations. For instance, the effect on the water interaction has been addressed by increasing the water coverage on the surface. They have studied several water coverages that include: (i) half or total saturation of coordination unsaturated sites (0.5 and 1.0 monolayers), (ii) the addition of water molecules coordinated by hydrogen bonds to surface oxygen atoms (1.5 and 2.0 monolayers) and (iii) the further addition of water molecules that do not interact directly with the surface. They found that at 0.5 and 1.0 monolayer coverages, the adsorbed water molecules dissociates spontaneously, whereas, at the higher coverages, the water dissociation is hampered promoting the formation of water chains along the surface.[177]

For other rutile-like materials like TiO_2 or RuO_2 several experimental and theoretical studies have been done.[171,179–194] For instance, the water-surface interaction for RuO_2 surfaces at different coverages has been addressed for (110), (011), (001) and (100) surfaces. Experimental results show that the degree of water dissociation depends

on the surface crystallographic orientation. The (011) surface has the maximum degree of dissociation, followed by the (110), (001) and (100) surfaces.[193] A previous contribution from the group on RuO_2 surfaces shows that three effects are crucial for determining the degree of deprotonation: (i) the intrinsic acidity of the unsaturated ruthenium centers and the intrinsic basicity of the oxygen bridge (O_{br}); (ii) the presence of strong cooperativity effects and (iii) the increase of the O_{br} basicity by the adsorption of water molecules to centers bonded to O_{br} groups.[171]

Regarding the nanoparticle-water interaction for IrO_2, experimental results suggest that all the adsorbed water molecules are dissociated, leading the nanoparticle surface hydroxylated.[91] However, to the best of our knowledge, there are no computational reports on the IrO_2 nanoparticle water interaction. For TiO_2 and RuO_2 computational studies shows that the water adsorption energy depends on the adsorption site and the cooperativity effects between adsorbed water molecules.[195,196] For instance, for TiO_2 nanoparticles, a single water molecule is more strongly adsorbed on the face of an ideal 1 nm nanoparticle than on an edge site. Moreover, for RuO_2 nanoparticles it has been identified that the dissociated form is the preferred one for an isolated water molecule coverage.[196] Regarding the cooperative effects on nanoparticle surfaces, the adsorption energy per water molecule in monolayer coverage for TiO_2 rutile nanoparticle is slightly lower than on single-site adsorption. The dissociation percentages between 25 and 54% has been reported for TiO_2 and RuO_2 rutile nanoparticles. Moreover, it has been proposed that the formation of $H_3O_2^-$ motifs determines the monolayer water

structure.[195,196]

4.2 Extended Surfaces

4.2.1 Bulk Material and Slabs

In Table 4.1 the main distances, cell parameters and computed net charges of Ir and O are reported. It can be observed that both Ir−O distances and cell parameters are in agreement with the experimentally determined values,[197] deviations being smaller than 1.5%. As found experimentally, Ir^{4+} exhibits a distorted octahedral environment due to tetrahedral compression with four longer Ir−O distances in the equatorial plane and two shorter Ir−O axial distances. Ir at IrO_2 is essentially Ir^{4+} with five 5d electrons that occupies three $t2_g$ orbitals, two of them are double occupied and stabilized by the elongation of the Ir-O distance in the equatorial plane, and monooccupies the third one. This unpaired electron can lead to magnetic properties. To clarify this point, spin-polarized PBE-D2 calculations were performed. The results indicate that the total magnetization, defined as the difference of α and β electronic densities is zero, in agreement with previous theoretical and experimental works.[86,198]

Table 4.1: Bulk Computed Distances (in Å), Cell Parameters, and Net Atomic Charges (a.u.). Experimental values in italics.

$a = b$	c	$d_{(Ir-O_{eq})}$	$d_{(Ir-O_{ax})}$	$d_{(Ir-Ir)}$	$q_{(Ir)}$	$q_{(O)}$
4.497	3.193	2.013	1.980	3.193, 3.584	1.66	-0.83
4.505	*3.159*	*1.998*	*1.958*			

Slab models for the four more stable surfaces [(110), (011), (100), and (001)] were built cutting out the slab from the optimized bulk structure, and the surface thickness was increased until the surface energy converged. The main Ir-O distances of the outermost layer, converged surface energies, their relative contribution to the Wulff-construction and net atomic charges are reported in Table 4.2. The surface structures are shown in Fig. 4.1. Values corresponding to the internal layers are very similar to the bulk ones and thus have not been included and will not be discussed further.

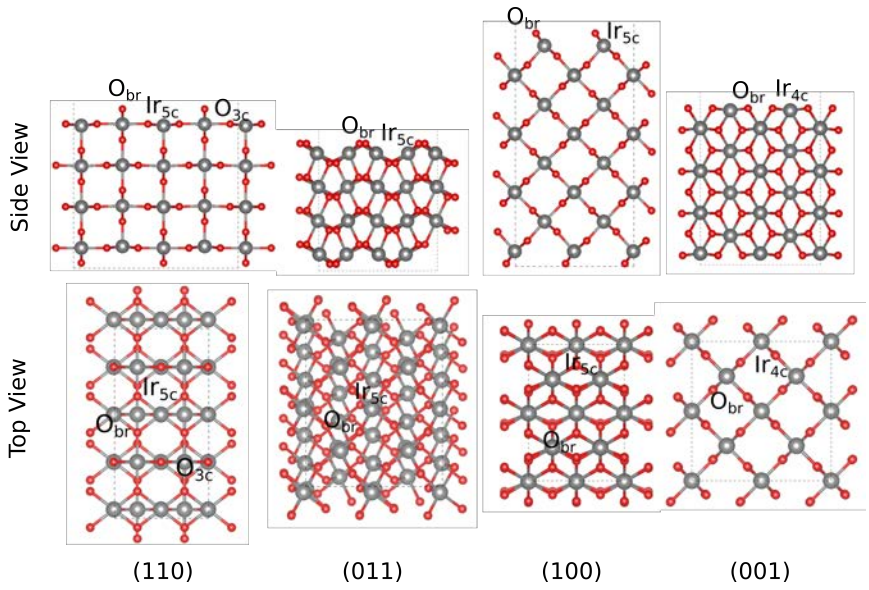

Figure 4.1: Top and side views of IrO_2 (110), (011), (100) and (001) surfaces. Coordination of surface species are also shown.

In all cases, bulk cutting to generate slab models leads to two-coordinated bridging oxygen (O_{br}) at the surface, as well as five-coordinated (Ir_{5c}) sites for (110), (011), and (100) and four-coordinated (Ir_{4c}) for (001). The vacant site of Ir_{5c} in the (110) and (100) surfaces

Table 4.2: Surface energies (γ in eV/Å^2), main surface distances (in Å) and net atomic charges (a.u.).

Surface	γ	$d_{(Ir-O_{br})}$	$d_{(Ir_{5/4c}-O_{eq})}$	$d_{(Ir_{5/4c}-O_{ax})}$	$d_{(Ir-Ir)}$	$q_{(Ir_{5/4c})}$	$q_{(O_{br})}$
(1 1 0)	0.150	1.982	2.012	1.943	3.187	1.47	–0.70
(0 1 1)	0.158	1.897, 1.926	2.000, 2.077	2.000	3.708	1.54	–0.74
(1 0 0)	0.185	1.960	1.960, 2.034	1.985	3.187	1.50	–0.71
(0 0 1)	0.206	1.905, 1.992	1.955	1.905	4.541	1.45	–0.77

is axial, whereas the vacant site of Ir_{5c} in the (011) surface is equatorial. For the Ir_{4c} sites in the (001) facet, both vacant sites are equatorial. Surface Ir−O distances corresponding to unsaturated Ir sites vary depending on the coordination environment, the shortest values being found for the axial Ir_{4c}−O bonds of the (001) surface. Ir−Ir distances largely vary depending on the crystal facet and range between 3 and 4.5 Å. By comparing the Ir−Ir distances with the bulk values, the (011) is the one that shows the largest differences, around 3%. The calculated surface energies are in agreement with the values reported in the literature and follows the same trend, being the (110) facet the most stable one (0.158 ev/Å^2) and the (001) the less stable (0.206 ev/Å^2).[72,199] The relative stability can be related to the number of broken bonds to per surface area. For instance, to get (001) surface, two Ir−O bonds for each Ir center are broken, meanwhile for (110) only one is.[199]

4.2.2 Surface-Single Water Interaction

The adsorption of one water molecule fills one of the four or eight oxygen vacancies found on (110) and (100) or (001) and (011) surfaces, respectively. For the (001) surface, it is assumed that two water molecules can be adsorbed per Ir_{4c} site. The interaction with the metal surface increases water acidity leading to the formation of a hydrogen bond between one H atom of the water molecule and the nearest O_{br}. The intensity of the $H \cdots O_{br}$ interaction and the increase in the water molecule acidity can promote the O_w−H bond

breaking. This leads to two fragments, OH^- and H^+, that are adsorbed on $Ir_{4/5c}$ and O_{br} respectively. Here, molecular *(mol)* form and dissociated *(diss)* one (H^+/OH^-) have been studied. In Table 4.3 the adsorption energies, relative stabilities between forms and main structural parameters are reported. The optimized structures are depicted in Fig. 4.2.

The H_2O adsorption energy ranges between 211.5 and 146.0 kJ mol^{-1}. The highest adsorption energy is found for the (110), the lowest adsorption energies are computed for the (011) surface, and intermediate values are computed for the (001) and (100) surfaces. The H_2O-IrO_2 surface interaction strength is highly related to the feasibility of the H_2O dissociation.

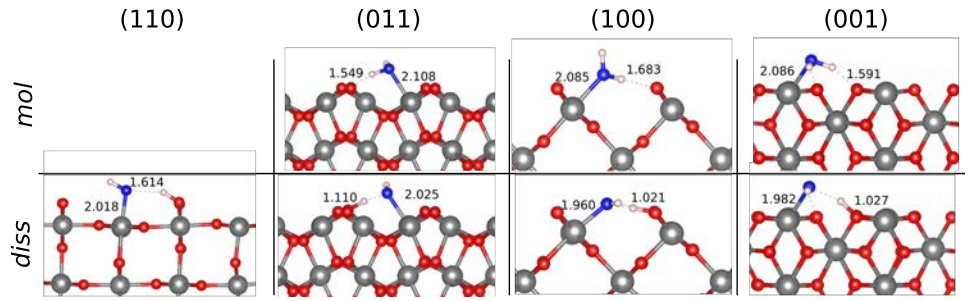

Figure 4.2: Optimized geometries for all considered IrO_2 surfaces for *mol* and *diss*.

For (110), only the dissociated form is a local minimum. For the other surfaces both conformations, *mol* and *diss*, were located. Indeed, the *diss* form is the most stable in the (110), (100) and (001), while the *mol* one is the preferred conformation on the (011) surface.

The differences between surfaces can be related to the coordination of the metal center, the nature of the vacant site, axial or equatorial

Table 4.3: Adsorption energies (E_ads in kJ mol^{-1}), relative stabilities between the molecular and dissociated forms (ΔE in kJ mol^{-1}), main distances (in Å), and net atomic charges. For water and O_{br} labels see Fig. 4.6.

Surface		E_{ads}	ΔE	$d_{(O_w-H_w)}$	$d_{(O_{br}-H_w)}$	$d_{(Ir-O_w)}$	$q_{(Ir)}$	$q_{(O_{br})}$	$q_{(H_2O)}$
(110)	*diss*	-211.5	–	1.614	1.014	2.018	1.68	-1.09	0.28
(011)	*mol*	-153.0	-7.0	1.043	1.549	2.108	1.65	-0.86	0.15
	diss	-146.0	0.0	1.372	1.110	2.025	1.69	-1.01	0.22
(100)	*mol*	-191.2	1.9	1.024	1.683	2.085	1.63	-0.83	0.17
	diss	-193.1	0.0	1.688	1.021	1.960	1.70	-1.06	0.30
(001)	*mol*	-201.7	1.4	1.034	1.591	2.086	1.57	-0.86	0.15
	diss	-203.1	0.0	1.632	1.027	1.982	1.64	-1.07	0.68

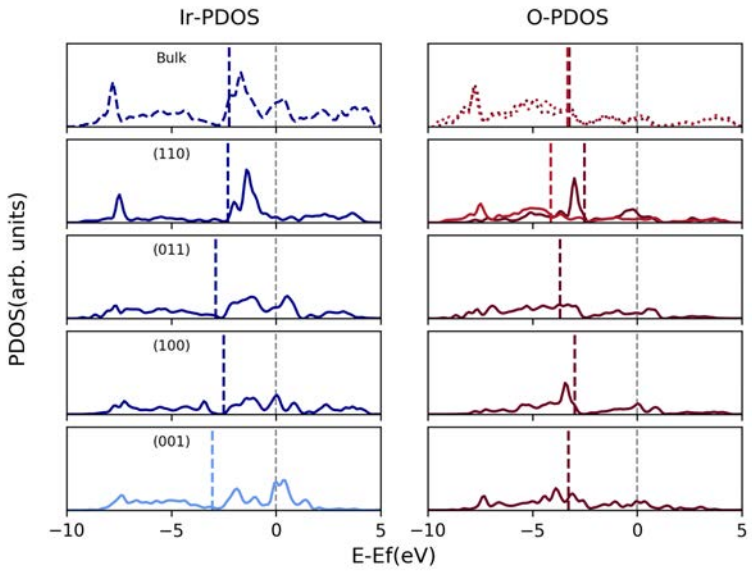

Figure 4.3: PDOS for d-$Ir_{5/4c}$ and p-O_{br}. The gray dashed line indicates the Fermi level. For bulk O_{eq} and O_{ax} are depicted. For (110) surface O_{br} and O_{3c} are shown in dark red and light red respectively.

on each surface and the tetragonal compression observed in the bulk material. First, tetracoordinated centers of the (001) surface are less stabilized an thus, even the vacant site are equatorial (See below), the H_2O-Ir interaction in this surface is strong. Since axial bonds are shorter than equatorial ones, surfaces with axial vacancies -(110) and (100)- have an stronger H_2O-Ir interaction than the surfaces with equatorial vacancies -(011) as reported in Table 4.3. The differences in the adsorption energies are also reflected in the PDOS. In Fig. 4.3 O-p and Ir-d bands for bulk and surfaces are shown. It can be observed that the PDOS bands are distributed similarly regardless of the surface, although with different intensities. A powerful method to characterize an electronic band is their band center ($\bar{\varepsilon}$)

defined as

$$\bar{\varepsilon} = \frac{\int_{\varepsilon_{min}}^{\varepsilon_{max}} \varepsilon \rho(\varepsilon) d\varepsilon}{\int_{\varepsilon_{min}}^{\varepsilon_{max}} \rho(\varepsilon) d\varepsilon}, \tag{4.1}$$

where $\rho(\varepsilon)$ is the PDOS and ε is the energy for a particular band.[172,173,200] In this work, ε_{min} and ε_{max} are -10 eV and 5 eV with respect to the Fermi energy. To identify the effect of the vacancy on the electronic properties of the material, the computed values of $\bar{\varepsilon}$ for the bulk material and the surfaces are reported in Table 4.4.

Table 4.4: Band centers ($\bar{\varepsilon}$) for bulk material and clean surfaces.

	$Ir_{5c/4c}$	O
Bulk	-2.2	-3.3[a]
(1 1 0)	-2.3	-2.5 (*-4.1*) [b]
(0 1 1)	-2.9	-3.7
(1 0 0)	-2.5	-3.0
(0 0 1)	-3.0	-3.3

[a] O_{ax} and O_{eq} have the same band center. [b] In italics, $\bar{\varepsilon}$ for outermost O_{3c}.

Surfaces with axial vacancies ((110) and (100)) have d-band centers (d-$\bar{\varepsilon}$) similar to that of the bulk, whereas surfaces with equatorial vacancies ((011) and (001)) have a lower d-band $\bar{\varepsilon}$. The d-band model argues that Ir d-$\bar{\varepsilon}$ close to the Fermi level (less negative) is related to strong metal-adsorbate interaction.[200] Hence, surfaces with axial vacancy ((110) and (100)), that have d-$\bar{\varepsilon}$ close to the Fermi level have a strong metal-water interaction. For instance, $Ir-O_w$ distance for the *mol* form are shorter shorter for (100) than for (011) surface (See Table 4.3).

Regarding O_{br}, the center of the band model shows that (110) has the most basic O_{br} centers and the order of O_{br} basicity as function of the surface is (119)>(100)>(001)>(011). Hence, the tendency for water dissociation is the same, in agreement to the fact only the *diss* form is found for the former and the *mol* conformation is the most stable structure for the latter.

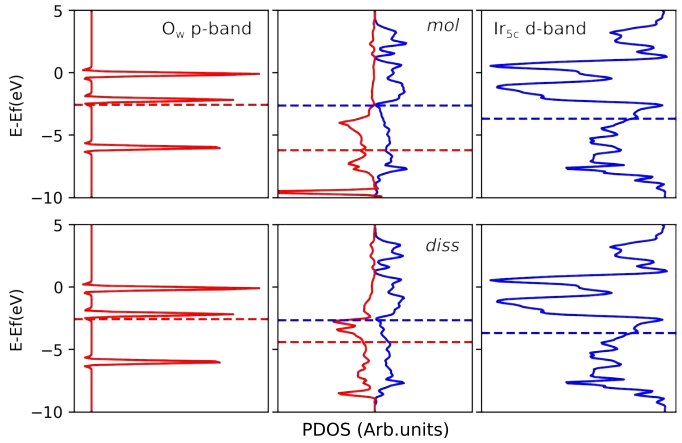

Figure 4.4: PDOS of O_w and Ir_{5c} and their change due water adsorption in *mol* and *diss* forms for (011) surface.

The p and d-bands of O_w and Ir_{5c} before and after dissociation has been analyzed in order to rationalize the $Ir_{5c}-O_w$ interaction. Fig. 4.4 shows the bands corresponding to the (011) surface for *mol* and *diss* forms. The non-adsorbed water molecule has the O p-$\bar{\varepsilon}$ at -2.5 eV with 3 highly populated states, around -6, -2 and 0 eV with respect to the Fermi level. (See Fig. 4.4, left panel). Once the water molecule is adsorbed, the p-band is shifted downwards decreasing the $\bar{\varepsilon}$.[173,200] As for molecular orbitals approximation, where molecular bonding and anti-bonding orbitals are formed by the interaction between atomic orbitals of interacting species, in solids, the adsorbate-metal

interaction gives bonding and anti-bonding states. In Fig. 4.4 central panel, we can see that the Ir d-$\bar{\varepsilon}$ increases and the O_w p-$\bar{\varepsilon}$ decreases. Therefore, low-lying states with a bonding character have a rich O_w-p character and the anti-bonding ones have larger Ir-d character. On the other hand, in *mol* conformation only the px and py bands participate in the bond formation, while in the *diss* form all p bands participate (See Fig. 4.5).

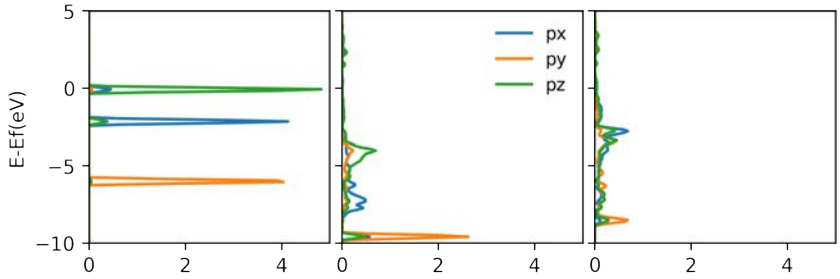

Figure 4.5: px, py and pz PDOS for O_w in vacuum (left) and in adsorbed forms (*mol* (center) and *diss* (right) on (011) surface.

Furthermore, Bader charge analysis shows an increase in the charge on the water molecule due to the $Ir-O_w$ interaction. The larger the interaction is, the larger the increase of acidity of the water molecule. Such increase is coupled to an increase of the O_{br} basicity, leading to an easier proton transfer on Ir_{5c} with axial vacancies ((110) and 100)) than with an equatorial vacancy (011). Moreover, less coordinated Ir centers have a larger $Ir-O_w$ interaction than those with a higher coordination promoting the water dissociation. A similar effect has been reported for other rutile-like materials.[164,171]

4.2.3 Surface-Water Monolayer Interaction

The previous section shows that the relative stability between the *mol* and *diss* adsorbed forms of water on the surface depends on the intensity of water-Ir interaction and the basicity of O_{br}. These factors depend on the crystallographic orientation. However, the adsorption of several water molecules on the surface promotes H-bond interactions, that directly affects the water adsorption and their dissociation regardless of the material form. Thus, we have analyzed the structure of a water monolayer on each surface. For that, we have added one or two water molecules at each $Ir_{5c/4c}$ unsaturated metal centers; that is, four molecules per unit cell at the (110) and (100) surfaces and eight water molecules at the (011) and (001) ones. We considered all possible combinations of *mol* and *diss* water molecules as initial structures. For instance, for the (110) surface, we considered seven possible structures: (i) 4 undissociated (molecular) water molecules (4 *mol*), (ii) 3 molecular and 1 dissociated (3 *mol*/1 *diss*), (iii) 2 *mol*/ 2*diss*, (iv) 1 *mol*/3 *diss*, and (v) 4 *diss*. Note that for the 2 *mol*/2 *diss* configuration three different starting situations are possible, two in which the two equal molecules (*mol* or *diss*) are neighbors and another one in which they are not. All possible combinations were also considered for the other surfaces. Adsorption energies per water molecule and structural parameters of main configurations are given in Table 4.5. Fig. 4.6 shows the optimized structures of the most stable configuration for each surface.

Again, the H_2O-(110) interarction is the strongest one, the computed E_{ads} per water molecule is essentially equal to that of the isolated water model. The lowest value is also computed for the (011) surfaces,

but in this case, cooperative effects strength the interaction about 20 kJ mol^{-1}. Finally, intermediate values are obtained for the (100) and (001) surfaces. It is worth mentioning that the adsorption of two water molecules on a Ir_{4c} center decrease the interaction about 20 kJ mol^{-1}.

As for the single water interaction, for the (110) surface full coverage only the conformation with all molecules dissociated (4 *diss*) is stable. Since the adsorption energy per water molecule is nearly equal to that obtained for an isolated water molecule, one can conclude that the H-bonding interactions are weak (the $O_{w1}-H_{w2}$ distance is 2.350 Å). This is in contrast to RuO_2 and TiO_2, where there is strong H-bonding interaction that stabilizes the formation of $H_3O_2{}^-$ dimer, thus favoring 50% of water dissociation and increasing the adsorption energy.[171]

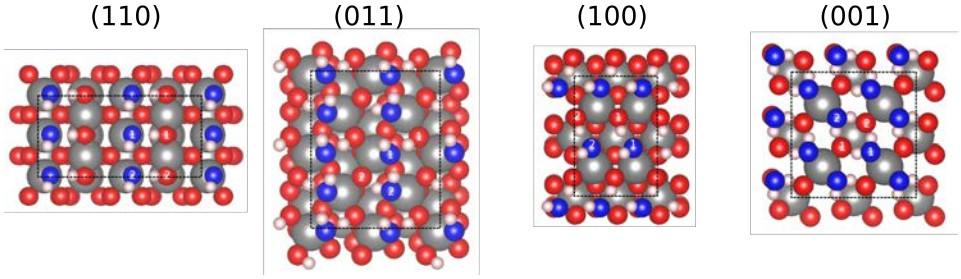

Figure 4.6: Most stable configurations for water monolayer. The numbers 1 and 2 refers to the interacting water molecules and define the main structural parameters included in Table 4.5.

For the (011) surface, the most stable conformation is 2 *mol*/6 *diss*. In contrast to (110), in the (011) surface, the dissociation of water molecules allows the formation of H-bonding interactions. In Fig. 4.7 the clean surface of the (110) and (011) surfaces and the vacancies

Table 4.5: Adsorption energies(E_{ads} in kJ/mol) per water molecule and main distances (in Å) for water monolayer. For water and O_{br} labels see Fig. 4.6

Surface	config	E_{ads}	Ir_1-O_{w1}	Ir_1-O_{w2}	$O_{w1}-H_{w1}$	$O_{w1}-H_{w2}$	$O_{br1}-H_{w1}$	$O_{br2}-H_{w2}$
(110)	4 *diss*	–210.5	2.002	2.000	1.759	2.350	1.019	1.019
(011)	4 *mol*/4*diss*	–156.7	2.030	2.141	1.598	1.503	1.021	2.410
	3 *mol*/5 *diss*	–160.7	2.057	2.135	1.512	1.499	1.042	2.505
	2 *mol*/6 *diss*	–172.8	2.060	2.102	1.458	1.679	1.069	1.534
(100)	4 *mol*	-183.0	2.135	2.135	1.060	2.779	1.546	1.546
	2 *mol*/2 *diss*	-191.5	2.008	2.137	1.840	2.604	1.008	1.560
	4 *diss*	-199.3	2.007	2.007	1.637	2.641	1.030	1.030
(001)	8 *mol*	-179.1	2.095	2.095	1.023	2.917	1.634	1.547

directions are represented. Thus, on the (011), the vacancies are confronted, whereas, on the (110) all vacancies are perpendicular to the surface. Therefore, on the (011) surface the average $O_{w1}-O_{w2}$ distance is shorter than the one on the (110) surface (2.743 vs 3.186 Å). In addition, $O_{br}-O_w$ average distances is shorter in (011) than in (110) , which allows forming additional hydrogen bonds between O_wH and $O_{br}H$ moieties. Hence, 2 *mol*/6 *diss* has twelve hydrogen bonds whereas conformations with a lower degree of dissociation such as 3 *mol*/5 *diss* and 4 *mol*/4 *diss* have ten and eight H-bonds, respectively. As mentioned, the adsorption energy per water molecule in this surface is around 20 kJ/mol more favorable than the one for the isolated water molecule. Therefore, the (011) surface is the one where cooperative effects are more important and promote water adsorption.

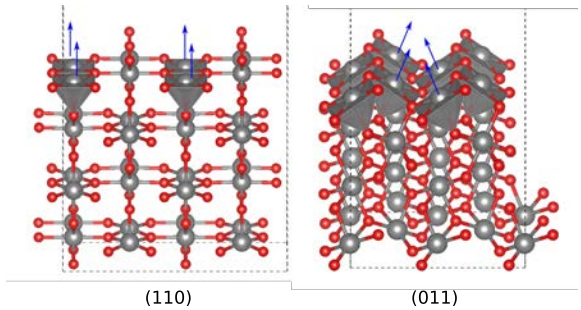

Figure 4.7: Polyhedral representation for the (110) and (011) surfaces. The direction of the vacancies are represented as a blue arrow. In the (110) surface, the vacancies are perpendicular to the facet plane, whereas for the (011) are confronted.

Regarding the (100) surface, the most stable configuration has all water molecules dissociated. For this conformation, the adsorption energy is slightly larger than the computed for the isolated water

(199.3 vs 193.1 kJ mol^{-1}). The subtle increase on the adsorption energy for the monolayer, even when the $Ir-O_w$ distance is larger (2.007 vs 1.960 Å) could be attributed to the fact that the Ow_1-Hw_1 hydrogen bond is stronger for the monolayer coverage (1.637 vs 1.683 Å). Moreover, lower dissociated configurations are also located. By comparison with the (110) surface that also has axial vacancies, the Ir_{5c} and O_{br} sites on (100) surface have band centers further to the Fermi level compared to those on the (110) surface (See Table 4.4) suggesting that the intrinsic surface-water interaction are weaker and thus structure with non-dissociated water molecule becomes closer in energy.

Finally, the most stable conformation on the (001) surface has all water molecules forming two H-Bonds with neighboring O_{br} (See Fig. 4.6) with a 0% dissociation (8 *mol*). Despite several efforts to locate conformations with a higher degree of dissociation, all attempts collapsed to 8 *mol*. For the monolayer, as reported in Table 4.5, the distances that denote the water-surface interaction, $Ir_{4c}-O_w$ and $O_{br}-H_w$ are almost the same that for an isolated water. However, the E_{ads} per water molecule in the monolayer is 24 kJ/mol less favorable than for the isolated water. Even though the *diss* form of the single isolated water is slightly more stable than the *mol* form, the presence of second water on the same center reduces the $Ir_{4c}-O_w$ interaction, decreasing the water molecule acidity and the E_{ads} and disfavoring the H_2O dissociation. As we can see in Table 4.4, the superficial Ir_{4c} and the O_{br} on the (001) surface have their band centers further from the Fermi level than those on the other studied

surfaces. Therefore, water-surface interaction is weaker here, particularly when the metal center is fully coordinated.

As reported above for each surface, the energy difference among configurations per water molecule is small (3-16 kJ/mol) and all of them may contribute to the behavior of the water-IrO_2 interface. On the other hand, thermal effects may modify the relative stability of these configurations. Therefore, we have run *Ab-Initio* molecular dynamics (AIMD) up to 8 ps starting from the most stable monolayer of the static calculations. Due to the enormous computational cost of AIMD, we only perform it for (110) and (011) surfaces as limit examples. That is no-cooperative effects appear to be relevant to the (110) and they have important consequences in the (011) facet. In Fig. 4.8 hydrogen bond distance and $Ir-O_w$ distance for two neigboring water molecules are shown. Table 4.6 shows the frequency of each possible conformation considering that proton transfer to an O_{br} occurs if the H-bond distance is smaller than 1.2 Å .

For the (011) surface, we observed large proton mobility. The most stable configuration from static calculations on this surface (2 *mol*/6 *diss*) is no longer the main one when including thermal effects. Indeed, two additional less dissociated conformations, 4 *mol*/4 *diss* and 3 *mol*/5 *diss* are preferred. The three conformations account for 95%, being the 3 *mol*/5 *diss* the most frequent one. For (110), as predicted by static calculations, the main configuration is a fully dissociated monolayer (4 *diss*) with an 83.7% frequency. Noticeably, there is a non-negligible frequency of the 1 *mol*/3 *diss* (11.4%) and of the 2 *mol*/2 *diss* (4.8%). By analyzing the $Ir-O_w$ distance, the thermal effects increase the bond distance, reducing the water-surface

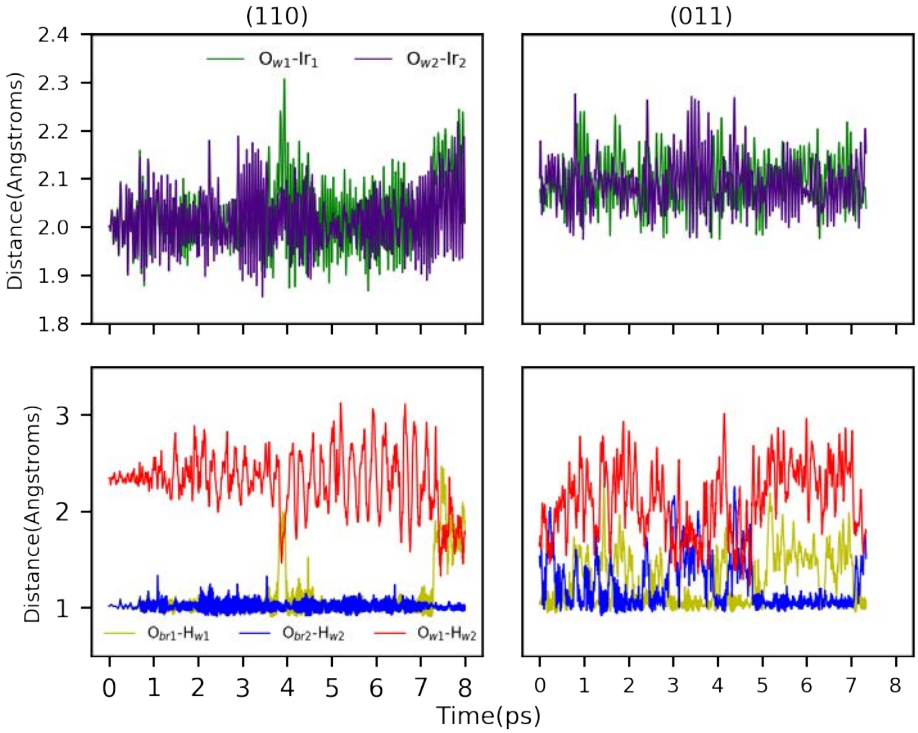

Figure 4.8: Ir$-O_w$ (Top) and H-Bond (Bottom) distances of two neighboring water molecules along the dynamics.

interaction and decreasing the dissociation degree. The presented results for (110) and (011) surfaces show that thermal effects increase the presence of less dissociated configurations by decreasing the surface-water interaction and thus, the adsorbed water acidity.

Table 4.6: Percentage of configurations with different degree of water dissociation on the (110) and (011) surfaces of IrO_2.

surface	configurations	percentage
(110)	4 *mol*	0.0
	3 *mol*/1 *diss*	0.0
	2 *mol*/2 *diss*	4.8
	1 *mol*/3 *diss*	11.4
	4 *diss*	83.7
(011)	8 *mol*	0.0
	7 *mol*/1 *diss*	0.0
	6 *mol*/2 *diss*	0.0
	5 *mol*/3 *diss*	2.6
	4 *mol*/4 *diss*	33.5
	3 *mol*/5 *diss*	42.7
	2 *mol*/6 *diss*	19.5
	1 *mol*/7 *diss*	1.4
	8 *diss*	0.3

4.3 Wulff-like Nanoparticles

The Wulff polyhedron of IrO_2 can be obtained using the computed surface energies. This gives us the guidelines to cut the nanoparticle from the bulk material. The {110} and {011} family surfaces have the largest surface area contribution (40.3 and 53.1%) whereas the {100} has the smallest one (6.6%). The {001} family has the highest surface energy and it does not contribute.

By using the previously computed surface energies and the material properties, several nanoparticles can be generated using the BCN-M tool.[157] From these, we selected the one that has a diameter of 1.2 nm, that is the smallest reported size for synthesized crystalline nanoparticles.[201] The selected model has 33 IrO_2 units, making it a

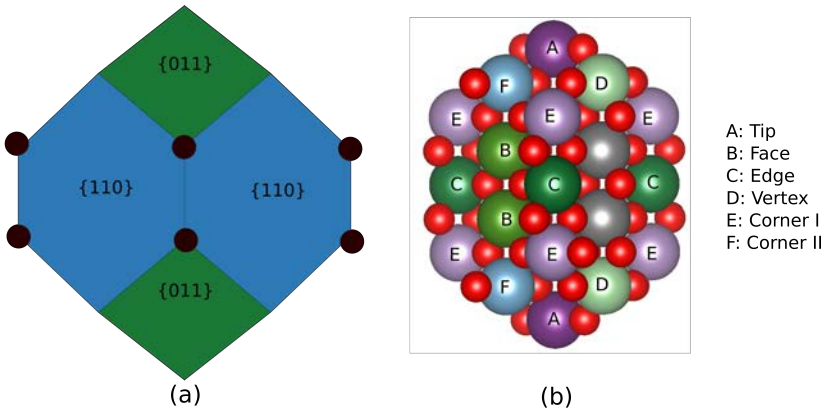

Figure 4.9: (a) Wulff polyhedron and (b) $(IrO_2)_{33}$ nanoparticle. Coordination of surperficial Ir centers are shown.

relevant model with an affordable computational cost. Note that the following size has 90 IrO_2 units, thus the computational cost becoming very large.

For the $(IrO_2)_{33}$ nanoparticle, only the {110} and {011} surface families are present, and the iridium centers on the surface are either 4, 5 or 6 coordinated. The undercoordinated centers are located at the {110} surfaces and the intersection among different facets. Fig. 4.9 shows the Wulff construction and the six different existing types of undercoordinated Ir centers. It is worth to mention that BCN-M generates seven isomers of $(IrO_2)_{33}$ nanoparticle. The difference among them is the location of two single coordinated oxygens in the intersection of two surfaces of the {110} family and one of the {011} facets

(Black dots and corner I atoms on Fig. 4.9). Further discussion of isomers of $(MO_2)_{33}$ rutile-like nanoparticles can be found in Chapter 3. One can distinguish the Ir_{5c} centers on the {110} facets, at the edge of two {110} surfaces and at the vertex of one (110) and two (011) facets (B, C and D centers on Fig. 4.9 (b), respectively). The corner I centers (E in Fig. 4.9 (b)) can either be penta- or tetracoordinated depending on the presence/absence of single coordinated oxygen atoms. They are located at the crossing between two {110} facets and one {011} surface. Two additional types of Ir_{4C} centers also exists on $(IrO_2)_{33}$. They are located at corner II and tip positions (F and A in Fig. 4.9 (b)). The corner II centers are on the intersection point of two {011} facets and one {110} surface and they always have a single coordinated oxygen, while the tip centers are at the crossing of four {011} facets. The adsorption of a single water molecule has been studied on five of these six centers, since we decided to avoid at this stage centers with single coordinated oxygen atoms (corner II and pentacoordinated corner I). Overall, three Ir_{5c} and two Ir_{4c} centers are considered. Two of the three Ir_{5c} centers present axial vacant (B and C) site and the other has an equatorial one (D). The tip center has two equatorial vacant sites, whereas the corner I center has one equatorial and one axial vacant site. That is, all combinations of coordination number and nature of the vacant site have been explored.

The seven $(IrO_2)_{33}$ nanoparticle isomers were fully optimized, and in all cases, their final structure shows the same similar features. The ionic relaxation induces a large reconstruction, which includes the formation of $Ir-Ir$ bonds and the breaking of $Ir-O$ ones. For instance, the initial and optimized structures of one of these seven

isomers are shown in Fig. 4.10 The optimized structure presents an IrIr bond between the tip and corner II, which occurs on both sides of the nanoparticle. This is evidenced by the fact that the initial Ir_{tip} – $Ir_{cornerII}$ distance, which is 3.584 Å, gets reduced to 2.614 Åafter optimization. Spin-polarized calculations show that each Ir center has an initial magnetization of 1.026 and -0.969 a.u., respectively, which couple during the optimization forming a bond. In parallel to the IrIr bond formation, both involved ions break one Ir–O bond. The broken Ir–O bond at the tip center implies an inner equatorial oxygen atom (the final Ir $\cdots$ O is 2.82 Å), which becomes more strongly bonded to the corner II center that is not involved in the Ir–Ir bond formation. The broken Ir–O bond at corner II implies also an equatorial oxygen, but in this case, located on the nanoparticle surface (See side view on Fig. 4.10). As a consequence, the center becomes tricoordinated with Ir–O bond distances ranging between 1.710 and 1.882 Å, shorter than those distances for bulk and surfaces. Moreover, the O–Ir–O angles are between 95.9 and 141°, resembling a planar structure (See Fig. 4.10 small box). The reorganization around the tip also induces a large reorganization on the neighborhood centers. For instance, corner I with a singly coordinated oxygen adopts a largely distorted tetrahedral conformation with O–Ir–O angles ranging between 72 and 138° and Ir–O distances between 1.720 and 2.298 Å. Finally, the other positions on the nanoparticle surface, albeit being slightly distorted, do not lose their initial structure.

As pointed out, geometric relaxation of the $(IrO_2)_{33}$ nanoparticle implies a large reconstruction of the tip, corner I and corner II centers.

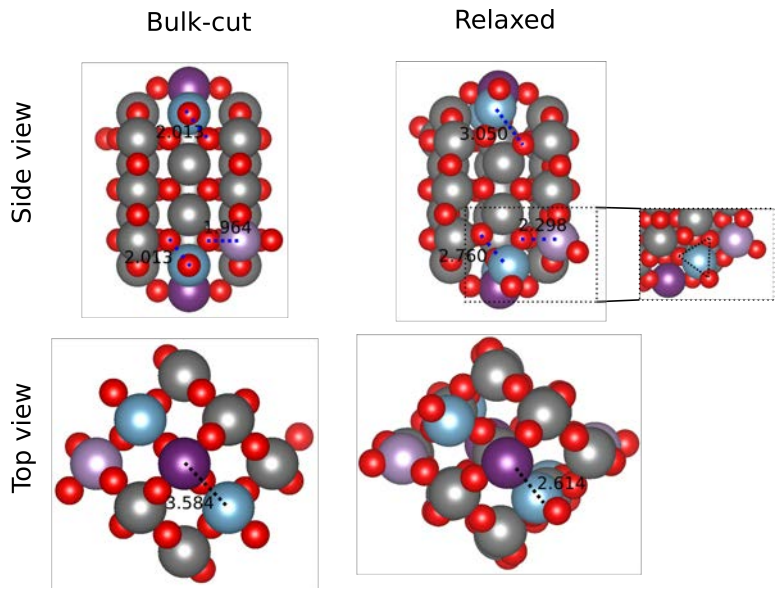

Figure 4.10: Side and top views of the initial and relaxed $(IrO_2)_{33}$ nanoparticle. Black and blue dashed lines indicates bond formation or breaking due to the structure relaxation. Detail of the corner II reconstruction is also shown.

However, experimental evidence shows that IrO_2 nanoparticles with sizes in the range of 1 and 4 nm could have a well defined crystalline structure, that is preserved even after OER.[201] IrO_2 nanoparticles are usually synthesized in the presence of water. Thus it is key to analyze if the reconstruction observed in vacuum also takes place in the presence of a water monolayer, that is created by adsorbing enough water molecules to ensure that each superficial Ir center was six coordinated. For $(IrO_2)_{33}$, the water monolayer has 38 molecules.

In this context, we performed the geometry optimization of $(IrO_2)_{33}$ with 38 water molecules and we observed a much smaller structuctural reorganization that in vacuum. Radial distribution functions

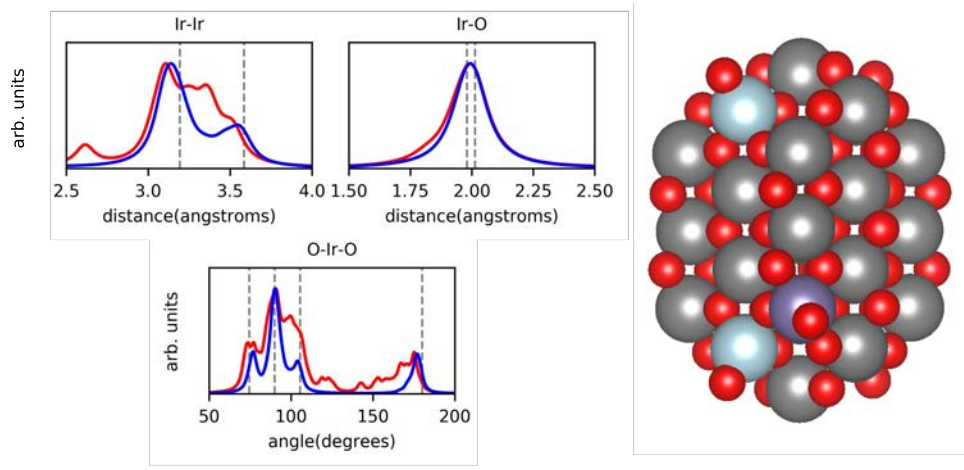

Figure 4.11: (a) Radial distribution function plots (RDFs) for optimized $(IrO_2)_{33}$ (red) and $(IrO_2)_{33} \cdot {}_{38}(H_2O)$ model (blue) and (b) non-reconstructed nanoparticle structure. For the non-reconstructed model, corner I and corner II sites are in light purple and light blue, respectively. Gray dashed lines indicates the bulk values.

(RDFs) provides information about the nanoparticle structure. In Fig. 4.11 (a), the RDFs for the Ir−O and Ir−Ir distances and O−Ir−O angle for the nanoparticle surface atoms are shown. Regardless of the model, the Ir−Ir distances are shorter on the nanoparticles than those in the bulk material, in agreement with experimental evidences.[91]

For the optimization in vacuum (red curve on Fig. 4.11 (a)), the broad-band around 3.3 Å reflects a considerable relaxation on outermost Ir centers. Moreover, the low-intensity peak at 2.6 Å is due to the formed Ir−Ir bonds. In contrast, the optimization in presence of a water monolayer leads to a RDF (blue curve on Fig. 4.11 (a)) with sharper peaks centered at 3.1 and 3.5 Å, and no low intensity peak at 2.6 Å. Concerning the Ir−O distances, they are very similar for

both models, and thus, the local effects described for the optimization in vacuum has not a large consequence in the whole set of Ir−O distances. Finally, the Ir−O−Ir angles show a large diversity of values reflected by the broad-band. In the optimization in vacuum the angles are widely spread along the range whereas the bulk values are preserved for the nanoparticle-water monolayer model. Overall, the presence of water monolayer prevents large reconstruction on the nanoparticle surface.

Since simulation including several water molecules is complex due to the computational cost and the large water possible conformations close in energy, we decided to construct an intermediate model where all coordinated water molecules are removed and the nanoparticle structure is fixed to the $(IrO_2)_{33} \cdot (H_2O)_{38}$, but the dangling oxygens are allowed to relax. This model will be the one used hereafter and will be reported as "non-reconstructed nanoparticle". The relaxation of the dangling oxygen atoms leads into a small peak close to 120°, that is due to the reorientation of those oxygen atoms. Dangling oxygens are bound to corner I and corner II, and these Ir centers adopt a distorted tetrahedron and distorted bipyramidal geometry, respectively (See Fig. 4.11 (b)). Moreover, the dangling oxygens shown an Ir−O bond distance around 1.730 Å , shorter than in the bulk material, suggesting a certain double bond character.

4.3.1 Nanoparticle-water Interaction

Here we analyze the nanoparticle-water interaction for the non-reconstructed nanoparticle model on two coverage schemes: (i) single

water adsorbed per site and (ii) a water monolayer. Moreover, for Ir_{4c} centers, the adsorption of two water molecules per site is explored.

We have considered the interaction of a single water molecule to 5 different sites including: tip (Ir_{4c}), face (Ir_{5c}), edge (Ir_{5c}), vertex (Ir_{5c}) and corner I (Ir_{4c}). In Table 4.7 the adsorption energies and main distances are reported. In Fig. 4.12 the most stable conformations are shown. The PDOS for $Ir_{4/5c}$, $O_{1c/br}$ and their $\bar{\varepsilon}$ are shown in Fig. 4.13.

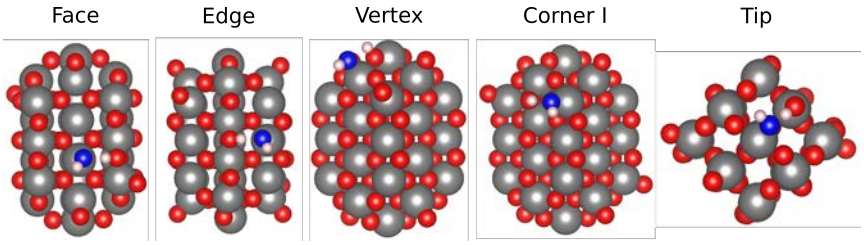

Figure 4.12: Most stable configurations of single water adsorption on selected Ir centers. Water oxygens are depicted in blue.

Face and edge have an axial vacancy and are closely related to those of the (110) surface. In both sites, the water molecule is strongly adsorbed having an Ir−O distance of 1.990 and 1.984 Å for face and edge sites, respectively. These distances are shorter than those in the (110) facet (2.018 Å). Moreover, the O_{br} that interacts with the water molecule has an O_{br} p-$\bar{\varepsilon}$ closer to the Fermi level compared to that of the O_{br} of the (110) surface, thereby being more basic (-1.6 vs -2.5 eV). The increasing of the two factors -stronger Ir−O interaction and O_{br} basicity- favors the water dissociation with respect to the (110) surface. Thus, this is the only conformation found as a minimum.

Table 4.7: Main distances (in Å) for water adsorption on non reconstructed $(IrO_2)_{33}$.

Position		E_{ads}	ΔE	$d_{(O_w-H_w)}$	$d_{(O_{np}-H_w)}$	$d_{(Ir-O_w)}$
face (5C)	*diss*	-229.8	–	1.775	1.012	1.990
edge (5C)	*diss*	-225.5	–	1.800	1.012	1.984
vertex (5C)	*mol*	-133.6	0.0	0.995	2.061	2.130
	diss	-148.7	-15.2	2.212	0.984	1.956
tip (4C)	*mol*	-169.0	0.0	1.091	1.427	2.066
	diss	-175.1	-6.1	1.556	1.050	1.983
corner I (4C)	*mol*	-172.3	0.0	1.032	1.732	2.137
	diss	-187.8	-15.5	1.556	1.050	1.983
tip (4C)	*mol/mol*	-158.5	0.0	1.024,1.046	1.688,1.549	2.104,2.089
	diss/mol	-157.3	1.2	1.018,1.407	1.720,1.092	2.006,2.097
	mol/diss	-157.7	0.8	1.450,1.038	1.075,1.583	2.110,2.008
corner I (4C)	*mol/mol*	-158.5	0.0	1.035,1.042	1.712,1.606	2.142,2.122
	mol/diss	-157.0	1.5	1.037,1.635	1.691,1.041	2.131,2.004
	diss/mol	-165.7	-7.2	2.165,1.037	0.996,1.625	1.969,2.120
	diss/diss	-163.5	-5.0	2.052,1.601	0.999,1.045	1.965,2.001

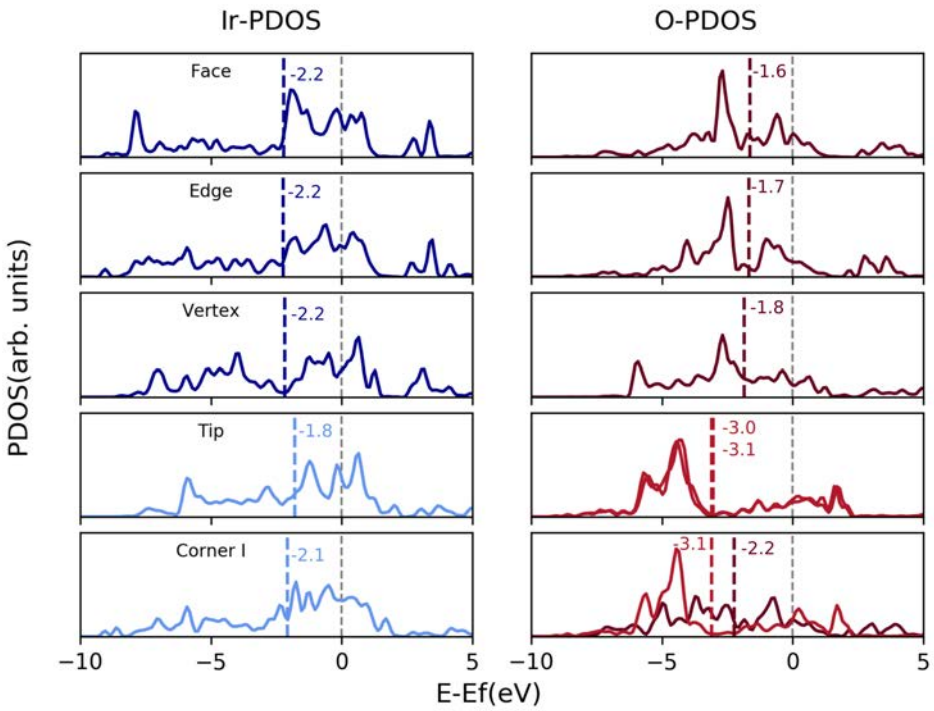

Figure 4.13: PDOS for $Ir_{4/5c}$ and $O_{1c/br}$ for face, edge, vertex, tip and corner I sites of the non-reconstructed nanoparticle. The band centers are depicted as colored dashed lines and their values are indicated. The dashed gray line indicates the Fermi level.

Moreover, the interaction energy is -229.8 and -225.5 kJ mol^{-1} for face and edge sites respectively, larger than this on the (110) surface(-211.5 kJ mol^{-1}). Similar results have been reported for other rutile-like materials.[195,196]

In contrast, in vertex, the two conformations *mol*/*diss* forms are locatated as minima, being *diss* the lowest in energy. Moreover, the adsorption energy is smaller than the reported for face and edge sites. This could be attributed to the nature of the vacancy. Face and edge

have an axial vacancy whereas vertex has an equatorial one. For extended surfaces, the one that has one equatorial vacancy (011), has the lowest adsorption energy and the computed E_{ads} energy is relatively close to that obtained for the vertex. However, it is worth mentioning that the *diss* form is preferred for the vertex instead of the *mol* form which is preferred on the (011) facet. This could be related to the O_{br} basicity, which according to the PDOS, is higher for the vertex. Thus, we suggest that the higher O_{br} basicity, the largest tendency to accept the H^+ from the H_2O.

For Ir_{4c} centers (tip and corner I) we explored the adsorption of one or two water molecules per site. For single water coverage the *diss* form is more stable than the *mol* one for both sites. In the tip, the water molecule fill one of the available equatorial vacancies, as in the extended surface (001), whereas on the corner I, fills an axial one. As a consecuence, the adsorption of water is higher in energy at corner I than at the tip site regardless of the adsorption form (*mol* or *diss*). However, unexpectedly in the corner I *mol* form has a larger $Ir_{4c}-O_w$ distance than in the tip site. Remarkably, the preference of the *diss* form in corner I is higher than for tip site. This could be related to two facts: (i) the highest $Ir-O_w$ interaction, and (ii) at the corner I, the H accepting O_{br} has a more basic character than the O_{1c} atom accepting the H on tip site. (See O-$\bar{\varepsilon}$ on Fig. 4.13).

For the adsorption of two water molecules at the tip, the *mol/mol* form is the most stable conformation. $Ir-O_w$ distances are larger than those for the single water adsorptions, suggesting that water molecules are more weakly adsorbed. This is also found for the case of the (001) surfaces where the adsorption of two water molecules

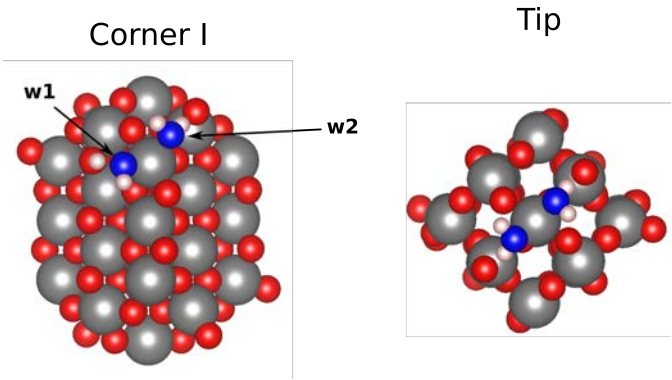

Figure 4.14: Most stable configurations for two water molecules adsorption on corner I and tip. Water oxygens are depicted in blue.

per Ir site implies the decrease of the $Ir-H_2O$ interaction, that prevents the H_2O dissociation. Therefore, *diss/mol* and *mol/diss* are less stable configurations, which could be related to the fact that the hydrogen atom is transferred to a less basic O_{1c} instead to an O_{br}.

Corner I is an interesting site that has two adsorbed water molecules that are coordinated to two different vacant sites and interact with a different type of oxygen, one with an O_{br} and the other one with O_{1c}. Here we explore the four possible configurations: *mol/mol*, *mol/diss*, *diss/mol* and *diss/diss* where the first water (w1) is adsorbed in the axial vacancy and the second one in the equatorial one (w2) (See Fig. 4.14). Even though it is difficult to separate the effects of the vacancy and the oxygen basicity on the water adsorption process, we can analyze it by comparing between configurations.

Within the four evaluated possibilities, the most stable configuration is *diss/mol* and the *diss/diss* form laying only 1.8 kJ mol-1 above. A similar energy diffence is found between the *mol/diss* and the *mol/mol*

conformations which are around 7 kJ mol−1 higher in energy. This suggest that the dissociation of w1 is favorable while the dissociation of w2 is unfavorable. Since the energy difference between these structures is very close to the gain/cost of dissociation of the corresponding water molecule, it can be concluded that the two water molecules behave independently of each other.

Overall, the results obtained on the five considered sites of the nanoparticle model reveals that the adsorption of water is highly controlled by the coordination of the metal center and the nature of the vacant sites as already found for the surfaces. Iridium on face and edge sites are pentacoordinated with an axial site as in the case of the (110) surface, thus the adsorption energy and the preference for the *diss* form are similar to that found for the (110) surface. The iridium center at the vertex site is pentacoordinated with the vacant site in equatorial as it is the case of the (011) surface and, as a consequence, the adsorption energy is similar to that of the (011). Finally, the iridium center at tip site resembles those on the (001) surface and thus, the water adsorption on the tip behaves similarly to the (001) facet. Nevertheless, extended surfaces and nanoparticles are different in nature, and thus subtle effects are observed. These effects are mainly focused on the fact that O_{br} tend to be more basic in the nanoparticle than in the extended surfaces and also the Ir centers tends to be more acid. That is, IrO_2 in the nanoparticle has a most pronounced ionic character than in the extended surfaces. Thus when the morphology of the nanoparticle allows the formation of hydrogen bonding between the adsorbed species and the O_{br}, a stronger adsorption energy and a larger preference for the *diss* conformation

is found.

As pointed above, adding a monolayer of water molecules on the $(IrO_2)_{33}$ nanoparticle prevents the surface reconstruction. In the same way as on full coverage regimes in surfaces, the molecular or dissociated water molecules adsorbed on the nanoparticle surface interacts forming H-bonds. Moreover, several degrees of dissociation can be found. To have an idea of the range of the adsorption energies we also optimized the nanoparticle-water interface with the maximum number of water dissociated (10 *mol*/28 *diss*) in addition to the optimization starting from a full coverage of molecular water. In Fig. 4.15 the optimized structures are shown.

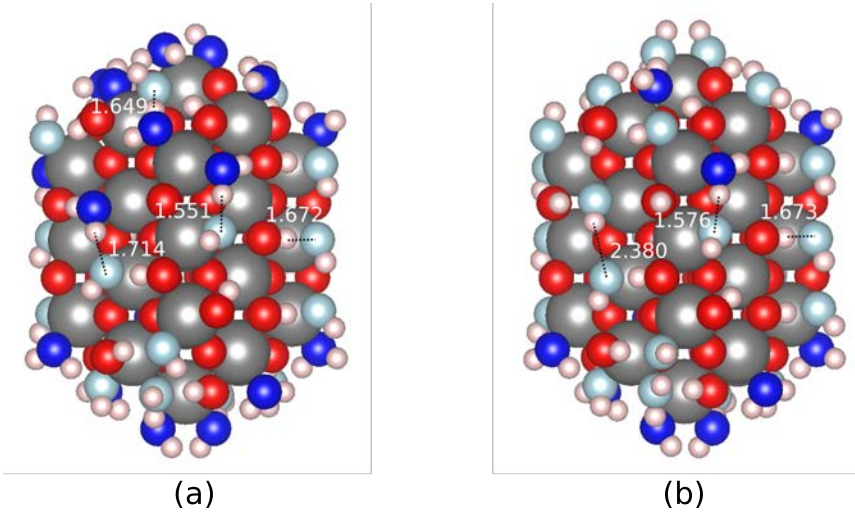

Figure 4.15: Optimized structures for $(IrO_2)_{33}$ nanoparticle with full water coverage. (a) starting from 38 *mol*. (b) starting from 10 *mol*/28 *diss*. Some H-bonds are indicated.

During the optimization the fully molecular monolayer evolves dissociating several water molecules, the final structure presenting 19

mol and 19 *diss* water molecules (50% of dissociation). In contrast, the 10 *mol*/28 *diss* evolves forming a new molecular water (11 *mol*/27 *diss*). This suggest that neither the full molecular nor the maximum dissociation configurations are the most stable ones, thus the dissociation degree could being close to 70%. The difference in adsorption energy per water molecule is rather small between the two structures. The E_{ads} per water molecule for 50% diss conformation is -186.9 kJ mol^{-1} whereas for the 70% one is -190.9 kJ mol^{-1}. If one assumes that there are no cooperative effects between water molecules and thus the monolayer behaves as the addition of single adsorbed water molecules one would expect that the most stable conformation would present between 22 and 26 *diss* water molecules and the associated adsorption energy would be around 180 kJ/mol. Therefore, cooperative effects appears to have an small effect on the most stable conformation and an non-negligible contribution on the adsorption energy.

Regadtless of the structure, the $Ir-O_w$ distances for molecular and dissociated forms are 2.142 ± 0.015 an 2.040 ± 0.032 Å , respectively. Thus, the water molecules are weakly adsorbed compared with their single-site counterparts. Moreover, the $Ir-O_w$ distances for the nanoparticle monolayer are longer than those reported for extended surface monolayers (See Table 4.5).

As shown in Fig. 4.15, due to the presence of *mol* and *diss* water forms, multiple hydrogen bonds involving O_{1c}, O_{br} and water molecules are formed around all the nanoparticle. The hydrogen bonds formed between water molecules (*mol* and *diss*) have an average O_w-HO_w

distance of 1.553 $\pm$ 0.109 Å whereas those formed with the surface are slightly longer (1.633 $\pm$ 0.427 Å). Therefore, the water-water H bonding is preferred over the water-surface. These results are in agreement with the reported for other rutile nanoparticle-water interface.[195,196]

It should be mentioned that those structures are two limits of the possible multiple isomers. A detailed study would require further exploration of the available configuration and particularly AIMD simulations.

4.4 Conclusions

IrO_2-water interactions have been analyzed for extended surfaces [(110), (011), (001) and (100)] and a $(IrO_2)_{33}$ Wulff-like nanoparticle with different coverages - single water and monolayer. Present results suggest that the water adsorption energy and the preference between dissociated and molecular forms are governed by two main factors: (i) Intrinsic acidity of unsaturated Ir and basicity of O_{br} and (ii) the presence of cooperative effects.

The acidity and basicity of $Ir_{4/5c}$ and O_{br} varies with the crystallographic orientation. The acidity depends on the type of vacancy and coordination. IrO_2-rutile exhibits a tetragonal compression; therefore, the axial bonds are shorter than the equatorial ones. Thus, undercoordinated iridium centers with an axial vacancy are more acidic than the ones with an equatorial one. Therefore, surfaces (110) and (100) with axial vacancies are more acidic, and the water

molecule is strongly adsorbed. Moreover, less coordinated centers are more acidic than the more coordinated ones. For instance, the adsorption energy on the Ir_{4c} on the (001) surface is larger than the one for the Ir_{5c} adsorption in the (011) and (100) surfaces. Furthermore, O_{br} basicity promotes water dissociation by forming $O_{br}-H$ bonds. For instance, for the (110) surface only the *diss* form is located, whereas for the (100) *mol* and *diss* forms are located. This could be related to the fact that on the O_{br} on the (110) surface has higher basicity than on the (100). The surface-water interaction increases the acidity of the water molecule. The larger the surface-water interaction is, the larger the water acidity is. Therefore, for the surfaces were Ir is more acidic and the O_{br} is more basic, the *diss* form is preferred.

For the monolayer adsorption, in addition to the intrinsic water interaction, other effects such as cooperative H-bond interactions and vacancy orientation come into play in determining whether dissociation occurs or not. For (110) and (100) the preferred configurations have all water molecules dissociated. Only for the latter, the presence of additional water molecules slightly increases the adsorption energy. For the (011) surface, their morphology allows shorter distances between water molecules than those for the aforementioned surfaces. Thus, the H-bond interactions are promoted, the cooperative effects between water molecules are larger and this favors the water dissociation. Furthermore, thermal effects seem to favor configurations with a smaller degree of dissociation because of an enlargement of $Ir-O$ distances, which leads to a smaller decrease of water acidity. On (110)-IrO_2, the main monolayer configuration is

the fully dissociated one, whereas on the (011) exhibits a degree of dissociation that ranges from 50 to 75%.

The nanoparticle-water interaction has been addressed on a $(IrO_2)_{33}$ nanoparticle as a function of the location and water coverage. Results suggest that the water adsorption at face and edge sites have higher adsorption energy than equivalent sites on a (110) surface. This could be attributed to two factors. Firstly, the Ir−Ir distances are shorter on the nanoparticle surface than on the extended surface; thus, on the nanoparticle, the H-O_{br} distance are shorter than those on (110) surface promoting hydrogen bond formation. Secondly, the Ir centers are more acid than on the extended surfaces. Thirdly, the O_{br} atoms on the nanoparticle surface are more basic than those on the (110) surface, enhancing the water dissociation as well as the adsorption. For the vertex site, the *diss* form is more stable than the *mol* one, even when the water is adsorbed to an equatorial vacancy. This could be attributed to the fact that the basicity of the O_{br}, that is directly connected to the Ir_{5c} is higher than this on the extended surfaces. Furthermore, the O_{br} basicity is increased by the adsorption of the water molecule boosting the water dissociation.

For tip and corner I sites, the determinant factor on the *mol*/*diss* preference could be attributed to the basicity of the oxygen atom that accepts the proton. For instance, on the tip site to get the *diss* forms, the hydrogens are transferred to a O_{1c}, that have a lower basicity compared to O_{br}. Thus, the formation of O_{1c}−H is not favorable. Hence, the *mol* form is more stable. In contrast, in the corner I, the water molecules interacts with O_{br} and O_{1c}, being the *diss* form preferred for the former and the *mol* for the latter. For the water monolayer,

the dissociation is close to 70%, the expected value from the preferred form of the single water adsorption on each site. The $Ir-H_2O$ interaction per molecule is slightly larger than the average value of the individual adsorption energies. Therefore, this suggest that cooperative effects are less important that on extended surfaces.

5 Oxygen Evolution Reaction on IrO_2 Materials

The oxygen evolution reaction (OER) is considered to be the limiting step for the water splitting process. In the desirable acidic conditions, the state-of-the-art catalysts are the expensive RuO_2 and IrO_2-based materials. Thus, the understanding of the factors controlling the reactivity of IrO_2 is mandatory for catalyst optimization. In this chapter, we analyze the catalytic activities of (110), (011), (100) and (001) surfaces as well as for the $(IrO_2)_{33}$. For each kind of model, we explore the oxo-coupling (I2M) and the water-nucleophilic attack (WNA) mechanisms. Results show that the oxo-coupling and the water attack should be viewed as homolytic couplings. Thus, the two processes are only accessible if the Ir=O species on the surfaces exhibit oxyl character. Regardless of the model, the required overpotentials depend on the feasibility to oxidize the Ir−OH to Ir−O species. It is determined by the coordination of the metal center, the nature of the vacant site and the dimensionality of the system -extended surface or nanoparticle.

5.1 Introduction

One of the major challenges of the 21st century is the substitution of fossil fuels for sustainable, renewable and environmentally friendly alternative sources of energy.[202,203] Most of the alternatives, such as wind or solar energy are sensitive to the environmental changes, and thus, their application requires the energy storage between its supply and consumption. One of the most promising solutions is to store energy in the form of chemical bonds in a similar manner to what plants do during the photosynthesis.[204] In this way, H_2 production by the splitting of water is seen as one of the most sustainable ways to store energy.[174,205–211]

Water splitting, as introduced in Chapter 1 implies two half reaction: i) At the cathode, H^+ cations are converted to H_2 through the usually referred as hydrogen evolution reaction (HER) and ii) H_2O is oxidized to O_2 through the so-called oxygen evolution reaction (OER), at the anode. The oxygen evolution reaction is considered the bottleneck of the global process due to the large overpotentials that have to be applied. Moreover, acidic conditions are preferred with respect to basic media for the practical application of water splitting.[80,212] However, these acidic media also imply working at harsh reaction conditions which limits the number of potential catalysts to the expensive IrO_2 and RuO_2.[80,213,214] In this context, understanding the key factors controlling catalyst efficiency is essential to find strategies that could lead to catalyst optimization. Regarding IrO_2, it is, nowadays, well accepted that amorphous IrO_X tends to be more active in terms of lower overpotential and higher currents per surface

area than crystalline IrO_2.[90–92,94,95] The larger catalytic activity has been associated to the presence of Ir(III) in the amorphous materials, so that the larger the amount of Ir(III), the larger the catalytic activity.[90–93] Regrettably, IrO_X also tends to be less stable than the crystalline analogues, the deactivation mechanisms being a key issue under discussion.[95,96,215] Moreover, the different IrO_2 rutile-like crystalline main facets do not show the same catalytic activities. Indeed, It has been found that the (100) surface is more active than the (110) one.[105] These different catalytic activities correlate reasonably well with the number of undercoordinated centers per surface area of the crystalline facets,[107] thereby suggesting that the undercoordinated centers are the main active sites in crystalline materials.

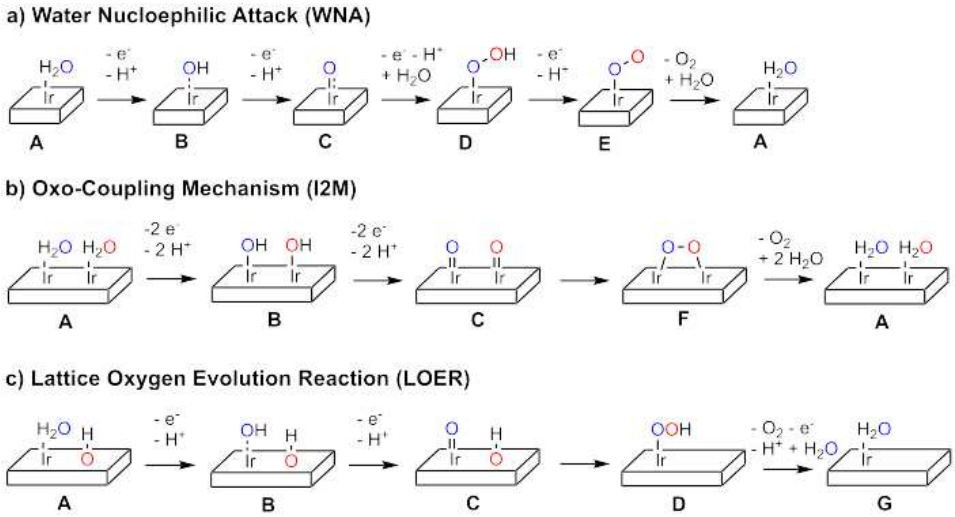

Figure 5.1: Proposed reaction mechanisms for the Oxygen Evolution Reaction

In-situ X-ray spectroscopy has been carried out to identify the oxidation state of the metal center depending on the applied potential.[90,95,98,101,216–218]

For IrO_2, many authors showed that while at potentials below 1.3 V, the metal centers are mainly Ir(IV) or Ir(III), at higher potentials they are oxidized to Ir(V).[101,219] The Ir(V) species are thought to be the ones involved in the catalytic process, which are probably reduced upon O_2 release.[98] The data for the most stable (110) surface is consistent with the IrO_2 being completely covered with *O (oxo) species coordinated to the unsaturated centers at reaction conditions (C in Fig. 5.1).[217] In addition, Infrared spectroscopy (FT-IR) allowed the detection of Ir-OOH species (D in Fig. 5.1) upon water oxidation with an IrO_2 nanocluster under pulsed excitation of a light sensitizer,[99] but the observation of this species in electrocatalytic conditions is controversial. Finally, the use of differential electrochemical mass spectroscopy (DEMS) with isotope-labeled electrolytes showed that both RuO_2 and IrO_2 exchanges oxygen with the electrolyte and thus actively participates in the catalysis through its lattice oxygen atoms.[95,97,220] Nevertheless, according to the most recent results of Shao-Horn and co-workers on RuO_2, this would be the case of none-crystalline materials, since no oxygen exchange is detected on rutile-like catalysts.[80,107]

Overall, three different reaction mechanisms have been proposed (Fig. 5.1):[80,212,221,222] i) the water nucleophilic attack (**WNA**), ii) the oxo-coupling mechanism (**I2M**) and iii) The lattice oxygen evolution reaction mechanism (**LOER**). The water nucleophilic attack mechanism (Fig. 5.1a) implies first the formation of an Ir-oxo species on the surface (Ir=O) through two proton coupled electron transfer steps (PCET). Then, the Ir=O species suffers the attack of a water molecule leading to the formation of an Ir−OOH hydroperoxo species that

after two additional PCET releases O_2 and regenerates the initial Ir−H_2O species. The **I2M** pathway (Fig. 5.1b) starts also with the formation of Ir=O species, but, in contrast to the **WNA** mechanism, O_2 is formed by the coupling of two neighbor Ir=O species. Finally, the **LOER** mechanism (Fig. 5.1c) implies the active role of vacant sites on the metal oxide surface.[95,97,220]

Computational chemistry has been widely used to shed light into the most plausible reaction mechanism.[83,84,87,104,108,177,223–235] This is mainly done by computing the thermodynamic cost of each PCET step, which is used to estimate the viability of the mechanism and the required overpotential. Only in a few cases, the energy barriers associated with some of the elementary steps have been computed.[104,223,225] Remarkably, most of the studies focusing on the reaction mechanism are centered on the most stable crystalline (110) surface[83,84,87,104,185,223–225,232–234] or defects and potential dissolution intermediates of this surface.[226–229] Only a very recent contribution of Rao et al. analyzed the differences in catalytic activity of the (110), (100) and (101) surfaces of RuO_2.[108] Despite the limitations in solvent representation among others,[224,225] the computed overpotentials are in good agreement with experiments, and they support that the **WNA** mechanism is usually the applied mechanism. Indeed, in the crystalline (110) surface the water nucleophilic attack to the oxo-species is computed to be kinetically easier than the oxo-coupling of the **I2M**,[104,223,225] which suggests that at least for this surface the **WNA** mechanism is preferred. Noteworthily, in some flexible systems such as oxidized iridium surfaces or supported dimeric Ir species the **I2M** mechanism has been suggested to be competitive with the **WNA** one.[230,231,233] Taking **WNA**

as the applying mechanism, three different rate determining steps have been proposed depending on the material, level of theory and subtle differences in the nature of the elementary steps: i) The Ir=O formation (B to C step in Fig. 5.1); ii) the electrochemical step associated with the Ir−OOH formation (C to E step in Fig. 5.1) and iii) O_2 release from Ir−OOH (E to A in Fig. 5.1). Controversy persists, and one can find recent contributions suggesting that either the formation of Ir−OOH or the O_2 release are the rate determining processes.[87,104,233]

The present chapter study the **WNA** and **I2M** mechanisms for the IrO_2 (110), (011), (100) and (001) extended surfaces and for $(IrO_2)_{33}$ non-reconstructed nanoparticle model. The models of those IrO_2 materials are the ones that have been used on Chapter 4 to study the material-water interaction. Hence, for extended surfaces calculations, all the atomic positions are fully relaxed whereas for the non-reconstructed nanoparticle only the relaxation of dangling oxygens and the adsorbed species are allowed. For the calculation of the Gibbs free energies of the OER process, solvation effects were included by using the implicit model implemented in VASPsol[146] through single point calculations at vacuum optimized geometries. Thermal corrections at 1 atm and T = 298.5 K were added considering only the vibrational contributions of the normal modes associated with the adsorbed species (Ir−H_2O, Ir−OH, Ir−O, Ir−OOH and Ir−OO) and the Ir−O_{ads} stretching mode. Entropy contributions for water and H_2 were obtained from the tabulated values for liquid water and $H_{2(gas)}$, respectively. Similarly to previous contributions, the energetics of the O_2 release were computed as the

energy difference between the experimental ΔG of the global reaction (4.92 eV for $2\,H_2O \rightarrow H_2 + O_2$) and the sum of all previous steps.[83,104,233,234]Finally, the ΔG° for the PCET steps were computed by using the computational standard hydrogen electrode as defined by Rossmeisl, Nørskov and co-workers, where the reaction free energy of $\frac{1}{2}\,H_2 \rightarrow H^+ + e^-$ is zero.[83]

For extended surfaces, the transition states associated with chemical steps were located by using either the climbing image nudged elastic band (CI-NEB)[236,237] strategy or restricted geometry optimizations. With the aim of saving computational time, for this intermediate calculation, the Brillouin zone was sampled with a (2,2,1) Monkhorst Pack K-point mesh. The highest in energy point of either the NEB or the restricted optimization was used for locating the final transition state by performing a geometry optimization with the quasi-Newton algorithm implemented in VASP and the same Monkhosrt Pack mesh as the standard geometry optimizations. Convergence was achieved when forces were smaller than 0.02 $eV \cdot Å^{-1}$. The nature of the stationary point was ensured by vibrational analysis that showed that the largest imaginary frequency in all cases corresponds to that of the transition state.

5.2 Oxygen Evolution Reaction on Extended Surfaces

We have studied the oxygen evolution reaction catalyzed by the main ((110), (011), (100) and (001)) defective free and non-polar crystallographic facets of rutile-like IrO_2, with the aim of analyzing their different catalytic activity. In this context, we first determine the potentials required for oxidizing the initial IrO_2-H_2O material to Ir=O without involving additional water molecules. We analyze the electronic structure of the Ir−OH and Ir=O intermediates and propose the most stable species at working potentials (around 1.5 V). In a second step, we compute the catalytic cycle of the two most usually proposed mechanisms (oxo-coupling and water nucleophilic attack) starting from the most stable termination at 1.5 V. This allow us determining the most favorable mechanism, proposing the rate determining electrochemical step and computing the overpotentials.

5.2.1 IrO_2-H_2O Oxidation Depending on the Applied Potential

Fig. 5.2 shows the most stable conformation associated to the adsorption of two water molecules on the different surfaces. As already mentioned, rutile-like IrO_2 structure presents a distorted octahedral environment around the metal center with two short Ir−O distances in axial position and four long ones in the equatorial plane. The most stable (110) surface and the (100) facet present unsaturated

pentacoordinated metal sites with the vacant site in axial position. The second most stable (011) surface also has unsaturated pentacoordinated metal sites but with the vacant site in equatorial. Finally, the least stable main crystallographic orientation, (001), presents tetracoordinated unsaturated metal centers, the two vacant sites being equatorial. In addition, all surfaces present non-saturated dicoordinated oxygen atoms, referred as oxygen bridge (O_{br}).

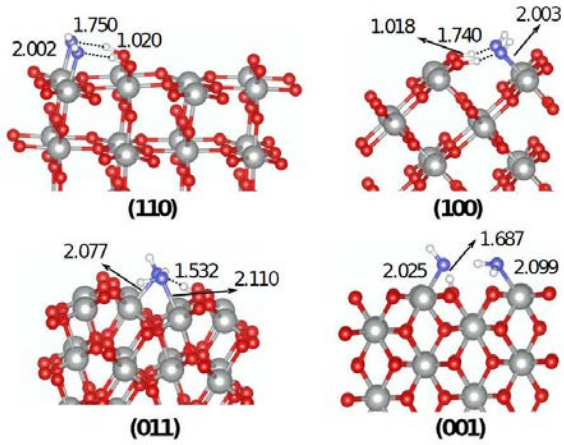

Figure 5.2: Most stable structures associated to the adsorption of two water molecules on the studied IrO_2 surfaces. Distances in Å.

In the Chapter 4, we showed that the different nature of the vacant at the metal center and the basicity of the O_{br} atoms influences the adsorption strength of a single water molecule and its facility to dissociate forming an Ir−OH moiety and a protonated O_{br}.[164,171] In addition, the Ir−H_2O local interaction is significantly tuned by the hydrogen bonding with vicinal adsorbed water molecules, which tends to favor a 50% of water dissociation.[164,190,192,193] Therefore, the final structure and H_2O degree of dissociation result from a subtle

balance between intrinsic interaction and cooperative effects (Fig. 5.2). For IrO_2, the adsorption energies are the highest when the vacant site is axial, and the most stable structures are: complete dissociation on the (110) and (100) surfaces and 50% or lower dissociation on the other two surfaces. At this point, it is worth mentioning that, although at least one water molecule dissociates in the majority of cases, the initial species is referred as $\mathbf{0}_{H_2O/H_2O}$ for simplicity, even though in each case the most stable conformation is considered as starting structure. The oxidation of $\mathbf{0}_{H_2O/H_2O}$ to $\mathbf{4}_{O/O}$ is expected to occur through successive PCET steps. The involved species in this process are shown in Fig. 5.3. With the aim of stablishing the most stable termination as a function of the applied potential (U), the relative stabilities without including pH effects of all species are obtained by

$$\mathbf{0}_{H_2O/H_2O} \rightarrow \mathbf{N}_{L_1/L_2}, \Delta G^0 = G_N^0 - nU, \tag{5.1}$$

where $\mathbf{N}_{L_1/L_2}$ indicates the species $\mathbf{1}_{OH/H_2O}$, $\mathbf{2}_{OH/OH}$, $\mathbf{3}_{O/OH}$ and $\mathbf{4}_{O/O}$. Fig. 5.4 shows the computed relative stabilities.

Figure 5.3: Intermediate species of the H_2O/H_2O oxidation to O/O.

Three different oxidation behaviors are observed. The (001) surface is more easily oxidized to $\mathbf{4}_{O/O}$ than the other facets, the potential at which $\mathbf{4}_{O/O}$ becomes the most stable termination being 0.93 V. The other three surfaces present pentacoordinated centers and they

behave in a more similar manner. However, the ability of the different surfaces to get oxidized depends also on the vacant site nature. The (110) and (100) surfaces have the vacant site in axial position, and they get oxidized to $\mathbf{2}_{OH/OH}$ at potentials of 1.15-1.16 V and to $\mathbf{4}_{O/O}$ at potentials over 1.46 V. The (011) surface, with the vacant site in the equatorial plane, is not easily oxidized to $\mathbf{4}_{O/O}$, which is only predicted to be the most favorable species over 1.64 V. As a consequence, at potentials around 1.50 V, $\mathbf{4}_{O/O}$ is still not formed and $\mathbf{3}_{O/OH}$ is the most stable termination. These values agree well with the computational data for the (110) surface reported by Ping, Nielsen and Goddard.[104] Moreover, the $\mathbf{2}_{OH/OH}$ to $\mathbf{4}_{O/O}$ transition is computed to occur at 1.46 V, which is only 0.16 V higher than the potential in which iridium is oxidized to its higher state according to experiments.[91,101] Thus, there is a fairly good agreement between our data and the existent values, which reinforces the validity of our approach.

Geometric parameters (Table 5.1 and Table B.3 on Appendix B) show that the Ir_1-O_L distance (O_L stands for the oxygen of the adsorbed species) decreases when going from $Ir-H_2O$ to $Ir-OH$ and $Ir=O$. The computed values are around 2.18-2.19 Å; 1.93-1.96 Å and 1.73-1.80 Å for $Ir-H_2O$, $Ir-OH$ and $Ir=O$, respectively. The $Ir-O_L$ distance tends to be shorter for the (001) surface than for the (110) and (100) facets, being the (011) surface the one that has the largest values. This is clearly observed for $\mathbf{4}_{O/O}$ where the shortest distances are those of the (001) surface and the largest ones for the (011) facet. Interestingly, the shortest distance in the (001) surface is related to the absence of magnetic moment over the oxo ligand and the Ir_{4C}

(Table 5.1), thus suggesting the formation of an oxo group with an Ir=O double bond and a metal center formally at its +6 oxidation state. In contrast, the larger distances of the (110), (100) and (011) are associated with unpaired electrons both on the metal and the oxo. This indicates that such species have an important metal oxyl $Ir^{\bullet}-O^{\bullet}$ radical character where the metal oxidation state is formally +5 (Table 5.1). This interpretation is in agreement with the proposal that Ir(V) species are the ones involved in the catalytic cycle and suggest that the reactivity of the (001) surface could be different to that of the other three facets.

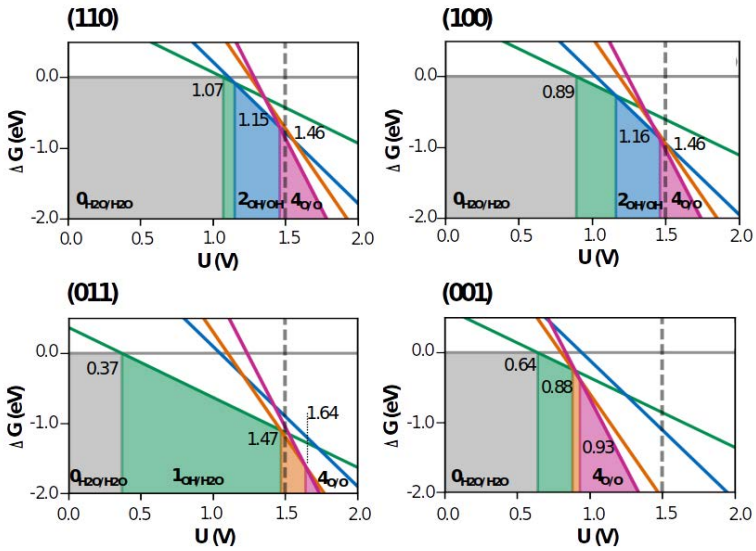

Figure 5.4: Surface phase diagram for extended surfaces of IrO_2 depending on of the applied potential. The color legend is based on Fig. 5.3.

In summary, the oxidation of these facets is largely controlled by the surface morphology and particularly by the coordination of the unsaturated metal centers and the nature of their vacant sites. The

Table 5.1: $Ir-O_L$ distances (in Å) and magnetic moments for the different surface terminations arising from the oxidation of hydrated IrO_2 (110), (011), (100) and (001) surfaces.

Surface	Species	Ir_1-O_{L1}	Ir_2-O_{L2}	S_{O1}	S_{O2}	S_{Ir1}	S_{Ir2}
(110)	$\mathbf{0}_{H_2O/H_2O}$	2.002	2.002	0.00	0.00	0.00	0.00
	$\mathbf{1}_{OH/H_2O}$	1.943	1.990	0.00	0.00	0.00	0.00
	$\mathbf{2}_{OH/OH}$	1.937	1.938	0.00	0.00	0.00	0.00
	$\mathbf{3}_{O/OH}$	1.788	1.925	0.54	0.02	0.48	0.15
	$\mathbf{4}_{O/O}$	1.789	1.789	0.67	0.67	0.52	0.52
(011)	$\mathbf{0}_{H_2O/H_2O}$	2.110	2.077	0.00	0.00	0.00	0.00
	$\mathbf{1}_{OH/H_2O}$	1.953	2.148	0.00	0.00	0.00	0.00
	$\mathbf{2}_{OH/OH}$	1.965	1.940	0.00	0.00	0.00	0.00
	$\mathbf{3}_{O/OH}$	1.810	1.933	0.57	0.02	0.55	0.00
	$\mathbf{4}_{O/O}$	1.797	1.797	0.59	0.62	0.52	0.57
(100)	$\mathbf{0}_{H_2O/H_2O}$	2.003	2.003	0.02	0.02	0.08	0.12
	$\mathbf{1}_{OH/H_2O}$	1.951	1.958	0.01	0.01	0.20	0.15
	$\mathbf{2}_{OH/OH}$	1.927	1.927	0.17	0.17	0.41	0.40
	$\mathbf{3}_{O/OH}$	1.796	1.924	0.19	0.02	0.24	0.03
	$\mathbf{4}_{O/O}$	1.771	1.771	0.57	0.56	0.26	0.26
(001)	$\mathbf{0}_{H_2O/H_2O}$	2.025	2.099	0.00	0.00	0.02	0.01
	$\mathbf{1}_{OH/H_2O}$	1.947	2.094	0.00	0.00	0.00	0.00
	$\mathbf{2}_{OH/OH}$	1.933	1.900	0.00	0.00	0.00	0.00
	$\mathbf{3}_{O/OH}$	1.729	1.898	0.00	0.00	0.00	0.00
	$\mathbf{4}_{O/O}$	1.732	1.727	0.00	0.00	0.00	0.00

least coordinated tetracoordinated centers of the (001) surface are the least stabilized ones and, consequently, those that more easily form the Ir=O group. This is evidenced in the PDOS (**??**) by the presence of a large number of occupied d states close to the Fermi Level in the (001) surface. Within the other three surfaces, the nature of the vacant site appears to be the key factor: Ligands at axial sites present stronger interactions than ligands at equatorial sites. Moreover, the oxo group (or oxyl radical) interacts more strongly than water with

the metal center. Consequently, the decrease in strength when going from axial vacant sites ((110) and (100) facets) to an equatorial one ((011)) is more pronounced for Ir=O, the latter becoming destabilized with respect to $\mathbf{0}_{H_2O/H_2O}$ and thus, requiring higher potentials to be formed.

5.2.2 OER Reaction Mechanisms

Starting from the most stable termination at potentials of 1.50 V ($\mathbf{4}_{O/O}$ for the (110), (100) and (001) surfaces and $\mathbf{3}_{O/OH}$ for the (011) surface), we have studied the two most commonly proposed reaction mechanisms: the oxo-coupling (**I2M**) and the water nucleophilic attack (**WNA**). The intermediates of the two pathways are shown in Fig. 5.5. We computed the thermodynamics of the whole cycle as well as the energy barriers associated with the chemical steps. Table 5.2 reports the energetics of the different steps, Table 5.3 presents the main geometry parameters and spin densities of the key intermediates and Figs. 5.6 and 5.7 show the optimized structures of the transition states. All other data can be found in the Appendix B.

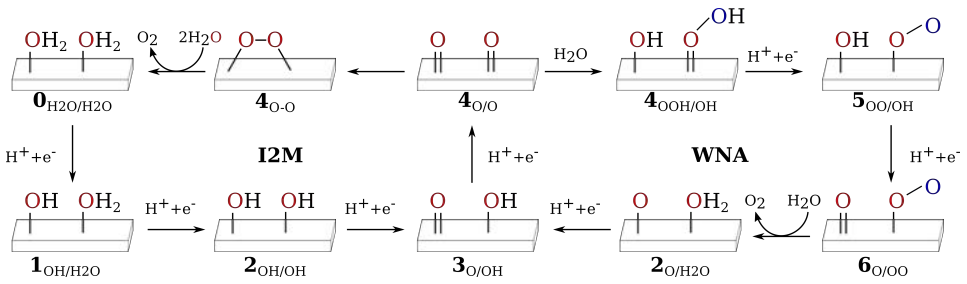

Figure 5.5: Oxygen evolution reaction mechanisms.

Table 5.2: Reaction Gibbs Energies (in eV) for the chemical and electrochemical steps of the **I2M** and **WNA** reaction mechanisms. Values in parenthesis correspond to the Gibbs energy barriers.

Reaction	(110)	(011)	(100)	(001)	$(001)_{1c}$[a]
	I2M				
$\mathbf{4}_{O/O} \rightarrow \mathbf{4}_{O-O}$	0.67	0.10	0.85	2.30	0.25
	(0.80)	(0.33)	(0.94)	(2.38)	(1.15)
$\mathbf{4}_{O-O} + 2\,H_2O \rightarrow \mathbf{0}_{H_2O/H_2O} + O_2$	-0.89	-0.13	-0.90	-0.72	-0.11
$\mathbf{0}_{H_2O/H_2O} \rightarrow \mathbf{1}_{OH/H_2O} + H^+ + e^-$	1.07	0.37	0.89	0.64	0.83
$\mathbf{1}_{OH/H_2O} \rightarrow \mathbf{2}_{OH/OH} + H^+ + e^-$	1.15	1.73	1.16	1.25	1.11
$\mathbf{2}_{OH/OH} \rightarrow \mathbf{3}_{O/OH} + H^+ + e^-$	1.56	1.21	1.50	0.52	1.38
$\mathbf{3}_{O/OH} \rightarrow \mathbf{4}_{O/O} + H^+ + e^-$	1.36	1.64	1.41	0.93	1.47
	WNA				
$\mathbf{4}_{O/O} + H_2O \rightarrow \mathbf{4}_{OOH/OH}$	-0.12	-0.05	0.08	1.24	0.25
	(0.43)	(0.42)	(0.42)		(0.55)
$\mathbf{4}_{OOH/OH} \rightarrow \mathbf{5}_{OO/OH} + H^+ + e^-$	1.11	0.86	1.22	0.84	1.20
$\mathbf{5}_{OO/OH} \rightarrow \mathbf{6}_{OO/O} + H^+ + e^-$	1.53	1.53	1.22	0.91	1.24
$\mathbf{6}_{OO/O} + H_2O \rightarrow \mathbf{2}_{H_2O/O} + O_2$	-0.17	-0.02	-0.40	0.56	-0.20
$\mathbf{2}_{H_2O/O} \rightarrow \mathbf{3}_{O/OH} + H^+ + e^-$	1.21	0.98	1.37	0.76	0.97
$\mathbf{3}_{O/OH} \rightarrow \mathbf{4}_{O/O} + H^+ + e^-$	1.36	1.64	1.41	0.93	1.47

[a] $(001)_{1c}$ stands for the OER on one single iridium center of the (001) surface.

The first step of the **I2M** mechanism is the oxo-coupling ($\mathbf{4}_{O/O}$ to $\mathbf{4}_{O-O}$ step). This step is a chemical process in which two oxo species on the surface couple forming an O−O bond.

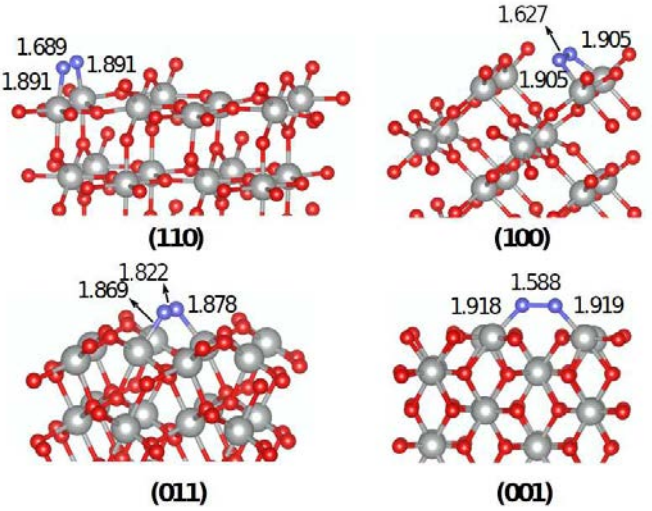

Figure 5.6: Transition states associated to the oxo-coupling chemical step on the main IrO_2 surfaces. Distances in Å.

The global process is endergonic for all IrO_2 main crystallographic facets, the reaction energies ranging between 0.10 and 2.30 eV (9.6 and 221.9 kJ·mol^{-1}). The most unfavorable oxo-coupling occurs at the (001), where the Ir=O species has the most pronounced oxo character. The least unfavorable process takes place at the (011), where the Ir=O species is less stabilized with respect to two adsorbed water molecules and the two Ir=O species are closer (2.887 Å vs. further than 3.180 Å). Intermediate values are obtained for the (110) and (100) facets. The energy barriers for the $\mathbf{4}_{O/O}$ to $\mathbf{4}_{O-O}$ step show similar trends as a function of the surface than those observed for

the thermodynamics of the oxo-coupling, the reaction being kinetically more challenging for the (001) surface, followed by the (100), (110) and (011) facets. Indeed, the process is only accessible at the (011) surface ($\Delta G^{\ddagger}$ = 0.33 eV (31.8 kJ $\cdot mol^{-1}$)). Noteworthily, the oxo-coupling at the (011) surface requires oxidizing first $\mathbf{3}_{O/OH}$ to $\mathbf{4}_{O/O}$, which requires potentials above 1.64 V to take place. These data suggest a relationship between the instability of $\mathbf{4}_{O/O}$, its oxyl character and the facility to form $\mathbf{4}_{O-O}$.

Table 5.3: $Ir-O_L$ distances (in Å) and magnetic moments of the key reaction intermediates associated to the **I2M** and **WNA** mechanisms.

	Species	Ir_1-O_{L1}	Ir_2-O_{L2}	O−O	S_{L1}	S_{L2}	S_{Ir1}	S_{Ir2}
(110)	$\mathbf{4}_{O/O}$	1.789	1.789	3.182	0.67	0.67	0.53	0.53
	$\mathbf{4}_{O-O}$	2.024	2.022	1.395	0.00	0.00	0.00	0.00
	$\mathbf{4}_{OOH/OH}$	1.931	1.913	1.417	0.00	0.10	0.00	-0.10
	$\mathbf{5}_{OO/OH}$	1.931	1.896	1.297	0.22	0.10	-0.10	-0.10
	$\mathbf{6}_{OO/O}$	1.923	1.781	1.289	-0.15	-0.31	0.12	-0.17
(011)	$\mathbf{4}_{O/O}$	1.797	1.797	2.887	0.62	0.59	0.57	0.52
	$\mathbf{4}_{O-O}$	2.043	2.016	1.404	0.00	0.00	0.00	0.00
	$\mathbf{4}_{OOH/OH}$	1.961	1.936	1.446	0.00	0.00	0.00	0.00
	$\mathbf{5}_{OO/OH}$	1.983	1.939	1.293	0.63	0.00	-0.12	0.00
	$\mathbf{6}_{OO/O}$	1.941	1.798	1.281	0.08	0.57	-0.04	0.54
(100)	$\mathbf{4}_{O/O}$	1.771	1.771	3.187	0.50	0.50	0.34	0.34
	$\mathbf{4}_{O-O}$	2.012	2.015	1.395	-0.02	-0.02	0.01	0.01
	$\mathbf{4}_{OOH/OH}$	1.927	1.914	1.406	0.00	0.00	0.00	0.00
	$\mathbf{5}_{OO/OH}$	1.958	1.912	1.286	-0.63	0.03	0.17	-0.02
	$\mathbf{6}_{OO/O}$	1.932	1.760	1.287	-0.43	-0.05	0.12	-0.01
(001)	$\mathbf{4}_{O/O}$	1.732	1.732	4.304	0.00	0.00	0.00	0.00
	$\mathbf{4}_{O-O}$	2.033	2.033	1.387	0.00	0.00	0.00	0.00
	$\mathbf{4}_{OOH/OH}$	1.885	1.895	1.464	0.00	0.00	0.00	0.00
	$\mathbf{5}_{OO/OH}$	1.853	1.889	1.280	0.00	0.00	0.00	0.00
	$\mathbf{6}_{OO/O}$	1.856	1.726	1.273	0.00	0.00	0.00	0.00

Analysis of the structure of reactants, products and transition states shows that during the oxo-coupling process the O···O distance, which ranges from 4.304 to 2.887 Å in $\mathbf{4}_{O/O}$, decreases to 1.387 -1.404 Å in $\mathbf{4}_{O-O}$, the values at the transition state structures being 1.588-1.822 Å. This is associated with an elongation of the Ir-O bond (2.012-2.043 Å in $\mathbf{4}_{O-O}$ and 1.869-1.919 Å in the transition state (See Table 5.3 and Fig. 5.6). The computed O−O distance in $\mathbf{4}_{O-O}$ suggests that O_2 acts as $\mu-\eta^1:\eta^1-{O_2}^{2-}$ peroxo ligand coordinated to two metal centers[238,239] and this is in agreement with the absence of magnetic moment over the oxygen atoms. Thus, the $\mathbf{4}_{O/O}$ to $\mathbf{4}_{O-O}$ process should be viewed as the homolytic coupling of two oxyl groups, without reduction of the metal center at the surface. Once the peroxo is formed, the subsequent steps are accessible at reaction conditions. The ligand exchange between O_2 and two water molecules is in all cases exergonic with reaction energies between -0.13 and -0.90 eV (-12.5 and -86.8 kJ·mol^{-1}) and implies the formal reduction of the two involved iridium centers. This regenerates $\mathbf{0}_{H_2O/H_2O}$ that as discussed in the first section can be easily reoxidized to $\mathbf{4}_{O/O}$ at 1.50 V with the exception of the (011) surface. Consequently, the electrochemical steps of the **I2M** mechanism in the (110), (100) and (001) are accessible at working potentials. However, this reaction mechanism is hampered in these three surfaces by the energy cost of the chemical oxo-coupling step. The **I2M** mechanism at the (011) surface appears to be chemically feasible (energy barrier of 0.33 eV), but this surface is not easily oxidized and thus higher overpotentials would be required.

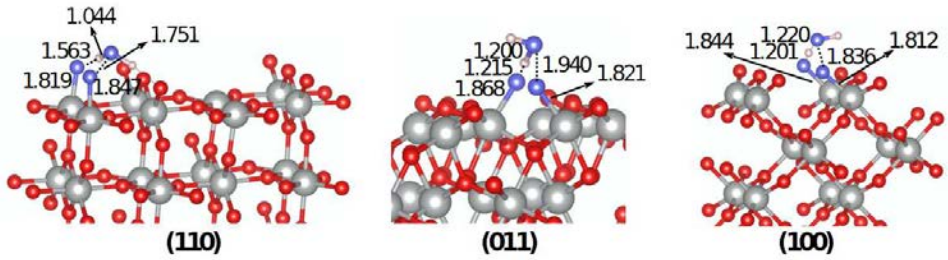

Figure 5.7: Transition states associated to the water nucleophilic attack step on the main IrO_2 surfaces. Distances in Å.

From $\mathbf{4}_{O/O}$, the **WNA** mechanism starts with a chemical step where water reacts with two oxo at the surface, forming $\mathbf{4}_{OOH/OH}$.[a] The reaction energies associated to the $\mathbf{4}_{O/O}$ to $\mathbf{4}_{OOH/OH}$ chemical step are within -0.12 and 1.24 eV (-11.6 and 119.6 kJ mol^{-1}). The reaction is slightly exergonic at the (110) (-0.12 eV), essentially isergonic at the (011) and (100) surfaces (-0.05 and 0.08 eV, respectively) and highly unfavorable at the (001) surface (1.24 eV). The Gibbs energy barrier estimated from an intermediate species ($\mathbf{4}_{O/O-H_2O}$) where one water molecule is interacting with $\mathbf{4}_{O/O}$ of the studied surfaces are in all cases low around 0.42 - 0.43 eV (41 kJ·mol^{-1})) except for the (001) surface where the process is thermodynamically hampered, and we were not able to localize the transition state. Overall, these data suggest that the reaction is easy on the (110), (011) and (100) surfaces. The Ir−O distances at $\mathbf{4}_{OOH/OH}$ are relatively similar to those computed for $\mathbf{2}_{OH/OH}$ and indicative of an Ir−O single bond. Moreover, the O−O distance in the Ir−OOH species ranges from 1.406 to 1.464 Å. These geometry features are associated with the absence of

[a] We also explored the possibility that the water attack occurs at $\mathbf{3}_{O/OH}$ in the (011) surface. However, we were unable to find any minimum of $\mathbf{3}_{OOH/H_2O}$, thus suggesting that $\mathbf{3}_{O/OH}$ has to be oxidized before to $\mathbf{4}_{O/O}$.

magnetization in any of the three oxygens of Ir−OOH and Ir−OH species, thus suggesting that Ir−OOH should be viewed as a hydroperoxo (OOH^-) species.[238,239] Consequently, despite the process has always been referred as a water nucleophilic attack, our data suggest that the $\mathbf{4}_{O/O}$ to $\mathbf{4}_{OOH/OH}$ process is best viewed as two concerted radical attacks resulting from the homolytic splitting of water. Indeed, the $OH^\bullet$ and $H^\bullet$ radicals attack two metal oxyl $M-O^\bullet$ species without modifying the oxidation state of the metal center. In this context, $\mathbf{4}_{O/O}$ shows an important oxyl character on the (110), (011) and (100) surfaces and thus the process is particularly accessible in these centers. In contrast, the Ir=O species in the (001) surface is mainly an oxo group and the H_2O attack is energetically forbidden. From $\mathbf{4}_{OOH/OH}$, two PCET steps ($\mathbf{4}_{OOH/OH}$ to $\mathbf{5}_{OO/OH}$ and $\mathbf{5}_{OO/OH}$ to $\mathbf{6}_{OO/O}$) take place before the release of O_2 occurs. While the O_2 release is a favorable chemical process, the two proton transfers are challenging. The $H^+ + e^-$ transfer from $\mathbf{4}_{OOH/OH}$ involves the H from the hydroperoxo and it is electrochemically accessible on all surfaces at relatively low potentials.[b] The two resulting Ir−O distances in $\mathbf{5}_{OO/OH}$ are similar to those of $\mathbf{2}_{OH/OH}$ and $\mathbf{4}_{OOH/OH}$, thus suggesting a single bond between Ir and the two adsorbed species (See Tables 5.1 and 5.3). Moreover, the O−O distance of the originally OOH^- species shortens significantly (from about 1.4 to about 1.3 Å) and the magnetization on the OO increases significantly. This appears to be indicative of the formation of $O_2^{\bullet-}$ and thus, the oxidation takes place at the O_2-based ligand. The $\mathbf{5}_{OO/OH}$ to $\mathbf{6}_{OO/O}$

[b] We also considered the possibility that the process involves the H from the hydroxyl, but the computed energies are similar or higher (see Supporting Information).

step is in all cases more challenging than the $\mathbf{4}_{OOH/OH}$ to $\mathbf{5}_{OO/OH}$ one. The geometrical parameters, as well as the spin distribution on the ligands of $\mathbf{6}_{OO/O}$, suggest that the Ir−OO fragment remains unchanged but the Ir−O fragment varies significantly. Indeed, Ir−O has an important oxyl character on the (110) and (011) facets, with a relatively large Ir−O distance and magnetic moment both on the oxygen and iridium. In contrast, Ir=O is best viewed as an oxo group on the (100) and (001) surfaces. Since the iridium oxo bond (Ir=O) is stronger than the iridium oxyl one ($Ir^{\bullet}-O^{\bullet}$), the $\mathbf{5}_{OO/OH}$ to $\mathbf{6}_{OO/O}$ step becomes particularly challenging for the (110) and (011) surfaces, where the required potentials are higher than 1.53 V. In summary, the **WNA** mechanism is accessible for the (110), (011) and (100) surfaces at reaction conditions. In addition, the two mechanisms appear to be competitive on the (011) being the oxo-coupling preferred. Finally, the (001) surface does not seem to be reactive if two metal centers are required to achieve the process, and this is clearly associated with the formation of Ir=O oxo species instead of oxyl radicals. We decided to explore if OER could occur on one single Ir center of the (001) surface, taking into account that Ir is tetracoordinated and has two vacant sites on this surface. Results are summarized on Fig. 5.8 and Table 5.2. Formation of two Ir−O groups requires overcoming higher potentials than those involved for the formation of one single oxo group. However, the computed values are lower than 1.50 eV. This suggests that bisoxo species on the (001) are expected to be formed at reaction conditions.

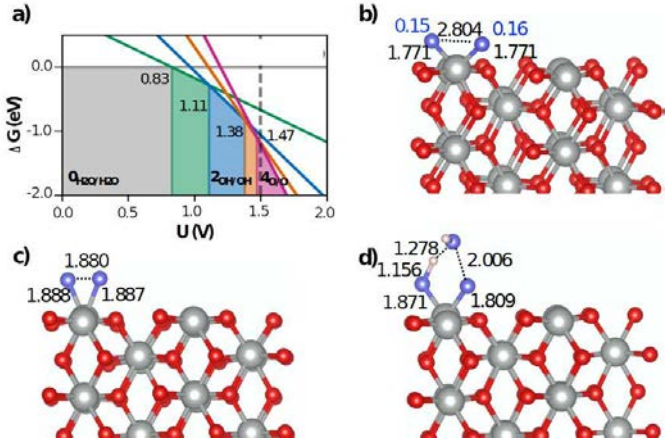

Figure 5.8: a) Phase diagram of IrO_2 (001) surface depending on of the applied potential; b) Optimized structure for the Ir-bisoxo intermediate; c) Transition state structure associated with the oxo-coupling chemical process; d) Transition state associated with the **WNA** step. Values in blue correspond to the spin densities over the oxo groups. Distances in Å

Structural analysis indicates that the two oxo groups present Ir−O distances closer to those of the other three surfaces than to the single oxo group on the (001) facet. The magnetization reveals a certain oxyl character (blue values in Fig. 5.8 b). As a consequence, the two chemical steps (oxo-coupling and water nucleophilic attack) are now easier than those occurring between two different centers. For the particular case of the **WNA** mechanism, formation of $\mathbf{4}_{OOH/OH}$ becomes accessible (ΔG^0 = 0.25 eV) and the reaction presents a low energy barrier ($\Delta G^{\ddagger}$ = 0.55 eV). Therefore, OER on the (001) is expected to occur on one single Ir center and through the **WNA** mechanism.

Overall, the **WNA** chemical step is the applying mechanism on the (110), (100) and (001) surfaces. The oxo-coupling appears to be the most favorable pathway on the (011) surface, where the spin density over the oxyl radicals is high and the interoxyl distance rather short. The computed overpotentials are: 0.30, 0.41, 0.18 and 0.24 V for the (110), (011), (100) and (001) surfaces. Thus, the potential required to produce O_2 increases as (100) < (001) < (110) < (011) surface. Moreover, the number of Ir vacant sites density varies as: (001) > (011) > (100) > (110) facet. Therefore, calculations predict that the highest activities per surface area would be obtained on the (100) and (001), as they require lower overpotentials for catalyzing the OER and they present a larger number of active sites per surface unit. In contrast, the two more stable facets ((011) and (110)) present either a smaller number of active sites per nm^2 -(110)- or require higher overpotentials for catalyzing the process -(011). These results reproduce the experimental trend when comparing the (100) and (110) surfaces[105] and suggest that (001) surface is at least as reactive as the (100) facet.

Our results suggest that the reactivity on the different surfaces is highly controlled by two main factors. On one hand, the oxo-coupling and the water nucleophilic attack chemical steps should be viewed as homolytic couplings between either two Ir−O species or between two Ir−O centers and an homolytically splitted $H^{\bullet}/OH^{\bullet}$ water molecule. Consequently, they are only feasible when two Ir−O species with a significant oxyl character and an Ir(V) center are close enough, the computed energy barriers being highly determined by the spin density over the oxyl group and the interatomic distance between Ir−O species. Noteworthily, the need for

two radical species indicate that only half of Ir centers are active, except if they present more than one vacant site. While the role of the oxyl character in determining the catalytic activity of molecular complexes[207,240–249] and first row transition metal oxides[250–256] has been discussed and shown to be important, its role in second and third row transition metal oxides has been mainly eluded. To the best of our knowledge, oxyl radicals on IrO_X-based OER catalysis are only mentioned by Pavlovic and colaborators.[257] According to our data, the oxyl character is crucial in the two main reaction mechanisms on IrO_2 surfaces, thus suggesting that these surfaces and the Ir or Ru molecular analogues have more similarities than one could initially suspect.

On the other hand, regardless of the considered surface, the overpotential required to perform the OER is determined by the oxidation of the Ir−OH hydroxyl group to Ir−O species ($\mathbf{3}_{O/OH}$ to $\mathbf{4}_{O/O}$ step or $\mathbf{5}_{OO/OH}$ to $\mathbf{6}_{OO/O}$). That is, for IrO_2 surfaces, the easiest the oxidation of the hydroxyl group the lowest the required overpotential. Unfortunately, when the formation of the oxo group is easy the resulting species has no oxyl character and, consequently, it does not react with the incoming water molecule. Indeed, the two factors are closely related and a subtle compromise between the feasibility of Ir−OH oxidation and oxyl character is a key issue.

Analysis of the electronic structure of the four surfaces shows that the two variables are tuned by the coordination and nature of the vacant sites of the undercoordinated iridium centers. Unsaturated tetracoordinated centers are so poorly stabilized that the formation of one Ir=O group per metal center is easy. However, when this

Ir=O group is formed on these centers, it does not have an oxyl character and thus it is not reactive. The oxidation of unsaturated pentacoordinated iridium centers is more challenging, the Ir−O group has a significant oxyl character and, consequently, they are more prone to react. When the vacant site is equatorial the $Ir-O_L$ interaction is weaker than for the other cases and, overall, higher overpotentials are required. In contrast, the stronger $Ir-O_L$ interaction at axial sites, leads to a good compromise between the oxyl character and oxidation feasibility, which explains the lower overpotentials of the (100) and (110) surfaces with respect to the (011) one. Oxidation of the tetracoordinated sites of the (001) surface to bisoxo species is as challenging as the oxidation of the (100) and (110) surfaces and the resulting species has enough oxyl character to undergo the **WNA**. Overall, this turns in very efficient single atom sites, which combines low overpotentials and a larger number of active centers. This suggests that Ir centers able to form bisoxo species at working potentials are of great potentiality as recently shown by Copéret and co-workers when using Single-Site Iridium species on ITO electrodes.[231]

5.3 OER on $(IrO_2)_{33}$ Nanoparticle

The OER reaction is studied on the $(IrO_2)_{33}$ nanoparticle arising from the optimization that includes the monolayer of water molecules. For the rest of the study, the atomic positions of the nanoparticle are kept fixed. As for extended surfaces, for the $(IrO_2)_{33}$ nanoparticle we first study the water oxidation of the adsorbed water to Ir=O.

In a second step the **I2M** and the **WNA** mechanisms were explored assuming that two mechanisms involve two Ir−O species and thus the local environment is fully oxidized. In this context four pairs or Ir centers and two single sites were selected on the nanoparticle surface. These sites take into account the diverse metal coordination, nature of the reactive site and chemical environment. The considered centers are shown in Fig. 5.9. The four pair sites are: **fase** involving two centers of the {110} facet that do not include single coordinated atoms; **A** involving one corner I center with a single coordinated atom and the edge site; **C** involving one corner I and one corner II centers that have three single coordinated atoms in total and **D** involves one face and one corner II with two single coordinated atoms. The two coordinated sites correspond to the tetracordinated tip and corner I centers.

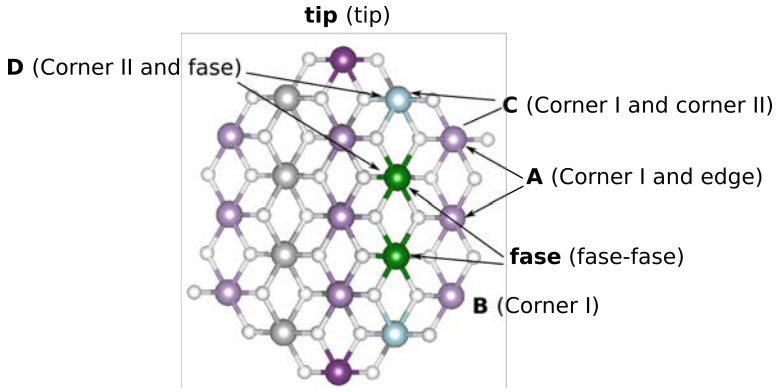

Figure 5.9: Selected sites to study OER proposed mechanisms.The color legend is based on Fig. 4.9. **face** centers are on a {110} facet.

5.3.1 $(IrO_2)_{33} - H_2O$ Oxidation Depending on the Applied Potential

The first part of the process is the adsorption of two water molecules. In Fig. 5.10, the most stable conformations are depicted. Water adsorption was discussed in detail in Chapter 4, here we only present the most stable conformations for the adsorption of two water molecules on the selected sites. In Fig. 5.2 the preferred water configurations are shown.

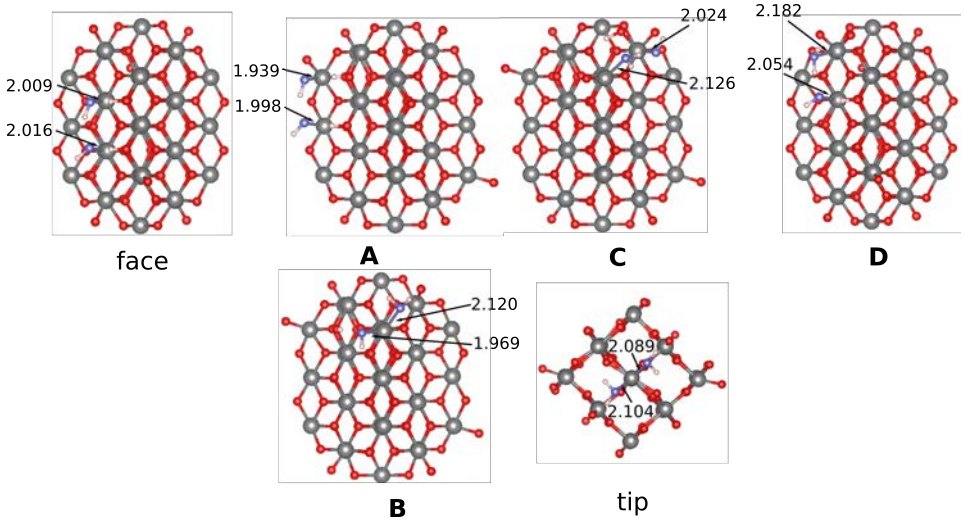

Figure 5.10: $IrO_2 - 2\,H_2O$ structures for the selected sites on the nanoparticle surface. Distances in Å.

For all the evaluated sites, the preferred configuration has at least one water dissociated except for the tip. As shown in Chapter 4, the preference of molecular or dissociated form depends on the type of vacancy, the coordination, the basicity of the O atom that interacts with the water molecule and the presence of cooperative effects. For

face and **A** sites, both water molecules are dissociated and no cooperative effects appear to be present according to the distance between water moieties. For **face**, the adsorption energy is slightly lower that the calculated for the single site adsorption (-212.4 vs -229.7 kJ mol^{-1}), and this is in agreement with the fact that the $Ir-O$ distance is larger for the adsorption of two water molecules than for the isolated water.

Similarly, for **A** the adsorption energy per water molecule (-153.7 kJ mol^{-1}) is smaller than that of the single water adsorption on an edge site (-225.5 kJ mol^{-1}) and that of a single water adsorption on a corner I (187.8 kJ mol^{-1}). This suggests that the adsorption or a water molecule on a pentacoordinated center with a single coordinated oxygen is weak. Furthermore, the $Ir-O$ distances are almost equal to those reported for the single site adsorption.

For the remaining pair sites - **C** and **D** - one water molecule is dissociated whereas the other one remains molecular. Unfortunately, the adsorption energy on both sites does not have an equivalent on the single site adsorption. This is because single coordinated oxygens have been added to the less coordinated sites due to the assumption that the local environment is fully oxidized. The $Ir-O$ distances show that molecular water form is less adsorbed than the dissociated ones. Moreover, the distance between water molecules is 1.547 and 1.627 Å, respectively. Thus, a strong H-bonding interaction between the adsorbed species is present on both sites. As for higher coverages where the water molecules interact between them the formation of $H_2O_3{}^-$ hinders the full water dissociation.

Finally, for the **tip** site, the preferred configuration has both water molecules in their molecular form. This could be attributed to the decrease of the Ir acidity due to the adsorption of two water molecules on the same center, and the low basicity of O_{1c} atoms close to the **tip** site, making less favorable the dissociated form. For **B** the preferred form has only one water molecule dissociated. This is due to the fact that the dissociated one interacts with a O_{br} and the molecular one with a less basic O_{1c}. Both centers has been analyzed in detail in Chapter 4.

The oxidation of the adsorbed water molecules is expected to occur through successive PCET steps. To determine the most stables species depending on the applied potential, the relative stabilities of all species according to Eq. (5.1) are shown in Fig. 5.11.

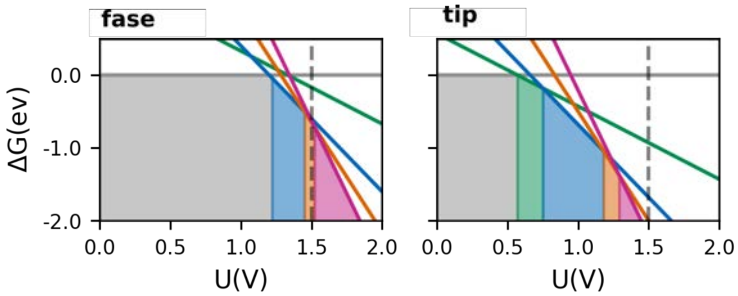

Figure 5.11: Phase diagram of IrO_2 depending on of the applied potential. Grey stands for $\mathbf{0}_{H_2O/H_2O}$, green stands for $\mathbf{1}_{OH/H_2O}$, blue stands for $\mathbf{2}_{OH/OH}$, orange stands for $\mathbf{3}_{O/OH}$ and pink for $\mathbf{4}_{O/O}$.

The adsorbed water molecules on the **tip** site are oxidized to $\mathbf{4}_{O/O}$ at 1.29 V, whereas those on the **face** site are oxidized at 1.52 V. Hence, the oxidation is more favorable on the **tip** center. For the **face** site, the adsorbed water molecules are oxidized to $\mathbf{2}_{OH/OH}$ at 1.22 V then

at 1.45 V to $\mathbf{3}_{O/OH}$ and finally to $\mathbf{4}_{O/O}$ at 1.52 V. This values are 0.07 V higher than those obtained for the (110) extended surfaces, suggesting that the larger ionic character of the nanoparticle makes the oxidation of water molecules more challenging. In contrast, $\mathbf{0}_{H_2O/H_2O} \rightarrow \mathbf{1}_{OH/H_2O} + H^+ + e^-$, $\mathbf{1}_{OH/H_2O} \rightarrow \mathbf{2}_{OH/OH} + H^+ + e^-$, $\mathbf{2}_{OH/OH} \rightarrow \mathbf{3}_{O/OH} + H^+ + e^-$ and $\mathbf{3}_{O/OH} \rightarrow \mathbf{4}_{O/O} + H^+ + e^-$ are computed to take place at 0.57, 0.75 1.18 and 1.29 V respectively. These values are about 0.20 V lower than those for the (001) surface, indicating that the tip behaves in a particular manner. Overall, the face and the tip sites will be fully oxidized at 1.50 V. Moreover, experimental evidence suggests that the surface of crystalline IrO_2 nanoparticles are fully oxidated at potentials above 1.50 V.[91,98] Thus, our results are in agreement with the experimental evidence.

Geometric and electronic parameters (Table 5.4 and Appendix B) show that the oxidation of the water molecule decreases the $Ir-O_L$ distance, going from 2.090-2.104 Å for $\mathbf{0}_{H_2O/H_2O}$ to 1.804-1.771 for $\mathbf{4}_{O/O}$ following the same tendency as the extended surfaces. For the face, the $Ir-O_{L2}$ distances on $\mathbf{4}_{O/O}$ are slightly larger than those reported for the (110) surface (1.805 vs 1.789 Å), but simmilar magnetic moments (0.63 vs 0.67 a.u.). This correlates with the larger potential to get fully oxidized species in the former case (1.52 vs 1.46 V).

Regarding the tip, the $Ir-O_L$ distances for $\mathbf{4}_{O/O}$ are similar to that ones reported for the $(001)_{1c}$ surface (1.772 vs 1.771 Å). However, the O_L atoms on the **tip** site have a larger magnetic moment than those for $(001)_{1c}$. Therefore, the OER reactions could be more favorable for the **tip** site on the nanoparticle than on the $(001)_{1c}$, showing again a remarkable different behavior when it is compared to the surface

Table 5.4: $Ir-O_L$ distances (in Å) and magnetic moments for water oxidation of hydratated sites on the $(IrO_2)_{33}$ nanoparticle.

Site	Species	Ir_1-O_{L1}	Ir_2-O_{L2}	S_{O1}	S_{O2}	S_{Ir1}	S_{Ir2}
	$\mathbf{0}_{H_2O/H_2O}$	2.016	2.090	0.00	0.00	-0.03	-0.03
	$\mathbf{1}_{OH/H_2O}$	2.010	1.934	0.00	0.12	-0.01	0.23
face	$\mathbf{2}_{OH/OH}$	1.966	1.931	0.01	-0.12	-0.01	-0.23
	$\mathbf{3}_{O/OH}$	1.814	1.930	0.16	0.50	0.30	0.49
	$\mathbf{4}_{O/O}$	1.804	1.805	0.64	0.63	0.53	0.53
	$\mathbf{0}_{H_2O/H_2O}$	2.089	2.104	0.00	0.00	0.00	0.00
	$\mathbf{1}_{OH/H_2O}$	2.085	1.930	0.00	0.00	0.37	0.37
tip	$\mathbf{2}_{OH/OH}$	1.928	1.925	0.06	0.06	0.47	0.47
	$\mathbf{3}_{O/OH}$	1.766	1.926	-0.30	-0.02	-0.31	-0.31
	$\mathbf{4}_{O/O}$	1.772	1.771	0.26	0.23	0.41	0.41

site. These results suggest that even when nanoparticle Ir centers shares coordination and nature of the vacant site with those on extended surfaces, their chemical behavior is not exactly the same. In this context, it is not easy to determine *a priori* if **A**, **B**, **C** and **D** are fully oxidized at 1.50 V. However, we expect that this will be arise when computing the **WNA** even if we assume as the starting point the fully oxidized surface.

5.3.2 OER Reaction Mechanisms on $(IrO_2)_{33}$

We have studied the OER reaction at the six sites described above and described in Fig. 5.9. For extended surfaces we found that the **WNA** is preferred over the **I2M** mechanism except on the (011) facet. Indeed, the viability of the **I2M** mechanism is limited by the accessibility of the oxo-coupling chemical step. Therefore, with the aim of saving computational time, we considered all steps for the **WNA**

mechanism and only the chemical steps for the **I2M**. This will allow us to have an idea of the preferred pathway and determine the required overpotential on each site. Table 5.5 reports the free Gibbs energies of the different steps, Table 5.6 shows the main geometry parameters and the spin densities of the key intermediates. Further details can be found in Appendix B.

Regarding the **I2M** mechanism, for all studied sites the coupling of the oxo species is endergonic with a ΔG in the range of 0.29 to 0.83 eV (27.98 to 80.08 $kJ{\cdot}mol^{-1}$). For **face** and **tip**, the oxo-coupling is more endergonic than this for their extended surface counterparts -(110) and (001_{1c}), respectively, but this could be associated to the constraints imposed by the fixation of the nanoparticle atomic positions. The computed values for **B**, **C** and **D** are closer to the values for the (011) surfaces indicating that the **I2M** can be competitive on this sites.

Table 5.5: Reaction Gibbs Energies (in eV) for the chemical and electrochemical steps of the **I2M** and **WNA** reaction mechanisms on the non-reconstructed $(IrO_2)_{33}$ nanoparticle.

Reaction	face	tip	A	B	C	D
I2M						
$\mathbf{4}_{O/O} \rightarrow \mathbf{4}_{O-O}$	0.83	0.83	0.61	0.38	0.39	0.29
$\mathbf{4}_{O-O} + 2\,H_2O \rightarrow \mathbf{0}_{H_2O/H_2O} + O_2$	-1.28	0.30	-0.54	-0.68	-1.40	-0.04
WNA						
$\mathbf{4}_{O/O} + H_2O \rightarrow \mathbf{4}_{OOH/OH}$	-0.57	0.48	-0.20	-0.20	-0.35	-0.25
$\mathbf{4}_{OOH/OH} \rightarrow \mathbf{5}_{OO/OH} + H^+ + e^-$	1.35	0.86	1.23	0.96	1.19	0.94
$\mathbf{5}_{OO/OH} \rightarrow \mathbf{6}_{OO/O} + H^+ + e^-$	1.62	1.25	1.40	1.41	1.63	1.62
$\mathbf{6}_{OO/O} + H_2O \rightarrow \mathbf{2}_{H_2O/O} + O_2$	-0.20	0.47	-0.14	0.19	-0.73	0.10
$\mathbf{2}_{H_2O/O} \rightarrow \mathbf{3}_{O/OH} + H^+ + e^-$	1.20	0.56	1.20	0.82	1.59	0.97
$\mathbf{3}_{O/OH} \rightarrow \mathbf{4}_{O/O} + H^+ + e^-$	1.52	1.29	1.44	1.74	1.59	1.53

Table 5.6: $Ir-O_L$ distances (in Å) and magnetic moments for the key intermediates associated to the **I2M** and **WNA** on selected sites of the non-reconstructed $IrO_2)_{33}$ nanoparticle.

	Species	Ir_1-O_{L1}	Ir_2-O_{L2}	O−O	S_{L1}	S_{L2}	S_{Ir1}	S_{Ir2}
face	$\mathbf{4}_{O/O}$	1.805	1.804	3.067	0.63	0.64	0.53	0.53
	$\mathbf{4}_{O-O}$	2.261	2.148	1.314	0.31	0.31	0.03	0.04
	$\mathbf{4}_{OOH/OH}$	1.950	1.941	1.347	0.44	0.13	0.07	0.22
	$\mathbf{5}_{OO/OH}$	1.953	1.908	1.300	0.50	0.12	-0.07	-0.23
	$\mathbf{6}_{OO/O}$	1.947	1.807	1.287	1.62	0.48	-0.10	0.28
tip	$\mathbf{4}_{O/O}$	1.770	1.772	2.900	0.23	0.26	0.41	0.41
	$\mathbf{4}_{O-O}$	1.989	1.976	1.371	0.21	0.22	0.01	0.01
	$\mathbf{4}_{OOH/OH}$	1.913	1.932	1.456	-0.07	-0.06	-0.22	-0.22
	$\mathbf{5}_{OO/OH}$	1.946	1.924	1.296	0.50	-0.06	-0.32	-0.32
	$\mathbf{6}_{OO/O}$	1.960	1.782	1.285	-0.61	0.47	0.43	0.43
A	$\mathbf{4}_{O/O}$	1.794	1.767	2.834	0.56	0.24	0.36	0.48
	$\mathbf{4}_{O-O}$	2.066	2.131	1.365	-0.21	-0.19	-0.01	0.66
	$\mathbf{4}_{OOH/OH}$	1.958	1.902	1.345	-0.45	0.03	0.00	0.63
	$\mathbf{5}_{OO/OH}$	1.963	1.879	1.307	0.57	0.04	-0.14	0.57
	$\mathbf{6}_{OO/O}$	1.971	1.781	1.289	0.46	-0.09	-0.06	0.35
B	$\mathbf{4}_{O/O}$	1.801	1.789	2.760	0.54	0.33	0.18	0.18
	$\mathbf{4}_{O-O}$	2.015	2.010	1.359	0.31	0.29	0.15	0.15
	$\mathbf{4}_{OOH/OH}$	1.920	1.935	1.448	-0.03	-0.01	0.01	0.01
	$\mathbf{5}_{OO/OH}$	1.996	1.940	1.286	0.83	-0.08	0.14	0.14
	$\mathbf{6}_{OO/O}$	2.044	1.788	1.281	0.89	-0.52	0.34	0.34
C	$\mathbf{4}_{O/O}$	1.783	1.793	3.037	0.47	-0.26	0.40	-0.11
	$\mathbf{4}_{O-O}$	2.033	3.443	1.283	-0.79	–	0.33	0.28
	$\mathbf{4}_{OOH/OH}$	2.016	1.954	1.287	0.83	0.02	-0.38	0.41
	$\mathbf{5}_{OO/OH}$	2.017	1.954	1.293	0.79	0.01	-0.36	0.10
	$\mathbf{6}_{OO/O}$	2.072	1.793	1.276	0.92	0.18	0.29	0.16
D	$\mathbf{4}_{O/O}$	1.806	1.786	3.152	0.57	0.23	0.57	0.41
	$\mathbf{4}_{O-O}$	1.947	3.371	1.291	0.47	–	0.08	0.57
	$\mathbf{4}_{OOH/OH}$	1.956	1.937	1.438	-0.01	0.01	-0.02	0.37
	$\mathbf{5}_{OO/OH}$	1.958	1.918	1.302	0.54	0	-0.02	0.38
	$\mathbf{6}_{OO/O}$	1.951	1.783	1.289	0.49	0.04	-0.06	-0.21

On the studied sites, the O−O distance of $\mathbf{4}_{O-O}$ specie ranges between 1.283 and 1.371 Å and the total magnetic moment of the whole adsorbate is in the range of 0.4 to 0.8 a.u., suggesting a superoxide species ($O_2^{\bullet -}$) instead of the peroxide found on the extended surfaces.[238,239] Therefore, the oxo-coupling in these cases is not only the homolitic coupling of two oxyl radicals but also a partial oxidation of the O_2^{-2} and a partial reduction of the metal center. Interestingly, the presence of single coordinated oxygens on the active centers determines the type of surface-superoxo interaction. Indeed, when the superoxo is formed on one site, like **tip** and **B**, the binding is a η^2-$O_2^{\bullet -}$ where both oxygens interact directly with the Ir center. For **face** and **A** sites, the superoxo-surface interaction is $\mu - \eta^1 : \eta^1$-$O_2^{\bullet -}$. Finally, for **C** and **D**, where both centers reactive centers has dangling oxygens, the $O_2^{\bullet -}$ moiety is only bounded to one Ir center. Therefore, this suggests that the presence of dangling oxygens on both reactive centers leads to η^1-$O_2^{\bullet -}$ species. Further analysis of the Ir−O_L distances shows that the superoxo adsorbate is loosely attached to the nanoparticle surface compared to the peroxo one on the extended surfaces.

The ligand exchange between the $O_2^{\bullet -}$ and two water molecules is slightly exergonic in all sites, except for the **tip** one. The reaction energies are in the range of -1.40 and 0.30 eV (-135.08 and 28.95 kJ·mol^{-1}), being only endergonic for the **tip** site. The required energy for the oxygen release on the **tip** site could be related to the fact that the water molecules are adsorbed in a molecular form, whereas for the other ones the preferred conformations has at least one water

molecule dissociated. Moreover, in the **C** and **D** sites, the dissociation of one of the adsorbed molecules leads into the formation of $H_2O_3^-$ dimer, that as has been suggested in Chapter 4, increases the adsorption energy, promoting the oxygen release.

Overall, the oxo-coupling process of two oxyl radicals is different on the nanoparticle model that on the extended surfaces. The main difference is the nature of the adsorbed O_2 species that is a superoxide on the nanoparticle and a peroxide on the extended surfaces. Moreover, this is not significantly influence the reaction energies of the oxo-coupling processes as their are similar on both kind of models. The fact that the obtained values are marginally higher on the nanoparticle could be associated to the geometry constraints imposed to avoid unrealistic relaxations. Further, the energy values for the oxygen release on the **face** site of the nanoparticle shows that this process is more favorable than on the (110) surface. Hence, we can suggest that the oxygen release is easily achieved if the adsorbed specie has a superoxide character than a peroxide one.

From $\mathbf{4}_{O/O}$, the **WNA** mechanism starts with a chemical step where a water molecule dissociates forming $\mathbf{4}_{OOH/OH}$. The reaction free energies for this process range between -0.57 and 0.48 eV (-55.00 to 46.31 kJ·mol^{-1}) and it is exergonic for all the sites except for the **tip** one. When comparing this values with the obtained for extended surfaces, one can observe that the **WNA** is more favorable on the nanoparticle. Then the energonicity of the **tip** site could be related to the fact that in this case, the oxo species of the $\mathbf{4}_{O/O}$ intermediate have the lower magnetic moment compared to the other nanoparticle sites.

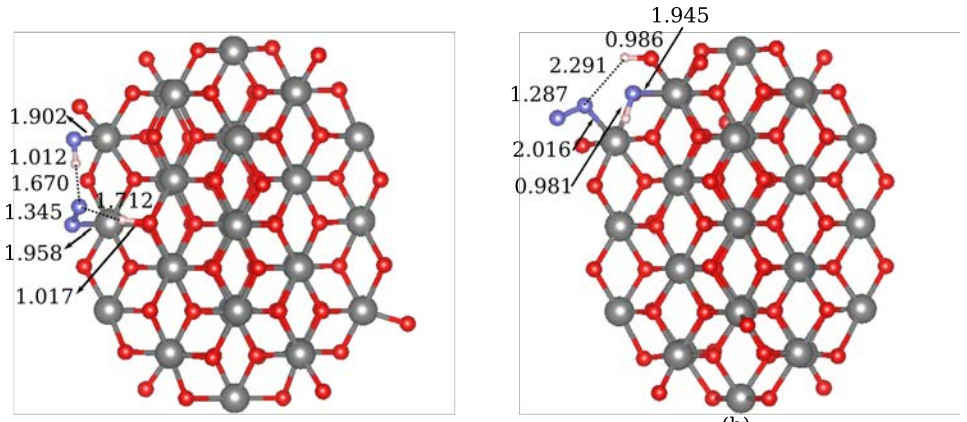

Figure 5.12: Optimized structures for $\mathbf{4}_{OOH/OH}$ intermediate for (a) A and (b) C sites on the non-restructured nanoparticle.

At this point is worth mentioning that the **WNA** could lead into two configurations, one where the OOH^- adsorbate is stable, and the other one where it is dissociated as OO/OH. That is the hydrogen atom of OOH^- is transferred to either O_{1c} or an O_{br} atom. In Fig. 5.12 the OH/OO/O_{br}H (a) and OH/OO/O_{1c}H (b) species are shown. For **face**, **A** and **C** sites, the OOH^- moiety is dissociated by transferring the proton to O_{br} (**face** and **A**), or to an dangling oxygen (**C**). The **face** and **A** sites are on one of the {110} nanoparticle facets, therefore it is possible to compare it to the (110) extended surface. The dissociation of OOH^- fragment on these nanoparticle sites can be attributed to the fact that the O_{br} atoms on the nanoparticle {110} facets are more basic than those on the (110) surface, favoring the H transfer. Moreover, the OH/OO/O_{br}H configuration on the (110) surface is 0.09 eV more stable than OOH/OH which leads into an slightly increase of 0.09 eV for the $\mathbf{4}_{OOH/OH} \rightarrow \mathbf{5}_{OO/OH}$

step. Distance analysis shows that OO−H bond is larger than the O_{br}−H one (1.002 vs 1.055 Å), confirming the PCET preference for the OOH/OH configuration (See Appendix B). For **face**, **A** and **C** sites, the adsorbed dioxygen specie has a O−O distance around 1.3 Å and magnetic moment ranging between 0.4 and 0.8 a.u., suggesting a $O_2^{\bullet-}$ intermediate. For the remaining sites, **tip**, **B** and **D**, the OOH^- have the same properties as extended surfaces, namely similar distances and magnetic moments (close to zero). It is worth to mention that regardless of the preferred configuration, the product of the water reaction with two Ir=O is refereed as $\mathbf{4}_{OOH/OH}$.

From $\mathbf{4}_{OOH/OH}$, two PCET have to take place before the oxygen release - $\mathbf{4}_{OOH/OH} \rightarrow \mathbf{5}_{OO/OH}$ and $\mathbf{5}_{OO/OH} \rightarrow \mathbf{6}_{OO/O}$. In all cases, the former is the most favorable step. Distances and magnetization analysis shows that the first PCET, the hydroperoxo deprotonation, leads to the formation of $O_2^{\bullet-}$, and the second one leads into an adsorbed oxyl specie. For centers with one adsorbate, the energy required for the oxidation of OH fragment is slightly related to the Ir−OH distance. For instance, this distance is shorter on **A** than on the **face** site. Hence, the second PCET is more favorable for the former than for the later (1.40 vs 1.62 eV). For **tip** and **B** analysis of the Ir−OH distance, the Ir magnetic moment and the Ir-d$\bar{\varepsilon}$ indicates that the $\mathbf{5}_{OO/OH} \rightarrow \mathbf{6}_{OO/O}$ step is more favorable for the former (1.25 vs 1.41 eV). This could be attributed to: (i) shorter Ir−OH distance, (ii) larger magnetic moment on Ir center and (iii) Ir-d$\bar{\varepsilon}$ close to the Fermi level on **tip** center compared to those on **B**.

Overall, the water chemical attack is more favorable than the oxo-coupling step, whereas the electrochemical step for both mechanisms

are affordable. Thus, the **WNA** mechanism is accessible for all the studied centers. The computed overpotentials are in the range of 0.06-0.51 V . Thus, we suggest that all of them participate in the OER reaction at overpotentials above than 0.51 V. Moreover, due to the almost insignificant overpotential of the **tip** site, (0.06 V), this could act as an ideal catalyst.

By assuming the working potential of 1.50 V, only tip, **face** and **A** sites could participate in the OER mechanism. The non-reconstructed $(IrO_2)_{33}$ has two tip, two **face** and six **A** sites. Thus, most of the O_2 production is done on the **A** type centers. However, for larger nanoparticles, **face** type centers could be more abundant. For instance, for $(IrO_2)_{90}$ nanoparticle model, the most abundant ones are the **face** ones (14), tip and type **A** sites remain equal and four additional tetracoordinated sites with metal coordination similar to the tip appears. This leads to a similar total number of active sites for the two models, suggesting that there is not a direct relation between nanoparticle sites and the catalytic activity.

5.4 Conclusions

The catalytic activity for the oxygen evolution reaction of the (110), (011), (100) and (001) main surfaces of rutile-like IrO_2 has been studied through spin-polarized DFT (PBE-D2) calculations. Both the oxo-coupling (**I2M**) and the water nucleophilic attack mechanisms have been considered and the energy barriers of the associated chemical processes calculated. Results show that the oxo-coupling and

water nucleophilic attack processes are best described as homolytic couplings either between two metal-oxyl radicals in **I2M** or between two metal-oxyl radicals and one homolytically split $H^{\bullet}/OH^{\bullet}$ water molecule in **WNA**. Consequently, the reaction only takes place when the $Ir-O$ species on the surface has an oxyl character. In these cases, the water nucleophilic attack is always accessible and easy, while the oxo-coupling chemical step requires that the $Ir-O^{\bullet}$ radicals are close and well-oriented. Overall, the water nucleophilic attack mechanism is preferred on the (110), (100) and (001) facets. In contrast, on the (011) surface, the two mechanisms are competitive, the **I2M** being the most favorable one. This suggests that the applying mechanism is highly dependent of the relative orientation of the $Ir-O^{\bullet}$ groups. The required overpotential for the OER to occur on the four IrO_2 considered surfaces is determined by the feasibility to oxidize the $Ir-OH$ species to $Ir-O$ (either the $\mathbf{3}_{O/OH}$ to $\mathbf{4}_{O/O}$ step or the $\mathbf{5}_{OO/OH}$ to $\mathbf{6}_{OO/O}$ one). Unfortunately, when the oxidation is too easy, the resulting $Ir=O$ species has no oxyl character. Surface morphology, unsaturated metal coordination and nature of the vacant sites tunes both the oxidation ability and oxyl character. Tetracoordinated species are so unsaturated that formation of one $Ir=O$ is easy, but the resulting species has no oxyl character and thus they do not further react. Pentacoordinated centers with equatorial vacant sites are hardly oxidized to $Ir=O$, due to the weaker $Ir-O_L$ interaction that destabilizes the most tightly bonded $Ir-O$ species. The pentacoordinated centers with axial vacant sites show an intermediate behavior and they appear to be more active. Finally, at working potentials the tetracoordinated iridium sites on the (001) surface can be oxidized to bisoxo species able to perform OER at low potentials.

In this case, the reaction occurs on one single atom, the number of sites per surface area is high and opens the door for the design of single atom catalysts.

The nanoparticle OER reactivity has been addressed on a the non-reconstructed $(IrO_2)_{33}$ nanoparticle. As for extended surfaces, both the oxo-coupling (**I2M**) and the water nucleophilic attack mechanisms have been considered. Results suggest that the chemical steps of both mechanisms - oxo-coupling and water nucleophilic attack - are radical processes. Therefore, both steps are favorable when the Ir=O have a strong oxyl character. For all the studied centers, the preferred mechanism is the **WNA**, whereas the **I2M** could be competitive in B,C and D sites. The potential determining step for the studied centers is the oxidation of Ir−OH species regardless of their morphology. Moreover, our results suggest that depending on the working potential, some centers can not participate actively in the process. However, our approach assumes that the selected sites do not interact between them; therefore, further research can be done in this line. The most efficient site is the **tip** one that almost behaves as the ideal catalyst for this reaction, the overpotential being only 0.06 V. Unfortunately, for Wulff-constructed nanoparticles, only two **tip** sites are available and, although a few similar sites appears at the edges between 011 facets when increasing the model, the number of so active centers is expected to be small. Nonetheless, this result could help to improve the development of more effective catalysts by maximizing the number of tip-like centers.

Remarkably, the importance of oxyl groups on molecular or first row transition metal oxide catalysts has been outlined before.[207,242,244,252]

However, the role of $M-O^{\bullet}$ on second and third row transition metal oxides has been essentially overlooked. Present results suggest that molecular and heterogeneous catalyst have larger similarities than initially expected and thus strategies for catalyst development on molecular systems may also be suitable to improve heterogeneously catalyzed OER.

6 Final Remarks

The use of nanoparticles in catalysis has several advantages with respect to the extended materials. On the one hand, they have a large specific surface area that decreases the catalyst cost per active center, something being particularly relevant for precious metals such as iridium. Moreover, their small size can also influence the catalytic activity either by modifying the electronic structure of the material or by the presence of active centers that do not exist in larger systems. The present thesis presents the modelling of nanoparticles and their activity in catalyzing the oxygen evolution reaction at DFT level of theory. Efforts were devoted to understand the similarities and differences between slab and nanoparticles models of IrO_2, the main conclusions being divided into three stages.

First of all, the modelling of nanoparticles requires the construction of solid and representative models. However, this is not always trivial for multicomponent Wulff-like structures, the resulting models often being dependent on human subjectivity. In this context, in this thesis we develop the computational tool BCN-M (https://bcnm.qf.uab.cat), which generates nanoparticle models in an automatized manner. BCN-M can build nanoparticle models with controlled stoichiometry solely from bulk material data and main

surfaces information. Our results show that it is possible to generate reproducible models minimizing human bias. Thus, they can serve as a starting point for computer simulations. Although the obtained nanoparticle models are ideal and probably differ from the experimental structures, they can be useful to evaluate the effect of capping agents on the final nanoparticle morphology, nature of the catalytic centers among other uses.

In a second stage, the thesis focuses on the IrO_2-water interface involving both extended surfaces and nanoparticles, as starting point of the oxygen evolution reaction. The four main crystallographic surfaces were taken into account as well as the representative $(IrO_2)_{33}$) nanoparticle model. Different water coverages were considered starting from isolated water molecules up to water monolayer. Results show that the water-IrO_2 interaction strength as well as the degree of dissociated water depend on three main factors: (i) the acidity and the basicity of the Ir and O centers, (ii) cooperative effects between adsorbed water molecules and (iii) thermal effects. Remarkably, the acidity and basicity of Ir and O, respectively are conditioned by the coordination, the type of vacancy and the dimensionality of the model. Moreover, the formation of hydrogen bonding between adsorbed water molecules tends to weaken the water-material interaction and favor 50% of dissociation, but this is significantly influenced by the material morphology. Finally, thermal effects weaken the material-water interactions, which is associated with a smaller degree of water dissociation. These effects apply to both the extended surfaces and the nanoparticle model, however subtle differences between the different models are observed and, particularly

IrO_2 on the nanoparticle shows a larger ionic character that tends to increase the IrO_2-H_2O interaction and the degree of H_2O dissociation in the majority of centers.

The last part of the thesis focuses on the oxygen evolution reaction (OER) itself. Again, the four main crystallographic surfaces and six different active sites on the $(IrO_2)_{33}$ nanoparticle model were taken into account. The two most commonly proposed mechanisms (water nucleophilic attack and oxo-coupling) were explored including the energy barriers of the key chemical steps. Results suggest that the two mechanisms implies the homolytic coupling of radical species and they are promoted by the presence of radical oxyl species on the surface. This has been described for homogeneous catalysts, but it has been eluded for IrO_2. Hence, computational approaches capable of representing radical species, like spin-polarized DFT, should be used to study this type of reactions. Regarding the preferred OER mechanism, our results shows that WNA mechanism is more favorable for the majority of tested sites on surfaces and nanoparticles. Indeed, the I2M mechanism requires well-oriented oxyl radicals to be competitive with WNA, something that only occurs on the (011) facet. Among the studied sites, the four coordinated centers with two equatorial vacancies present the highest reactivity requiring lower overpotentials to evolve oxygen from water. Indeed, the tip center can be considered as a very promising catalyst with very low overpotentials. These findings can be used to enhance the performance of IrO_2 nanoparticles for OER reaction by maximizing the presence of four coordinated centers.

The here summarized conclusions and the expertise acquired along

the thesis pave the way for future work both for proposing new materials with improved catalytic activities for the OER as well as for the modelling of nanoparticles. Regarding the OER catalytic activity, the knowledge acquired on the influence of the metal coordination and the acidity and basicity of surface metal and anion atoms should allow the design of hybrid materials, such as core-shell nanoparticles with tuned surface properties in the appropriate manner that could decrease the overpotentials.

On the other hand, the use of large and realistic nanoparticle models with the methodology used along the thesis increases the computational cost significantly preventing the computation of even middle size nanoparticle models. Therefore, the appropriate strategy appears to be the use of relatively small models, including the most relevant sites on the nanoparticle in combination with extended surfaces. This allows identifying key sites on the nanoparticle and evaluate the differences between the two systems. Bigger models can be used for further statistical treatment allowing to determine the percentage of each catalytic site as a function of the nanoparticle size and shape. In a recent future, it would be desirable to define cost-efficient strategies, probably by the use of machine learning, to include in this statistical treatment the effect on the electronic structure originated from size increase and morphology modifications.

Bibliography

(1) Cheng, K.-T. In *Proceedings International Test Conference 1998 (IEEE Cat. No. 98CH36270)*, 1998, pp 1157–1161.

(2) Doll, K.; Schön, J. C.; Jansen, M. Ab initio energy landscape of LiF clusters. *J. Chem. Phys.* **2010**, *133*, 024107.

(3) Bromley, S.; Flikkema, E. Columnar-to-disk structural transition in nanoscale (SiO2)N clusters. *Phys. Rev. Lett.* **2005**, *95*.

(4) Kleis, J.; Greeley, J.; Romero, N. A.; Morozov, V. A.; Falsig, H.; Larsen, A. H.; Lu, J.; Mortensen, J. J.; Dułak, M.; Thygesen, K. S.; Nørskov, J. K.; Jacobsen, K. W. Finite Size Effects in Chemical Bonding: From Small Clusters to Solids. *Catal. Lett.* **2011**, *141*, 1067–1071.

(5) Viñes, F., *Chapter 2 - Simulating heterogeneous catalysis on metallic nanoparticles: From under-coordinated sites to extended facets*; Bromley, S. T., Woodley, S. M., Eds.; Frontiers of Nanoscience, Vol. 12; Elsevier: 2018, pp 101 –128.

(6) Roldán, A.; González, S.; Ricart, J. M.; Illas, F. Critical Size for O2 Dissociation by Au Nanoparticles. *ChemPhysChem* **2009**, *10*, 348–351.

(7) Viñes, F.; Lykhach, Y.; Staudt, T.; Lorenz, M. P. A.; Papp, C.; Steinrück, H.-P.; Libuda, J.; Neyman, K. M.; Görling, A. Methane Activation by Platinum: Critical Role of Edge and Corner

Sites of Metal Nanoparticles. *Chemistry – A European Journal* **2010**, *16*, 6530–6539.

(8) Roldán, A.; Ricart, J. M.; Illas, F. Origin of the size dependence of Au nanoparticles toward molecular oxygen dissociation. *Theor. Chem. Acc.* **2011**, *128*, 675–681.

(9) Viñes, F.; Gomes, J. R. B.; Illas, F. Understanding the reactivity of metallic nanoparticles: beyond the extended surface model for catalysis. *Chem. Soc. Rev.* **2014**, *43*, 4922–4939.

(10) Kozlov, S. M.; Neyman, K. M. Insights from methane decomposition on nanostructured palladium. *J. Catal.* **2016**, *337*, 111 –121.

(11) Valden, M.; Lai, X.; Goodman, D. W. Onset of Catalytic Activity of Gold Clusters on Titania with the Appearance of Nonmetallic Properties. *Science* **1998**, *281*, 1647–1650.

(12) Fajín, J. L. C.; Bruix, A.; Cordeiro, M. N.D. S.; Gomes, J. R. B.; Illas, F. Density functional theory model study of size and structure effects on water dissociation by platinum nanoparticles. *J. Chem. Phys.* **2012**, *137*, 034701.

(13) Polarz, S. Shape Matters: Anisotropy of the Morphology of Inorganic Colloidal Particles – Synthesis and Function. *Adv. Funct. Mater.* **2011**, *21*, 3214–3230.

(14) Altavilla, C.; Ciliberto, E., *Inorganic nanoparticles: synthesis, applications, and perspectives*; CRC Press: 2017.

(15) Nguyen, T.-D. From formation mechanisms to synthetic methods toward shape-controlled oxide nanoparticles. *Nanoscale* **2013**, *5*, 9455–9482.

(16) *Nanoscience, Volume 1: Nanostructures through Chemistry*; O'Brien, P., Ed.; SPR - Nanoscience; The Royal Society of Chemistry: 2012, P001–286.

(17) LaMer, V. K.; Dinegar, R. H. Theory, Production and Mechanism of Formation of Monodispersed Hydrosols. *J. Am. Chem. Soc.* **1950**, *72*, 4847–4854.

(18) Murray, C. B.; Norris, D. J.; Bawendi, M. G. Synthesis and characterization of nearly monodisperse CdE (E = sulfur, selenium, tellurium) semiconductor nanocrystallites. *J. Am. Chem. Soc.* **1993**, *115*, 8706–8715.

(19) Jun, Y.-w.; Casula, M. F.; Sim, J.-H.; Kim, S. Y.; Cheon, J.; Alivisatos, A. P. Surfactant-Assisted Elimination of a High Energy Facet as a Means of Controlling the Shapes of TiO2 Nanocrystals. *J. Am. Chem. Soc.* **2003**, *125*, 15981–15985.

(20) Jang, E.; Won, J.-H.; Hwang, S.-J.; Choy, J.-H. Fine Tuning of the Face Orientation of ZnO Crystals to Optimize Their Photocatalytic Activity. *Advanced Materials* **2006**, *18*, 3309–3312.

(21) Sekerka, R. F. Equilibrium and growth shapes of crystals: how do they differ and why should we care? *Cryst. Res. Technol.* **2005**, *40*, 291–306.

(22) Nguyen, T.-D.; Dinh, C.-T.; Nguyen, D.-T.; Do, T.-O. A Novel Approach for Monodisperse Samarium Orthovanadate Nanocrystals: Controlled Synthesis and Characterization. *J. Phys. Chem. C* **2009**, *113*, 18584–18595.

(23) Zhao, N.; Nie, W.; Liu, X.; Tian, S.; Zhang, Y.; Ji, X. Shape- and Size-Controlled Synthesis and Dependent Magnetic Properties of Nearly Monodisperse Mn3O4 Nanocrystals. *Small* **2008**, *4*, 77–81.

(24) Hoertz, P. G.; Kim, Y.-I.; Youngblood, W. J.; Mallouk, T. E. Bidentate Dicarboxylate Capping Groups and Photosensitizers Control the Size of IrO2 Nanoparticle Catalysts for Water Oxidation. *The Journal of Physical Chemistry B* **2007**, *111*, 6845–6856.

(25) Sayle, T. X. T.; Molinari, M.; Das, S.; Bhatta, U. M.; Möbus, G.; Parker, S. C.; Seal, S.; Sayle, D. C. Environment-mediated structure, surface redox activity and reactivity of ceria nanoparticles. *Nanoscale* **2013**, *5*, 6063–6073.

(26) Tang, C.; Spencer, M. J. S.; Barnard, A. S. Activity of ZnO polar surfaces: an insight from surface energies. *Phys. Chem. Chem. Phys.* **2014**, *16*, 22139–22144.

(27) Mourdikoudis, S.; Pallares, R.; Thanh, N. Characterization techniques for nanoparticles: Comparison and complementarity upon studying nanoparticle properties. *Nanoscale* **2018**, *10*, 12871–12934.

(28) Titus, D.; Samuel, E.; Roopan, S. Chapter 12 - nanoparticle characterization techniques. *Green Synthesis, Characterization and Applications of Nanoparticles Book* **2019**, 303–319.

(29) Nakamura, E.; Sommerdijk, N. A.J. M.; Zheng, H. Transmission Electron Microscopy for Chemists. *Acc. Chem. Res.* **2017**, *50*, 1795–1796.

(30) Buhr, E; Senftleben, N; Klein, T; Bergmann, D; Gnieser, D; Frase, C. G.; Bosse, H Characterization of nanoparticles by scanning electron microscopy in transmission mode. *Meas. Sci. Technol.* **2009**, *20*, 084025.

(31) Seo, Y.; Jhe, W. Atomic force microscopy and spectroscopy. *Rep. Prog. Phys.* **2007**, *71*, 016101.

(32) Eaton, P.; Quaresma, P.; Soares, C.; Neves, C.; de Almeida, M.; Pereira, E.; West, P. A direct comparison of experimental methods to measure dimensions of synthetic nanoparticles. *Ultramicroscopy* **2017**, *182*, 179 –190.

(33) Dao, A. T. N.; Mott, D. M.; Maenosono, S. In *Handbook of Nanoparticles*, Aliofkhazraei, M., Ed.; Springer International Publishing: Cham, 2016, pp 217–244.

(34) Korin, E.; Froumin, N.; Cohen, S. Surface Analysis of Nanocomplexes by X-ray Photoelectron Spectroscopy (XPS). *ACS Biomaterials Science & Engineering* **2017**, *3*, 882–889.

(35) Als-Nielsen, J.; McMorrow, D., *Elements of modern X-ray physics*; John Wiley & Sons: 2011.

(36) Billinge, S.; Levin, I. The problem with determining atomic structure at the nanoscale. *Science* **2007**, *316*, 561–565.

(37) Gong, X.-Q.; Selloni, A.; Batzill, M.; Diebold, U. Steps on anatase TiO2(101). *Nat. Mater.* **2006**, *5*, 665–670.

(38) Weissenrieder, J.; Kaya, S.; Lu, J.-L.; Gao, H.-J.; Shaikhutdinov, S.; Freund, H.-J.; Sierka, M.; Todorova, T.; Sauer, J. Atomic structure of a thin silica film on a Mo(112) substrate: A two-dimensional network of SiO4 tetrahedra. *Phys. Rev. Lett.* **2005**, *95*.

(39) Tasker, P. W. The stability of ionic crystal surfaces. *J. Phys. C: Solid State Phys.* **1979**, *12*, 4977–4984.

(40) Noguera, C., *Physics and chemistry at oxide surfaces*; Cambridge University Press: 1996.

(41) Noguera, C. Polar oxide surfaces. *J. Phys.: Condens. Matter* **2000**, *12*, R367–R410.

(42) Goniakowski, J.; Finocchi, F.; Noguera, C. Polarity of oxide surfaces and nanostructures. *Rep. Prog. Phys.* **2007**, *71*, 016501.

(43) Honkala, K.; Hellman, A.; Remediakis, I. N.; Logadottir, A.; Carlsson, A.; Dahl, S.; Christensen, C. H.; Nørskov, J. K. Ammonia Synthesis from First-Principles Calculations. *Science* **2005**, *307*, 555–558.

(44) Jacobsen, C. J.; Dahl, S.; Hansen, P. L.; Törnqvist, E.; Jensen, L.; Topsøe, H.; Prip, D. V.; Møenshaug, P. B.; Chorkendorff, I. Structure sensitivity of supported ruthenium catalysts for ammonia synthesis. *J. Mol. Catal. A: Chem.* **2000**, *163*, 19–26.

(45) Chen, M.; Felmy, A.; Dixon, D. Structures and stabilities of (MgO)n nanoclusters. *J. Phys. Chem. A* **2014**, *118*, 3136–3146.

(46) Lamiel-Garcia, O.; Cuko, A.; Calatayud, M.; Illas, F.; Bromley, S. Predicting size-dependent emergence of crystallinity in nanomaterials: Titania nanoclusters: Versus nanocrystals. *Nanoscale* **2017**, *9*, 1049–1058.

(47) Chen, M.; Dixon, D. Machine-Learning Approach for the Development of Structure-Energy Relationships of ZnO Nanoparticles. *J. Phys. Chem. C* **2018**, *122*, 18621–18639.

(48) Guo, H.; Barnard, A. Thermodynamic modelling of nanomorphologies of hematite and goethite. *J. Mater. Chem.* **2011**, *21*, 11566–11577.

(49) Lamiel-Garcia, O.; Ko, K.; Lee, J.; Bromley, S.; Illas, F. When Anatase Nanoparticles Become Bulklike: Properties of Realistic TiO2 Nanoparticles in the 1-6 nm Size Range from All Electron Relativistic Density Functional Theory Based Calculations. *J. Chem. Theory Comput.* **2017**, *13*, 1785–1793.

(50) Bruno, M.; Massaro, F.; Prencipe, M.; Demichelis, R.; De La Pierre, M.; Nestola, F. Ab initio calculations of the main crystal surfaces of forsterite (Mg 2SiO4): A preliminary study to understand the nature of geochemical processes at the olivine interface. *J. Phys. Chem. C* **2014**, *118*, 2498–2506.

(51) Ringe, E.; Van Duyne, R.; Marks, L. Wulff construction for alloy nanoparticles. *Nano Lett.* **2011**, *11*, 3399–3403.

(52) Johnston, R. L. Evolving better nanoparticles: Genetic algorithms for optimising cluster geometries. *Dalton Trans.* **2003**, 4193–4207.

(53) Wales, D. J.; Scheraga, H. A. Global Optimization of Clusters, Crystals, and Biomolecules. *Science* **1999**, *285*, 1368–1372.

(54) Call, S. T.; Zubarev, D. Y.; Boldyrev, A. I. Global minimum structure searches via particle swarm optimization. *J. Comput. Chem.* **2007**, *28*, 1177–1186.

(55) Zhang, J.; Dolg, M. ABCluster: the artificial bee colony algorithm for cluster global optimization. *Phys. Chem. Chem. Phys.* **2015**, *17*, 24173–24181.

(56) Kirkpatrick, S.; Gelatt, C. D.; Vecchi, M. P. Optimization by Simulated Annealing. *Science* **1983**, *220*, 671–680.

(57) Goedecker, S. Minima hopping: An efficient search method for the global minimum of the potential energy surface of complex molecular systems. *J. Chem. Phys.* **2004**, *120*, 9911–9917.

(58) Spanó, E.; Hamad, S.; Catlow, C. Computational Evidence of Bubble ZnS Clusters. *J. Phys. Chem. B* **2003**, *107*, 10337–10340.

(59) Woodley, S.; Sokol, A.; Catlow, C. Structure prediction of inorganic nanoparticles with predefined architecture using a genetic algorithm. *Z. Anorg. Allg. Chem.* **2004**, *630*, 2343–2353.

(60) Woodley, S. Structure Prediction of Ternary Oxide Sub-Nanoparticles. *Mater. Manuf. Processes* **2009**, *24*, 255–264.

(61) Haertelt, M.; Fielicke, A.; Meijer, G.; Kwapien, K.; Sierka, M.; Sauer, J. Structure determination of neutral MgO clusters—hexagonal nanotubes and cages. *Phys. Chem. Chem. Phys.* **2012**, *14*, 2849–2856.

(62) Lazauskas, T.; Sokol, A. A.; Woodley, S. M. An efficient genetic algorithm for structure prediction at the nanoscale. *Nanoscale* **2017**, *9*, 3850–3864.

(63) Farrow, M. R.; Chow, Y.; Woodley, S. M. Structure prediction of nanoclusters; a direct or a pre-screened search on the DFT energy landscape? *Phys. Chem. Chem. Phys.* **2014**, *16*, 21119–21134.

(64) Viñes, F.; Lamiel-Garcia, O.; Illas, F.; Bromley, S. T. Size dependent structural and polymorphic transitions in ZnO: from nanocluster to bulk. *Nanoscale* **2017**, *9*, 10067–10074.

(65) Rahm, J.; Erhart, P. Beyond Magic Numbers: Atomic Scale Equilibrium Nanoparticle Shapes for Any Size. *Nano Lett.* **2017**, *17*, 5775–5781.

(66) Cleveland, C.; Landman, U. The energetics and structure of nickel clusters: Size dependence. *J. Chem. Phys.* **1991**, *94*, 7376–7396.

(67) Barnard, A. A thermodynamic model for the shape and stability of twinned nanostructures. *J. Phys. Chem. B* **2006**, *110*, 24498–24504.

(68) Marks, L. Modified Wulff constructions for twinned particles. *J. Cryst. Growth* **1983**, *61*, 556–566.

(69) Marks, L.; Peng, L. Nanoparticle shape, thermodynamics and kinetics. *Journal of Physics Condensed Matter* **2016**, *28*.

(70) Wang, Y.; He, J.; Liu, C.; Chong, W.; Chen, H. Thermodynamics versus kinetics in Nanosynthesis. *Angewandte Chemie - International Edition* **2015**, *54*, 2022–2051.

(71) Barmparis, G. D.; Lodziana, Z.; Lopez, N.; Remediakis, I. N. Nanoparticle shapes by using Wulff constructions and first-principles calculations. *Beilstein J. Nanotechnol.* **2015**, *6*, 361–368.

(72) Novell-Leruth, G.; Carchini, G.; López, N. On the properties of binary rutile MO2 compounds, M = Ir, Ru, Sn, and Ti: A DFT study. *J. Chem. Phys.* **2013**, *138*, 194706.

(73) Hjorth Larsen, A. et al. The atomic simulation environment - A Python library for working with atoms. *Journal of Physics Condensed Matter* **2017**, *29*.

(74) Mathew, K.; Singh, A.; Gabriel, J.; Choudhary, K.; Sinnott, S.; Davydov, A.; Tavazza, F.; Hennig, R. MPInterfaces: A Materials Project based Python tool for high-throughput computational screening of interfacial systems. *Comput. Mater. Sci* **2016**, *122*, 183–190.

(75) Momma, K.; Izumi, F. VESTA 3 for three-dimensional visualization of crystal, volumetric and morphology data. *J. Appl. Crystallogr.* **2011**, *44*, 1272–1276.

(76) Dovesi, R.; Orlando, R.; Erba, A.; Zicovich-Wilson, C.; Civalleri, B.; Casassa, S.; Maschio, L.; Ferrabone, M.; De La Pierre, M.; D'Arco, P.; Noël, Y.; Causà, M.; Rérat, M.; Kirtman, B.

CRYSTAL14: A program for the ab initio investigation of crystalline solids. *Int. J. Quantum Chem.* **2014**, *114*, 1287–1317.

(77) Chatzigoulas, A.; Karathanou, K.; Dellis, D.; Cournia, Z. NanoCrystal: A Web-Based Crystallographic Tool for the Construction of Nanoparticles Based on Their Crystal Habit. *J. Chem. Inf. Model.* **2018**, *58*, 2380–2386.

(78) Diebold, U.; Li, S.-C.; Schmid, M. Oxide surface science. *Annu. Rev. Phys. Chem.* **2010**, *61*, 129–148.

(79) Andersen, T.; Fong, D.; Marks, L. Pauling's rules for oxide surfaces. *Surf. Sci. Rep.* **2018**, *73*, 213–232.

(80) Reier, T.; Nong, H. N.; Teschner, D.; Schlögl, R.; Strasser, P. Electrocatalytic Oxygen Evolution Reaction in Acidic Environments – Reaction Mechanisms and Catalysts. *Adv. Energy Mater.* **2017**, *7*, 1601275.

(81) Carmo, M.; Fritz, D. L.; Mergel, J.; Stolten, D. A comprehensive review on PEM water electrolysis. *Int. J. Hydrogen Energy* **2013**, *38*, 4901 –4934.

(82) Danilovic, N.; Subbaraman, R.; Chang, K.-C.; Chang, S. H.; Kang, Y. J.; Snyder, J.; Paulikas, A. P.; Strmcnik, D.; Kim, Y.-T.; Myers, D., et al. Activity–stability trends for the oxygen evolution reaction on monometallic oxides in acidic environments. *J. Phys. Chem. Lett.* **2014**, *5*, 2474–2478.

(83) Rossmeisl, J.; Qu, Z.-W.; Zhu, H; Kroes, G.-J.; Nørskov, J. K. Electrolysis of water on oxide surfaces. *J. Electroanal. Chem.* **2007**, *607*, 83–89.

(84) Man, I. C.; Su, H.-Y.; Calle-Vallejo, F.; Hansen, H. A.; Martínez, J. I.; Inoglu, N. G.; Kitchin, J.; Jaramillo, T. F.; Nørskov, J. K.;

Rossmeisl, J. Universality in oxygen evolution electrocatalysis on oxide surfaces. *ChemCatChem* **2011**, *3*, 1159–1165.

(85) Xu, Z.; Rossmeisl, J.; Kitchin, J. R. A Linear Response DFT+U Study of Trends in the Oxygen Evolution Activity of Transition Metal Rutile Dioxides. *J. Phys. Chem. C* **2015**, *119*, 4827–4833.

(86) Ping, Y.; Galli, G.; Goddard III, W. A. Electronic structure of IrO2: the role of the metal d orbitals. *J. Phys. Chem. C* **2015**, *119*, 11570–11577.

(87) Gauthier, J. A.; Dickens, C. F.; Chen, L. D.; Doyle, A. D.; Norskov, J. K. Solvation Effects for Oxygen Evolution Reaction Catalysis on IrO2(110). *J. Phys. Chem. C* **2017**, *121*, 11455–11463.

(88) Dickens, C. F.; Kirk, C.; Nørskov, J. K. Insights into the Electrochemical Oxygen Evolution Reaction with ab Initio Calculations and Microkinetic Modeling: Beyond the Limiting Potential Volcano. *J. Phys. Chem. C* **2019**, *123*, 18960–18977.

(89) Nakagawa, T.; Beasley, C. A.; Murray, R. W. Efficient Electro-Oxidation of Water near Its Reversible Potential by a Mesoporous IrOx Nanoparticle Film. *J. Phys. Chem. C* **2009**, *113*, 12958–12961.

(90) Oh, H.-S.; Nong, H. N.; Reier, T.; Bergmann, A.; Gliech, M.; Ferreira de Araújo, J.; Willinger, E.; Schlögl, R.; Teschner, D.; Strasser, P. Electrochemical Catalyst–Support Effects and Their Stabilizing Role for IrOx Nanoparticle Catalysts during the Oxygen Evolution Reaction. *J. Am. Chem. Soc.* **2016**, *138*, 12552–12563.

(91) Abbott, D. F.; Lebedev, D.; Waltar, K.; Povia, M.; Nachtegaal, M.; Fabbri, E.; Copéret, C.; Schmidt, T. J. Iridium Oxide for

the Oxygen Evolution Reaction: Correlation between Particle Size, Morphology, and the Surface Hydroxo Layer from Operando XAS. *Chem. Mater.* **2016**, *28*, 6591–6604.

(92) Cheng, J.; Yang, J.; Kitano, S.; Juhasz, G.; Higashi, M.; Sadakiyo, M.; Kato, K.; Yoshioka, S.; Sugiyama, T.; Yamauchi, M.; Nakashima, N. Impact of Ir-Valence Control and Surface Nanostructure on Oxygen Evolution Reaction over a Highly Efficient Ir–TiO2 Nanorod Catalyst. *ACS Catal.* **2019**, *9*, 6974–6986.

(93) Spöri, C.; Briois, P.; Nong, H. N.; Reier, T.; Billard, A.; Kühl, S.; Teschner, D.; Strasser, P. Experimental Activity Descriptors for Iridium-Based Catalysts for the Electrochemical Oxygen Evolution Reaction (OER). *ACS Catal.* **2019**, *9*, 6653–6663.

(94) Willinger, E.; Massué, C.; Schlögl, R.; Willinger, M. G. Identifying Key Structural Features of IrOx Water Splitting Catalysts. *J. Am. Chem. Soc.* **2017**, *139*, 12093–12101.

(95) Kasian, O.; Geiger, S.; Li, T.; Grote, J.-P.; Schweinar, K.; Zhang, S.; Scheu, C.; Raabe, D.; Cherevko, S.; Gault, B.; Mayrhofer, K. J. J. Degradation of iridium oxides via oxygen evolution from the lattice: correlating atomic scale structure with reaction mechanisms. *Energy Environ. Sci.* **2019**, *12*, 3548–3555.

(96) Povia, M.; Abbott, D. F.; Herranz, J.; Heinritz, A.; Lebedev, D.; Kim, B.-J.; Fabbri, E.; Patru, A.; Kohlbrecher, J.; Schäublin, R.; Nachtegaal, M.; Copéret, C.; Schmidt, T. J. Operando X-ray characterization of high surface area iridium oxides to decouple their activity losses for the oxygen evolution reaction. *Energy Environ. Sci.* **2019**, *12*, 3038–3052.

(97) Fierro, S.; Nagel, T.; Baltruschat, H.; Comninellis, C. Investigation of the oxygen evolution reaction on Ti/IrO2 electrodes

using isotope labelling and on-line mass spectrometry. *Electrochem. Commun.* **2007**, *9*, 1969 –1974.

(98) Sanchez Casalongue, H. G.; Ng, M. L.; Kaya, S.; Friebel, D.; Ogasawara, H.; Nilsson, A. In Situ Observation of Surface Species on Iridium Oxide Nanoparticles during the Oxygen Evolution Reaction. *Angew. Chem. Int. Ed.* **2014**, *53*, 7169–7172.

(99) Pfeifer, V. et al. The electronic structure of iridium and its oxides. *Surf. Interface Anal.* **2016**, *48*, 261–273.

(100) Pfeifer, V. et al. The electronic structure of iridium oxide electrodes active in water splitting. *Phys. Chem. Chem. Phys.* **2016**, *18*, 2292–2296.

(101) Minguzzi, A.; Lugaresi, O.; Achilli, E.; Locatelli, C.; Vertova, A.; Ghigna, P.; Rondinini, S. Observing the oxidation state turnover in heterogeneous iridium-based water oxidation catalysts. *Chem. Sci.* **2014**, *5*, 3591–3597.

(102) Sivasankar, N.; Weare, W. W.; Frei, H. Direct Observation of a Hydroperoxide Surface Intermediate upon Visible Light-Driven Water Oxidation at an Ir Oxide Nanocluster Catalyst by Rapid-Scan FT-IR Spectroscopy. *J. Am. Chem. Soc.* **2011**, *133*, 12976–12979.

(103) Kuo, D.-Y.; Kawasaki, J. K.; Nelson, J. N.; Kloppenburg, J.; Hautier, G.; Shen, K. M.; Schlom, D. G.; Suntivich, J. Influence of Surface Adsorption on the Oxygen Evolution Reaction on IrO2(110). *J. Am. Chem. Soc.* **2017**, *139*, 3473–3479.

(104) Ping, Y.; Nielsen, R. J.; Goddard, W. A. The Reaction Mechanism with Free Energy Barriers at Constant Potentials for the Oxygen Evolution Reaction at the IrO2 (110) Surface. *J. Am. Chem. Soc.* **2017**, *139*, 149–155.

(105) Stoerzinger, K. A.; Qiao, L.; Biegalski, M. D.; Shao-Horn, Y. Orientation-Dependent Oxygen Evolution Activities of Rutile IrO2 and RuO2. *The Journal of Physical Chemistry Letters* **2014**, *5*, 1636–1641.

(106) Seitz, L. C.; Dickens, C. F.; Nishio, K.; Hikita, Y.; Montoya, J.; Doyle, A.; Kirk, C.; Vojvodic, A.; Hwang, H. Y.; Norskov, J. K.; Jaramillo, T. F. A highly active and stable IrOx/SrIrO3 catalyst for the oxygen evolution reaction. *Science* **2016**, *353*, 1011–1014.

(107) Stoerzinger, K. A.; Diaz-Morales, O.; Kolb, M.; Rao, R. R.; Frydendal, R.; Qiao, L.; Wang, X. R.; Halck, N. B.; Rossmeisl, J.; Hansen, H. A.; Vegge, T.; Stephens, I. E. L.; Koper, M. T. M.; Shao-Horn, Y. Orientation-Dependent Oxygen Evolution on RuO2 without Lattice Exchange. *ACS Energy Letters* **2017**, *2*, 876–881.

(108) Rao, R. R.; Kolb, M. J.; Giordano, L.; Pedersen, A. F.; Katayama, Y.; Hwang, J.; Mehta, A.; You, H.; Lunger, J. R.; Zhou, H., et al. Operando identification of site-dependent water oxidation activity on ruthenium dioxide single-crystal surfaces. *Nature Catalysis* **2020**, *3*, 1–10.

(109) Schrödinger, E. An Undulatory Theory of the Mechanics of Atoms and Molecules. *Phys. Rev.* **1926**, *28(6)*, 1049–1070.

(110) Hartree, D. R. The Wave Mechanics of an Atom with a Non-Coulomb Central Field. Part I. Theory and Methods. *Math. Proc. Cambridge* **1928**, *24 (1)*, 89–110.

(111) Hartree, D. R. The Wave Mechanics of an Atom with a Non-Coulomb Central Field. Part II. Some Results and Discussion. *Math. Proc. Cambridge* **1928**, *24 (1)*, 111–132.

(112) Hartree, D. R. The Wave Mechanics of an Atom with a Non-Coulomb Central Field. Part III. Term Values and Intensities in Series in Optical Spectra. *Math. Proc. Cambridge* **1928**, *24 (3)*, 426–437.

(113) Slater, J. C. Note on Hartree'e Method. *Phys. Rev.* **1930**, *35*, 210–211.

(114) Szabo, A.; Ostlund, N. S., *Modern quantum chemistry: introduction to advanced electronic structure theory*; Courier Corporation: 2012.

(115) Hohenberg, P.; Kohn, W. Inhomogeneous Electron Gas. *Phys. Rev.* **1964**, *136(3B)*, B864–B871.

(116) Kohn, W.; Sham, L. J. Self-Consistent Equations Including Exchange and Correlation Effects. *Phys. Rev.* **1965**, *140(4A)*, A1133–A1138.

(117) Von Barth, U.; Hedin, L. A local exchange-correlation potential for the spin polarized case. I. *J. Phys. C: Solid State Phys.* **1972**, *5*, 1629–1642.

(118) Gunnarsson, O.; Lundqvist, B. I. Exchange and correlation in atoms, molecules, and solids by the spin-density-functional formalism. *Phys. Rev. B* **1976**, *13*, 4274–4298.

(119) Perdew, J.; Ruzsinszky, A.; Constantin, L.; Sun, J.; Csonka, G. Some fundamental issues in ground-state density functional theory: A guide for the perplexed. *J. Chem. Theory Comput.* **2009**, *5*, 902–908.

(120) Jacob, C. R.; Reiher, M. Spin in density-functional theory. *International Journal of Quantum Chemistry* **2012**, *112*, 3661–3684.

(121) Dirac, P. A. M. Note on Exchange Phenomena in the Thomas Atom. *Math. Proc. Cambridge* **1930**, *26 (3)*, 376–385.

(122) Perdew, J. P.; Zunger, A. Self-interaction correction to density-functional approximations for many-electron systems. *Phys. Rev. B* **1981**, *23*, 5048–5079.

(123) Perdew, J. P.; Wang, Y. Accurate and simple analytic representation of the electron-gas correlation energy. *Phys. Rev. B* **1992**, *45*, 13244–13249.

(124) Perdew, J.; Burke, K.; Ernzerhof, M. Generalized gradient approximation made simple. *Phys. Rev. Lett.* **1996**, *77*, 3865–3868.

(125) Van Voorhis, T.; Scuseria, G. A novel form for the exchange-correlation energy functional. *J. Chem. Phys.* **1998**, *109*, 400–410.

(126) Grimme, S. Accurate Description of Van der Walls Complexes by Density Functional Theory Including Empirical Corrections. *J. Comput. Chem.* **2004**, *25*, 1463–1473.

(127) Grimme, S. Semiempirical GGa-Type Density Functional Constructed with a Long-Range Dispersion Correction. *J. Comput. Chem.* **2006**, *27*, 1787–1799.

(128) Grimme, S.; Ehrlich, S.; Goerigk, L. Effect of the Damping Function in Dispersion Corrected Density Functional Theory. *J. Comput. Chem.* **2011**, *32*, 1456–1465.

(129) Cottenier, S. et al. Density Functional Theory and the family of (L) APW-methods: a step-by-step introduction. *Instituut voor Kern-en Stralingsfysica, KU Leuven, Belgium* **2002**, *4*, 41.

(130) Blöchl, P. Projector augmented-wave method. *Phys. Rev. B* **1994**, *50*, 17953–17979.

(131) Vanderbilt, D. Soft self-consistent pseudopotentials in a generalized eigenvalue formalism. *Phys. Rev. B* **1990**, *41*, 7892–7895.

(132) Brillouin, L. Les électrons dans les métaux et le classement des ondes de de Broglie correspondantes. *Comptes Rendus Hebdomadaires des Séances de l'Académie des Sciences* **1930**, *191*, 292.

(133) Monkhorst, H. J.; Pack, J. D. Special Points for Brillouin-Zone Investigations. *Phys. Rev. B* **1976**, *13 (12)*, 5188–5192.

(134) Martin, R. M.; Martin, R. M., *Electronic structure: basic theory and practical methods*; Cambridge university press: 2004.

(135) Kohanoff, J., *Electronic structure calculations for solids and molecules: theory and computational methods*; Cambridge University Press: 2006.

(136) Lee, J. G., *Computational materials science: an introduction*; Crc Press: 2016.

(137) Dupont, C.; Andreussi, O.; Marzari, N. Self-consistent continuum solvation (SCCS): The case of charged systems. *J. Chem. Phys.* **2013**, *139*, 214110.

(138) Ismail-Beigi, S.; Arias, T. New algebraic formulation of density functional calculation. *Comput. Phys. Commun.* **2000**, *128*, 1–45.

(139) Fattebert, J.-L.; Gygi, F. First-principles molecular dynamics simulations in a continuum solvent. *Int. J. Quantum Chem.* **2003**, *93*, 139–147.

(140) Petrosyan, S.; Rigos, A.; Arias, T. Joint density-functional theory: Ab initio study of Cr_2O_3 surface chemistry in solution. *J. Phys. Chem. B* **2005**, *109*, 15436–15444.

(141) Petrosyan, S.; Briere, J.-F.; Roundy, D.; Arias, T. Joint density-functional theory for electronic structure of solvated systems. *Phys. Rev. B* **2007**, *75*.

(142) Letchworth-Weaver, K.; Arias, T. Joint density functional theory of the electrode-electrolyte interface: Application to fixed electrode potentials, interfacial capacitances, and potentials of zero charge. *Physical Review B - Condensed Matter and Materials Physics* **2012**, *86*.

(143) Schwarz, K.; Sundararaman, R.; Letchworth-Weaver, K.; Arias, T.; Hennig, R. Framework for solvation in quantum Monte Carlo. *Physical Review B - Condensed Matter and Materials Physics* **2012**, *85*.

(144) Andreussi, O.; Dabo, I.; Marzari, N. Revised self-consistent continuum solvation in electronic-structure calculations. *J. Chem. Phys.* **2012**, *136*.

(145) Gunceler, D.; Letchworth-Weaver, K.; Sundararaman, R.; Schwarz, K.; Arias, T. The importance of nonlinear fluid response in joint density-functional theory studies of battery systems. *Modell. Simul. Mater. Sci. Eng.* **2013**, *21*.

(146) Mathew, K.; Sundararaman, R.; Letchworth-Weaver, K.; Arias, T.; Hennig, R. Implicit solvation model for density-functional study of nanocrystal surfaces and reaction pathways. *J. Chem. Phys.* **2014**, *140*.

(147) Mathew, K.; Kolluru, V. S. C.; Mula, S.; Steinmann, S. N.; Hennig, R. G. Implicit self-consistent electrolyte model in plane-wave density-functional theory. *J. Chem. Phys.* **2019**, *151*, 234101.

(148) Verlet, L. Computer "Experiments" on Classical Fluids. I. Thermodynamical Properties of Lennard-Jones Molecules. *Phys. Rev.* **1967**, *159 (1)*, 98–103.

(149) Verlet, L. Computer "Experiments" on Classical Fluids. II. Equilibrium Correlation Functions. *Phys. Rev.* **1968**, *165*, 201–214.

(150) Rahman, A. Correlations in the Motion of Atoms in Liquid Argon. *Phys. Rev.* **1964**, *136*, A405–A411.

(151) Car, R.; Parrinello, M. Unified Approach for Molecular Dynamics and Density-Functional Theory. *Phys. Rev. Lett.* **1985**, *55*, 2471–2474.

(152) Berendsen, H. J. C.; Postma, J. P. M.; van Gunsteren, W. F.; DiNola, A.; Haak, J. R. Molecular dynamics with coupling to an external bath. *J. Chem. Phys.* **1984**, *81*, 3684–3690.

(153) Nosé, S. A unified formulation of the constant temperature molecular dynamics methods. *J. Chem. Phys.* **1984**, *81*, 511–519.

(154) Kresse, G.; Hafner, J. Ab initio molecular dynamics for liquid metals. *Phys. Rev. B* **1993**, *47*, 558–561.

(155) Kresse, G.; Furthmüller, J. Efficient iterative schemes for ab initio total-energy calculations using a plane-wave basis set. *Physical Review B - Condensed Matter and Materials Physics* **1996**, *54*, 11169–11186.

(156) Kresse, G. From ultrasoft pseudopotentials to the projector augmented-wave method. *Phys. Rev. B* **1999**, *59*, 1758–1775.

(157) González, D.; Camino, B.; Heras-Domingo, J.; Rimola, A.; Rodríguez-Santiago, L.; Solans-Monfort, X.; Sodupe, M. BCN-M: A Free Computational Tool for Generating Wulff-like Nanoparticle

Models with Controlled Stoichiometry. *J. Phys. Chem. C* **2020**, *124*, 1227–1237.

(158) Mutaftschiev, B., *The atomistic nature of crystal growth*; Springer Science & Business Media: 2013; Vol. 43.

(159) Walt, S. v. d.; Colbert, S. C.; Varoquaux, G. The NumPy array: a structure for efficient numerical computation. *Computing in science & engineering* **2011**, *13*, 22–30.

(160) Oliphant, T. E. Python for scientific computing. *Computing in Science & Engineering* **2007**, *9*, 10–20.

(161) Ong, S. P.; Richards, W. D.; Jain, A.; Hautier, G.; Kocher, M.; Cholia, S.; Gunter, D.; Chevrier, V. L.; Persson, K. A.; Ceder, G. Python Materials Genomics (pymatgen): A robust, open-source python library for materials analysis. *Computational Materials Science* **2013**, *68*, 314–319.

(162) Simonov, K. PyYAML., 2014.

(163) Kittel, C.; McEuen, P.; McEuen, P., *Introduction to solid state physics*; Wiley New York: 1996; Vol. 8.

(164) González, D.; Heras-Domingo, J.; Pantaleone, S.; Rimola, A.; Rodríguez-Santiago, L.; Solans-Monfort, X.; Sodupe, M. Water Adsorption on MO2 (M = Ti, Ru, and Ir) Surfaces. Importance of Octahedral Distortion and Cooperative Effects. *ACS Omega* **2019**, *4*, 2989–2999.

(165) Pietrucci, F.; Andreoni, W. Graph Theory Meets Ab Initio Molecular Dynamics: Atomic Structures and Transformations at the Nanoscale. *Phys. Rev. Lett.* **2011**, *107*, 085504.

(166) Vázquez, S.; Otero, X.; Martinez-Nunez, E. A Trajectory-Based Method to Explore Reaction Mechanisms. *Molecules* **2018**, *23*, 3156.

(167) Trovarelli, A.; Llorca, J. Ceria Catalysts at Nanoscale: How Do Crystal Shapes Shape Catalysis? *ACS Catal.* **2017**, *7*, 4716–4735.

(168) Blatov, V. A. Voronoi–dirichlet polyhedra in crystal chemistry: theory and applications. *Crystallogr. Rev.* **2004**, *10*, 249–318.

(169) Diebold, U.; Koplitz, L. V.; Dulub, O. Atomic-scale properties of low-index ZnO surfaces. *Appl. Surf. Sci.* **2004**, *237*, 336 – 342.

(170) Wöll, C. The chemistry and physics of zinc oxide surfaces. *Prog. Surf. Sci.* **2007**, *82*, 55 –120.

(171) Heras-Domingo, J.; Sodupe, M.; Solans-Monfort, X. Interaction between Ruthenium Oxide Surfaces and Water Molecules. Effect of Surface Morphology and Water Coverage. *J. Phys. Chem. C* **2019**, *123*, 7786–7798.

(172) Xu, Z.; Kitchin, J. R. Relating the electronic structure and reactivity of the 3d transition metal monoxide surfaces. *Catal. Commun.* **2014**, *52*, 60 –64.

(173) Dickens, C. F.; Montoya, J. H.; Kulkarni, A. R.; Bajdich, M.; Nørskov, J. K. An electronic structure descriptor for oxygen reactivity at metal and metal-oxide surfaces. *Surf. Sci.* **2019**, *681*, 122 –129.

(174) Walter, M.; Warren, E.; McKone, J.; Boettcher, S.; Mi, Q.; Santori, E.; Lewis, N. Solar water splitting cells. *Chem. Rev.* **2010**, *110*, 6446–6473.

(175) Reier, T.; Oezaslan, M.; Strasser, P. Electrocatalytic oxygen evolution reaction (OER) on Ru, Ir, and pt catalysts: A comparative study of nanoparticles and bulk materials. *ACS Catal.* **2012**, *2*, 1765–1772.

(176) Suen, N.-T.; Hung, S.-F.; Quan, Q.; Zhang, N.; Xu, Y.-J.; Chen, H. Electrocatalysis for the oxygen evolution reaction: Recent development and future perspectives. *Chem. Soc. Rev.* **2017**, *46*, 337–365.

(177) Siahrostami, S.; Vojvodic, A. Influence of Adsorbed Water on the Oxygen Evolution Reaction on Oxides. *The Journal of Physical Chemistry C* **2015**, *119*, 1032–1037.

(178) Jaimes, R.; Vazquez-Arenas, J.; González, I.; Galván, M. Theoretical evidence of the relationship established between the HO[rad] radicals and H2O adsorptions and the electroactivity of typical catalysts used to oxidize organic compounds. *Electrochim. Acta* **2017**, *229*, 345–351.

(179) Diebold, U. Perspective: A controversial benchmark system for water-oxide interfaces: H2O/TiO2(110). *Journal of Chemical Physics* **2017**, *147*.

(180) Serrano, G.; Bonanni, B.; Di Giovannantonio, M.; Kosmala, T.; Schmid, M.; Diebold, U.; Di Carlo, A.; Cheng, J.; Vandevondele, J.; Wandelt, K.; Goletti, C. Molecular Ordering at the Interface between Liquid Water and Rutile TiO2(110). *Advanced Materials Interfaces* **2015**, *2*.

(181) Wang, Z.-T.; Wang, Y.-G.; Mu, R.; Yoon, Y.; Dahal, A.; Schenter, G.; Glezakou, V.-A.; Rousseau, R.; Lyubinetsky, I.; Dohnálek, Z. Probing equilibrium of molecular and deprotonated water on TiO2(110). *Proceedings of the National Academy of Sciences of the United States of America* **2017**, *114*, 1801–1805.

(182) Sun, C.; Liu, L.-M.; Selloni, A.; Lu, G.; Smith, S. Titania-water interactions: A review of theoretical studies. *Journal of Materials Chemistry* **2010**, *20*, 10319–10334.

(183) Balajka, J.; Aschauer, U.; Mertens, S.; Selloni, A.; Schmid, M.; Diebold, U. Surface Structure of TiO2 Rutile (011) Exposed to Liquid Water. *Journal of Physical Chemistry C* **2017**, *121*, 26424–26431.

(184) Mu, R.; Zhao, Z.-J.; Dohnálek, Z.; Gong, J. Structural motifs of water on metal oxide surfaces. *Chemical Society Reviews* **2017**, *46*, 1785–1806.

(185) Siahrostami, S.; Vojvodic, A. Influence of adsorbed water on the oxygen evolution reaction on oxides. *J. Phys. Chem. C* **2014**, *119*, 1032–1037.

(186) Zhang, Z.; Bondarchuk, O.; Kay, B.; White, J.; Dohnálek, Z. Imaging water dissociation on TiO2(110): Evidence for inequivalent geminate OH groups. *Journal of Physical Chemistry B* **2006**, *110*, 21840–21845.

(187) Bikondoa, O.; Pang, C.; Ithnin, R.; Muryn, C.; Onishi, H.; Thornton, G. Direct visualization of defect-mediated dissociation of water on TiO 2(110). *Nature Materials* **2006**, *5*, 189–192.

(188) Ketteler, G.; Yamamoto, S.; Bluhm, H.; Andersson, K.; Starr, D.; Ogletree, D.; Ogasawara, H.; Nilsson, A.; Salmeron, M. The nature of water nucleation sites on TiO2(110) surfaces revealed by ambient pressure X-ray photoelectron spectroscopy. *Journal of Physical Chemistry C* **2007**, *111*, 8278–8282.

(189) Björneholm, O.; Hansen, M.; Hodgson, A.; Liu, L.-M.; Limmer, D.; Michaelides, A.; Pedevilla, P.; Rossmeisl, J.; Shen, H.; Tocci, G.; Tyrode, E.; Walz, M.-M.; Werner, J.; Bluhm, H. Water at Interfaces. *Chemical Reviews* **2016**, *116*, 7698–7726.

(190) Mu, R.; Cantu, D.; Lin, X.; Glezakou, V.-A.; Wang, Z.; Lyubinetsky, I.; Rousseau, R.; Dohnálek, Z. Dimerization induced

deprotonation of water on RuO2(110). *Journal of Physical Chemistry Letters* **2014**, *5*, 3445–3450.

(191) Mu, R.; Cantu, D.; Glezakou, V.-A.; Lyubinetsky, I.; Rousseau, R.; Dohnálek, Z. Deprotonated Water Dimers: The Building Blocks of Segmented Water Chains on Rutile RuO2(110). *Journal of Physical Chemistry C* **2015**, *119*, 23552–23558.

(192) Nguyen, M.-T.; Mu, R.; Cantu, D.; Lyubinetsky, I.; Glezakou, V.-A.; Dohnálek, Z.; Rousseau, R. Dynamics, Stability, and Adsorption States of Water on Oxidized RuO2(110). *Journal of Physical Chemistry C* **2017**, *121*, 18505–18515.

(193) Rao, R. R.; Kolb, M. J.; Hwang, J.; Pedersen, A. F.; Mehta, A.; You, H.; Stoerzinger, K. A.; Feng, Z.; Zhou, H.; Bluhm, H.; Giordano, L.; Stephens, I. E. L.; Shao-Horn, Y. Surface Orientation Dependent Water Dissociation on Rutile Ruthenium Dioxide. *The Journal of Physical Chemistry C* **2018**, *122*, 17802–17811.

(194) Lobo, A.; Conrad, H. Interaction of H2O with the RuO2(1 1 0) surface studied by HREELS and TDS. *Surface Science* **2003**, *523*, 279–286.

(195) Hummer, D. R.; Kubicki, J. D.; Kent, P. R. C.; Heaney, P. J. Single-Site and Monolayer Surface Hydration Energy of Anatase and Rutile Nanoparticles Using Density Functional Theory. *J. Phys. Chem. C* **2013**, *117*, 26084–26090.

(196) Heras-Domingo, J. modeling of RuO_2 surfaces and nanoparticles: their potential use as catalysts for the oxygen evolution reaction., Ph.D. Thesis, Universidad Autónoma de Barcelona, 2020.

(197) Bolzan, A. A.; Fong, C.; Kennedy, B. J.; Howard, C. J. Structural Studies of Rutile-Type Metal Dioxides. *Acta Crystallographica Section B* **1997**, *53*, 373–380.

(198) Ryden, W.; Lawson, A. Magnetic Susceptibility of IrO2 and RuO2. *J. Chem. Phys.* **1970**, *52*, 6058–6061.

(199) Matz, O.; Calatayud, M. Periodic DFT Study of Rutile IrO2: Surface Reactivity and Catechol Adsorption. *J. Phys. Chem. C* **2017**, *121*, 13135–13143.

(200) Hammer, B.; Nørskov, J. Electronic factors determining the reactivity of metal surfaces. *Surf. Sci.* **1995**, *343*, 211–220.

(201) Frame, F. A.; Townsend, T. K.; Chamousis, R. L.; Sabio, E. M.; Dittrich, T.; Browning, N. D.; Osterloh, F. E. Photocatalytic Water Oxidation with Nonsensitized IrO2 Nanocrystals under Visible and UV Light. *J. Am. Chem. Soc.* **2011**, *1331*, 7264–7267.

(202) Winkler-Goldstein, R.; Rastetter, A. Power to Gas: The Final Breakthrough for the Hydrogen Economy? *Green* **2013**, *3*, 69–78.

(203) Gahleitner, G. Hydrogen from renewable electricity: An international review of power-to-gas pilot plants for stationary applications. *International Journal of Hydrogen Energy* **2013**, *38*, 2039–2061.

(204) Hammarström, L. Artificial Photosynthesis and Solar Fuels. *Accounts of Chemical Research* **2009**, *42*, ed. by Hammes-Schiffer, S., 1859–1860.

(205) Montoya, J. H.; Seitz, L. C.; Chakthranont, P.; Vojvodic, A.; Jaramillo, T. F.; Nørskov, J. K. Materials for solar fuels and chemicals. *Nature Materials* **2017**, *16*, 70–81.

(206) Spöri, C.; Kwan, J. T. H.; Bonakdarpour, A.; Wilkinson, D. P.; Strasser, P. The Stability Challenges of Oxygen Evolving Catalysts: Towards a Common Fundamental Understanding and Mitigation of Catalyst Degradation. *Angewandte Chemie International Edition* **2017**, *56*, 5994–6021.

(207) Sala, X.; Maji, S.; Bofill, R.; García-Antón, J.; Escriche, L.; Llobet, A. Molecular Water Oxidation Mechanisms Followed by Transition Metals: State of the Art. *Accounts of Chemical Research* **2014**, *47*, 504–516.

(208) Kärkäs, M. D.; Verho, O.; Johnston, V. E.; Åkermark, B. Artificial Photosynthesis: Molecular Systems for Catalytic Water Oxidation. *Chemical Reviews* **2014**, *114*, 11863–12001.

(209) Blakemore, J. D.; Crabtree, R. H.; Brudvig, G. W. Molecular Catalysts for Water Oxidation. *Chemical Reviews* **2015**, *115*, 12974–13005.

(210) Hunter, B. M.; Gray, H. B.; Müller, A. M. Earth-Abundant Heterogeneous Water Oxidation Catalysts. *Chemical Reviews* **2016**, *116*, 14120–14136.

(211) Burke, M. S.; Enman, L. J.; Batchellor, A. S.; Zou, S.; Boettcher, S. W. Oxygen Evolution Reaction Electrocatalysis on Transition Metal Oxides and (Oxy)hydroxides: Activity Trends and Design Principles. *Chemistry of Materials* **2015**, *27*, 7549–7558.

(212) Fabbri, E.; Habereder, A.; Waltar, K.; Kötz, R.; Schmidt, T. J. Developments and perspectives of oxide-based catalysts for the oxygen evolution reaction. *Catal. Sci. Technol.* **2014**, *4*, 3800–3821.

(213) McCrory, C. C. L.; Jung, S.; Ferrer, I. M.; Chatman, S. M.; Peters, J. C.; Jaramillo, T. F. Benchmarking Hydrogen Evolving

Reaction and Oxygen Evolving Reaction Electrocatalysts for Solar Water Splitting Devices. *Journal of the American Chemical Society* **2015**, *137*, 4347–4357.

(214) Yu, J.; He, Q.; Yang, G.; Zhou, W.; Shao, Z.; Ni, M. Recent Advances and Prospective in Ruthenium-Based Materials for Electrochemical Water Splitting. *ACS Catalysis* **2019**, *9*, 9973–10011.

(215) Sun, Y.; Yuan, L.; Liu, Z.; Wang, Q.; Huang, K.; Feng, S. Optimization of oxygen evolution dynamics on RuO 2 via controlling of spontaneous dissociation equilibrium. *Materials Chemistry Frontiers* **2019**, *3*, 1779–1785.

(216) Pfeifer, V.; Jones, T.; Vélez, J. V.; Massué, C.; Greiner, M.; Arrigo, R.; Teschner, D.; Girgsdies, F.; Scherzer, M.; Allan, J., et al. The electronic structure of iridium oxide electrodes active in water splitting. *Phys. Chem. Chem. Phys.* **2016**, *18*, 2292–2296.

(217) Pedersen, A. F.; Escudero-Escribano, M.; Sebok, B.; Bodin, A.; Paoli, E.; Frydendal, R.; Friebel, D.; Stephens, I. E. L.; Rossmeisl, J.; Chorkendorff, I.; Nilsson, A. Operando XAS Study of the Surface Oxidation State on a Monolayer IrO x on RuO x and Ru Oxide Based Nanoparticles for Oxygen Evolution in Acidic Media. *The Journal of Physical Chemistry B* **2018**, *122*, 878–887.

(218) Chang, C.-J.; Chu, Y.-C.; Yan, H.-Y.; Liao, Y.-F.; Chen, H. M. Revealing the structural transformation of rutile RuO 2 via in situ X-ray absorption spectroscopy during the oxygen evolution reaction. *Dalton Transactions* **2019**, *48*, 7122–7129.

(219) Steegstra, P.; Busch, M.; Panas, I.; Ahlberg, E. Revisiting the Redox Properties of Hydrous Iridium Oxide Films in the Context of Oxygen Evolution. *The Journal of Physical Chemistry C* **2013**, *117*, 20975–20981.

(220) Macounova, K.; Makarova, M.; Krtil, P. Oxygen evolution on nanocrystalline RuO2 and Ru0.9Ni0.1O2-δ electrodes - DEMS approach to reaction mechanism determination. *Electrochem. Commun.* **2009**, *11*, 1865–1868.

(221) Dau, H.; Limberg, C.; Reier, T.; Risch, M.; Roggan, S.; Strasser, P. The Mechanism of Water Oxidation: From Electrolysis via Homogeneous to Biological Catalysis. *ChemCatChem* **2010**, *2*, 724–761.

(222) Fabbri, E.; Schmidt, T. J. Oxygen Evolution Reaction—The Enigma in Water Electrolysis. *ACS Catalysis* **2018**, *8*, 9765–9774.

(223) Fang, Y.-H.; Liu, Z.-P. Mechanism and Tafel Lines of Electro-Oxidation of Water to Oxygen on RuO 2 (110). *Journal of the American Chemical Society* **2010**, *132*, 18214–18222.

(224) Briquet, V. L. G.; Sarwar, M.; Mugo, J.; Jones, G.; Calle-Vallejo, F. A New Type of Scaling Relations to Assess the Accuracy of Computational Predictions of Catalytic Activities Applied to the Oxygen Evolution Reaction. *ChemCatChem* **2017**, *9*, 1261–1268.

(225) Dickens, C. F.; Kirk, C.; Nørskov, J. K. Insights into the Electrochemical Oxygen Evolution Reaction with ab Initio Calculations and Microkinetic Modeling: Beyond the Limiting Potential Volcano. *The Journal of Physical Chemistry C* **2019**, *123*, 18960–18977.

(226) Dickens, C. F.; Nørskov, J. K. A Theoretical Investigation into the Role of Surface Defects for Oxygen Evolution on RuO 2. *The Journal of Physical Chemistry C* **2017**, *121*, 18516–18524.

(227) Klyukin, K.; Zagalskaya, A.; Alexandrov, V. Role of Dissolution Intermediates in Promoting Oxygen Evolution Reaction at RuO 2 (110) Surface. *The Journal of Physical Chemistry C* **2019**, *123*, 22151–22157.

(228) Zagalskaya, A.; Alexandrov, V. Mechanistic Study of IrO 2 Dissolution during the Electrocatalytic Oxygen Evolution Reaction. *The Journal of Physical Chemistry Letters* **2020**, *11*, 2695–2700.

(229) Zagalskaya, A.; Alexandrov, V. Role of Defects in the Interplay between Adsorbate Evolving and Lattice Oxygen Mechanisms of the Oxygen Evolution Reaction in RuO 2 and IrO 2. *ACS Catalysis* **2020**, *10*, 3650–3657.

(230) Klyukin, K.; Zagalskaya, A.; Alexandrov, V. Ab Initio Thermodynamics of Iridium Surface Oxidation and Oxygen Evolution Reaction. *The Journal of Physical Chemistry C* **2018**, *122*, 29350–29358.

(231) Lebedev, D.; Ezhov, R.; Heras-Domingo, J.; Comas-Vives, A.; Kaeffer, N.; Willinger, M.; Solans-Monfort, X.; Huang, X.; Pushkar, Y.; Copéret, C. Atomically Dispersed Iridium on Indium Tin Oxide Efficiently Catalyzes Water Oxidation. *ACS Central Science* **2020**, *6*, 1189–1198.

(232) Xu, Z.; Rossmeisl, J.; Kitchin, J. R. A Linear Response DFT+ U Study of Trends in the Oxygen Evolution Activity of Transition Metal Rutile Dioxides. *The Journal of Physical Chemistry C* **2015**, *119*, 4827–4833.

(233) García-Melchor, M.; Vilella, L.; López, N.; Vojvodic, A. Computationally Probing the Performance of Hybrid, Heterogeneous, and Homogeneous Iridium-Based Catalysts for Water Oxidation. *ChemCatChem* **2016**, *8*, 1792–1798.

(234) Rao, R. R. et al. Towards identifying the active sites on RuO 2 (110) in catalyzing oxygen evolution. *Energy & Environmental Science* **2017**, *10*, 2626–2637.

(235) Watanabe, E.; Ushiyama, H.; Yamashita, K.; Morikawa, Y.; Asakura, D.; Okubo, M.; Yamada, A. Charge Storage Mechanism of RuO 2 /Water Interfaces. *The Journal of Physical Chemistry C* **2017**, *121*, 18975–18981.

(236) Henkelman, G.; Uberuaga, B. P.; Jónsson, H. A climbing image nudged elastic band method for finding saddle points and minimum energy paths. *The Journal of Chemical Physics* **2000**, *113*, 9901–9904.

(237) Henkelman, G.; Jónsson, H. Improved tangent estimate in the nudged elastic band method for finding minimum energy paths and saddle points. *The Journal of Chemical Physics* **2000**, *113*, 9978–9985.

(238) Cramer, C. J.; Tolman, W. B.; Theopold, K. H.; Rheingold, A. L. Variable character of O—O and M—O bonding in side-on (η2) 1:1 metal complexes of O_2. *Proceedings of the National Academy of Sciences* **2003**, *100*, 3635–3640.

(239) Holland, P. L. Metal–dioxygen and metal–dinitrogen complexes: where are the electrons? *Dalton Trans.* **2010**, *39*, 5415–5425.

(240) Siegbahn, P. E. M.; Crabtree, R. H. Manganese Oxyl Radical Intermediates and O-O Bond Formation in Photosynthetic

Oxygen Evolution and a Proposed Role for the Calcium Cofactor in Photosystem II. *Journal of the American Chemical Society* **1999**, *121*, 117–127.

(241) Wang, L.-P.; Van Voorhis, T. Direct-Coupling O 2 Bond Forming a Pathway in Cobalt Oxide Water Oxidation Catalysts. *The Journal of Physical Chemistry Letters* **2011**, *2*, 2200–2204.

(242) Mattioli, G.; Giannozzi, P.; Amore Bonapasta, A.; Guidoni, L. Reaction Pathways for Oxygen Evolution Promoted by Cobalt Catalyst. *Journal of the American Chemical Society* **2013**, *135*, 15353–15363.

(243) Crandell, D. W.; Xu, S.; Smith, J. M.; Baik, M.-H. Intramolecular Oxyl Radical Coupling Promotes O–O Bond Formation in a Homogeneous Mononuclear Mn-based Water Oxidation Catalyst: A Computational Mechanistic Investigation. *Inorganic Chemistry* **2017**, *56*, 4435–4445.

(244) Siegbahn, P. E. M. Structures and Energetics for O 2 Formation in Photosystem II. *Accounts of Chemical Research* **2009**, *42*, 1871–1880.

(245) Yang, X.; Baik, M.-H. cis,cis-[(bpy)2RuVO]2O4+ Catalyzes Water Oxidation Formally via in Situ Generation of Radicaloid RuIV-O•. *Journal of the American Chemical Society* **2006**, *128*, 7476–7485.

(246) Yang, K. R.; Matula, A. J.; Kwon, G.; Hong, J.; Sheehan, S. W.; Thomsen, J. M.; Brudvig, G. W.; Crabtree, R. H.; Tiede, D. M.; Chen, L. X.; Batista, V. S. Solution Structures of Highly Active Molecular Ir Water-Oxidation Catalysts from Density Functional Theory Combined with High-Energy X-ray Scattering

and EXAFS Spectroscopy. *Journal of the American Chemical Society* **2016**, *138*, 5511–5514.

(247) Shaffer, D. W.; Xie, Y.; Concepcion, J. J. O-O bond formation in ruthenium-catalyzed water oxidation: single-site nucleophilic attack vs. O-O radical coupling. *Chemical Society Reviews* **2017**, *46*, 6170–6193.

(248) Duan, L.; Bozoglian, F.; Mandal, S.; Stewart, B.; Privalov, T.; Llobet, A.; Sun, L. A molecular ruthenium catalyst with water-oxidation activity comparable to that of photosystem II. *Nature Chemistry* **2012**, *4*, 418–423.

(249) Brodsky, C. N.; Hadt, R. G.; Hayes, D.; Reinhart, B. J.; Li, N.; Chen, L. X.; Nocera, D. G. In situ characterization of cofacial Co(IV) centers in Co 4 O 4 cubane: Modeling the high-valent active site in oxygen-evolving catalysts. *Proceedings of the National Academy of Sciences* **2017**, *114*, 3855–3860.

(250) Cummings, C. Y.; Marken, F.; Peter, L. M.; Upul Wijayantha, K. G.; Tahir, A. A. New Insights into Water Splitting at Mesoporous α-Fe 2 O 3 Films: A Study by Modulated Transmittance and Impedance Spectroscopies. *Journal of the American Chemical Society* **2012**, *134*, 1228–1234.

(251) Klahr, B.; Hamann, T. Water Oxidation on Hematite Photoelectrodes: Insight into the Nature of Surface States through In Situ Spectroelectrochemistry. *The Journal of Physical Chemistry C* **2014**, *118*, 10393–10399.

(252) Herlihy, D. M.; Waegele, M. M.; Chen, X.; Pemmaraju, C. D.; Prendergast, D.; Cuk, T. Detecting the oxyl radical of photocatalytic water oxidation at an n-SrTiO3/aqueous interface

through its subsurface vibration. *Nature Chemistry* **2016**, *8*, 549–555.

(253) McAlpin, J. G.; Stich, T. A.; Ohlin, C. A.; Surendranath, Y.; Nocera, D. G.; Casey, W. H.; Britt, R. D. Electronic Structure Description of a [Co(III) 3 Co(IV)O 4] Cluster: A Model for the Paramagnetic Intermediate in Cobalt-Catalyzed Water Oxidation. *Journal of the American Chemical Society* **2011**, *133*, 15444–15452.

(254) Bediako, D. K.; Costentin, C.; Jones, E. C.; Nocera, D. G.; Savéant, J.-M. Proton-Electron Transport and Transfer in Electrocatalytic Films. Application to a Cobalt-Based O 2 -Evolution Catalyst. *Journal of the American Chemical Society* **2013**, *135*, 10492–10502.

(255) Chen, X.; Choing, S. N.; Aschaffenburg, D. J.; Pemmaraju, C. D.; Prendergast, D.; Cuk, T. The Formation Time of Ti–O • and Ti–O • –Ti Radicals at the n-SrTiO 3 / Aqueous Interface during Photocatalytic Water Oxidation. *Journal of the American Chemical Society* **2017**, *139*, 1830–1841.

(256) Ullman, A. M.; Brodsky, C. N.; Li, N.; Zheng, S.-L.; Nocera, D. G. Probing Edge Site Reactivity of Oxidic Cobalt Water Oxidation Catalysts. *Journal of the American Chemical Society* **2016**, *138*, 4229–4236.

(257) Pavlovic, Z.; Ranjan, C.; van Gastel, M.; Schlögl, R. The active site for the water oxidising anodic iridium oxide probed through in situ Raman spectroscopy. *Chemical Communications* **2017**, *53*, 12414–12417.

A BCN models

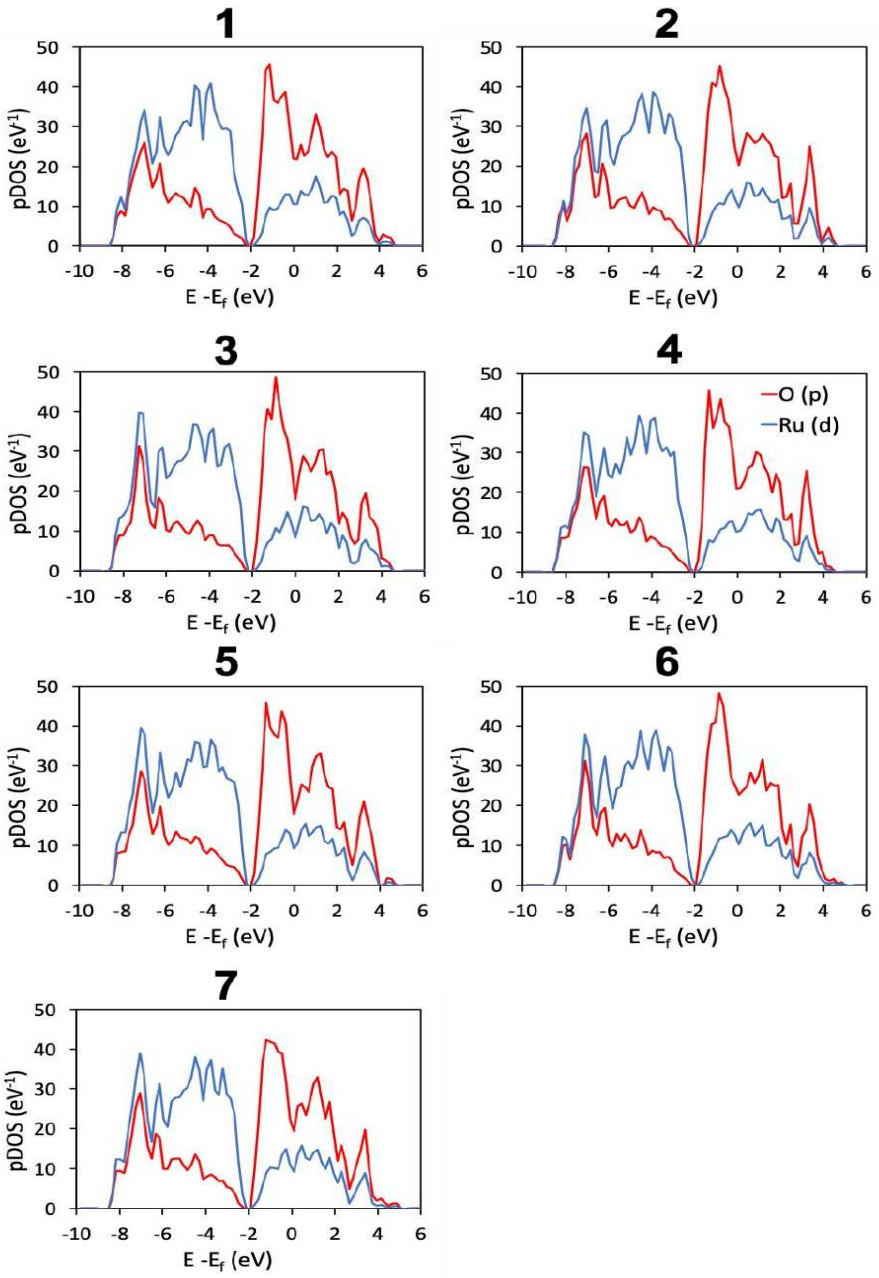

Figure A.1: Projected Density of States of the different nanoparticle isomers of $(RuO_2)_{33}$

Table A.1: Nanoparticle origins considered as function of the Bravais Lattice (space group symmetry).The selected originsare associated with the special positions presenting lower symmetry multiplicity.

Bravais Lattice	Origins	Space Group Index
F Orthorombic	(0.250, 0.250, 0.250) (0.500, 0.000, 0.000) (0.750, 0.250, 0.250) (0.000, 0.500, 0.000) (0.250, 0.750, 0.250) (0.000, 0.000, 0.500) (0.250, 0.250, 0.750) (0.500, 0.500, 0.500)	22, 42, 43, 69, 70.
F Cubic	(0.250, 0.250, 0.250) (0.500, 0.000, 0.000) (0.750, 0.250, 0.250) (0.500, 0.500, 0.500)	196, 202, 203, 209, 210, 216, 219, 225, 226, 227, 228.
I Orthorombic	(0.500, 0.000, 0.000) (0.500, 0.500, 0.000) (0.000, 0.500, 0.000) (0.000, 0.000, 0.500) (0.000, 0.500, 0.500) (0.500, 0.000, 0.500)	23, 24, 44, 45, 46, 71, 72, 73, 74
I Tetragonal	(0.500, 0.000, 0.000) (0.500, 0.500, 0.000) (0.000, 0.000, 0.500) (0.000, 0.500, 0.500)	79, 80, 82. 87, 88, 97, 98, 107, 108, 109, 110, 119, 120, 121, 122, 139, 140, 141, 142.
I Cubic	(0.500, 0.000, 0.000) (0.500, 0.500, 0.000)	197, 199, 204, 206, 211, 214, 217, 220, 229, 230.
C Monoclininc	(0.500, 0.000, 0.000) (0.000, 0.500, 0.500)	5, 8, 9, 12, 15.
C Orthorombic	(0.000, 0.500, 0.000) (0.500, 0.000, 0.500) (0.000, 0.000, 0.500) (0.500, 0.500, 0.500)	20, 21, 35, 36, 37, 63, 64, 65, 66, 67, 68.
A Orthorombic	(0.500, 0.000, 0.000) (0.500, 0.500, 0.000) (0.000, 0.500, 0.000) (0.500, 0.000, 0.500) (0.000, 0.000, 0.500) (0.500, 0.500, 0.500)	38, 39, 40, 41
P Triclinic	(0.500, 0.000, 0.000) (0.000, 0.500, 0.500)	1, 2.
P Monoclininc	(0.000, 0.500, 0.000) (0.500, 0.000, 0.500)	3, 4, 6, 7, 10, 11, 13, 14.
P Orthorombic	(0.000, 0.000, 0.500) (0.500, 0.500, 0.500) (0.500, 0.500, 0.000)	16, 17, 18, 19, 25, 26, 27, 28, 29, 30, 31, 32, 33, 34, 47, 48, 49, 50, 51, 52, 53, 54, 55, 56, 57, 58, 59, 60, 61, 62.
P Tetragonal	(0.500, 0.000, 0.000) (0.500, 0.000, 0.500) (0.000, 0.000, 0.500) (0.500, 0.500, 0.500) (0.500, 0.500, 0.000)	75, 76, 77, 78, 81, 83, 84, 85, 86, 89, 90, 91, 82, 93, 94, 95, 96, 99, 100, 101, 102,103, 104, 105, 106, 111, 112, 113, 114, 115, 116, 117, 118, 123, 124, 125, 126, 127, 128 ,129, 130, 131, 132, 133, 134, 135, 136, 137, 138.
P Cubic	(0.500, 0.000, 0.000) (0.500, 0.500, 0.500) (0.500, 0.500, 0.000)	195, 198, 200, 201, 205, 207, 208, 212, 213, 215, 218, 221, 222, 223, 224.
P Hexagonal	(0.000, 0.000, 0.000) (0.500, 0.500, 0.500) (0.000, 0.000, 0.500) (0.333, 0.333, 0.000) (0.500, 0.000, 0.000) (0.333, 0.667, 0.000) (0.500, 0.500, 0.000) (0.333, 0.333, 0.500) (0.500, 0.000, 0.500) (0.333, 0.667, 0.500)	168, 169, 170, 171, 172, 173, 174, 175, 176, 177, 178, 179, 180, 181, 182, 183, 184, 185, 186, 187, 188, 189, 190, 191, 192, 193, 194.

Table A.2: Input data required for achieving the models described in the main text. These data are formed by: cell parameters (Å and degrees), atomic positions of the irreducible atoms (fractional coordinates) and surface energies (J m^{-2}) of the representative facets.

Material	a	b	c	α	β	γ	cation	anion	E1	E2	E3	E4	Ref
MgO	4.211	4.211	4.211	90	90	90	0.0,0.0,0.0	0.5,0.5,0.5	(100) 1.16	N.A.	N.A.	N.A.	1
CeO_2	5.378	5.378	5.378	90	90	90	0.0,0.0,0.0	0.25,0.25,0.25	(111) 0.71	(110) 1.09	(100) 1.54	N.A.	2–4
Li_2O	4.569	4.569	4.569	90	90	90	0.25,0.25,0.25	0.0,0.0,0.0	(111) 0.561	(110) 0.993	(100) 1.346	N.A.	5,6
In_2O_3	10.3	10.3	10.3	90	90	90	0.0,0.25,0.47 0.25,0.25,0.25	0.11,0.15,0.62	(111) 0.891	(110) 1.079	(100) 1.759	N.A.	7
TiO_2[a]	3.859	3.859	9.763	90	90	90	0.0,0.0,0.0	0.0,0.0,0.2081	(101) 0.373	(100) 0.745	(001) 1.002	N.A.	8,9
TiO_2[b]	4.603	4.603	2.977	90	90	90	0.0,0.0,0.0	0.306, 0.306, 0.0	(110) 0.673	(100) 0.961	(011) 1.186	(001) 1.362	10
RuO_2[b]	4.487	4.487	3.149	90	90	90	0.0,0.0,0.0	0.306, 0.306, 0.0	(110) 1.570	(011) 1.682	(100) 1.907	(001) 2.147	10,11
IrO_2[b]	4.497	4.497	3.193	90	90	90	0.0,0.0,0.0	0.306, 0.306, 0.0	(110) 2.403	(011) 2.531	(100) 2.964	(001) 3.300	10
CuO	4.683	3.421	5.129	90	99.6	90	0.25, 0.25, 0.0	0.00, 0.4179, 0.25	(111) 0.75	(-111) 0.89	(101) 1.17	(110) 1.00	12,13
ReO_3	3.742	3.742	3.742	90	90	90	0.0,0.0,0.0	0.5,0.0,0.0	(001)-O rich 0.86	N.A.	N.A.	N.A.	14
Cu_2O	4.27	4.27	4.27	90	90	90	0.25,0.25,0.25	0.0, 0.0, 0.0	(111) 0.599	(110) 0.757	(100) 1.171	N.A.	15
PdO	3.096	3.096	5.442	90	90	90	0.0, 0.5, 0.5	0.0,0.0,0.25	(100)-O rich 0.529	(101) 0.913	(001) 0.319	N.A.	16,17
ZnO[c]	3.247	3.247	5.27	90	90	120	1/3, 2/3, 0.345	1/3, 2/3, 0.0	(100)-O rich 0.839	(110) 0.872	(001) 0.96	N.A.	18,19
ZnS[c]	3.823	3.823	6.261	90	90	120	1/3, 2/3, 0.3748	1/3, 2/3, 0.0	(110)-Zn rich 0.49	(100) 0.52	(001) 0.90	N.A.	20–22
CdSe[c]	4.299	4.299	7.015	90	90	120	1/3, 2/3, 0.375	1/3, 2/3, 0.0	(110)-Se rich 0.59	(100) 0.67	(001) 1.15	N.A.	23,24

[a] Anatase [b] Rutile [c] Wurtzite

Table A.3: Selected NP Models without Polar Surfaces Obtained with BCN-M. Two possible centers (1 and 2) are reported. For each one the size of the NP model are shown.

Material	Center	Formula[a]	Formula[b]	Size[c]
MgO	(0.25,0.25,0.25)	$(MgO)_{256}$,$(MgO)_{500}$, $(MgO)_{864}$,$(MgO)_{1372}$, $(MgO)_{2048}$	N/A	2.4,3.2, 3.9,4.7, 5.4
	N/A	N/A	N/A	N/A
CeO_2	Cation	$(CeO_2)_{231}$,$(CeO_2)_{489}$, $(CeO_2)_{891}$,	$Ce_{231}O_{448}$,$Ce_{489}O_{960}$, $Ce_{891}O_{1760}$	3.2, 4.3 5.4
	(0.5,0.0,0.0)	$(CeO_2)_{344}$, $(CeO_2)_{670}$	$Ce_{344}O_{672}$,$Ce_{670}O_{1320}$	3,8, 4,8
	(0.25,0.25,0.25)	$(CeO_2)_{224}$,$(CeO_2)_{336}$, $(CeO_2)_{480}$,$(CeO_2)_{660}$, $(CeO_2)_{880}$,	$Ce_{224}O_{437}$,$Ce_{336}O_{659}$, $Ce_{480}O_{945}$,$Ce_{660}O_{1303}$, $Ce_{880}O_{1741}$	3.2, 3.8 4.3, 4.8 5.4
Li_2O	Anion	$(Li_2O)_{231}$,$(Li_2O)_{489}$ $(Li_2O)_{891}$	$Li_{448}O_{231}$,$Li_{960}O_{489}$ $Li_{1760}O_{891}$	3.0, 3.9 4.8
	(0.5,0.0,0.0)	$(Li_2O)_{344}$, $(Li_2O)_{670}$	$Li_{672}O_{344}$,$Li_{1320}O_{670}$	3.4,4.3
Cu_2O	Cation	$(Cu_2O)_{240}$,$(Cu_2O)_{440}$ $(Cu_2O)_{728}$, $(Cu_2O)_{1120}$	$Cu_{399}O_{240}$,$Cu_{759}O_{440}$ $Cu_{1287}O_{728}$, $Cu_{2015}O_{1120}$	3.4, 4.3 5.1, 6.0
	N/A	N/A	N/A	N/A
In_2O_3	(0.5, 0.0, 0.0)	$(In_2O_3)_{172}$, $(In_2O_3)_{335}$ $(In_2O_3)_{578}$	$In_{344}O_{504}$,$In_{670}O_{990}$, $In_{1156}O_{1716}$	3.6, 4.6 5.7
	N/A	N/A	N/A	N/A
TiO_2[d]	(0.0, 0.0, 0.5)	$(TiO_2)_{286}$, $(TiO_2)_{680}$	N/A	4.9, 6.8
	Cation	$(TiO_2)_{455}$,	N/A	5.9,
TiO_2[e]	(0.5, 0.5, 0.0)	$(TiO_2)_{616}$, $(TiO_2)_{714}$ $(TiO_2)_{1260}$	$Ti_{616}O_{1218}$,$Ti_{714}O_{1414}$ $Ti_{1260}O_{2502}$	4.5, 5.1 5.7
	Cation	$(TiO_2)_{567}$, $(TiO_2)_{665}$ $(TiO_2)_{1341}$	$Ti_{567}O_{1218}$,$Ti_{665}O_{1316}$ $Ti_{1341}O_{2664}$	4.2, 4.8 6
RuO_2[e]	(0.5, 0.5, 0.0)	$(RuO_2)_{216}$, $(RuO_2)_{322}$, $(RuO_2)_{596}$, $(RuO_2)_{612}$ $(RuO_2)_{1018}$, $(RuO_2)_{1926}$	$Ru_{216}O_{418}$,$Ru_{322}O_{630}$ $Ru_{596}O_{1174}$,$Ru_{612}O_{1206}$ $Ru_{1018}O_{2014}$,$Ru_{1926}O_{3226}$	2.2,2.8 3.5,3.5 4.1, 5.4
	Cation	$(RuO_2)_{519}$, $(RuO_2)_{693}$ $(RuO_2)_{1135}$	$Ru_{519}O_{1020}$,$Ru_{693}O_{1368}$, $Ru_{1135}O_{2248}$	3.1, 3.8 5
IrO_2[e]	(0.5, 0.5, 0.0)	$(IrO_2)_{140}$, $(IrO_2)_{216}$ $(IrO_2)_{322}$, $(IrO_2)_{612}$ $(IrO_2)_{760}$, $(IrO_2)_{1018}$	$Ir_{140}O_{270}$,$Ir_{216}O_{418}$ $Ir_{322}O_{630}$,$Ir_{612}O_{1206}$ $Ir_{760}O_{1438}$,$Ir_{1018}O_{2014}$	2.2, 2.2 2.9, 3.5, 3.5,4.2
	Cation	$(IrO_2)_{273}$,$(IrO_2)_{1135}$ $(IrO_2)_{1155}$,$(IrO_2)_{1761}$	$Ir_{273}O_{532}$,$Ir_{1135}O_{2248}$ $Ir_{1155}O_{2288}$,$Ir_{1761}O_{3496}$	2.6, 4.5 4.5, 5.1
CuO	Anion	$(CuO)_{280}$, $(CuO)_{570}$ $(CuO)_{1012}$, $(CuO)_{1638}$	$Cu_{280}O_{273}$,$Cu_{570}O_{561}$, $Cu_{1012}O_{1001}$, $Cu_{1638}O_{1625}$	3.4, 4.4 5.4, 6.5
	N/A	N/A	N/A	N/A

[a] Stoichiometric nanoparticle [b] Nanoparticle model without dangling atoms
[c] In nm, measured as the largest distance between cations [d] Anatase [e] Rutile.

Table A.4: Selected NP Models with Polar Surfaces Obtained with BCN-M. Two possible centers (1 and 2) are reported. For each one the size of the NP model are shown.

Material	Center	Formula[a]	Formula[b]	Size[c]
ReO_3	Cation	$Re_{343}O_{1176}$	$H_{294}Re_{343}O_{1176}$	3.9
		$Re_{729}O_{2430}$	$H_{486}Re_{729}O_{2430}$	5.2
		$Re_{1331}O\,4356$	$H_{726}Re_{1331}O_{4356}$	6.5
	(0.5, 0.5, 0.5)	$Re_{512}O_{1728}$	$H_{384}Re_{512}O_{1728}$	4.5
		$Re_{1000}O\,3300$	$H_{600}Re_{1000}O_{3300}$	5.8
PdO	Anion	$Pd_{160}O_{189}$	N/A	3
		$Pd_{200}O_{239}$		3.5
		$Pd_{240}O_{289}$		4.1
		$Pd_{560}O_{625}$		5.2
	N/A	N/A	N/A	N/A
ZnO[d]	(0.0, 0.0, 0.0)	$Zn_{480}O_{528}$	$H_{96}Zn_{480}O_{528}$	3.3
		$Zn_{975}O_{1050}$	$H_{150}Zn_{975}O_{1050}$	4.3
		$Zn_{1620}O_{1728}$	$H_{216}Zn_{1620}O_{1728}$	5.1
	N/A	N/A	N/A	N/A
ZnS[d]	(0.0, 0.0, 0.0)	$Zn_{714}S_{672}$	$Zn_{714}S_{672}(OH)_{84}$	5.5
		$Zn_{1380}S_{1311}$	$Zn_{1380}S_{1311}(OH)_{138}$	6.7
		$Zn_{1449}S_{1380}$	$Zn_{1449}S_{1380}(OH)_{138}$	6.9
	N/A	N/A	N/A	N/A
CdSe[d]	(0.0, 0.0, 0.0)	$Cd_{231}Se_{252}$	$H_{42}Cd_{231}Se_{252}$	4
		$Cd_{360}Se_{390}$	$H_{60}Cd_{360}Se_{390}$	4.6
		$Cd_{420}Se_{450}$	$H_{60}Cd_{420}Se_{450}$	5.2
		$Cd_{672}Se_{714}$	$H_{84}Cd_{672}Se_{714}$	5.9
	N/A	N/A	N/A	N/A

[a] Formula models with either metal or non-metal rich termiation
[b] Formula models with additional OH groups
[c] In nm, measured as the largest distance between cations [d] Wurtzite

B Oxygen evolution reaction on IrO_2 materials

Table B.1: Reaction Gibbs Energies (in eV) for the chemical and electrochemical steps of the **I2M** and **WNA** reaction mechanisms obtained with two different models of the (110) surface

Reaction	(2x2)	(2x1)
I2M		
$\mathbf{4}_{O/O} \rightarrow \mathbf{4}_{O-O}$	0.67	0.64
$\mathbf{4}_{O-O} + 2\,H_2O \rightarrow \mathbf{0}_{H_2O/H_2O} + O_2$	-0.89	-1.01
$\mathbf{0}_{H_2O/H_2O} \rightarrow \mathbf{1}_{OH/H_2O} + H^+ + e^-$	1.07	1.08
$\mathbf{1}_{OH/H_2O} \rightarrow \mathbf{2}_{OH/OH} + H^+ + e^-$	1.15	1.21
$\mathbf{2}_{OH/OH} \rightarrow \mathbf{3}_{O/OH} + H^+ + e^-$	1.56	1.58
$\mathbf{3}_{O/OH} \rightarrow \mathbf{4}_{O/O} + H^+ + e^-$	1.36	1.42
WNA		
$\mathbf{4}_{O/O} + H_2O \rightarrow \mathbf{4}_{OOH/OH}$	-0.12	-0.21
$\mathbf{4}_{OOH/OH} \rightarrow \mathbf{5}_{OO/OH} + H^+ + e^-$	1.11	1.13
$\mathbf{5}_{OO/OH} \rightarrow \mathbf{6}_{OO/O} + H^+ + e^-$	1.53	1.52
$\mathbf{6}_{OO/O} + H_2O \rightarrow \mathbf{2}_{H_2O/O} + O_2$	-0.17	-0.22
$\mathbf{2}_{H_2O/O} \rightarrow \mathbf{3}_{O/OH} + H^+ + e^-$	1.21	1.28
$\mathbf{3}_{O/OH} \rightarrow \mathbf{4}_{O/O} + H^+ + e^-$	1.36	1.42

Table B.2: $Ir-O_L$ distances (in Å), Bader atomic charges and spin moments for the different surface terminations arising from the oxidation of hydrated IrO_2 (110), (011), (100) and (001) surfaces.

Surface	Species	Ir_1-O_{L1}	Ir_1-O_{L2}	$q_{O_{L1}}$	$q_{O_{L2}}$	q_{Ir_1}	q_{Ir_2}	S_{OL1}	S_{OL2}	S_{Ir1}	S_{Ir2}
(110)	$\mathbf{0}_{H_2O/H_2O}$	2.002	2.002	-1.15	-1.15	1.65	1.65	0.00	0.00	0.00	0.00
	$\mathbf{1}_{OH/H_2O}$	1.943	1.990	-1.03	-1.12	1.72	1.66	0.00	0.00	0.00	0.00
	$\mathbf{2}_{OH/OH}$	1.937	1.938	-1.05	-1.05	1.73	1.73	0.00	0.00	0.00	0.00
	$\mathbf{3}_{O/OH}$	1.788	1.925	-0.52	-0.96	1.84	1.72	0.54	0.02	0.48	0.15
	$\mathbf{4}_{O/O}$	1.789	1.789	-0.46	-0.46	1.83	1.83	0.67	0.67	0.52	0.52
(011)	$\mathbf{0}_{H_2O/H_2O}$	2.110	2.077	-1.22	-1.59	1.65	1.64	0.00	0.00	0.00	0.00
	$\mathbf{1}_{OH/H_2O}$	1.953	2.148	-1.00	-1.15	1.75	1.67	0.00	0.00	0.00	0.00
	$\mathbf{2}_{OH/OH}$	1.965	1.940	-1.03	-1.02	1.73	1.74	0.00	0.00	0.00	0.00
	$\mathbf{3}_{O/OH}$	1.810	1.933	-0.50	-0.96	1.84	1.75	0.57	0.02	0.55	0.00
	$\mathbf{4}_{O/O}$	1.797	1.797	-0.48	-0.46	1.84	1.84	0.59	0.62	0.52	0.57
(100)	$\mathbf{0}_{H_2O/H_2O}$	2.003	2.003	-1.15	-1.15	1.70	1.70	0.02	0.02	0.08	0.12
	$\mathbf{1}_{OH/H_2O}$	1.951	1.958	-1.10	-1.07	1.77	1.79	0.01	0.01	0.20	0.15
	$\mathbf{2}_{OH/OH}$	1.927	1.927	-1.05	-1.05	1.70	1.70	0.17	0.17	0.41	0.40
	$\mathbf{3}_{O/OH}$	1.796	1.924	-0.55	-1.02	1.99	1.86	0.19	0.02	0.24	0.03
	$\mathbf{4}_{O/O}$	1.771	1.771	-0.52	-0.52	1.75	1.75	0.57	0.56	0.26	0.26
(001)	$\mathbf{0}_{H_2O/H_2O}$	2.025	2.099	-1.16	-1.27	1.59	1.58	0.00	0.00	0.02	0.01
	$\mathbf{1}_{OH/H_2O}$	1.947	2.094	-1.08	-1.26	1.65	1.58	0.00	0.00	0.00	0.00
	$\mathbf{2}_{OH/OH}$	1.933	1.900	-1.00	-1.01	1.66	1.70	0.00	0.00	0.00	0.00
	$\mathbf{3}_{O/OH}$	1.729	1.898	-0.53	-1.00	1.74	1.70	0.00	0.00	0.00	0.00
	$\mathbf{4}_{O/O}$	1.732	1.727	-0.52	-0.52	1.74	1.74	0.00	0.00	0.00	0.00

Table B.3: $Ir-O_L$ distances (in Å), Bader atomic charges and spin moments for the different different reaction intermediates of the **WNA** and **I2M** mechanisms on IrO_2 (110), (011), (100) and (001) surfaces.

Surface	Species	Ir_1-O_{L1}	Ir_2-O_{L2}	$O_{L1}-O_{L2}$	$q_{O_{L1}}$	$q_{O_{L2}}$	q_{Ir_1}	q_{Ir_2}	S_{OL1}	S_{OL2}	S_{Ir1}	S_{Ir2}
(110)	$\mathbf{4}_{OOH/OH}$	1.931	1.913	1.417	-0.91	-0.95	1.70	1.73	0.00	0.00	0.00	0.00
	$\mathbf{5}_{OO/OH}$	1.931	1.896	1.297	-1.02	-0.93	1.67	1.75	0.22	0.10	-0.10	-0.10
	$\mathbf{6}_{OO/O}$	1.923	1.781	1.287	-0.25	-0.45	1.67	1.84	-0.15	-0.31	-0.12	-0.17
	$\mathbf{2}_{H_2O/O}$	1.976	1.790	3.391	-1.06	-0.56	1.65	1.85	0.00	-0.10	0.00	-0.10
	$\mathbf{4}_{O-O}$	2.024	2.022	1.395	-0.30	-0.21	1.61	1.61	0.00	0.00	0.00	0.00
(011)	$\mathbf{4}_{OOH/OH}$	1.961	1.936	1.446	-0.98	-1.00	1.70	1.75	0.00	0.00	0.00	0.00
	$\mathbf{5}_{OOH/O}$	1.949	1.796	2.804	-0.88	-0.48	1.70	1.83	-0.17	0.57	-0.14	0.53
	$\mathbf{5}_{OO/OH}$	1.983	1.939	1.293	-0.36	-0.98	1.67	1.75	0.63	0.00	-0.12	0.00
	$\mathbf{6}_{OO/O}$	1.941	1.798	1.281	-0.29	-0.48	1.69	1.84	0.08	0.57	-0.04	0.54
	$\mathbf{2}_{H_2O/O}$	2.108	1.832	2.643	-1.26	-0.63	1.66	1.80	0.02	0.45	0.00	0.48
	$\mathbf{4}_{O-O}$	2.043	2.016	1.404	-0.30	-0.31	1.68	1.65	0.00	0.00	0.00	0.00
(100)	$\mathbf{4}_{OOH/OH}$	1.961	1.936	1.446	-0.98	-1.00	1.70	1.75	0.00	0.00	0.00	0.00
	$\mathbf{5}_{OOH/O}$	1.949	1.796	2.804	-0.88	-0.48	1.70	1.83	-0.17	0.57	-0.14	0.53
	$\mathbf{5}_{OO/OH}$	1.983	1.939	1.293	-0.36	-0.98	1.67	1.75	0.63	0.00	-0.12	0.00
	$\mathbf{6}_{OO/O}$	1.932	1.760	1.287	-0.26	-0.48	1.67	1.90	-0.43	-0.05	0.12	-0.01
	$\mathbf{2}_{H_2O/O}$	2.108	1.832	2.643	-1.26	-0.63	1.66	1.80	0.02	0.45	0.00	0.48
	$\mathbf{4}_{O-O}$	2.043	2.016	1.404	-0.30	-0.31	1.68	1.65	0.00	0.00	0.00	0.00
(001)	$\mathbf{4}_{OOH/OH}$	1.885	1.895	1.464	-0.97	-1.00	1.59	1.70	0.00	0.00	0.00	0.00
	$\mathbf{5}_{OOH/O}$	1.887	1.732	1.452	-0.96	-0.51	1.61	1.71	0.00	0.00	0.00	0.00
	$\mathbf{5}_{OO/OH}$	1.853	1.889	1.280	-0.38	-0.99	1.62	1.70	0.00	0.00	0.00	0.00
	$\mathbf{6}_{OO/O}$	1.856	1.726	1.273	-0.34	-0.53	1.60	1.74	0.00	0.00	0.00	0.00
	$\mathbf{2}_{H_2O/O}$	2.007	1.731	3.790	-1.10	-0.53	1.63	1.72	0.00	0.00	-0.01	0.00
	$\mathbf{4}_{O-O}$	2.033	2.033	1.387	-0.32	-0.32	1.60	1.59	0.00	0.00	0.00	0.00

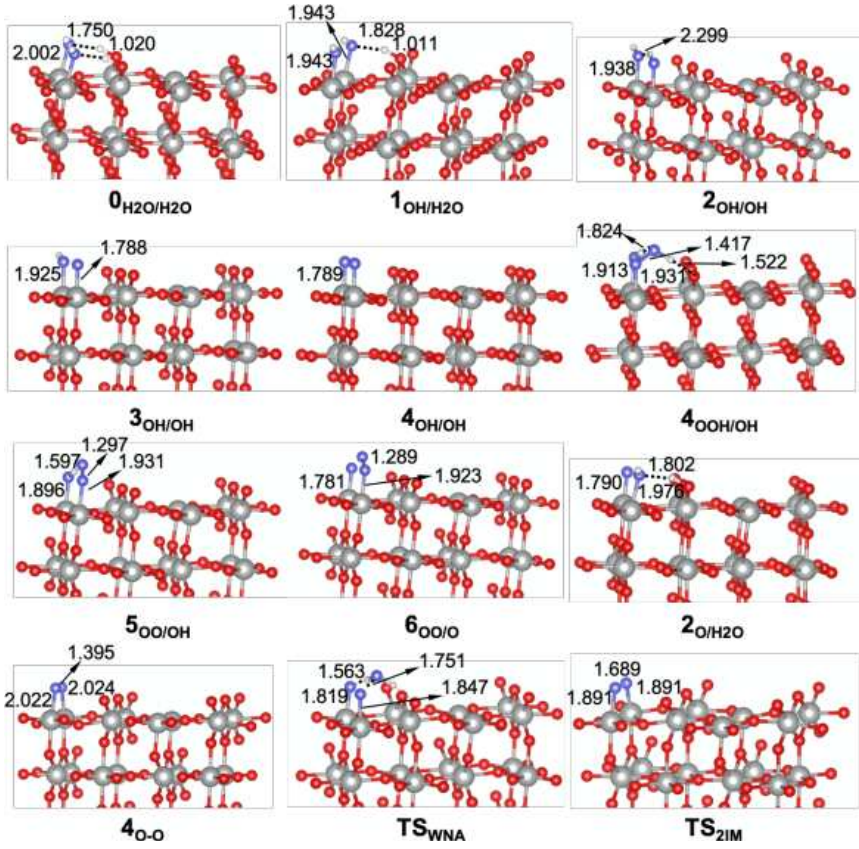

Figure B.1: Optimized structures for all intermediates and transition states associated to the OER reaction on the (110) surface. Distances in Å.

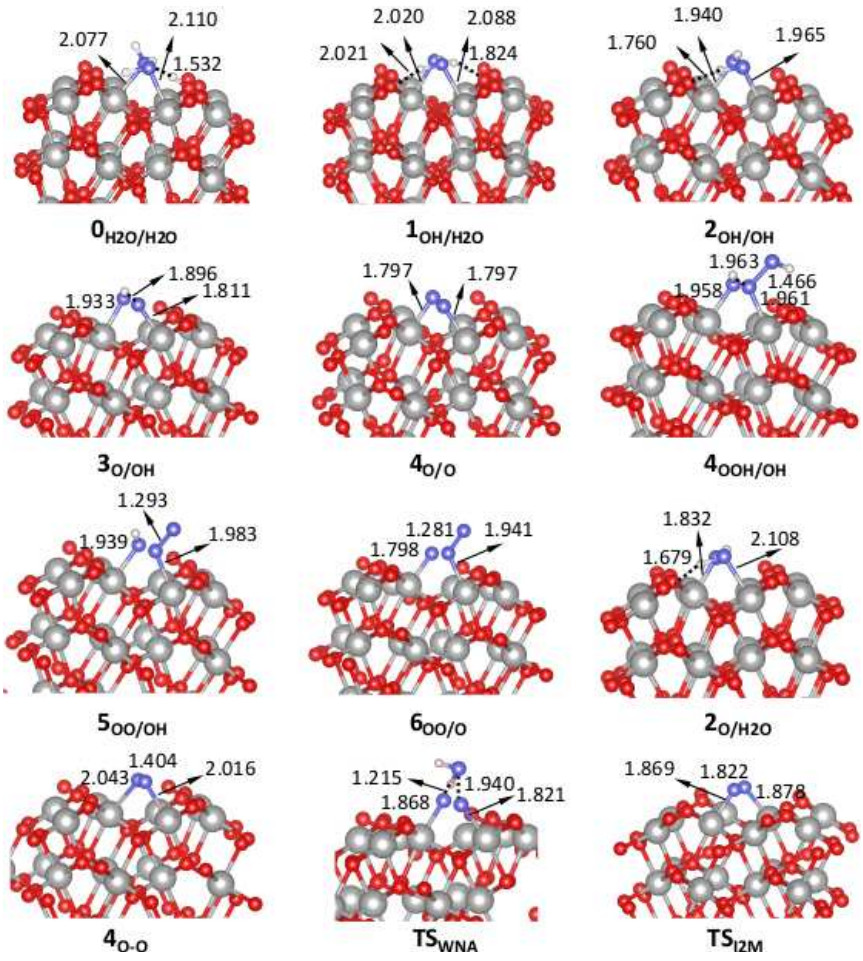

Figure B.2: Optimized structures for all intermediates and transition states associated to the OER reaction on the (011) surface. Distances in Å.

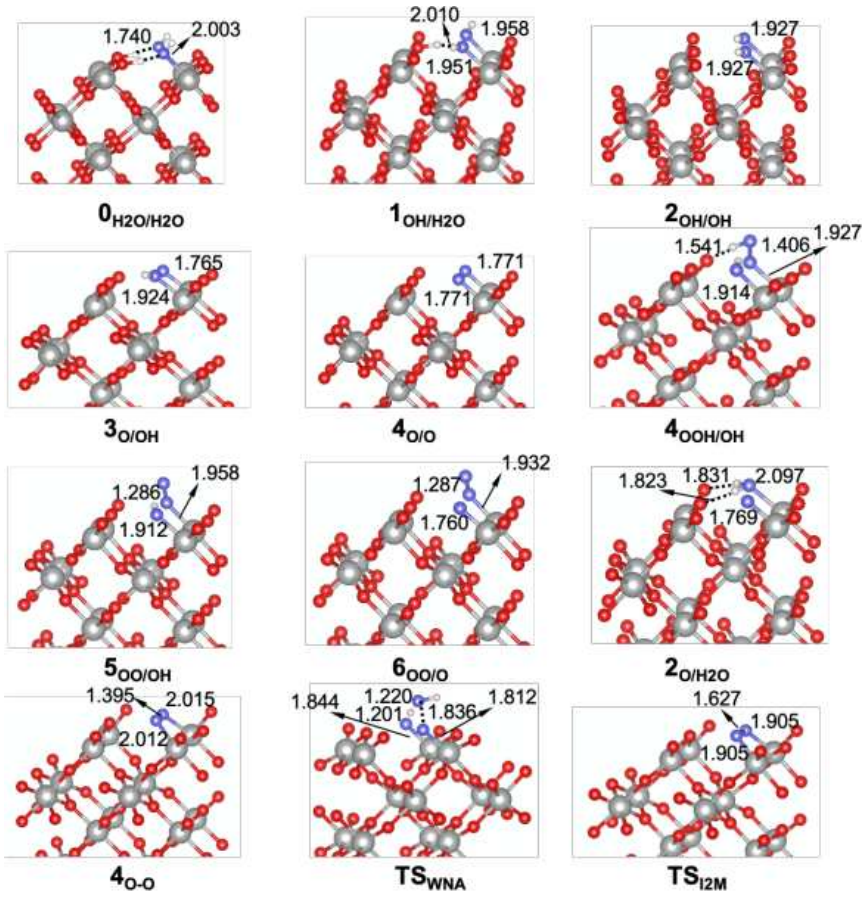

Figure B.3: Optimized structures for all intermediates and transition states associated to the OER reaction on the (100) surface. Distances in Å.

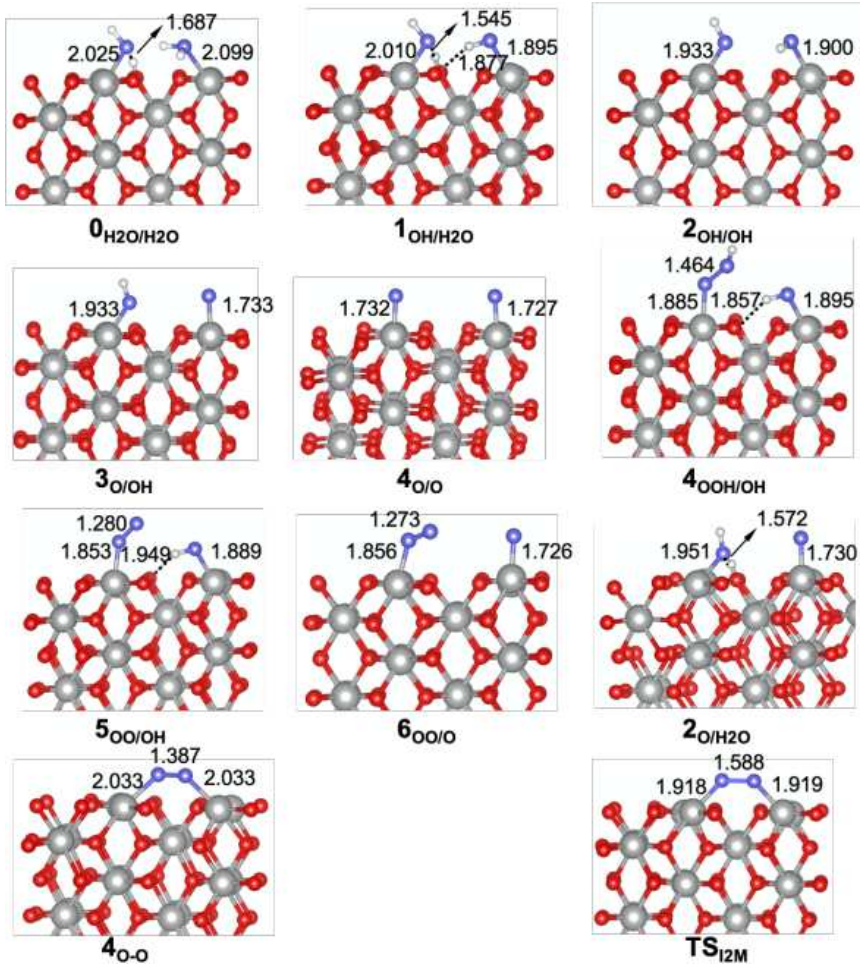

Figure B.4: Optimized structures for all intermediates and transition states associated to the OER reaction on the (110) surface. Distances in Å.

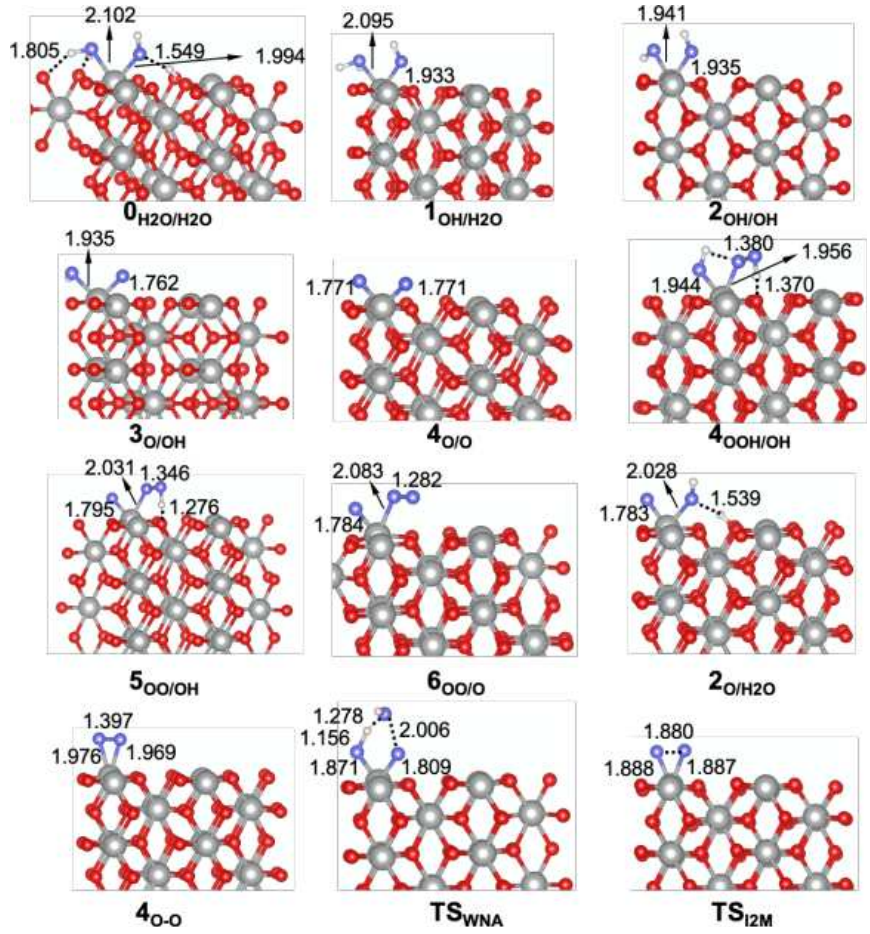

Figure B.5: Optimized structures for all intermediates and transition states associated to the OER reaction on the (001-1c) surface. Distances in Å.

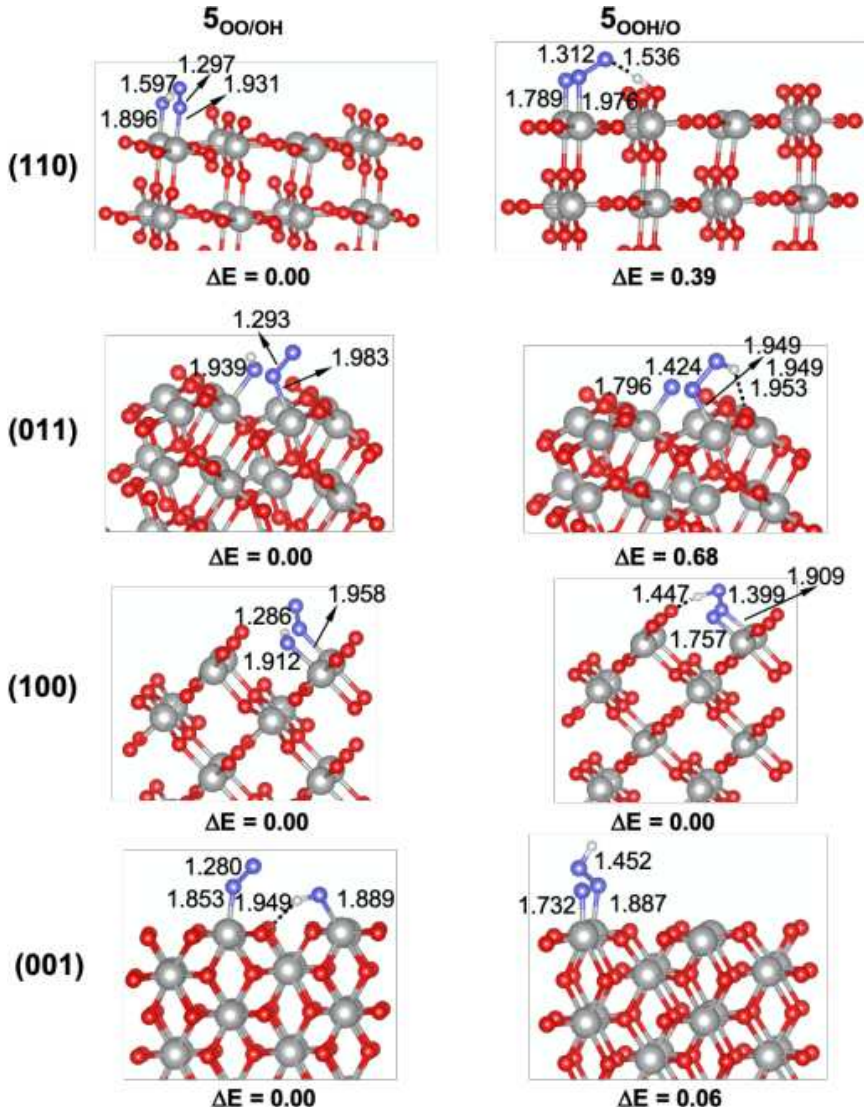

Figure B.6: Optimized structures for the $5_{OO/OH}$ and $5_{OOH/O}$ intermediates on the (110), (011), (100) and (001) considered surfaces. Distances in Å and energies in eV.

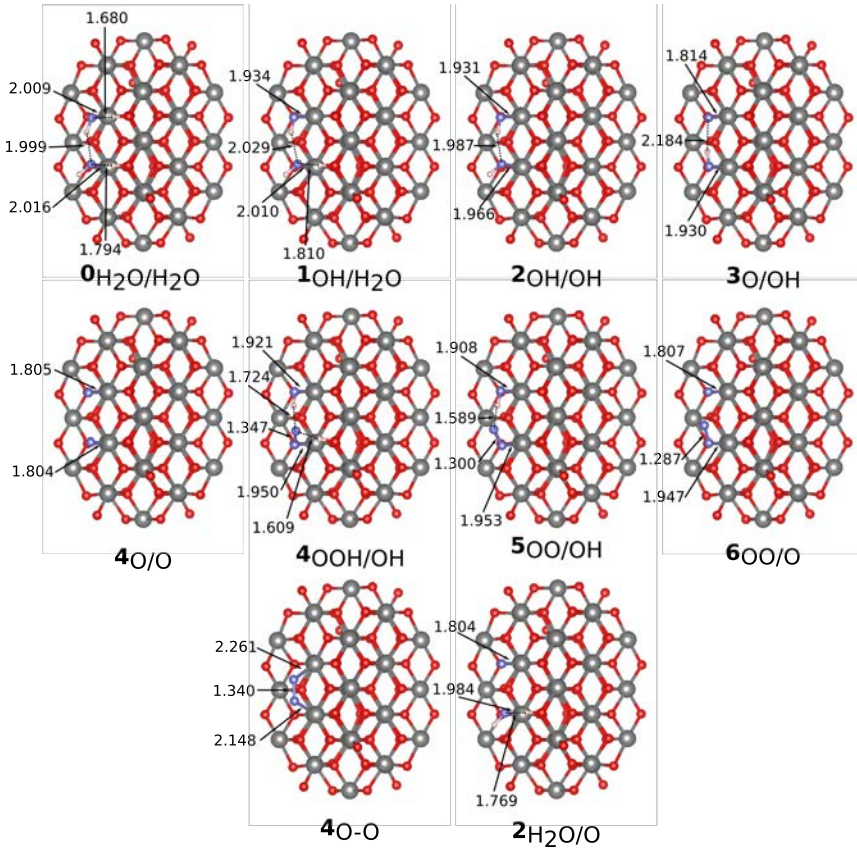

Figure B.7: Optimized structures for all intermediates and transition states associated to the OER reaction on the nanoparticle face site. Distances in Å.

Table B.4: $Ir-O_L$ distances (in Å) and magnetic moments for water oxidation steps on the studied sites of $(IrO_2)_{33}$ nanoparticle.

Site	Species	Ir_1-O_{L1}	Ir_2-O_{L2}	S_{O1}	S_{O2}	S_{Ir1}	S_{Ir2}
face	$\mathbf{0}_{H_2O/H_2O}$	2.016	2.090	0.00	0.00	-0.03	-0.03
	$\mathbf{1}_{OH/H_2O}$	2.010	1.934	0.00	0.12	-0.01	0.23
	$\mathbf{2}_{OH/OH}$	1.966	1.931	0.01	-0.12	-0.01	-0.23
	$\mathbf{3}_{O/OH}$	1.814	1.930	0.16	0.50	0.30	0.49
	$\mathbf{4}_{O/O}$	1.804	1.805	0.64	0.63	0.53	0.53
tip	$\mathbf{0}_{H_2O/H_2O}$	2.089	2.104	0.00	0.00	0.00	0.00
	$\mathbf{1}_{OH/H_2O}$	2.085	1.930	0.00	0.00	0.37	0.37
	$\mathbf{2}_{OH/OH}$	1.928	1.925	0.06	0.06	0.47	0.47
	$\mathbf{3}_{O/OH}$	1.766	1.926	-0.30	-0.02	-0.31	-0.31
	$\mathbf{4}_{O/O}$	1.772	1.771	0.26	0.23	0.41	0.41
A	$\mathbf{0}_{H_2O/H_2O}$	1.940	1.999	0.00	0.00	0.00	0.00
	$\mathbf{3}_{O/OH}$	1.760	1.930	0.18	-0.04	0.50	-0.13
	$\mathbf{4}_{O/O}$	1.767	1.794	0.24	0.56	0.48	0.36
B	$\mathbf{0}_{H_2O/H_2O}$	1.972	2.115	0.00	0.00	0.00	0.00
	$\mathbf{3}_{O/OH}$	1.777	1.947	0.39	0.00	0.24	0.24
	$\mathbf{4}_{O/O}$	1.789	1.801	-0.33	0.54	0.18	0.18
C	$\mathbf{0}_{H_2O/H_2O}$	2.024	2.126	0.00	0.00	0.00	0.00
	$\mathbf{3}_{O/OH}$	1.793	1.918	-0.20	-0.01	-0.31	-0.17
	$\mathbf{4}_{O/O}$	1.793	1.789	-0.26	0.47	-0.11	0.40
D	$\mathbf{0}_{H_2O/H_2O}$	2.183	2.055	0.00	0.00	0.55	0.04
	$\mathbf{3}_{O/OH}$	1.797	1.937	0.10	0.00	0.20	0.10
	$\mathbf{4}_{O/O}$	1.986	1.806	0.27	0.64	0.22	0.52

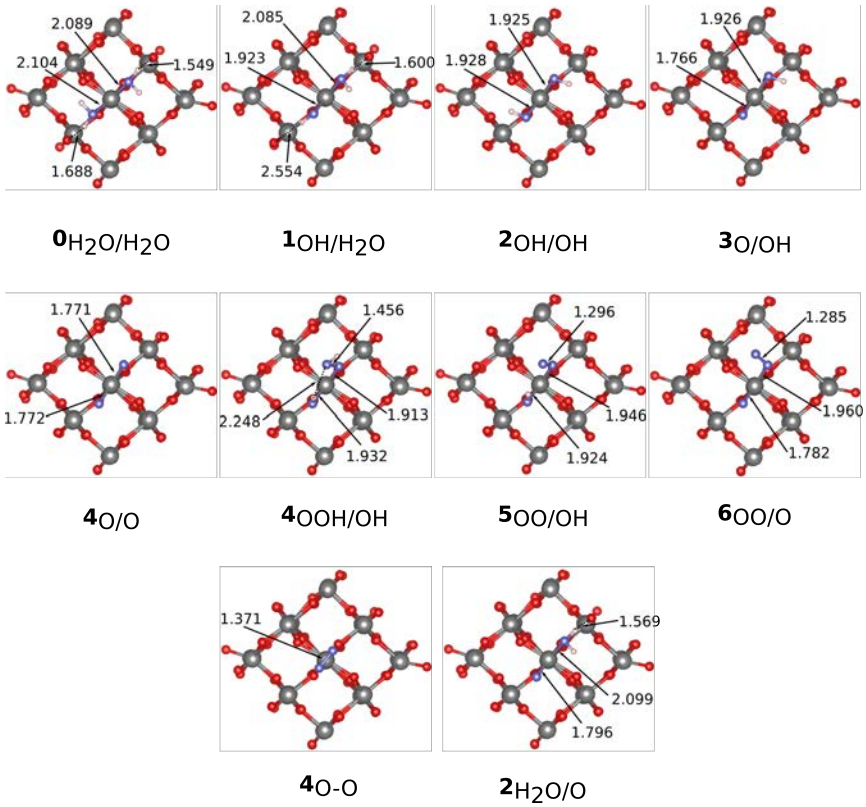

Figure B.8: Optimized structures for all intermediates and transition states associated to the OER reaction on the nanoparticle tip site. Distances in Å.

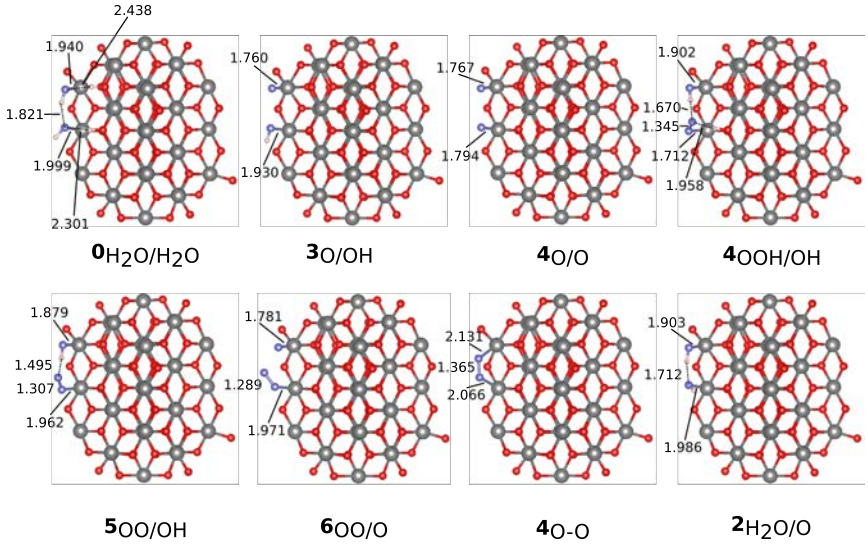

Figure B.9: Optimized structures for all intermediates and transition states associated to the OER reaction on the nanoparticle **A** site. Distances in Å.

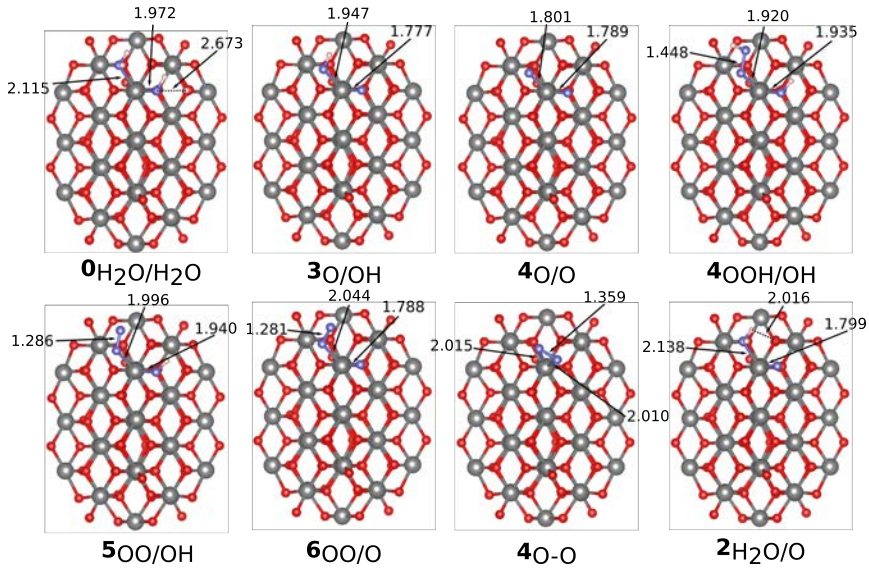

Figure B.10: Optimized structures for all intermediates and transition states associated to the OER reaction on the nanoparticle **B**site. Distances in Å.

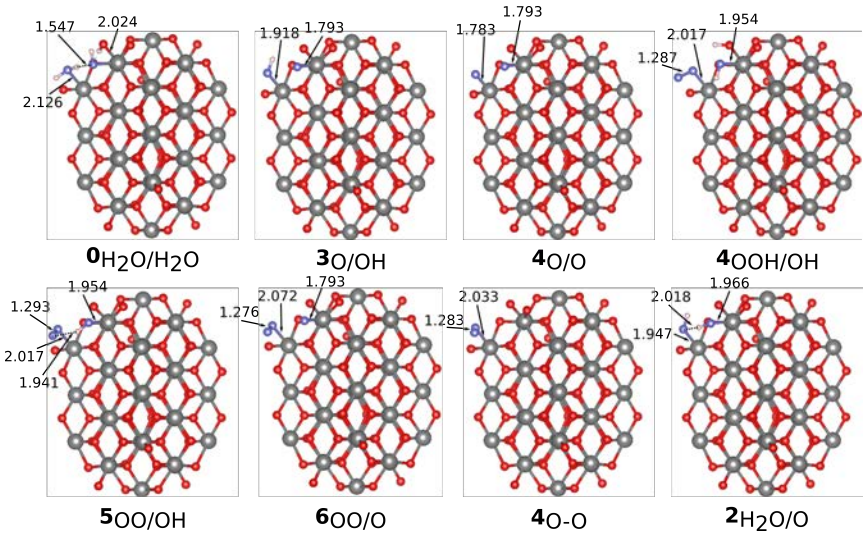

Figure B.11: Optimized structures for all intermediates and transition states associated to the OER reaction on the nanoparticle **C** site. Distances in Å.

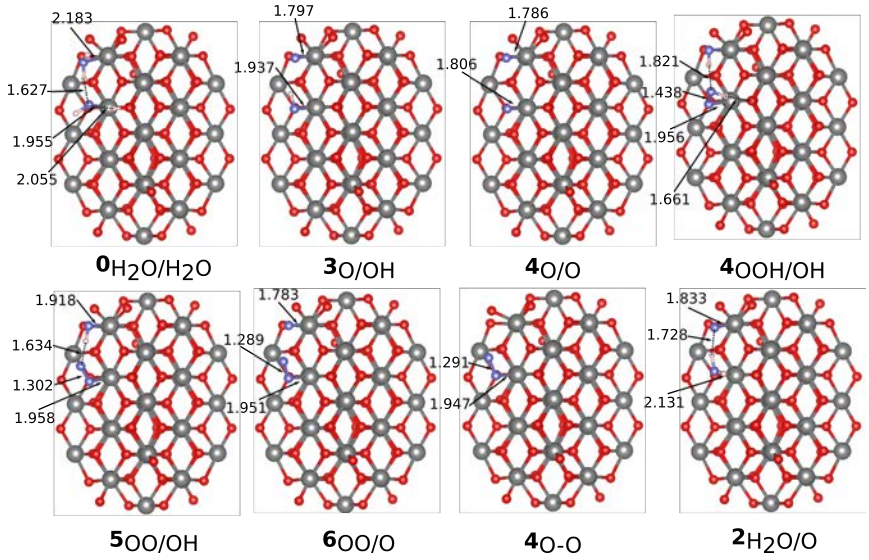

Figure B.12: Optimized structures for all intermediates and transition states associated to the OER reaction on the nanoparticle **D** site. Distances in Å.

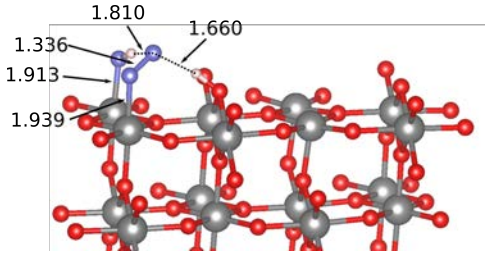

Figure B.13: Optimized structure for $\mathbf{4}_{OH/OO/O_{br}H}$ specie on the (110) surface. Distances in Å.